

Concept and Realization of the A4 Compton Backscattering Polarimeter at MAMI

Dissertation

zur Erlangung des Grades
„Doktor der Naturwissenschaften“

am Fachbereich Physik
der Johannes Gutenberg-Universität
in Mainz

von
Jeong Han Lee
geb. in Busan,
Republic of Korea

Mainz, den 15. Dezember 2008

Dekan des Fachbereichs Physik :
Erster Berichterstatter :
Zweiter Berichterstatter :
Datum der mündlichen Prüfung :

Zusammenfassung

Das Hauptinteresse der A4-Kollaboration am Mainzer Mikrotron MAMI gilt dem Beitrag der Strangequarks zu den elektromagnetischen Formfaktoren des Nukleons. Diese werden durch Messung von Einzelspin-Asymmetrien im Wirkungsquerschnitt der elastischen Streuung polarisierter Elektronen an unpolarisierten Nukleonen bestimmt. Hierzu ist es notwendig, die Polarisierung des Elektronstrahls präzise und nichtdestruktiv zu bestimmen. Deshalb wurde das A4-Compton-Rückstreu-Polarimeter entworfen und gebaut, welches eine absolute Messung der Polarisierung parallel zum Paritäts-experiment erlaubt.

Die hier vorgelegte Arbeit dokumentiert den Entwurf einer speziellen Strahl-führung für das Compton-Rückstreu-Polarimeter, die als Schikane bezeichnet wird. Diese erlaubt es, einen Wechselwirkungsbereich zwischen Laser- und Elektronstrahl herzustellen. Die Eigenschaften dieser Strahlführung werden vorgestellt. Zusätzlich wurde ein Steuerungssystem implementiert, welches in kurzer Zeit und einfach bedienbar einen Überlapp zwischen Laser- und Elektronstrahl herstellt und im Regelbetrieb verwendet werden kann.

Weiterhin wird in dieser Arbeit die Entwicklung eines Faserdetektors vorgestellt, welcher die Compton-gestreuten Elektronen nachweist und den statistischen Fehler in der Messung der Elektronpolarisation reduziert. Dieser Faserdetektor wurde von Grund auf neu entworfen und im Jahre 2008 in Koinzidenz mit dem Photon-Detektor betrieben. Die Meßdaten weisen eine Untergrund-Unterdrückung von etwa 80% auf, während die Compton-Spektren nahezu unverändert bleiben. In der hier vorgelegten vorläufigen Analyse konnte so der statistische Fehler in der Messung der Elektron-Polarisation um 40% gegenüber dem Betrieb ohne Faser-Detektor gesenkt werden. Dies stellt einen signifikanten Fortschritt auf dem Gebiet der Polarisationsmessungen dar.

Abstract

The main concern of the A4 parity violation experiment at the Mainz Microtron accelerator facility is to study the electric and magnetic contributions of strange quarks to the charge and magnetism of the nucleons at the low momentum transfer region. More precisely, the A4 collaboration investigates the strange quarks' contribution to the electric and magnetic vector form factors of the nucleons. Thus, it is important that the A4 experiment uses an adequate and precise non-destructive online monitoring tool for the electron beam polarization when measuring single spin asymmetries in elastic scattering of polarized electrons from unpolarized nucleons. As a consequence, the A4 Compton backscattering polarimeter was designed and installed such that we can take the absolute measurement of the electron beam polarization without interruption to the parity violation experiment.

The present study shows the development of an electron beam line that is called the chicane for the A4 Compton backscattering polarimeter. The chicane is an electron beam transport line and provides an interaction region where the electron beam and the laser beam overlap. After studying the properties of beam line components carefully, we developed an electron beam control system that makes a beam overlap between the electron beam and the laser beam. Using the system, we can easily achieve the beam overlap in a short time. The electron control system, of which the performance is outstanding, is being used in production beam times.

And the study presents the development of a scintillating fiber electron detector that reduces the statistical error in the electron polarization measurement. We totally redesigned the scintillating fiber detector. The data that were taken during a 2008 beam time shows a huge background suppression, approximately 80 percent, while leaving the Compton spectra almost unchanged when a coincidence between the fiber detector and the photon detector is used. Thus, the statistical error of the polarization measurement is reduced by about 40 percent in the preliminary result. They are the significant progress in measuring a degree of polarization of the electron beam.

Contents

1	Introduction	1
2	The Parity Violation Experiment	5
2.1	First-Generation Parity Violation Experiments	5
2.2	Strangeness in the Proton	8
2.3	Parity Violation and Strangeness	10
2.3.1	Theoretical Formalism	10
2.3.2	Beam Polarization Effect	16
2.3.3	Experimental Programs	16
2.4	The A4 Experiment	22
2.4.1	The Realization of the A4 Experiment	22
2.4.2	Results at Forward Scattering Angles	28
2.4.3	Measurements at Backward Scattering Angles	30
3	Compton Backscattering Polarimeter	35
3.1	Compton Scattering	36
3.1.1	Kinematics	36
3.1.2	Cross Section	40
3.1.3	Compton Asymmetry	42
3.2	Polarimeter	44
3.2.1	Measurement Time and the Luminosity	46
3.2.2	Requirements for High Luminosity	47
3.2.3	The A4 Compton Backscattering Polarimeter	48
4	Compton Backscattering Polarimeter Chicane	55
4.1	Beam Optics	55
4.1.1	Reference Particle and Beam Coordinate	56
4.1.2	Transfer Matrix	57
4.1.3	Collective Description of a Beam	58
4.2	Chicane Components	61
4.2.1	Drift Space	61

4.2.2	Dipole Magnet	61
4.2.3	Quadrupole Magnet	66
4.3	Study on the Chicane	67
4.3.1	Dispersion	67
4.3.2	Periodic System	68
4.3.3	The Chicane Simulation with TRANSPORT	71
4.4	Installation of the Compton Backscattering Polarimeter	75
5	Chicane Development	81
5.1	Wire Scanner Analysis	81
5.1.1	The Equation of Motion of the Wire Scanner	83
5.1.2	Determination of the Beam Position	89
5.1.3	Determination of the Beam Emittance	93
5.2	Realistic Chicane Simulation	95
5.2.1	Non-Ideal Properties of the Chicane	95
5.2.2	The Realistic Chicane Simulation	109
5.3	Spatial Beam Overlap at the Early Stage	110
5.4	End Result of the Chicane Development	111
5.4.1	Beam Alignment Program	112
5.4.2	Performance and Limitations	115
6	Scintillating Fiber Detector Development	121
6.1	Plastic Scintillating Fiber	122
6.1.1	Scintillation Light	122
6.1.2	Kuraray SCSF-78M Fiber	124
6.2	Construction of the Fiber Detector	125
6.2.1	Scintillating Fiber Array	125
6.2.2	Multianode Photomultiplier Tube	130
6.2.3	Fiber Array Mount	132
6.2.4	Hermetic Sealing with Epoxy	135
6.2.5	Mechanical Parts	138
6.3	Formulas and Data Handling	140
6.3.1	Cross Section Formula	140
6.3.2	Electron Polarization from A_{exp}^{CT}	142
6.3.3	Photon Spectra and Event Number	143
6.4	Preliminary Result of the Fiber Detector Development	147
6.4.1	Detector Status and Background Reduction	147
6.4.2	Experimental Compton Asymmetry	153
6.4.3	Electron Polarization Estimation	153
7	Summary and Outlook	157

Appendices	173
A Synchrotron Radiation	173
A.1 Overview of Synchrotron Radiation	173
A.1.1 Instantaneous synchrotron radiation power	173
A.1.2 Angular distribution	174
A.1.3 Spectral distribution	174
A.2 Energy Loss in the Chicane	176
A.3 Radiation on the Photon Detector	179
A.3.1 Exposure angle	180
B Input and Output of TRANSPORT	187
B.1 Input	187
B.2 Output	188
C Magnetic Field and Shunt Current Measurements	195
D Mass Attenuation Coefficients	199
E Drawings of the Scintillating Fiber Electron Detector	201
F O-ring Gland for the Vacuum Sealing	209

Chapter 1

Introduction

An *electron* is assumed to be a point-like particle and is classified as a lepton within the Standard Model framework. We also assume a *quark* has no structure. Electrons and quarks are believed to be truly elementary particles and the fundamental constituents of matter in nature. An electron is a free particle and is observable. Quarks, however, are not observable and can exist in bound states. This phenomenon is called *quark confinement*. The strong interaction by the exchange of a gluon explains the confinement.

A *proton* is observable, is a stable particle based on our knowledge, and is described as the bound state of three quarks (two *up* and one *down*). In the nonrelativistic approximation, this quark model is successful, especially, in describing the magnetic moment of the proton. However, the simple model does not take account of the dynamics of quarks and gluons. From quark distribution functions from neutrino experiments, we know that quark-antiquark pairs and gluons contribute to the proton structure. Moreover, they make a contribution to fundamental properties of the proton.

Nowadays, *polarized* leptons, especially electrons, are being used as a tool in experiments that study the fundamental constituents of matter and that understand their interactions that is known as electromagnetic and weak interactions. The electromagnetic interaction is mediated by the photon. The weak interaction has two mediators: (1) the intermediate charged bosons for the charged-current weak interaction, and (2) the neutral boson for the neutral-current weak interaction. Masses of these weak bosons are around 100 times larger than the proton mass.

The A4 experiment at the Mainzer Microtron accelerator facility (MAMI) uses a polarized electron beam to investigate the structure of the nucleon by measuring single spin asymmetries in elastic scattering of polarized electrons from unpolarized nucleons. Using longitudinally polarized electrons with alternating helicities, one asymmetry A^{PV} , which is called *parity violating*

asymmetry, allows us to access the electromagnetic vector form factors of the nucleon. These electromagnetic vector form factors are decomposed into several form factors according to quark contributions. Thus, we can study the electromagnetic contribution of strange quarks to the charge and magnetism of the nucleon at the low momentum transfer region. In addition, using transversely polarized electrons, another asymmetry A_{\perp} allows to access the combination of the imaginary parts of three generalized form factors of the proton arising from the exchange of two hard photons.

In order to determine both asymmetries, it is crucial to measure the degree of polarization of the electron beam, so polarimeters are of great importance in the A4 experiment. We used a Møller polarimeter of the A1 collaboration at MAMI to measure the beam polarization. Two experimental programs for A^{PV} [1, 2] and one program for A_{\perp} [3] were accomplished by using this Møller polarimeter. Since the Møller polarimeter is located in the experimental hall of the A1 collaboration, we cannot use it in order to monitor the polarization of the electron beam in parallel with asymmetry measurements. The main drawback of using the Møller polarimeter is that we must consider an additional error of the electron beam polarization when we use the polarization done by the Møller polarimeter to determine the asymmetries. And it takes roughly six hours to change the beam line to the A1 experimental hall, to measure the electron beam polarization, and to change the beam line to the A4 experimental halls in total. For this reason, in recent years, the A4 Compton backscattering polarimeter has been designed and has been installed as a non-destructive online monitoring tool for the electron beam polarization, so it is expected to make significant strides in reducing the error and in saving time.

The Compton polarimeter uses Compton events between an electron and a laser beam in order to determine the polarization of the electron beam if the polarization of the laser beam is known. This thesis describes the development of the Compton backscattering polarimeter chicane that contains the interaction region of the Compton backscattering and serves as the beam transport line for the A4 experiment. In addition, we study properties of this chicane and, eventually, find an electron beam control system that is cost-effective in time, easy to use, and reliable. Furthermore, we develop a scintillating fiber electron detector so as to reduce the statistical error in the polarization measurement.

The Compton polarimeter was designed for the parity violating asymmetry program and for the measurement of the longitudinal polarization of the electron beam. Thus, in chapter 2, we discuss the parity violation experiments in general and the A4 experiment in detail. In chapter 3, we summarize the

concept and implementation of the A4 Compton backscattering polarimeter. In chapter 4, we present how the chicane of the A4 Compton backscattering polarimeter works. And we study each component of the chicane and its ideal behavior. In chapter 5, we extend the study on the chicane with considering non-ideal properties of chicane components and develop an electron beam control system. In chapter 6, we describe a new design concept of the scintillating fiber detector, discuss a construction process of the detector, and present its preliminary result when this redesigned fiber detector was first used in the A4 Compton backscattering polarimeter.

Chapter 2

The Parity Violation Experiment

Weak neutral currents were introduced to make the theory of the weak interaction a renormalizable theory. In 1973, the existence of weak neutral currents was first confirmed at CERN in the Gargamelle bubble chamber [4]. Since the weak neutral currents violate parity conservation, we see the parity violation in the interference between the electromagnetic scattering amplitude and the weak one in electron-nucleon reactions. And the renormalizable theory that is called the electroweak theory can predict this interference. In this chapter, we review the first-generation parity violation experiments that supported the electroweak theory and determined coupling coefficients of electron-nucleon reactions concisely. Then we summarize strangeness contributions to the proton and its theoretical relations with the parity violation. Finally, we will discuss the second-generation parity violation experiments, which are the A4 and other parity violation experiment programs, related to the strangeness contribution to the charge and magnetism of the proton at the low momentum transfer region, i.e. the strange vector form factors of the proton.

2.1 First-Generation Parity Violation Experiments

The parity violating (PV) effective Lagrangian, which describes the parity violating part of the neutral weak current interactions between electrons and nucleons, contains four coupling coefficients $\tilde{\alpha}$, $\tilde{\beta}$, $\tilde{\gamma}$, and $\tilde{\delta}$, and is given by

[5, 6]

$$\begin{aligned} \mathcal{L}_{PV} = -\frac{G_F}{\sqrt{2}} \left\{ \bar{e}\gamma_\mu\gamma_5e \left[\frac{\tilde{\alpha}}{2} (\bar{u}\gamma^\mu u - \bar{d}\gamma^\mu d) + \frac{\tilde{\gamma}}{2} (\bar{u}\gamma^\mu u + \bar{d}\gamma^\mu d) \right] \right. \\ \left. + \bar{e}\gamma_\mu e \left[\frac{\tilde{\beta}}{2} (\bar{u}\gamma^\mu\gamma^5 u - \bar{d}\gamma^\mu\gamma^5 d) + \frac{\tilde{\delta}}{2} (\bar{u}\gamma^\mu\gamma^5 u + \bar{d}\gamma^\mu\gamma^5 d) \right] \right\}, \end{aligned} \quad (2.1)$$

where G_F is the Fermi coupling constant, $\bar{e}\gamma^\mu\gamma^5e$ and $\bar{e}\gamma^\mu e$ are referred to as the *leptonic* axial vector and vector current respectively, and u and d refer to up and down quarks. The *hadronic* currents are a combination of strong *isovector* $(\bar{u}u - \bar{d}d)/2$ and *isoscalar* $(\bar{u}u + \bar{d}d)/2$ currents. These phenomenological PV couplings $\tilde{\alpha}$, $\tilde{\beta}$, $\tilde{\gamma}$, and $\tilde{\delta}$ mean isovector vector, isovector axial vector, isoscalar vector, and isoscalar axial vector respectively. They are accessible by experiments and can be predicted by theories.

And the four coupling coefficients are redefined in terms of their combinations as follows:

$$\begin{aligned} \epsilon_{AV}^{eu} &= \frac{\tilde{\alpha} + \tilde{\gamma}}{2}, & \epsilon_{AV}^{ed} &= \frac{-\tilde{\alpha} + \tilde{\gamma}}{2}, \\ \epsilon_{VA}^{eu} &= \frac{\tilde{\beta} + \tilde{\delta}}{2}, & \epsilon_{VA}^{ed} &= \frac{-\tilde{\beta} + \tilde{\delta}}{2}. \end{aligned} \quad (2.2)$$

Thus, the PV effective Lagrangian is rewritten [7, 8]

$$\begin{aligned} \mathcal{L}_{PV} = -\frac{G_F}{\sqrt{2}} \left\{ \bar{e}\gamma_\mu\gamma_5e \left[\epsilon_{AV}^{eu}\bar{u}\gamma^\mu u + \epsilon_{AV}^{ed}\bar{d}\gamma^\mu d \right] \right. \\ \left. + \bar{e}\gamma_\mu e \left[\epsilon_{VA}^{eu}\bar{u}\gamma^\mu\gamma^5 u + \epsilon_{VA}^{ed}\bar{d}\gamma^\mu\gamma^5 d \right] \right\}, \end{aligned} \quad (2.3)$$

in terms of the hadronic axial vector current $\bar{q}\gamma^\mu\gamma^5q$ and the hadronic vector current $\bar{q}\gamma^\mu q$ where q represents each quark flavor u and d.

Using the scattering of longitudinally polarized electrons from deuterons, the SLAC $\vec{e}D$ experiment measured the parity violating effect [9, 10, 6]. In this case, these PV effects are manifested in the asymmetry $A = (\sigma_R - \sigma_L)/(\sigma_R + \sigma_L)$, where $\sigma_R(\sigma_L)$ is the cross section for scattering of right-(left-)handed electrons from deuterons. The SLAC experiment was more sensitive to the hadronic vector current than to the hadronic axial vector current, and determined linear combinations of the PV coupling constants. In the Weinberg-Salam model, the four coupling constants are related to just one

parameter $\sin^2 \theta_W$, which is called the weak-mixing angle, as follows [6]:

$$\begin{aligned}\tilde{\alpha} &= -(1 - 2 \sin^2 \theta_W), \\ \tilde{\beta} &= -(1 - 4 \sin^2 \theta_W), \\ \tilde{\gamma} &= \frac{2}{3} \sin^2 \theta_W, \\ \tilde{\delta} &= 0\end{aligned}\tag{2.4}$$

Thus, the SLAC experiment obtained the weak mixing angle

$$\sin^2 \theta_W = 0.224 \pm 0.020.$$

This result was in good agreement with the determinations of $\sin^2 \theta_W$ from various neutrino experiments. As a result, the $\vec{e}D$ experiment independently contributed the vital support for the electroweak theory in the late 1970s.

In 1989, the Mainz $\vec{e}^9\text{Be}$ experiment measured the parity violating asymmetry for quasi-elastic scattering of polarized electrons from a ^9Be target in the backward direction [11]. The experiment was designed for a separate determination of the four coupling constants and was more sensitive to the hadronic axial vector current than to the hadronic vector current. In this experiment, the PV asymmetry is directly related to a linear combination of the four coupling constants. The weak mixing angle was obtained as

$$\sin^2 \theta_W = 0.221 \pm 0.015,$$

where the error is calculated by the quadratic sum¹ of their original errors. This result improved the previous error limits on the region of $\tilde{\beta}$ and $\tilde{\delta}$, which are related to the hadronic axial vector current, by a factor of three compared with the SLAC experiment.

One year later, the Bates $\vec{e}^{12}\text{C}$ parity violation experiment measured the parity violating asymmetry in elastic scattering of polarized electron from ^{12}C nuclei [12]. In this experiment, the PV asymmetry depends on $\tilde{\gamma}$ that is the coupling constant for an axial vector coupling to the electron and an isoscalar vector coupling to the hadronic components. Then, the Bates experiment obtained

$$\tilde{\gamma} = \frac{2}{3} \sin^2 \theta_W = 0.136 \pm 0.033.$$

¹From now on we show only the quadratic sum of errors for brevity.

2.2 Strangeness in the Proton

According to *quantum chromodynamics* (QCD), the nucleon consists of three constituent quarks and is their bound state by the strong force, which is mediated by gluons. With deep inelastic scattering and e^+e^- annihilation data, QCD makes it possible to understand the internal structure of the nucleon to some degree, i.e. existence of gluons and quark-antiquark ($q\bar{q}$) pairs, which are considered to be a “*sea*”, inside the nucleon [13, 14, 15]. The quark-gluon sea contribution to the fundamental properties of the nucleon such as its mass, spin, charge radius, and magnetic moment has been an important concern, because it might provide us with vital clues about the nucleon internal structure as well as non-perturbative treatment for QCD.

The CCFR collaboration used neutrino charm production by neutrino-nucleon deep inelastic scattering to determine the size of the strange sea relative to the non-strange sea at the Fermilab Tevatron [16]. This result indicated that there is a difference between the strange and non-strange quarks in the sea of the nucleon and that the strange quarks carry about 2% of the nucleon momentum [17]. The recent result of the NuTeV collaboration was in agreement with the previous experiment [18] and they studied the difference between the nucleon strange and anti-strange quark distributions [19].

A contribution of strange quarks to the nucleon mass arises from the so-called the “ $\sigma_{\pi N}$ puzzle” that is a factor-of-two discrepancy between the empirical data for the pion-nucleon sigma term $\Sigma_{\pi N}(t)$ with momentum transfer² $t = -Q^2$ and the estimate of the σ -term from the baryon mass difference when the flavor SU(3) breaking exists [20, 21]. The empirical data of $\Sigma_{\pi N}$ can be obtained from analysis of on-shell pion-nucleon scattering amplitudes at the Cheng-Dashen point ($t = 2m_\pi^2$) [22, 20, 21, 23, 24]. One possible explanation of the discrepancy is that strange quarks in the nucleon make a large contribution to the nucleon mass [25, 21]. After $\Sigma_{\pi N}(0)$ and $\Sigma_{\pi N}(2m_\pi^2)$ were re-examined with various corrections by dispersion relations [26], it was concluded that there is no evidence for a large strange quark contribution to the nucleon mass [27]. In addition, within QCD analysis, it was argued the total strange contribution is quite small [28]. However, on the other hand one recent analysis of $\Sigma_{\pi N}(2m_\pi^2)$ shows the larger strangeness contribution to the nucleon than the previous predictions [29].

The longitudinal spin-dependent structure function $g_1(x, Q^2)$, with the Bjorken scaling variable x , as determined by deep inelastic lepton scattering from a polarized nucleon target, contains experimental information about the strange quark contribution to the nucleon spin and can be extracted from the

² Q^2 is the squared four momentum transfer.

asymmetry $A = (\sigma^{++} - \sigma^{-+})/(\sigma^{++} + \sigma^{-+})$, where σ^{++} and σ^{-+} refer to cross sections for parallel and anti-parallel lepton and nucleon spins [13, 24]. For the proton, the integral over the spin-dependent structure function provides explicit information on the quark spin structure at long distance scales and is [24]

$$\Gamma_1^p(Q^2) = \int_0^1 dx g_1(x, Q^2) = \frac{4}{18}\Delta u + \frac{1}{18}\Delta d + \frac{1}{18}\Delta s,$$

where Δu , Δd , and Δs are the first moments of the polarized u, d, and s quark distribution. The u quark distribution is defined as

$$\Delta u = \int_0^1 dx (u^+(x) - u^-(x) + \bar{u}^+(x) - \bar{u}^-(x)),$$

where $+(-)$ denotes that quark whose helicity is parallel (anti-parallel) to that of the nucleon and \bar{u} is the u anti-quark. The similar definition applies Δd and Δs . It is convenient to write the integral in terms of the isovector (Δq^3), octet (Δq^8), and singlet (Δq^0) combinations, such that

$$\Gamma_1^p(Q^2) = \frac{\Delta q^3}{12} + \frac{\Delta q^8}{36} + \frac{\Delta q^0}{9}, \quad (2.5)$$

where

$$\begin{aligned} \Delta q^3 &= \Delta u - \Delta d, \\ \Delta q^8 &= \Delta u + \Delta d - 2\Delta s, \\ \Delta q^0 &= \Delta u + \Delta d + \Delta s, \end{aligned} \quad (2.6)$$

in the naive parton model. The isovector combination Δq^3 , which will be discussed later, can be obtained from neutron beta decay, and Δq^8 from hyperon beta decay. Thus, Δq^0 , which is the fraction of the spin of the proton carried by the spins of the quarks, can also be determined. Since the Ellis-Jaffe sum rule assumed that polarized strange quarks do not contribute to the spin-dependent structure function ($\Delta s = 0$), the integral is rewritten [30, 24]

$$\Gamma_1^p(Q^2) = \frac{1}{12}\Delta q^3 + \frac{5}{36}\Delta q^8, \quad (2.7)$$

where $\Delta q^0 = \Delta q^8$. The first measurement of this integral was taken by European Muon Collaboration (EMC) and found a disagreement with the Ellis-Jaffe sum rule. This result indicated that the quark spins carry $(1 \pm 27)\%$ of the proton spin if $\Delta s \neq 0$ was assumed [31]. The EMC collaboration combined their data with the SLAC-Yale E80 and E130 data to extend the

kinematic range of the spin-dependent structure function. This result indicated that the strange quarks polarized antiparallel to the proton spin and the quark spins carry $(12 \pm 17)\%$ of the proton spin [32]. The E143 collaboration found that their result is more than two standard deviations below the Ellis-Jaffe sum rule prediction and that the strange quark contribution is $\Delta s = -0.10 \pm 0.04$, inconsistent with zero by using the naive quark-parton model [33]. The Spin Muon Collaboration (SMC) found that the integral is also below the prediction of the Ellis-Jaffe sum rule and that the quark spin contributions to the proton spin as a function of the gluon contribution Δg in QCD [34]. They obtained the gluon contribution to the proton spin ($\Delta g \simeq 2$) in the Adler-Bardeen renormalization scheme. This gluon contribution implies that $\Delta s = 0$. However, they mentioned that the gluon contribution could be smaller than what they obtained. In this case, Δs could be negative. More recently, the COmmon Muon Proton Apparatus for Structure and Spectroscopy (COMPASS) experiment at CERN measured the deuteron spin-dependent structure function g_1^d . They found that the strange quark distribution is $\Delta s = -0.08 \pm 0.02$ [35].

2.3 Parity Violation and Strangeness

Feasible measurements of the strange-quark vector current matrix element for the proton $\langle p | \bar{s} \gamma_\mu s | p \rangle$, which is related to the electromagnetic properties of the proton, were suggested to perform parity violating electron scattering from protons [36, 37, 38]. These measurements provide one opportunity to study a possible strange quark contribution to the nucleon electromagnetic properties such as charge distribution and magnetism if the existing data on the nucleon electromagnetic form factors are used.

2.3.1 Theoretical Formalism

The parity violating asymmetry is

$$A_{\text{phys}}^{PV} = \frac{d\sigma_R - d\sigma_L}{d\sigma_R + d\sigma_L},$$

where $d\sigma_R(d\sigma_L)$ is the cross section for right(left)-handed electron scattering. For convenience, A_{phys}^{PV} is called the physics asymmetry so as to distinguish between A_{phys}^{PV} and the experimental asymmetry A_{exp}^{PV} . Since the cross section is proportional to the square of the scattering amplitude

$$d\sigma \propto |\overline{\mathcal{M}}|^2 = \overline{\sum_{\text{spins}} |\mathcal{M}|^2},$$

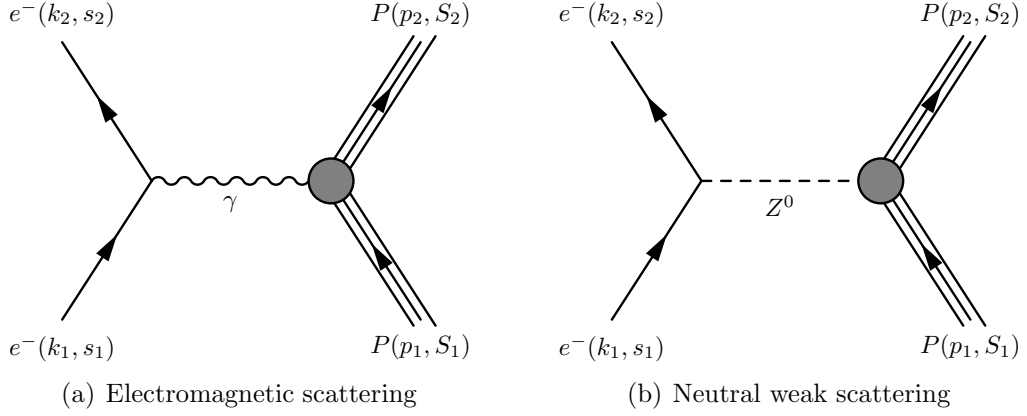


Figure 2.1 The two lowest-order Feynman diagrams for the electron proton scattering. The initial four momentum and the spin state of the electron (the proton) are denoted as k_1 and s_1 (p_1 and S_1) and the final one k_2 and s_2 (p_2 and S_2) respectively. The four momentum q of the internal line is $q = k_1 - k_2 = p_2 - p_1$ due to momentum conservation.

where $\overline{\sum_{\text{spins}}}$ represents an average and a sum over the spin orientations of particles, the asymmetry is

$$A_{\text{phys}}^{PV} = \frac{|\overline{\mathcal{M}_R}|^2 - |\overline{\mathcal{M}_L}|^2}{|\overline{\mathcal{M}_R}|^2 + |\overline{\mathcal{M}_L}|^2}. \quad (2.8)$$

Figure 2.1 shows the two lowest-order Feynman diagrams for the electron proton scattering that contribute to the squared amplitude $|\overline{\mathcal{M}}|^2$. The first diagram 2.1(a) represents the electromagnetic interaction and the other one 2.1(b) the weak interaction. Thus we rewrite the squared scattering amplitude

$$|\overline{\mathcal{M}_{R,L}}|^2 = |\overline{\mathcal{M}_{R,L}^\gamma + \mathcal{M}_{R,L}^{Z^0}}|^2 = |\overline{\mathcal{M}_{R,L}^\gamma}|^2 + 2\overline{\mathcal{M}_{R,L}^{\dagger\gamma} \mathcal{M}_{R,L}^{Z^0}} + |\overline{\mathcal{M}_{R,L}^{Z^0}}|^2,$$

where \dagger is the Hermitian adjoint and $\overline{\mathcal{M}_{R,L}^{\dagger\gamma} \mathcal{M}_{R,L}^{Z^0}} = \overline{\mathcal{M}_{R,L}^\gamma \mathcal{M}_{R,L}^{\dagger Z^0}}$. The first term is the contribution from the electromagnetic interaction, the last one from the weak interaction, and the middle one the interference between both interactions. The parity violating asymmetry becomes

$$A_{\text{phys}}^{PV} \approx 2 \frac{\overline{\mathcal{M}_R^{\dagger\gamma} \mathcal{M}_R^{Z^0}} - \overline{\mathcal{M}_L^{\dagger\gamma} \mathcal{M}_L^{Z^0}}}{|\overline{\mathcal{M}_R^\gamma}|^2 + |\overline{\mathcal{M}_L^\gamma}|^2} = 2 \frac{\sum \mathcal{M}_R^{\dagger\gamma} \mathcal{M}_R^{Z^0} - \sum \mathcal{M}_L^{\dagger\gamma} \mathcal{M}_L^{Z^0}}{\sum |\mathcal{M}^\gamma|^2}, \quad (2.9)$$

where \sum represents $\sum_{s_1} \sum_{s_2} \sum_{S_1} \sum_{S_2}$, which means the spin sum over all initial and final spins of the proton and the electron, and we use the relation

$$\sum |\mathcal{M}_R^\gamma|^2 = \sum |\mathcal{M}_L^\gamma|^2 \equiv \frac{1}{2} \sum |\mathcal{M}^\gamma|^2,$$

which means that the electromagnetic interaction conserves a parity. We can ignore the interference term in the denominator and the weak contribution term $|\overline{\mathcal{M}}_{R,L}^{Z^0}|^2$, because of the low momentum transfer region ($-q^2 \ll M_Z^2$).

The invariant matrix element of the electromagnetic interaction in the ultra-relativistic limit, where the electron mass can be ignored ($m_e \approx 0$), is [39]

$$\mathcal{M}_{R,L}^\gamma = -i \frac{e^2}{q^2} \bar{\mathcal{U}}(p_2, S_2) \Gamma^\mu \mathcal{U}(p_1, S_1) \bar{u}(k_2, s_2) \gamma_\mu u_{R,L}(k_1, s_1), \quad (2.10)$$

where

$$\begin{aligned} \Gamma^\mu &= \gamma^\mu F_1^p(q^2) + \frac{i\sigma^{\mu\nu} q_\nu}{2M_p} F_2^p(q^2), \\ u_{R,L}(k_1) &= \frac{1 \pm \gamma^5}{2} u(k_1), \end{aligned} \quad (2.11)$$

M_p is the proton mass, $u(k_i, s_i)$ represents the Dirac spinor with the four momentum k_i and the spin s_i for the electron with $i = 1, 2$, and $\mathcal{U}(p_i, S_i)$ is the proton spinor. F_1^p and F_2^p are two independent electromagnetic form factors that describe the structure of a proton. F_1^p is called the Dirac form factor and F_2^p the Pauli form factor of the proton. In the same manner, the invariant matrix element of the weak interaction in the ultra-relativistic limit and the low momentum transfer region is

$$\mathcal{M}_{R,L}^Z = +i \frac{g_Z^2}{16M_Z^2} \bar{\mathcal{U}}(p_2, S_2) \tilde{\Gamma}^\mu \mathcal{U}(p_1, S_1) \bar{u}(k_2, s_2) \tilde{\gamma}_\mu u_{R,L}(k_1, s_1), \quad (2.12)$$

where

$$\begin{aligned} \tilde{\Gamma}^\mu &= \gamma^\mu \tilde{F}_1^p(q^2) + \frac{i\sigma^{\mu\nu} q_\nu}{2M_p} \tilde{F}_2^p(q^2) + \gamma^\mu \gamma^5 \tilde{G}_A^p(q^2), \\ \tilde{\gamma}_\mu &= q_Z^e \gamma_\mu + a_Z^e \gamma_\mu \gamma_5, \\ \frac{g_Z^2}{16M_Z^2} &= \frac{G_F}{2\sqrt{2}}, \end{aligned} \quad (2.13)$$

with \tilde{F}_1^p and \tilde{F}_2^p being the two weak form factors, \tilde{G}_A^p the weak axial form factor, θ_W the weak mixing angle, g_Z the neutral weak coupling constant for the Z^0 boson, and G_F the Fermi coupling constant. The coefficients q_Z^e and a_Z^e are defined in table 2.1. The expression $\frac{g_Z^2}{16M_Z^2}$ for the leading coefficient of (2.12) can be easily interpreted that the neutral weak current interaction is

f	I_3	q_γ^f	q_Z^f	a_Z^f
e^-	$-\frac{1}{2}^*$	-1	$-1 + 4 \sin^2 \theta_W$	$+1$
u quark	$+\frac{1}{2}$	$+\frac{2}{3}$	$+1 - \frac{8}{3} \sin^2 \theta_W$	-1
d quark	$-\frac{1}{2}$	$-\frac{1}{3}$	$-1 + \frac{4}{3} \sin^2 \theta_W$	$+1$
s quark	$-\frac{1}{2}$	$-\frac{1}{3}$	$-1 + \frac{4}{3} \sin^2 \theta_W$	$+1$

Table 2.1 Electroweak couplings of electron and quarks [17, 13]. The weak vector coupling denotes as q_Z^f , the weak axial coupling a_Z^f , the electromagnetic coupling or the electric charge q_γ^f , and the third component of the weak isospin I . Here $q_Z^f = 2I_3 - 4q_\gamma^f \sin^2 \theta_W$. And the symbol * means that I_3 of the left-handed electron is $-1/2$, and the right-handed electron has $I = 0$.

weak owing to the mass of Z^0 boson. The expression $\frac{G_F}{2\sqrt{2}}$, however, is more convenient when calculating radiative corrections at one-loop order [40].

The asymmetry therefore can be calculated from (2.9) at tree level and is

$$\begin{aligned}
A_{\text{phys}}^{PV} = & -\frac{G_F Q^2}{4\sqrt{2}\pi\alpha} \\
& \times \left\{ \left(2\tau \tan^2 \frac{\theta}{2} (F_1^p + F_2^p) (\tilde{F}_1^p + \tilde{F}_2^p) + F_1 \tilde{F}_1^p + \tau F_2^p \tilde{F}_2^p \right) \right. \\
& \quad \left. - \frac{E + E'}{M_p} \tan^2 \frac{\theta}{2} (1 - 4 \sin^2 \theta_W) \tilde{G}_A^p (F_1^p + F_2^p) \right\} \\
& \times \left\{ (F_1^p)^2 + \tau (F_2^p)^2 + (F_1^p + F_2^p)^2 2\tau \tan^2 \frac{\theta}{2} \right\}^{-1},
\end{aligned} \tag{2.14}$$

where

$$\begin{aligned}
\alpha = \frac{e^2}{4\pi}, \quad Q^2 = -q^2 > 0, \quad \tau = \frac{Q^2}{4M_p}, \\
\frac{E + E'}{M_p} = \sqrt{4\tau(1 + \tau) \csc^2 \frac{\theta}{2}},
\end{aligned}$$

with θ is the electron scattering angle. Note that the physics asymmetries in the references [37, 38] have different constant factors compared with (2.14), because the weak form factors (\tilde{F}_1^p , \tilde{F}_2^p , and \tilde{G}_A^p) are defined in the different forms. Since we consider only the low momentum transfer, it is preferable to use the Sachs form factor notation

$$\begin{aligned}
G_E = F_1 - \tau F_2, \quad G_M = F_1 + F_2, \\
\tilde{G}_E = \tilde{F}_1 - \tau \tilde{F}_2, \quad \tilde{G}_M = \tilde{F}_1 + \tilde{F}_2,
\end{aligned} \tag{2.15}$$

where G_E and G_M of the proton describe the distribution of charge and magnetization within the proton. The physics asymmetry, therefore, is rewritten as [41]

$$A_{\text{phys}}^{PV} = - \frac{G_F Q^2}{4\sqrt{2}\pi\alpha} \frac{\epsilon G_E^p \tilde{G}_E^p + \tau G_M^p \tilde{G}_M^p - \epsilon'(1 - 4\sin^2\theta_W)\tilde{G}_A^p G_M^p}{\epsilon (G_E^p)^2 + \tau (G_M^p)^2}, \quad (2.16)$$

where

$$\begin{aligned} \epsilon^{-1} &= 1 + 2(1 + \tau) \tan^2 \frac{\theta}{2}, \\ \epsilon' &= \sqrt{\tau(1 + \tau)(1 - \epsilon)(1 + \epsilon)}. \end{aligned}$$

Considering only u, d, and s quarks, nucleon form factors, by which the hadronic structure of the electroweak interaction is parametrized, are decomposed into three different flavor quark form factors [38]. Using the electroweak coupling constants defined in table 2.1, we can write

$$\begin{aligned} \Gamma^\mu &= \sum_f q_\gamma^f \left[F_1^f \gamma^\mu + \frac{i\sigma^{\mu\nu} q_\nu}{2M_p} F_2^f \right], \\ \tilde{\Gamma}^\mu &= \sum_f \left[q_Z^f \left(F_1^f \gamma^\mu + \frac{i\sigma^{\mu\nu} q_\nu}{2M_p} F_2^f \right) + a_Z^f G_A^f \gamma^\mu \gamma^5 \right], \end{aligned} \quad (2.17)$$

with $f = u, d, s$. Then, the electromagnetic and weak form factors are

$$\begin{aligned} G_{E,M}^p &= \sum_f q_\gamma^f G_{E,M}^f = \frac{2}{3} G_{E,M}^u - \frac{1}{3} G_{E,M}^d - \frac{1}{3} G_{E,M}^s, \\ \tilde{G}_{E,M}^p &= \sum_f q_Z^f G_{E,M}^f = \left(1 - \frac{8}{3} \sin^2 \theta_W \right) G_{E,M}^u \\ &\quad + \left(-1 + \frac{4}{3} \sin^2 \theta_W \right) G_{E,M}^d + \left(-1 + \frac{4}{3} \sin^2 \theta_W \right) G_{E,M}^s, \\ \tilde{G}_A^p &= \sum_f a_Z^f G_A^f = G_A^u - G_A^d - G_A^s. \end{aligned} \quad (2.18)$$

In the above equation, the proton weak axial form factor \tilde{G}_A^p without higher order terms is [41]

$$\tilde{G}_A^p(Q^2) = -2G_A^{(3)}(Q^2) + G_A^{(s)}(Q^2), \quad (2.19)$$

where

$$G_A^{(3)}(Q^2) = \frac{\Delta q^3}{2 \left(1 + \frac{Q^2}{M_A^2}\right)^2} \equiv -\frac{1}{2} \tilde{G}_A^{T=1}(Q^2),$$

$$G_A^{(s)}(Q^2) = \frac{G_A^{(s)}(Q^2=0)}{\left(1 + \frac{Q^2}{M_A^2}\right)^2} \equiv \tilde{G}_A^{T=0}(Q^2),$$

with $\tilde{G}_A^{T=0,1}(Q^2)$ being the isoscalar ($T = 0$) and isovector ($T = 1$) components of $G_A^p(Q^2)$. In these equations, M_A is the axial vector dipole mass parameter obtained from neutrino scattering. Δq^3 is the same quantity as in (2.5) and is determined from neutron beta decay. $G_A^{(s)}(0)$ may be rewritten in terms of Δq^8 and Δq^0 , also defined in (2.5) and can be extracted from measurements of $\int dx g_1(x)$ [41, 17, 14, 42].

Assuming isospin symmetry, i.e. proton and neutron are treated as an isospin doublet of the nucleon, we get the following relations

$$\begin{aligned} G_{E,M}^u &\equiv G_{E,M}^{u,p} = G_{E,M}^{d,n}, \\ G_{E,M}^d &\equiv G_{E,M}^{d,p} = G_{E,M}^{u,n}, \\ G_{E,M}^s &\equiv G_{E,M}^{s,p} = G_{E,M}^{s,n}. \end{aligned} \quad (2.20)$$

Then, the neutron electromagnetic form factor becomes

$$G_{E,M}^n = \frac{2}{3} G_{E,M}^d - \frac{2}{3} G_{E,M}^u - \frac{1}{3} G_{E,M}^s, \quad (2.21)$$

and the weak vector form factor $\tilde{G}_{E,M}^p$ of the proton is shown in terms of $G_{E,M}^p$, $G_{E,M}^n$, and $G_{E,M}^s$ as

$$\tilde{G}_{E,M}^p = (1 - 4 \sin^2 \theta_W) G_{E,M}^p - G_{E,M}^n - G_{E,M}^s. \quad (2.22)$$

With (2.16) and (2.22), we can rewrite the asymmetry A_{phys}^{PV} without electroweak radiative corrections as

$$A_{\text{phys}}^{PV} = A_V + A_A = A_V^0 + A_V^s + A_A, \quad (2.23)$$

where

$$\begin{aligned} A_V^0 &= -\frac{G_F Q^2}{4\sqrt{2}\pi\alpha} \left[(1 - 4 \sin^2 \theta_W) - \frac{\epsilon G_E^p G_E^n + \tau G_M^p G_M^n}{\epsilon (G_E^p)^2 + \tau (G_M^p)^2} \right], \\ A_V^s &= +\frac{G_F Q^2}{4\sqrt{2}\pi\alpha} \left[\frac{\epsilon G_E^p G_E^s + \tau G_M^p G_M^s}{\epsilon (G_E^p)^2 + \tau (G_M^p)^2} \right], \\ A_A &= +\frac{G_F Q^2}{4\sqrt{2}\pi\alpha} \left[\frac{(1 - 4 \sin^2 \theta_W) \epsilon' G_M^p \tilde{G}_A^p}{\epsilon (G_E^p)^2 + \tau (G_M^p)^2} \right]. \end{aligned} \quad (2.24)$$

The term A_V represents the asymmetry that comes from the vector coupling on the proton vertex and A_A does the asymmetry that comes from the axial vector coupling. In addition, A_V can be rewritten in terms of A_V^0 and A_V^s in order to separate the strangeness contribution to the vector coupling. The PV physics asymmetry A_{phys}^{PV} , therefore, depends on G_E^p , G_E^n , G_M^p , and G_M^n that are well-known form factors for the proton and neutron. Using them and (2.19), in principle, the equation (2.23) leads us to get $A_V^0 + A_A$ and a linear combination of the Sachs form factors G_E^s and G_M^s , in the A_V^s term, when neglecting electroweak radiative corrections and assuming the isospin symmetry. For more detailed information about radiative corrections and charge symmetry, see the references [40, 43, 17]. The linear combination of the strange electric and magnetic form factors is

$$G_E^s + \eta G_M^s = \frac{4\sqrt{2}\pi\alpha\epsilon(G_E^p)^2 + \tau(G_M^p)^2}{G_F Q^2 \epsilon G_E^p} (A_{\text{phys}}^{PV} - A_V^0 - A_A), \quad (2.25)$$

with $\eta = \tau G_M^p / \epsilon G_E^p$.

2.3.2 Beam Polarization Effect

The PV experimental asymmetry A_{exp}^{PV} is related to the physics asymmetry via

$$A_{\text{exp}}^{PV} = \frac{N^R - N^L}{N^R + N^L} = P_e \cdot A_{\text{phys}}^{PV}, \quad (2.26)$$

where $N^{R(L)}$ is the number of elastic scattering events for each polarization state of electrons and P_e the longitudinal polarization of the electron beam. Thus, it is crucial to measure the beam polarization P_e so as to extract the physics asymmetry. For an absolute P_e measurement, the A4 Compton backscattering polarimeter has been installed. A detailed study of the polarimeter will be discussed in chapter 3.

2.3.3 Experimental Programs

The SAMPLE experiment

The first experiment to determine the strange quark-antiquark ($s\bar{s}$) contributions to the electromagnetic properties of the proton by the parity violating asymmetry in electron scattering was the SAMPLE experiment at the MIT/Bates Linear Accelerator Center. Using a 200 MeV longitudinally polarized electron, they measured the asymmetry at backward angles with an average $Q^2 = 0.1$ (GeV/c)² [44, 45]. The electron beam polarization was

measured using a Møller apparatus and is typically 35%. Under these kinematic conditions, the PV asymmetries for a hydrogen target (SAMPLE I) and a deuterium target (SAMPLE II) [46] were measured. The results can be interpreted as a small strange quarks contribution to the proton magnetic moment. Moreover, the experimental result of $\tilde{G}_A^{T=1}(Q^2 = 0.1)^3$ has the substantially different value compared with the theoretical expected value. This may indicate that the electroweak radiative corrections to the axial vector form factor are larger than the theoretical expectation [47, 48, 49]. Because of this discrepancy, the third SAMPLE experiment (SAMPLE III) measured the parity violating asymmetry in quasielastic electron scattering from deuterons at backward angles at $Q^2 = 0.038$ (GeV/c)² so as to determine the axial vector form factor experimentally [50]. In the same manner of the analysis of SAMPLE III, they re-evaluated the theoretical asymmetry and the measured asymmetry for the SAMPLE II data. The resulting theoretical asymmetry is

$$A_d(Q^2 = 0.091) = \left(-7.06 + 1.66\tilde{G}_A^{T=1} + 0.77G_M^s \right) \text{ ppm}, \quad (2.27)$$

where d stands for a deuterium target and ppm is *part per million*. The physics asymmetry is

$$A_d(Q^2 = 0.091) = (-7.77 \pm 0.92) \text{ ppm}. \quad (2.28)$$

These results from the SAMPLE III ($Q^2 = 0.038$) data and from the updated SAMPLE II ($Q^2 = 0.091$) data are in agreement with the theoretical calculations of the neutral weak axial vector form factor \tilde{G}_A [47]. With the confirmation of the theoretical estimation of the weak axial vector form factor, they re-evaluated the SAMPLE I hydrogen data. Thus, the theoretical asymmetry is obtained as

$$A_p(Q^2 = 0.1) = \left(-5.56 + 1.54\tilde{G}_A^{T=1} + 3.37G_M^s \right) \text{ ppm}, \quad (2.29)$$

where p stands for a hydrogen target and the asymmetry is

$$A_p(Q^2 = 0.1) = (-5.61 \pm 1.11) \text{ ppm}. \quad (2.30)$$

Using equations (2.27), (2.28), (2.29), (2.30), and the theoretical calculation of $\tilde{G}_A^{T=1} = -0.83 \pm 0.26$, the results of the SAMPLE experiment [51, 52] are shown in figure 2.2 and the strange magnetic form factor is

$$G_M^s(Q^2 = 0.1) = 0.37 \pm 0.34. \quad (2.31)$$

³For the sake of simplicity, we omit (GeV/c)², the unit of Q^2 .

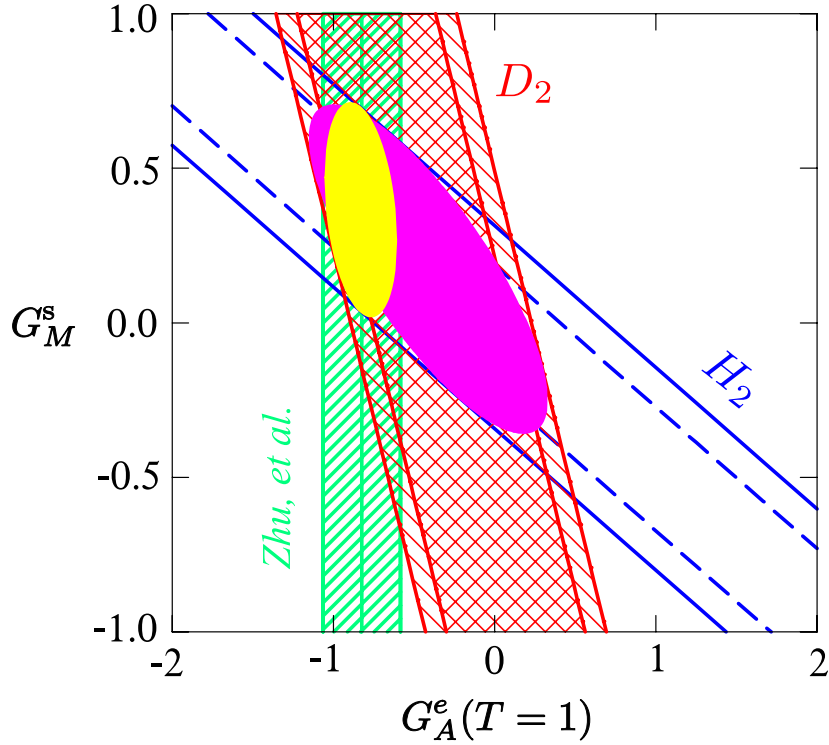


Figure 2.2 The result of the SAMPLE experiment at $Q^2 = 0.1 \text{ (GeV}/c)^2$ [52, 51]. In the plot, $\tilde{G}_A^{T=1}$ is denoted as $G_A^e(T=1)$ and the band labeled *Zhu, et al.* represents the theoretical expectation [47]. The deuterium and hydrogen data are denoted as D_2 and H_2 respectively. The small ellipse is the overlap between the hydrogen data and the theoretical expectation and the large one between the hydrogen and deuterium data. The plotted uncertainties are calculated by the sum in quadrature of the statistical and systematic uncertainties.

The HAPPEX experiment

Just as the SAMPLE experiment determined the strange magnetic form factor G_M^s of the proton, similarly, the HAPPEX experiment in Hall A at the Thomas Jefferson National Accelerator Facility (TJNAF) was designed to determine the strange electric form factor G_E^s . The first HAPPEX experiment (HAPPEX I) chose a small forward angle ($\theta_{\text{lab}} = 12.3^\circ$) and the higher $Q^2 = 0.477 \text{ (GeV}/c)^2$ in order to measure a combination of G_M^s and G_E^s . Using elastic scattering of longitudinally polarized electrons from protons, the linear combination of strange form factors [53, 54, 55] is

$$G_E^s + 0.392G_M^s|_{Q^2=0.477} = 0.014 \pm 0.022. \quad (2.32)$$

The second HAPPEX experiment (HAPPEX- ^4He) opted for ^4He target with a very small forward angle ($\theta_{\text{lab}} = 6^\circ$) and $Q^2 = 0.1 \text{ (GeV}/c)^2$ so as to isolate G_E^s . Since ^4He is an isoscalar target, which consists of equal number of protons and neutrons, the parity violating asymmetry is sensitive to only G_E^s . The strange electric form factor G_E^s is [56]

$$G_E^s(Q^2 = 0.091) = -0.038 \pm 0.043. \quad (2.33)$$

The third HAPPEX experiment (HAPPEX-H) used a proton target at $Q^2 = 0.091$. The linear combination of G_E^s and G_M^s [57] is

$$G_E^s + 0.080G_M^s|_{Q^2=0.091} = 0.030 \pm 0.066. \quad (2.34)$$

The most recent HAPPEX experiment [58, 59] reported the strange electric form factor for ^4He target with $Q^2 = 0.077 \text{ (GeV}/c)^2$ and an angle ($\theta_{\text{lab}} \sim 6^\circ$)

$$G_E^s(Q^2 = 0.077) = +0.002 \pm 0.016. \quad (2.35)$$

And they reported the linear relation between G_E^s and G_M^s with $Q^2 = 0.109 \text{ (GeV}/c)^2$ for a hydrogen target

$$G_E^s + 0.09G_M^s|_{Q^2=0.109} = 0.007 \pm 0.013. \quad (2.36)$$

Using extrapolation to $Q^2 = 0.1 \text{ (GeV}/c)^2$ with assumptions that $G_E^s \propto Q^2$ and that G_M^s is constant, the HAPPEX collaboration combined (2.35), (2.36), (2.33), (2.34) and extracted G_E^s and G_M^s as [58]

$$\begin{aligned} G_E^s(Q^2 = 0.1) &= -0.005 \pm 0.019, \\ G_M^s(Q^2 = 0.1) &= +0.18 \pm 0.27. \end{aligned} \quad (2.37)$$

This result at $Q^2 = 0.1 \text{ (GeV}/c)^2$ is shown in figure 2.3.

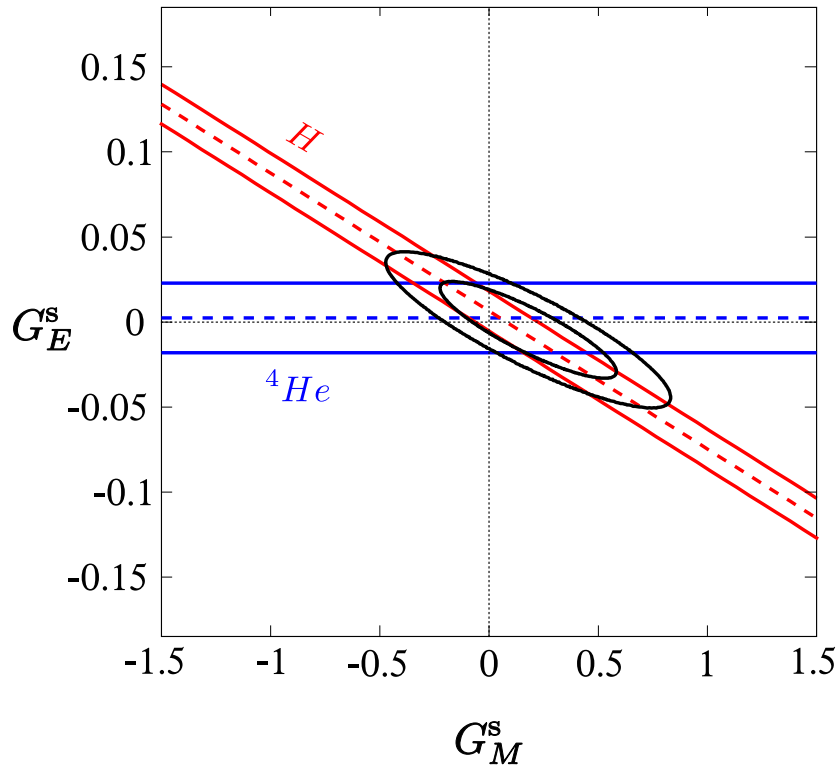


Figure 2.3 The result of the HAPPEX experiment at $Q^2 = 0.1 \text{ (GeV}/c)^2$ [58]. Two elliptical circles represent 68% and 95% confidence level constraints from the HAPPEX experiment. The helium and hydrogen data are denoted as ${}^4\text{He}$ and H respectively. The dashed lines are central values and the solid lines represent the uncertainties calculated by the quadratic sum of the statistical and systematic uncertainties.

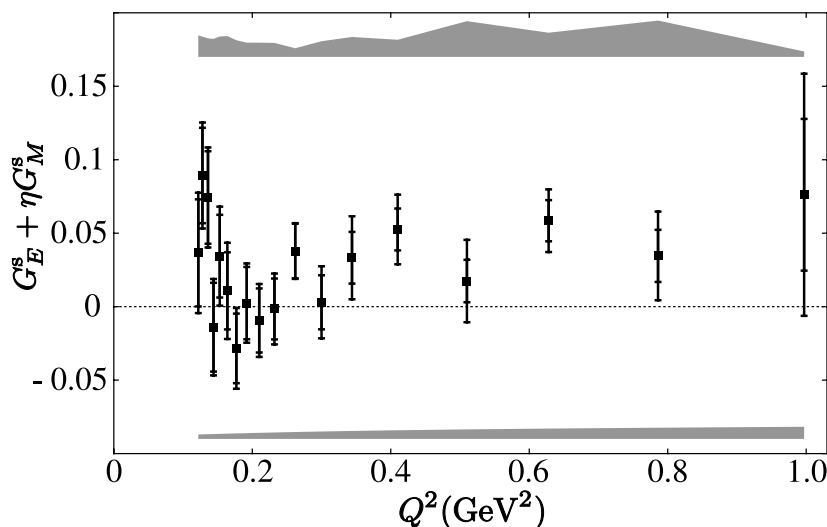


Figure 2.4 The result of the G0 experiment [63]. The inner error bars represent the statistical uncertainty and the outer the sum in quadrature of the statistical and systematic uncertainties. The upper gray error band represents the systematic uncertainties from the measurement and the lower one is due to the electroweak radiative corrections to $A_V^0 + A_A$, defined in (2.23) (See [63] for details).

The G0 experiment

The main aim of the G0 experiment in Hall C at TJNAF is a separation of the three contributions, G_E^s , G_M^s , and \tilde{G}_A^N , to the proton structure, and will be achieved by performing two separate experiments: (1) electron-proton scattering at forward angles over the Q^2 range between 0.12 and 1.0 $(\text{GeV}/c)^2$, and (2) electron-proton and electron-deuteron scattering at backward angles for two Q^2 values, 0.23 and 0.62 $(\text{GeV}/c)^2$ [60, 61, 62]. In the forward experiment, asymmetries are measured by detecting the proton recoiling from a liquid hydrogen target. A toroidal spectrometer was designed to focus recoil protons, which have the same momentum and the same recoil angle, onto a focal plane and to make the asymmetry measurements possible over a wide range of Q^2 simultaneously. The result of the G0 forward measurement is shown in figure 2.4. The linear combination of $G_E^s + \eta G_M^s$ is defined in (2.25). With the G0 data of the forward angle measurements, the hypothesis of $G_E^s + \eta G_M^s = 0$ was disfavored with 89% confidence level, and nonzero strange quark contributions that are dependent on Q^2 are implied [63]. The G0 backward angle measurements are now underway and they will provide data on the strange quark contributions to the nucleon over a large Q^2 range soon [61, 62].

2.4 The A4 Experiment

2.4.1 The Realization of the A4 Experiment

The A4 experiment at MAMI investigates the inner structure of the nucleon by measuring single spin asymmetries from elastic electron-proton scattering. The floor map of MAMI is shown in figure 2.5. The continuous-wave (cw) electron accelerator MAMI is formed from three cascaded racetrack microtrons (RTMs) and a harmonic double sided microtron (HDSM). The longitudinally polarized electrons are produced using a strained layer GaAs crystal onto which a circularly polarized laser beam is incident, and their average beam polarization is roughly 80%. The polarization state of the electron beam is switched between two patterns (+ - -+ and - + +-) randomly at 20 ms intervals by a Pockels cell in the optical system of the electron source. After the spin rotation system that is based on a Wien filter and is located in the 100 keV injection beam line, the polarized electrons are transferred to an injector linac and are accelerated up to 3.97 MeV. There follow three RTMs that accelerate the beam up to 855.1 MeV and HDSM that does the beam up to 1508 MeV. After that, the polarized electron beam is delivered into the experimental halls.

The expected parity violating asymmetry is in the order of 10^{-5} . Thus, a precise beam control system is necessary for the implementation of the parity violation experiment. Beam monitors watch and check three important beam parameters, which are the beam positions (XYMO), the beam current (PIMO), and the beam energy (ENMO) and make it possible for the beam control system to stabilize the beam parameters. The signals of the beam monitors also are recorded by the A4 data acquisition system during measurement [64, 65].

Figure 2.6 shows the target and detector system in the forward angle configuration. A powerful liquid hydrogen target system was developed for the precise study of parity violating electron scattering from hydrogen and deuterium [66]. The heat absorbed in the liquid hydrogen and in the aluminum window of the 10 cm liquid hydrogen target at a $20 \mu\text{A}$ electron beam current is approximately 100 W. The target cell has been designed to dissipate the absorbed heat transversely by a high turbulent flow that improves the transverse mixing of the liquid hydrogen in the target cell. In addition, the target cell has an 140° wide aperture for scattered electrons and an axial symmetry around the beam axis as required by the A4 parity violation experiment. The target cooling system in figure 2.6 consists of a closed liquid hydrogen circulation loop and a cold helium gas cooling loop. The helium cooling loop was designed to keep the liquid hydrogen temperature close to the freezing

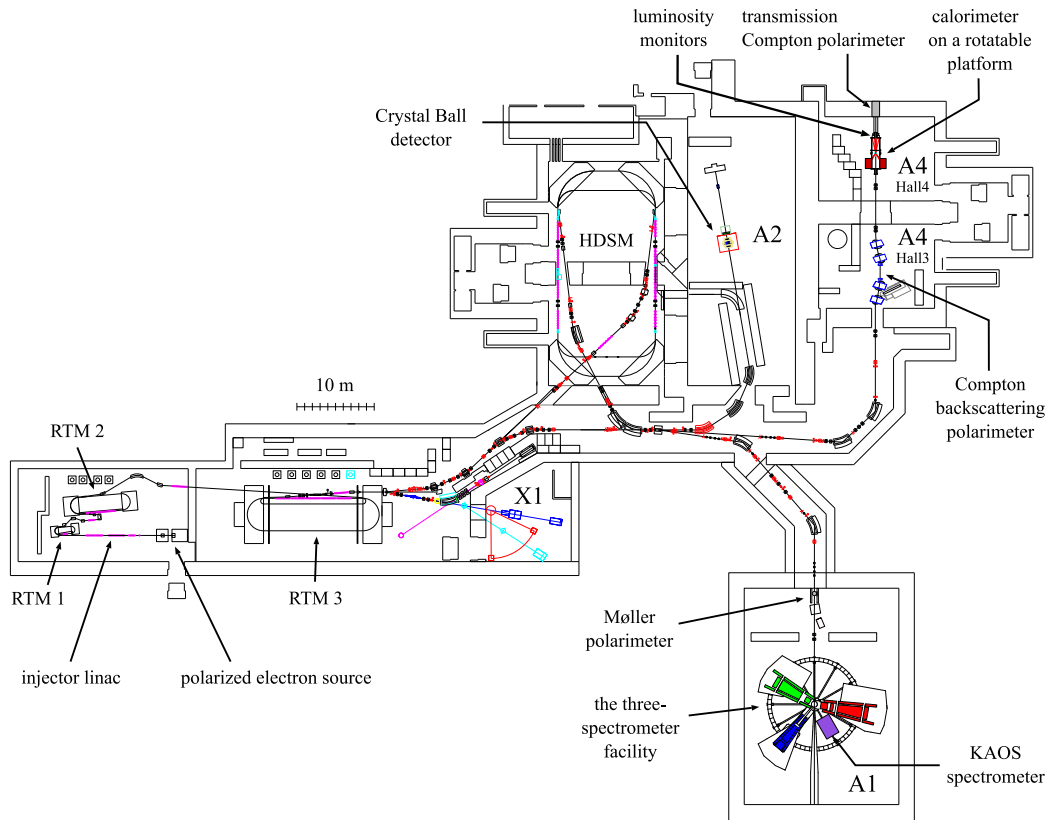


Figure 2.5 The floor map of MAMI. The accelerator is composed of three racetrack microtrons, which are denoted as RTM1, RTM2, and RTM3, and a harmonic double sided microtron, HDSM. A1, A2, and X1 are other collaborations at MAMI and represent their corresponding experimental halls. The Møller polarimeter is used to measure the absolute polarization of the electron beam and the Transmission Compton polarimeter measures the relative polarization.

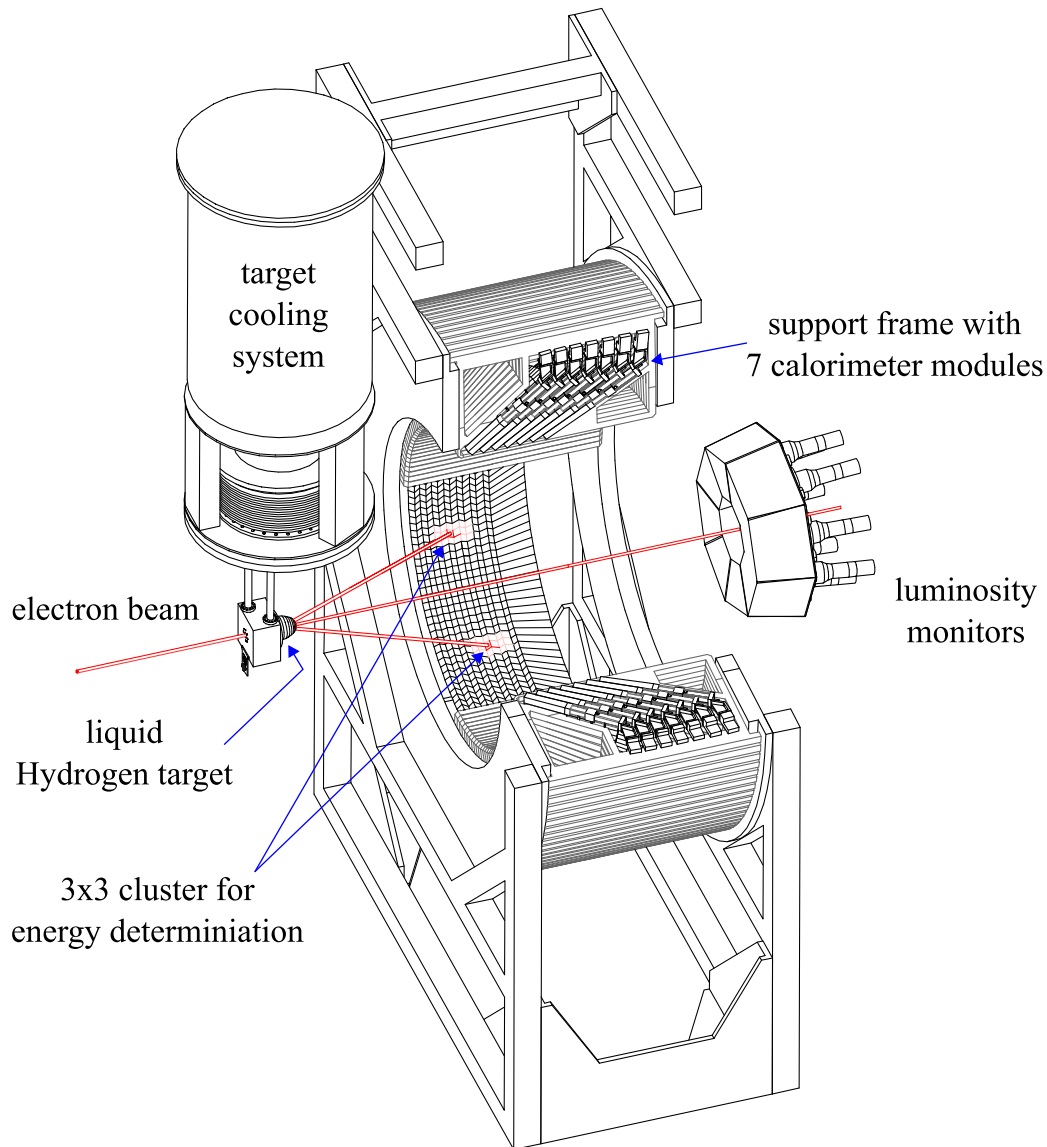


Figure 2.6 A sectional drawing of the PbF₂ calorimeter with the hydrogen target and the luminosity monitors in the forward angle measurement. The direction of the polarized electrons is from left to right. The electron beam enters the 10 cm liquid hydrogen target cell, which is made of thin aluminum. The scattered electrons are detected by the lead fluoride calorimeter at electron scattering angles θ_e of $30^\circ < \theta_e < 40^\circ$. The eight water Cherenkov luminosity monitors are placed at electron scattering angles θ_e of $4.4^\circ < \theta_e < 10^\circ$, and they measure the luminosity and monitor the target stability.

point so as to prevent the boiling point of the target from the absorbed heat.

A water Cherenkov luminosity monitor system detects target density fluctuations. When a liquid hydrogen target begins to boil due to the absorbed electron energies, this leads to target density fluctuations detected as luminosity fluctuations. These fluctuations can be reduced by optimization of the target position and beam diameter. The luminosity fluctuations introduce false asymmetry into the measured experimental PV asymmetry A_{exp}^{PV} . The signals of the luminosity monitors (LUMI) are recorded by the A4 data acquisition system during measurement. Then, the experimental asymmetry can be corrected by this luminosity measurement [64, 67].

The lead fluoride calorimeter consists of 1022 crystals and figure 2.6 shows a sectional view of the calorimeter. It is arranged in 146 support frames with 7 calorimeter modules. Each support frame covers an azimuthal angle of 2.47° . One calorimeter module consists of one lead fluoride crystal with a photomultiplier and covers a range of an electron scattering angle $\delta\theta_e = 1.43^\circ$. As a result, each support frame covers a scattering angle of $30^\circ < \theta_e < 40^\circ$. The solid angle coverage of the PbF_2 calorimeter is 0.63 sr. A pure Cherenkov radiator PbF_2 was selected as a detector material and the associated photomultiplier was also selected to match the properties of PbF_2 [68, 69]. The radiation hardness of the lead fluoride detector is ten times higher than that of a lead glass detector. In addition, damaged crystals can be regenerated by blue light [70]. The calorimeter can detect scattered electrons with an energy resolution of $3.9\%/\sqrt{E}(\text{GeV})$. Figure 2.7 shows the associated readout electronics (MEDUSA). The losses of the total event rate, which is the sum of inelastic events (roughly 90 MHz) and elastic events (roughly 10 MHz), are 1% at a $20 \mu\text{A}$ electron beam current due to the short dead time.

The signals from a 3×3 cluster (9 crystals) are summed and are integrated for 20 ns in the analog module that corresponds to the center crystal of the cluster. Then, the integrated signal is digitized by a 8-bit analog-to-digital converter (ADC), and the digitized energy value is saved in the VMEbus based memory. Figure 2.8 shows typical energy spectra of scattered electrons from the liquid hydrogen target at $20 \mu\text{A}$ beam current and at the 854.3 MeV electron beam during a standard data taking run (5 min.). The energy spectrum is a direct output of the VMEbus based memory and the elastic scattering events are easily distinguished from inelastic background. The number of elastically scattered electrons for each helicity state $N^{R,L}$ can be used to determine the experimental parity violating asymmetry A_{exp}^{PV} . Since an asymmetry from the background events would dilute the relevant physics asymmetry, background subtraction is essential. And it is necessary to choose the region of elastic events by introducing elastic cuts. For detailed

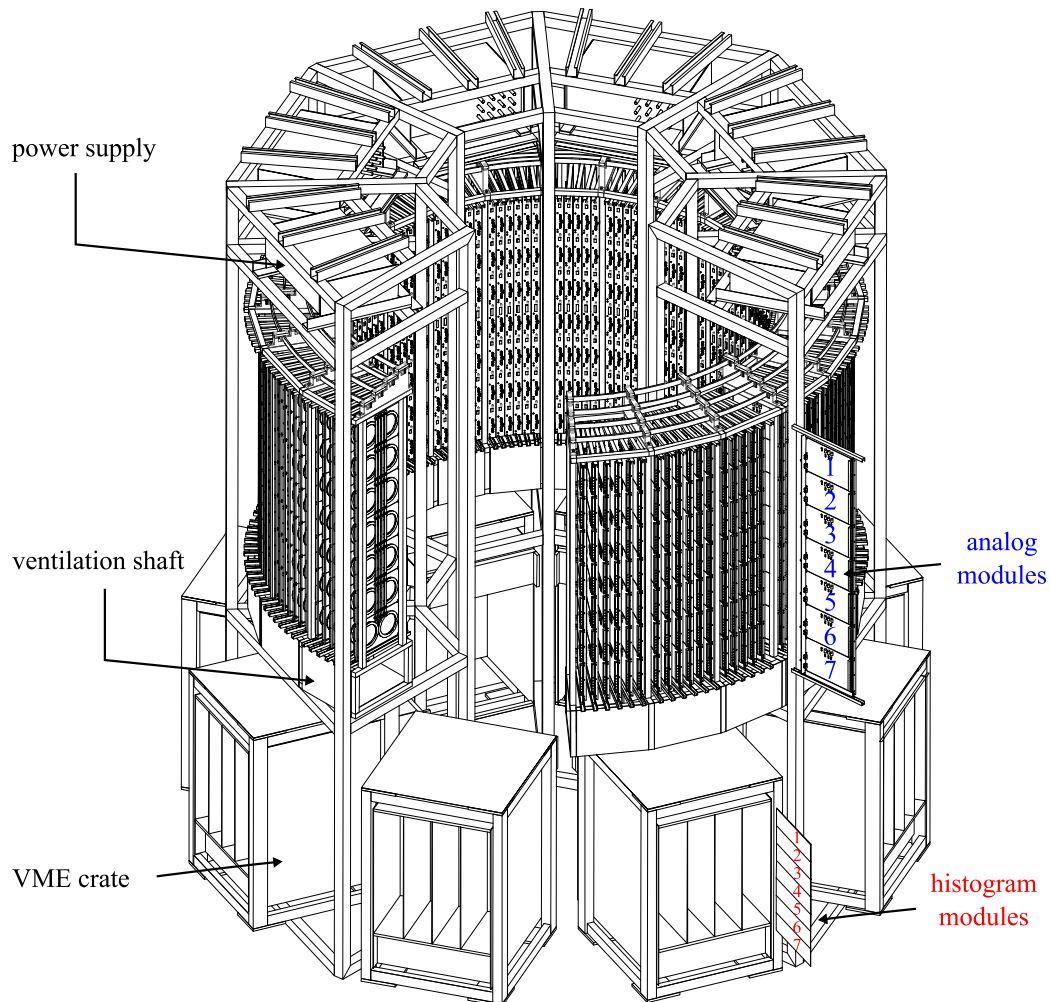


Figure 2.7 A sectional view of the readout electronics MEDUSA. The tower for the readout electronics consists of a radial array of 146 analog frames, 146 histogram frames, and 8 power supplies. One analog frame contains 7 analog modules that correspond to 7 crystals of the calorimeter. Each analog module is connected with one histogram module. The height of the tower is approximately 2.7 m and its inner diameter of the radial arrangement of the frame is roughly 1.6 m. For more information about the readout electronics, see the references [69, 71].

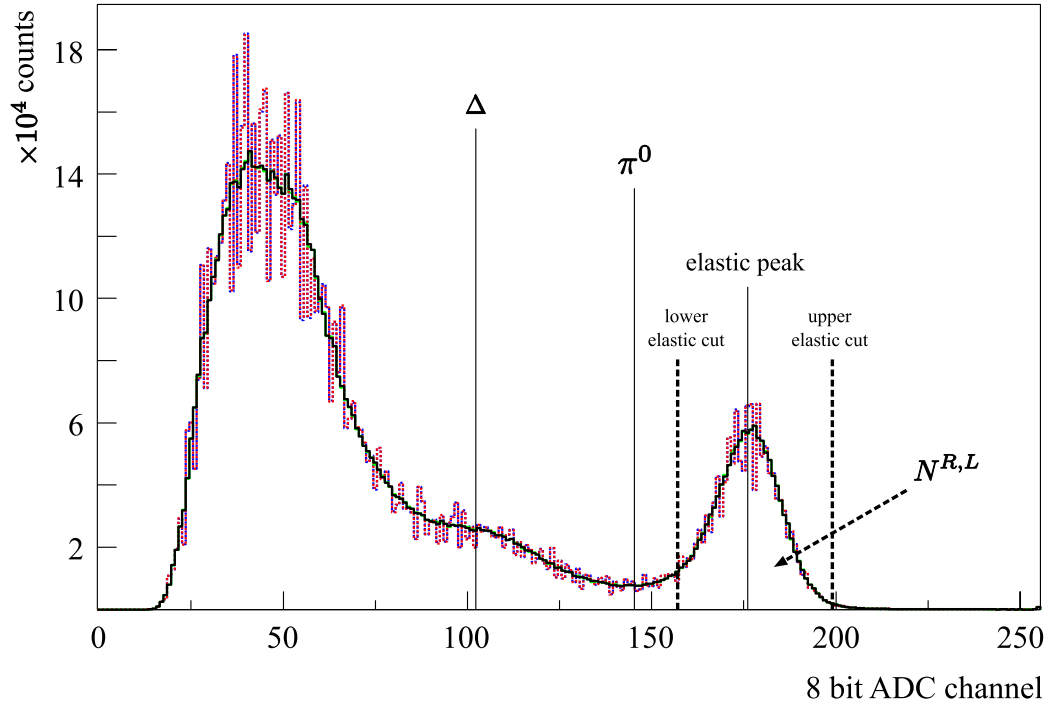


Figure 2.8 Energy spectra of a 3×3 cluster at 854.3 MeV. The spectra with a broken line represent the raw energy spectra of the different helicity states. The raw spectrum is read from the hardware memory of the readout electronics and is corrected for the differential nonlinearity of ADC. The spectra with a continuous line represent the corrected ones for the two helicities. Δ on the plot denotes the Δ resonance, π^0 the threshold for π^0 production, and $N^{R,L}$ the number of elastically scattered electrons for each helicity state according to the elastic cuts.

information about elastic cuts, consult the references [65, 72].

A transmission Compton polarimeter (TCP) was developed so as to monitor in parallel to the experiment and relatively the longitudinal polarization of the electron beam between the absolute Møller measurements. In addition, TCP can check the spin angle of the electron beam. The polarimeter is located between the target and the beam dump and is aligned along the beam axis inside a wide beam pipe with an 60 cm inner diameter. Figure 2.9 shows a simplified schematic drawing.

The polarized electron beam produces polarized photons inside the target by Bremsstrahlung. Because of the spin-dependent of the Compton cross section, the Compton asymmetry is proportional to the longitudinal beam polarization and can be measured when polarized photons are transmitted through the water-cooled Samarium-Cobalt permanent magnet, which is magnetized

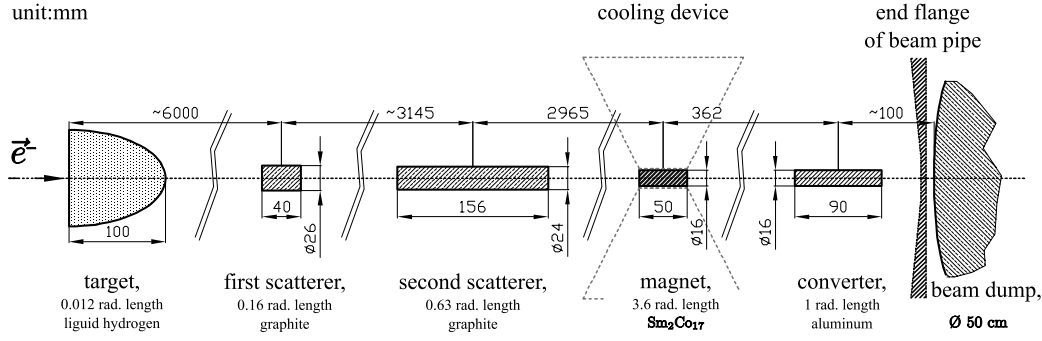


Figure 2.9 A schematic drawing of the transmission Compton polarimeter. The target, the scatterers, the magnet, the converter, the flange, and the beam dump on the drawing are symmetric around the beam axis [73].

axially. Two graphite scatterers are used to separate the photons from the electrons. The converter is used to convert the transmitted photons to electrons that are measured [74]. Since exact determination of the transmitted Compton photon flow and the analyzing power of the magnet is impossible, TCP is available to measure the electron beam polarization relatively. The measured Compton asymmetry A^{pola} of the transmitted photons is approximately 55.2 ppm at 854.3 MeV and is 94.0 ppm at 570 MeV. TCP can be used to check the sign of the parity violating asymmetry. In addition, the spin angle of the electron beam can be determined by a spin rotation measurement with the Wien filter, which is a spin rotation system of MAMI [75]. Figure 2.10 shows the spin rotation measurement at 570 MeV.

2.4.2 Results of the A4 Parity Violation Experiment at Forward Scattering Angles

The A4 experiment uses the counting technique to measure the parity violating asymmetry by the elastic scattering of longitudinally polarized electrons from an unpolarized proton target. We completed the two experiments in the forward angle configuration, which is shown in figure 2.6, at beam energies of 854.3 MeV and 570.4 MeV.

The first measurement of the parity violating asymmetry at the 854.3 MeV beam energy and at $Q^2 = 0.23 \text{ (GeV}/c)^2$ is [1]

$$A_{\text{phys}}^{\text{PV}}(Q^2 = 0.23) = (-5.44 \pm 0.60) \text{ ppm.} \quad (2.38)$$

The four momentum transfer $Q^2 = 0.23 \text{ (GeV}/c)^2$ was selected according to a maximum strangeness contribution predicted by [77]. And the calculated asymmetry is $A_V^0 + A_A = -6.30 \pm 0.43 \text{ ppm}$. The second one at

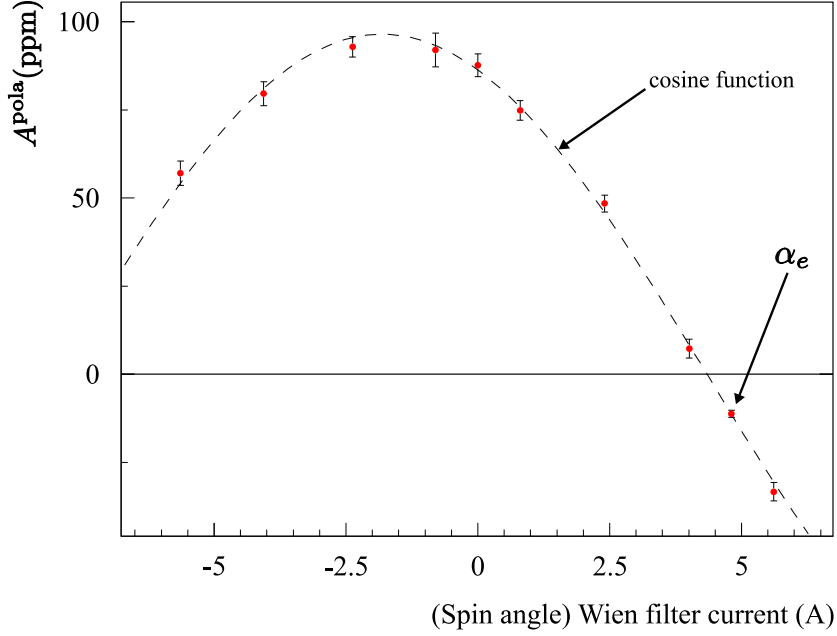


Figure 2.10 The spin rotation measurement at 570.4 MeV [73]. The transmission Compton asymmetry is displayed as a function of the magnet current of the Wien filter. This current is proportional to the spin rotation angle and the data point α_e on the plot corresponds to the spin angle of $96.8 \pm 0.8^\circ$ [76]. The zero crossing point corresponds to transverse polarization of the electron beam.

$Q^2 = 0.108 \text{ (GeV}/c)^2$ and at 570.4 MeV is [2]

$$A_{\text{phys}}^{PV}(Q^2 = 0.108) = (-1.36 \pm 0.32) \text{ ppm}. \quad (2.39)$$

The four momentum transfer $Q^2 = 0.108 \text{ (GeV}/c)^2$ was selected to match the SAMPLE measurement conditions, so that G_E^s and G_M^s can be isolated by combining the results of both measurements. The asymmetry $A_V^0 + A_A$ is $-2.06 \pm 0.16 \text{ ppm}$. Using the two measurements at $Q^2 = 0.23 \text{ (GeV}/c)^2$ and at $Q^2 = 0.108 \text{ (GeV}/c)^2$, we extract the linear relations $G_E^s + \eta G_M^s$ defined in (2.25) as follows:

$$G_E^s + 0.225 G_M^s |_{Q^2=0.230} = 0.039 \pm 0.034, \quad (2.40)$$

$$G_E^s + 0.106 G_M^s |_{Q^2=0.108} = 0.071 \pm 0.036, \quad (2.41)$$

and these are shown in figure 2.11.

In addition, if we combine the SAMPLE result for G_M^s (2.31) with our result for the linear relation (2.41), we extract the strange electric form factor

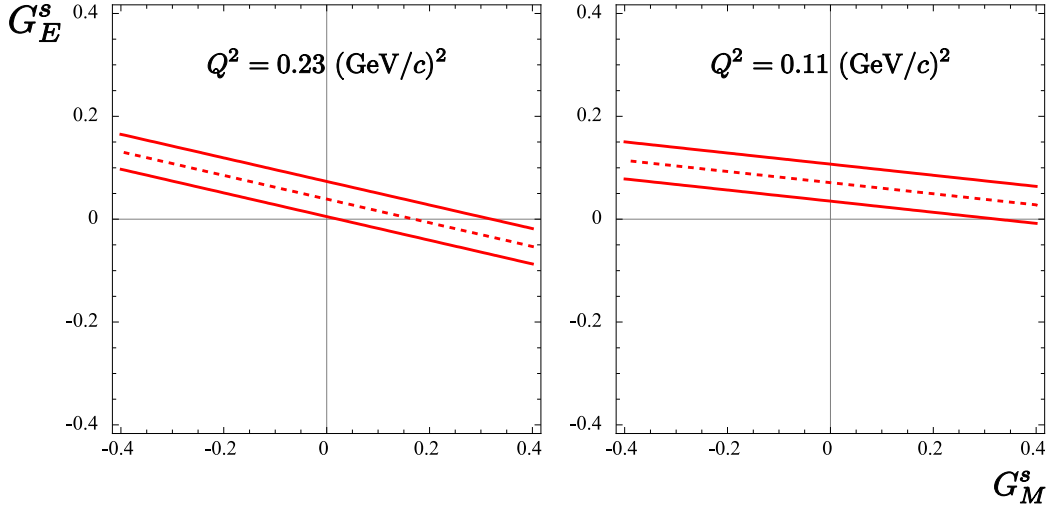


Figure 2.11 The results of the A4 experiment at $Q^2 = 0.23 \text{ (GeV/c)}^2$ [1] and at $Q^2 = 0.11 \text{ (GeV/c)}^2$ [2]. The dashed lines are central values and the solid lines represent the uncertainties.

of the proton G_E^s as

$$G_E^s(Q^2 = 0.108) = 0.032 \pm 0.051, \quad (2.42)$$

with an assumption that G_M^s is constant.

2.4.3 Measurements of the Parity Violating Asymmetries at Backward Scattering Angles

The next program for the parity violation experiment is the measurement of A^{PV} for longitudinally polarized electron scattering in the backward direction from unpolarized protons and unpolarized deuterons at $Q^2 = 0.23 \text{ (GeV/c)}^2$. In the backward angle configuration, the range of the electron scattering angle θ_e , which the PbF_2 calorimeter covers, is $140^\circ < \theta_e < 150^\circ$. As a result, we opted for 315.1 MeV as the electron beam energy. When we use a proton target, we can separate G_E^s and G_M^s by using the forward measurement at $Q^2 = 0.23 \text{ (GeV/c)}^2$.

In the backward angle configuration, we use the 23 cm target cell, which is longer than the target cell of the forward angle configuration, so as to increase the luminosity, because the backward angle cross section and its Q^2 dependency are much smaller than the forward angle one. And we developed a rotatable platform and an extension of the scattering chamber that are shown in figure 2.12 [78, 79]. The new platform makes it possible that the

PbF₂ calorimeter can be rotated between the forward and backward angle measurements.

And, at backward angles, it is hard to separate elastic events from inelastic events, in contrast to the situation at the forward angles, in the energy spectrum of the PbF₂ calorimeter. Photons from π^0 -decay mainly contributes to these inelastic events. Since these photons produce similar electromagnetic showers in the calorimeter as elastic electrons do, the calorimeter is unable to distinguish them. For this reason, we developed a plastic scintillator trigger system to distinguish the elastic electrons and the photons [71, 80]. The system consists of 72 scintillator detectors, a steel support, and an interface electronics. The steel support is located between the scattering chamber and the calorimeter. Figure 2.12 shows the 72 plastic scintillator detectors and the support. The interface electronics were developed in order to handle the scintillation trigger signals properly and to send the signals to the existing data acquisition electronics (MEDUSA). Currently, the background contributions to the calorimeter spectra are being studied by Monte Carlo simulations [81]. The preliminary parity violating asymmetry at the backward angles is

$$A_{\text{phys}}^{PV}(Q^2 = 0.23) = (-16.22 \pm 1.15) \text{ ppm} \quad (2.43)$$

and the calculated asymmetry is $A_V^0 + A_A = -16.3 \pm 1.2$ ppm [82]. The corresponding linear relation is

$$G_M^s + 0.25G_E^s|_{Q^2=0.23} = 0.004 \pm 0.146. \quad (2.44)$$

After we combine the forward measurement (2.38) with the backward measurement (2.44), we extract the strange electric and magnetic form factor as

$$\begin{aligned} G_M^s(Q^2 = 0.23) &= -0.01 \pm 0.15, \\ G_E^s(Q^2 = 0.23) &= +0.03 \pm 0.05, \end{aligned} \quad (2.45)$$

and this preliminary result is shown in figure 2.13.

Furthermore, the A4 collaboration conducts experiments, which are related with the asymmetry from transversely polarized electrons. Using the proton target, the asymmetry A_{\perp} was preliminarily extracted at 315 MeV electron beam [83]. And the asymmetry with a deuterium target was studied [84]. For more information about A_{\perp} , consult the references [3, 85, 86, 87].

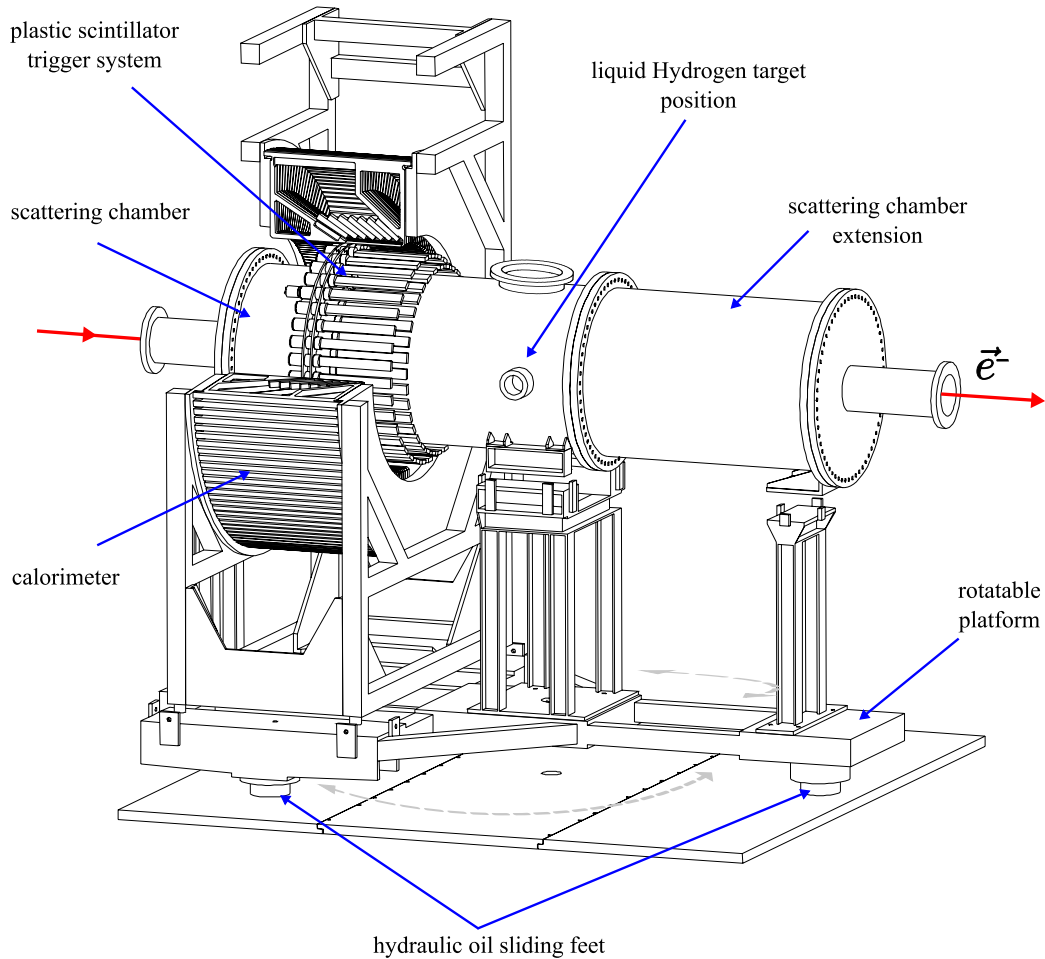


Figure 2.12 A schematic drawing of the PbF_2 calorimeter in the backward angle configuration, installed on the rotatable platform [78, 79]. The extension of the scattering chamber is necessary to keep the luminosity monitors in the same positions as in the forward angle configuration. The rotatable platform has three hydraulic oil sliding feet in order to rotate the calorimeter easily and to minimize vibration and shocks from rotation. The plastic scintillator trigger system was developed so as to separate the elastic events from the inelastic events [71, 80].

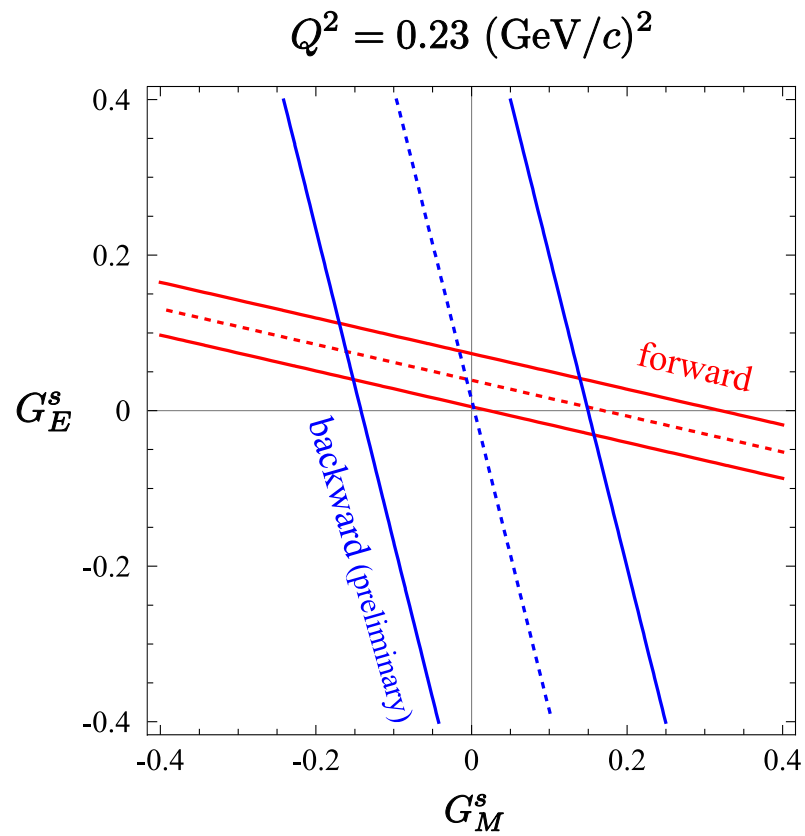


Figure 2.13 The preliminary result of the A4 experiment at $Q^2 = 0.23 \text{ (GeV/c)}^2$. The dashed lines are central values and the solid lines represent the uncertainties.

Chapter 3

Compton Backscattering Polarimeter

A Compton backscattering polarimeter is based on the polarized cross section in the scattering of circularly polarized photons from polarized electrons. With known photon polarization, the electron beam polarization can be determined by detecting the backscattered photons. Figure 3.1 shows the conceptual drawing of the A4 Compton backscattering polarimeter. Since a small percentage of incident electrons are associated with the scattering before a target, which is located in the experimental hall 4, it can be used to measure the electron beam polarization in parallel to the parity violating electron scattering experiment of the A4 collaboration.

After Compton backscattering, the scattered electrons and the backscattered photons move in the forms of highly collimated beams into the direction of incident electrons in the laboratory frame. A dipole magnet can separate both beams owing to the electric charge of the electron beam. The scattered electrons can be detected by a scintillating fiber electron detector and

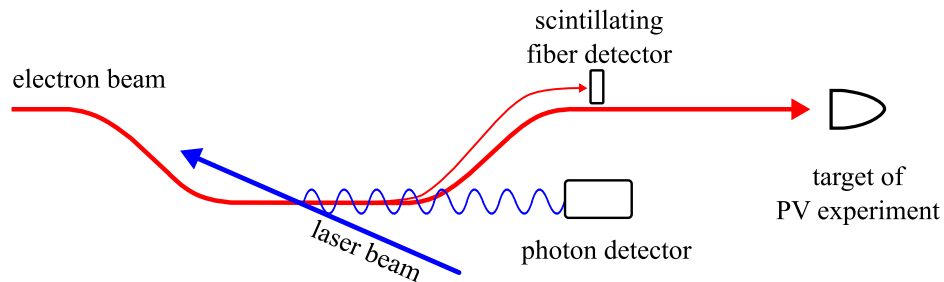


Figure 3.1 The conceptual drawing of the A4 Compton backscattering polarimeter

the backscattered photons can be done by a photon detector. We record the backscattered photon spectra with and without a coincidence between the photon detector and the electron detector. And we use the photon spectra so as to calculate the experimental Compton asymmetry A_{exp}^{CT} .

The experimental Compton asymmetry is related to an analyzing power Compton asymmetry A_{ap}^{CT} through the electron polarization P_e and the photon polarization P_γ by

$$A_{\text{exp}}^{CT} = P_e P_\gamma A_{\text{ap}}^{CT}, \quad (3.1)$$

where A_{ap}^{CT} depends on a theoretical asymmetry A_{th}^{CT} and a detector response function. Since A_{exp}^{CT} and P_γ are measurement variables, A_{th}^{CT} can be calculated within the framework of *quantum electrodynamics* (QED), and the detector response function can be determined by a measurement of the Compton edge in the photon spectrum, by a measurement with a radioactive source, and by a detector simulation independently, we can determine the electron polarization P_e . In this chapter, we discuss the Compton scattering process, the asymmetry in the Compton cross section, and the design concept and components of the A4 Compton backscattering polarimeter.

3.1 Compton Scattering

After Compton published his quantum theory of the scattering of X-rays by light elements [88], the Compton effect or Compton scattering has become eminent in physics. In this case of Compton scattering, a photon loses its energy and an electron, which is considered to be at rest, gains the energy. In the Compton backscattering, however, the electron loses its energy and the photon gains the energy. In high energy astrophysics, this process is called inverse Compton scattering because of the inverse energy transfer. In this section, we discuss the Compton backscattering process, its differential cross section, and the Compton asymmetry of the cross section.

3.1.1 Kinematics

Figure 3.2 shows the Lorentz transformation from the laboratory frame to the electron rest frame as

$$\begin{aligned} k_i^\mu &\rightarrow k_0^\mu = \Lambda^\mu{}_\nu k_i^\nu, \\ k_f^\mu &\rightarrow k^\mu = \Lambda^\mu{}_\nu k_f^\nu, \end{aligned} \quad (3.2)$$

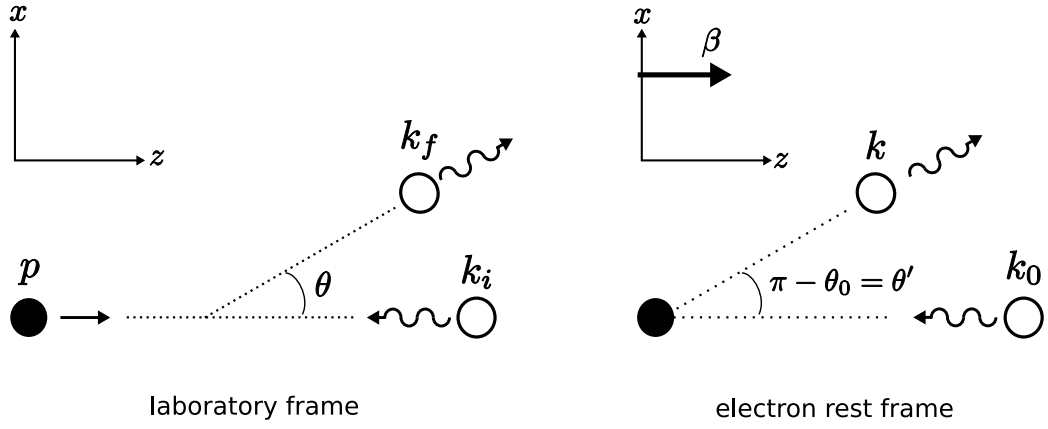


Figure 3.2 Two reference frames for the Compton scattering.

where $\Lambda^\mu{}_\nu$, a so-called Lorentz tensor, is

$$\Lambda^\mu{}_\nu = \begin{pmatrix} \gamma & 0 & 0 & -\gamma\beta \\ 0 & 1 & 0 & 0 \\ 0 & 0 & 1 & 0 \\ -\gamma\beta & 0 & 0 & \gamma \end{pmatrix},$$

the velocity β is along the z axis, $\gamma = 1/\sqrt{1-\beta^2}$, and the incident and scattered 4-momentum vectors of the photon are

$$k_0^\mu = (k_0, 0, 0, -k_0), \quad k^\mu = (k, k \sin \theta', 0, k \cos \theta'), \quad (3.3)$$

in the electron rest frame and

$$k_i^\mu = (k_i, 0, 0, -k_i), \quad k_f^\mu = (k_f, k_f \sin \theta, 0, k_f \cos \theta), \quad (3.4)$$

in the laboratory frame, where k_0 and k_i are the initial momentum vectors of the photon and k and k_f are the final momentum vectors. These give the kinematic relations between the frames as

$$k_0 = (1 + \beta)\gamma k_i, \quad (3.5)$$

$$k = \gamma k_f (1 - \beta \cos \theta), \quad (3.6)$$

$$k \sin \theta' = k_f \sin \theta, \quad (3.7)$$

$$k \cos \theta' = \gamma k_f (\cos \theta - \beta). \quad (3.8)$$

Note that the angle θ' is introduced to be consistent with the common angle notation for the Compton formula [88].

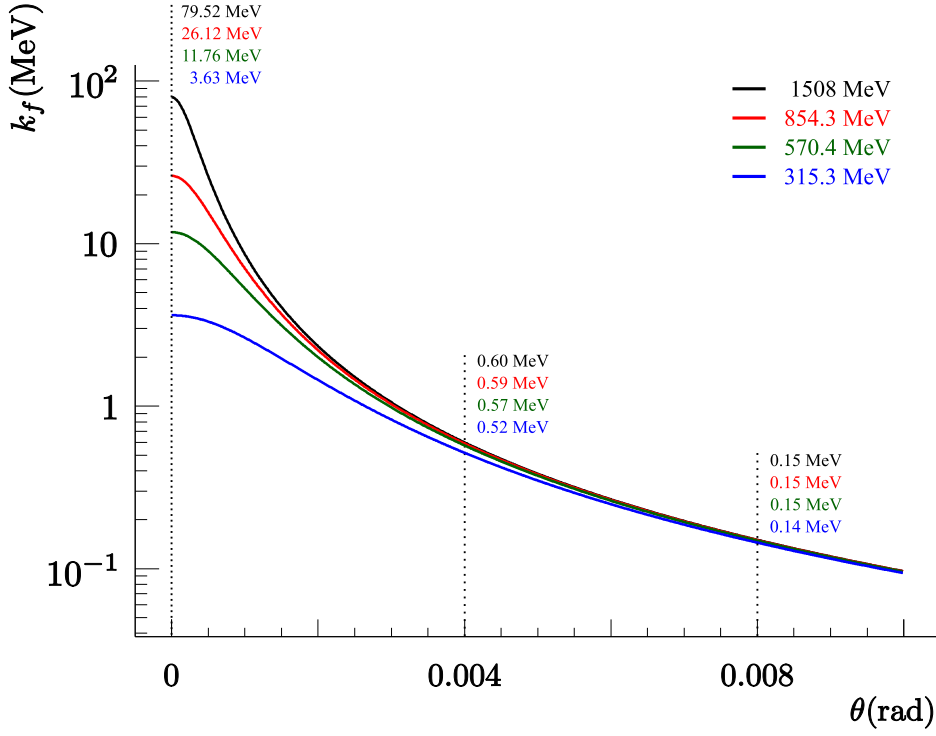


Figure 3.3 Scattered photon energy for four different electron energies as a function of the scattering angle θ . The wavelength of the green laser is 514.5 nm and its corresponding energy is 2.41 eV. Note that all scattered photons with a reasonable energy are within the very small range of θ .

In the electron rest frame, the well-known relation between k_0 and k is

$$k = \frac{k_0}{1 + \frac{k_0}{m}(1 - \cos \theta_0)}, \quad (3.9)$$

where m is the electron mass. If we use the 4-momentum conservation $m^2 = (p + k_i - k_f)^2$, we obtain the relation between k_i and k_f in the laboratory frame as

$$k_f = \frac{k_i}{1 + \frac{k_i - p}{E + p}(1 + \cos \theta)}, \quad (3.10)$$

where the electron energy $E = \gamma m$ and its momentum $p = \beta E$. Since figure 3.3 shows that the very small values of the scattered angle θ are of great importance, the energy of the scattered electron can be approximated as

$$k_f \approx \frac{k_f^{\max}}{1 + \frac{k_f^{\max}}{2k_i} \left(\frac{k_i - p}{E + p} \right) \theta^2}, \quad (3.11)$$

k_i (eV)	E (MeV)	k_f^{\max} (MeV)	a	θ_γ (mrad)	ρ_γ
2.41	1508.00	79.52	0.95	0.34	0.51
2.41	854.30	26.12	0.97	0.60	0.51
2.41	570.40	11.76	0.98	0.90	0.51
2.41	315.25	3.63	0.99	1.62	0.50

Table 3.1 The values of k_f^{\max} , a , θ_γ , and ρ_γ for different kinematics.

where the maximum scattered energy k_f^{\max} with $\theta = 0$ is defined as

$$k_f^{\max} = \frac{k_i}{1 + \frac{2(k_i - p)}{E + p}} = k_i \frac{(1 + \beta)^2 \gamma^2}{1 + \frac{2k_i \gamma}{m}(1 + \beta)}.$$

In the ultra-relativistic limit, where the velocity of the electron is nearly equal to the speed of light ($\beta \approx 1$), k_f^{\max} becomes

$$k_f^{\max} \approx k_i \frac{4\gamma^2}{1 + \frac{4k_i \gamma}{m}} = 4a\gamma^2 k_i, \quad (3.12)$$

where the kinematic parameter a is

$$a = (1 + 4k_i \gamma / m)^{-1}. \quad (3.13)$$

This limit is a good approximation for our case.

When the incident energies of the electron and the photon are assigned, the kinematic parameter a is a constant owing to the dependence on the incident energies of the two particles. In addition, for simplicity, a normalized energy ρ is defined as

$$\rho \equiv \frac{k_f}{k_f^{\max}} = \frac{1}{1 - \frac{k_f^{\max}}{2k_i} \frac{k_i - p}{E + p} \theta^2} \cong \frac{1}{1 + a\gamma^2 \theta^2}, \quad (3.14)$$

where $\beta \approx 1$ is used and θ the scattered angle of the photon in the laboratory frame. When θ is close to $\theta_\gamma = 1/\gamma$, ρ is close to $\rho_\gamma = 1/(1 + a)$. The angle θ_γ and the normalized energy ρ_γ are the important features of the Compton cross section. They will be taken up in section 3.1.2 and 3.1.3.

Table 3.1 shows the maximum scattered photon energy k_f^{\max} , the kinematic parameter a , the angle θ_γ , and the normalized energy ρ_γ for the different incident energies of the electron.

3.1.2 Cross Section

The Compton cross section for a circularly polarized photon scattering from a polarized electron in the electron rest frame [89] can be written as

$$\frac{d\sigma_{\pm}}{d\Omega} = \frac{d\sigma_0}{d\Omega} \mp P_e P_{\gamma} \left[\frac{d\sigma_1}{d\Omega} \cos \psi + \frac{d\sigma_2}{d\Omega} \sin \psi \cos \phi \right], \quad (3.15)$$

where

$$\begin{aligned} \frac{d\sigma_0}{d\Omega} &= \frac{1}{2} r_0^2 \frac{k^2}{k_0^2} \left[\frac{(k_0 - k)^2}{kk_0} + 1 + \cos \theta_0^2 \right], \\ \frac{d\sigma_1}{d\Omega} &= \frac{1}{2} r_0^2 \frac{k^2}{k_0^2} \left(\frac{k}{k_0} - \frac{k_0}{k} \right) \cos \theta_0, \\ \frac{d\sigma_2}{d\Omega} &= \frac{1}{2} r_0^2 \frac{k^2}{k_0^2} \left(1 - \frac{k}{k_0} \right) \sin \theta_0, \end{aligned}$$

with the classical electron radius r_0 , the solid angle $d\Omega = d\phi d\cos\theta'$, and a scattering angle θ_0 and an azimuth angle ϕ of the scattered photon. The spin of the electron lies in the $x - z$ plane defined in figure 3.2. Thus, $P_e \cos \psi$ is along the z -axis and $P_e \sin \psi$ along the x -axis. See figure 2 in more detail in the reference [89]. This cross section is mainly divided into two parts: (1) the unpolarized cross section $d\sigma_0/d\Omega$ that is known as the Klein-Nishina formula; and (2) two terms, which contain $d\sigma_1/d\Omega$ and $d\sigma_2/d\Omega$, that include polarization effects from the electron and the photon. σ_+ is chosen for the case of the longitudinal component of the photon spin parallel to its direction of motion [89]. The sign for P_e is positive for electron spins parallel to incident electron direction, which is the z -axis.

Since the photon detector is an electromagnetic calorimeter and measures energy spectra of the scattered photon, the cross sections per unit energy for the scattered photon are relevant, as we will see later. Each cross section $d\sigma_i/d\Omega$ in the electron rest frame can be transformed to the laboratory frame in terms of the normalized energy ρ , defined in (3.14), by the following relation

$$\frac{d^2\sigma_i}{d\phi d\rho} = \frac{d^2\sigma_i}{d\phi d\cos\theta'} \frac{d\cos\theta'}{d\rho} = \frac{d\sigma_i}{d\Omega} \frac{d\cos\theta'}{d\rho},$$

where $i = 0, 1, 2$. Therefore, the Compton cross section in the laboratory frame can be expressed as

$$\frac{d^2\sigma_{\pm}}{d\phi d\rho} = \frac{d^2\sigma_0}{d\phi d\rho} \mp P_e P_{\gamma} \left[\frac{d^2\sigma_1}{d\phi d\rho} \cos \psi + \frac{d^2\sigma_2}{d\phi d\rho} \sin \psi \cos \phi \right]. \quad (3.16)$$

To transform each cross section $d\sigma_i/d\Omega$ to $d^2\sigma_i/d\phi d\rho$, it is necessary to express k_0 , k , and $\cos\theta_0$ in terms of more convenient laboratory variables. Using (3.6) and (3.8), we obtain

$$k = \frac{k_f}{\gamma(1 + \beta \cos\theta')}. \quad (3.17)$$

And using (3.5) and (3.17), k_0 and k are substituted into (3.9). Thus, $\cos\theta_0$ can be expressed as

$$\cos\theta_0 = -\cos\theta' = -\frac{\frac{m\gamma}{k_f} - \frac{m}{k_i\gamma(1+\beta)} - 1}{1 - \frac{m\gamma\beta}{k_f}} \approx \frac{1 - \rho(1+a)}{1 - \rho(1-a)}, \quad (3.18)$$

In addition, (3.5), (3.17), and (3.18) give the following relations

$$\begin{aligned} \frac{(k_0 - k)^2}{kk_0} &= \frac{\rho^2(1-a)^2}{1 - \rho(1-a)}, \\ \frac{k}{k_0} - \frac{k_0}{k} &= 1 - \rho(1-a) + \frac{1}{1 - \rho(1-a)}, \\ 1 - \frac{k}{k_0} &= \rho(1-a), \\ \frac{1}{2} \frac{k^2}{k_0^2} \frac{d\cos\theta'}{d\rho} &= a, \\ \sin\theta_0 &= \frac{k_f}{k} \sin\theta \approx \gamma\theta(1 + \cos\theta') = \frac{\sqrt{4a\rho(1-\rho)}}{1 - \rho(1-a)}. \end{aligned}$$

Therefore, the three cross sections in terms of the normalized energy ρ and the kinematic parameter a , which is defined in (3.13), are

$$\frac{d^2\sigma_0}{d\phi d\rho} = r_0^2 a \left[\frac{\rho^2(1-a)^2}{1 - \rho(1-a)} + 1 + \left(\frac{1 - \rho(1+a)}{1 - \rho(1-a)} \right)^2 \right], \quad (3.19)$$

$$\frac{d^2\sigma_1}{d\phi d\rho} = r_0^2 a \left[(1 - \rho(1+a)) \left(1 - \frac{1}{(1 - \rho(1-a))^2} \right) \right], \quad (3.20)$$

$$\frac{d^2\sigma_2}{d\phi d\rho} = r_0^2 a \left[\rho(1-a) \frac{\sqrt{4a\rho(1-\rho)}}{1 - \rho(1-a)} \right]. \quad (3.21)$$

If the electron polarization has a transverse component, the azimuthal symmetry is broken in the Compton scattering. In that case, (3.21) plays a role as a transverse spin contribution to the cross section. For an effect of two-photon exchange in the elastic electron-nucleon scattering, we are interested

in the transverse component. However, we do not consider the transverse component in this thesis, as mentioned in chapter 1. Therefore, the Compton cross section for the longitudinal spin contribution is obtained by integrating over all azimuthal angles ϕ ,

$$\frac{d\sigma_{\pm}}{d\rho} = \frac{d\sigma_0}{d\rho} \mp P_e P_{\gamma} \cos \psi \frac{d\sigma_1}{d\rho}. \quad (3.22)$$

The differential cross section now has two parts: (1) a spin independent part $\frac{d\sigma_0}{d\rho}$; and (2) a spin-dependent part $P_{\gamma} P_e \cos \psi \frac{d\sigma_1}{d\rho}$. Note that we call $\frac{d\sigma_1}{d\rho}$ the spin-dependent part for simplicity. Figure 3.4 shows two differential cross sections as a function of the normalized photon energy ρ .

When $\theta \rightarrow \theta_{\gamma}$, i.e. the scattering angle is close to $1/\gamma$ as mentioned in section 3.1.2, the above cross section (3.22) becomes the unpolarized cross section

$$\frac{d\sigma_{\pm}}{d\rho} = \frac{d\sigma_0}{d\rho}, \quad (3.23)$$

where

$$\frac{d\sigma_0}{d\rho} = \pi r_0^2 \rho (1 + 3a^2),$$

and the spin-dependent part of the cross section $d\sigma_1/d\rho$ becomes zero at ρ_{γ} , which is also shown in figure 3.4. Thus, the Compton cross section is independent of the polarizations of the electron and the photon at θ_{γ} . The precise values of the scattered angle θ_{γ} and the normalized energy ρ_{γ} are listed in table 3.1.

3.1.3 Compton Asymmetry

The significance of the cross section σ_{\pm} can be understood by computing the theoretical Compton asymmetry that is defined as

$$A_{\text{th}}(\rho) = \frac{d\sigma_{+}/d\rho - d\sigma_{-}/d\rho}{d\sigma_{+}/d\rho + d\sigma_{-}/d\rho} = -P_e P_{\gamma} \cos \psi \frac{d\sigma_1/d\rho}{d\sigma_0/d\rho}.$$

For the sake of simplicity, we redefine the theoretical Compton asymmetry as

$$A_{\text{th}}^{CT}(\rho) = \frac{d\sigma_1/d\rho}{d\sigma_0/d\rho}. \quad (3.24)$$

It is also called the longitudinal Compton asymmetry. Since the kinematic parameter a is a constant owing to the kinematics, A_{th}^{CT} is only a function of the normalized photon energy ρ . And the asymmetry is represented as a function of the angle θ due to (3.14). The theoretical Compton asymmetry

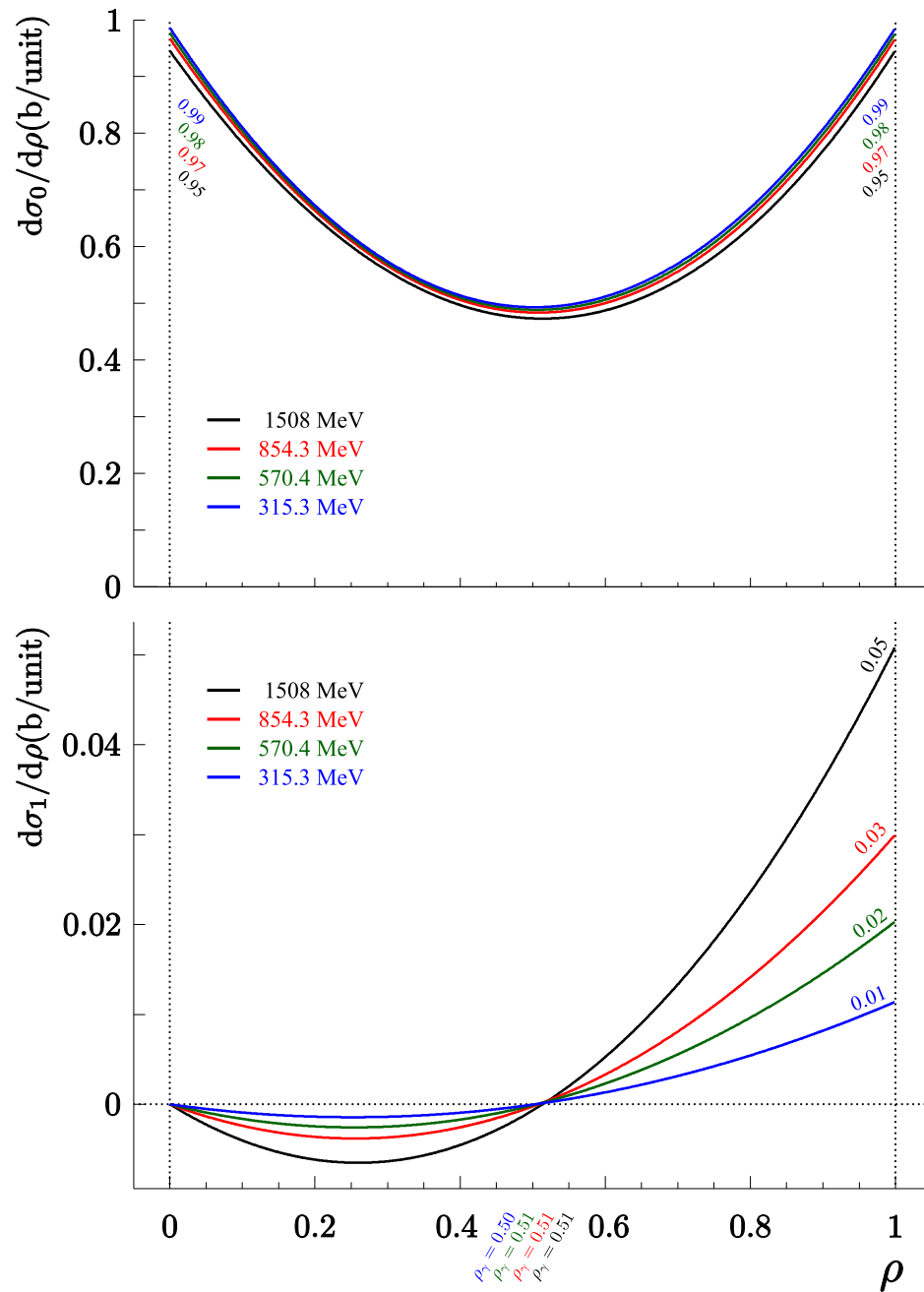


Figure 3.4 The differential Compton cross sections. The top picture is the spin independent part $d\sigma_0/d\rho$ and the bottom picture the spin-dependent part $d\sigma_1/d\rho$ with four different electron energies and green laser light (2.41 eV). ρ_γ with four different incident electron energies and the calculated cross sections at $\rho = 0, 1$ are shown.

is plotted in figure 3.5 and has interesting features: (1) $A_{\text{th}}^{CT}(\rho)$ becomes zero when $\rho \rightarrow \rho_\gamma$ and (2) $A_{\text{th}}^{CT}(\rho)$ has the largest asymmetry when $\rho \rightarrow 1$. In chapter 6, we study these interesting features of the theoretical Compton asymmetry in measurement of the experimental Compton asymmetry A_{exp}^{CT} .

3.2 Polarimeter

As mentioned earlier, the polarization of the electron beam P_e can be obtained by the following relation

$$A_{\text{exp}}^{CT} = \frac{n_+ - n_-}{n_+ + n_-} = P_e P_\gamma A_{\text{ap}}^{CT}, \quad (3.25)$$

where $\cos\psi = 1$ is assumed and A_{ap}^{CT} is called an analyzing power. The number of the scattering events of the different helicity states, denoted by the \pm symbol, is [90]

$$n_\pm = \mathcal{L}_\pm T_\pm \sigma_\pm^{\text{tot}}, \quad (3.26)$$

where \mathcal{L}_\pm is the luminosity, T_\pm the total measurement time, and σ_\pm^{tot} the total scattering cross section. The expression of n_\pm varies according to the measurement method that is applied to obtain the experimental Compton asymmetry A_{exp}^{CT} .

There are three variations of the measurement: (1) differential polarization measurement; (2) integrated polarization measurement; and (3) energy weighted polarization measurement [91]. In differential polarization measurement, the numbers of the Compton scattering events n_+^i and n_-^i are measured as a function of the normalized energy ρ per one energy bin $\Delta\rho^i$, where i is the bin number. The electron polarization per each bin, P_e^i , can be calculated by the asymmetry from n_+^i and n_-^i . Thus the weighted average of P_e^i is the electron polarization P_e . In integrated polarization measurement, the numbers of the scattering events integrated over the normalized energy range, N_+ and N_- , can be measured. Using the asymmetry from N_+ and N_- , the electron polarization P_e can be determined. In energy weighted polarization measurement, the deposited energies integrated over the normalized energy range, E_+ and E_- , are measured and the asymmetry can be calculated by using E_+ and E_- . Therefore, the electron polarization P_e can be calculated.

For example, using differential polarization measurement, the number of the events per $\Delta\rho^i$ is given by

$$n_\pm^i = \mathcal{L}_\pm T_\pm \int_{\Delta\rho^i} d\rho \frac{d\sigma_0}{d\rho} \epsilon(\rho) [1 \mp P_e P_\gamma A_{\text{th}}^{CT}(\rho)], \quad (3.27)$$

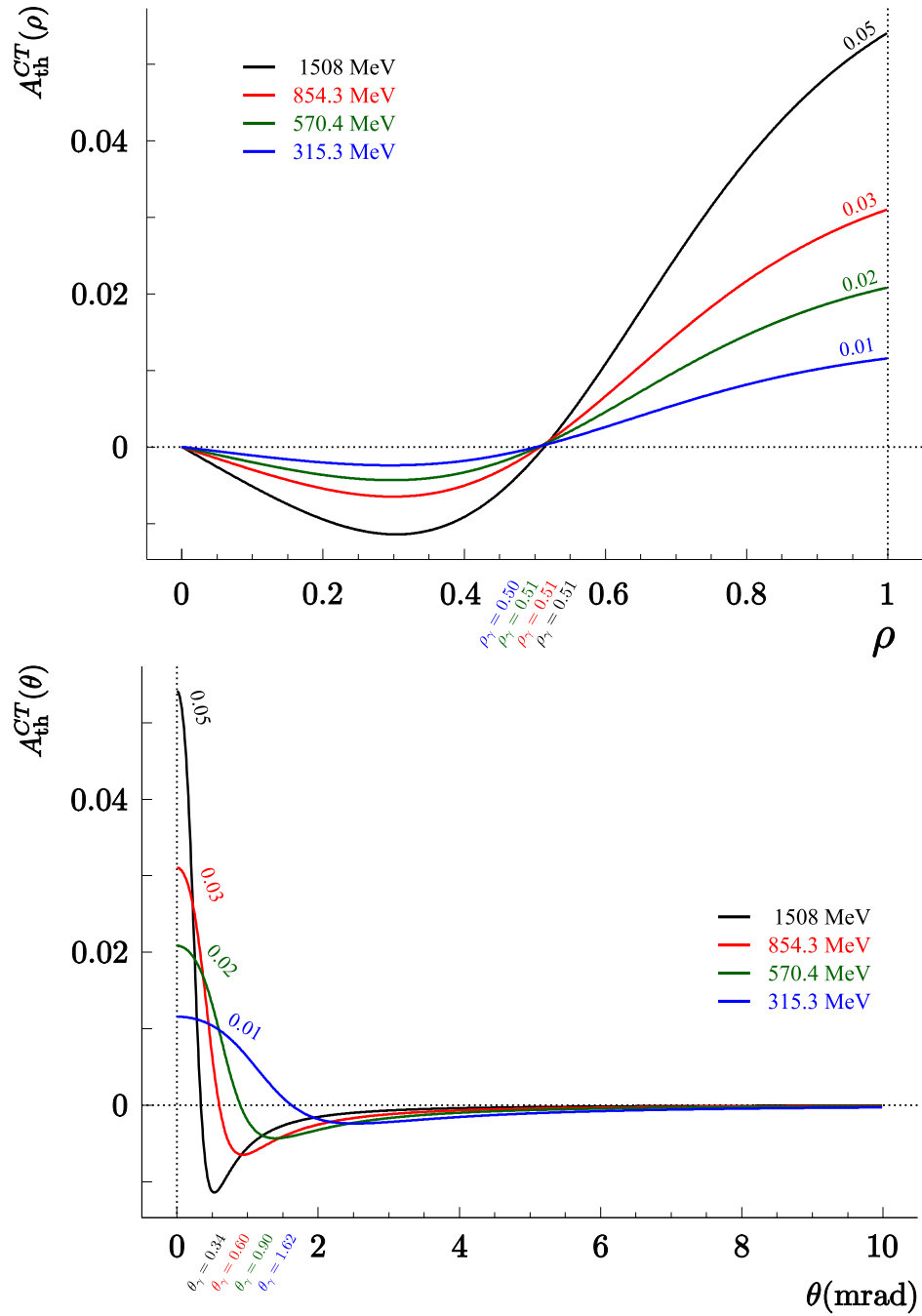


Figure 3.5 The theoretical asymmetry A_{th}^{CT} . The top picture is the asymmetry as a function of ρ and the bottom one the asymmetry as a function of the laboratory angle θ with four different electron energies and green laser light (2.41 eV). The calculated asymmetries, ρ_γ , and θ_γ are shown.

where $d\sigma_0/d\rho$ is the unpolarized differential cross section defined in (3.22), A_{th}^{CT} the theoretical Compton asymmetry defined in (3.24) and $\epsilon(\rho)$ the detection efficiency of the photon detector. Here, we assume that $\cos\psi = 1$ and $\epsilon(\rho) = \epsilon_+(\rho) = \epsilon_-(\rho)$.

3.2.1 Measurement Time and the Luminosity

The most interesting parameter during polarization measurement is the measurement time that is required to achieve an accuracy $\Delta P_e/P_e$. The required measurement time t is [91]

$$t \propto \frac{1}{\mathcal{L} \cdot \sigma \cdot \mathcal{A}^2 \cdot (\Delta P_e/P_e)^2}, \quad (3.28)$$

where the mean luminosity \mathcal{L} with the total time $T = T_+ + T_-$ is

$$\mathcal{L} = \frac{\mathcal{L}_+ T_+ + \mathcal{L}_- T_-}{T}, \quad (3.29)$$

σ is the detector efficiency-weighted average of the unpolarized cross section over the range of the energy threshold ρ_t to the maximum energy

$$\sigma = \int_{\rho_t}^1 d\rho \epsilon(\rho) \frac{d\sigma_0}{d\rho}(\rho), \quad (3.30)$$

and \mathcal{A}^2 is a quantity that has three different forms for the three polarization measurement methods. Since the differential polarization measurement method has the largest \mathcal{A}^2 , the required measurement time is the shortest one. In this case, \mathcal{A}^2 is given by

$$\mathcal{A}^2 = \frac{\int_{\rho_t}^1 d\rho \epsilon(\rho) \frac{d\sigma_0}{d\rho}(\rho) [A_{\text{th}}^{CT}(\rho)]^2}{\int_{\rho_t}^1 d\rho \epsilon(\rho) \frac{d\sigma_0}{d\rho}(\rho)}. \quad (3.31)$$

To achieve the shortest measurement time, maximizing the mean luminosity \mathcal{L} is far preferable to maximizing σ , \mathcal{A}^2 , or both, because σ and \mathcal{A}^2 are determined by kinematics, detector efficiency, and measurement methods and $\Delta P_e/P_e$ is the desired accuracy. If the energy of the electron beam is 855 MeV, the energy of the laser beam 2.41 eV for green light, the photon polarization $P_\gamma = 1.0$, the electron polarization $P_e = 0.8$ with no background assumption, the mean luminosities \mathcal{L} with 5%, 3%, and 1% accuracies for 15 min. are 4.59, 12.76, and 114.86 kHz/barn, respectively, according to the results obtained in [92]. In addition, the luminosity \mathcal{L} strongly depends on the beam focusing and beam crossing angle α_c between the electron and the laser

beam. The expected luminosities of different laser beam profiles were calculated [93]. The maximum of the expected luminosity is under 4 kHz/barn at $\alpha_c = 0$ and the luminosity decreases to around 1 kHz/barn when α_c increases up to 0.1 mrad.

3.2.2 Requirements for High Luminosity

According to the study on the luminosity \mathcal{L} and the crossing angle α_c [91], the total luminosity \mathcal{L}_{tot} is

$$\mathcal{L}_{\text{tot}} \propto \mathcal{C} \cdot P_L, \quad (3.32)$$

where $\mathcal{C} = (1 + \cos \alpha_c)/\sin \alpha_c$ and P_L is the laser power, when the angular divergences of the electron and the laser beams are smaller than α_c . As a result, maximum power P_L of a laser and a minimum crossing angle α_c are crucial in order to achieve maximum luminosity of a Compton backscattering polarimeter. Here, two cavity designs are discussed here.

Fabry-Pérot cavity design

Inside a laser device, two mirrors and a gain medium form an optical resonant cavity. One of the mirrors is a highly reflective mirror and the other one is a partly reflective mirror. A fraction of the photons inside the cavity is transmitted through the partly transmissive mirror. These photons, the laser, enter an additional external cavity with two highly reflective mirrors. Since it is necessary to build up the power of the laser inside the external cavity, this cavity design needs a feedback control system between the laser device and the external cavity. This design is called the Fabry-Pérot cavity design. The Compton polarimeter built at TJNAF uses the external Fabry-Pérot cavity that has a fixed crossing angle $\alpha_c = 23$ mrad ($\mathcal{C} = 87$) due to a safety of the mirrors [94, 95]. The maximum power of the cavity was measured at around 1600 W using a 229 mW laser with 85% circularly polarized light.

Internal cavity design

One can extend the laser cavity length and replace a partly reflective mirror with a highly reflective mirror. The power of the laser is built up inside one internal cavity with two highly reflective mirrors. Thus, in an internal cavity design, the feedback control system is non-essential. As a result, the internal cavity is much less complex than the Fabry-Pérot cavity. We use this internal cavity so as to build the A4 Compton backscattering polarimeter [93]. A maximum cavity power of 83 W with 90% circularly polarized light has been achieved by using a 10 W laser [96]. This maximum power achieved by the

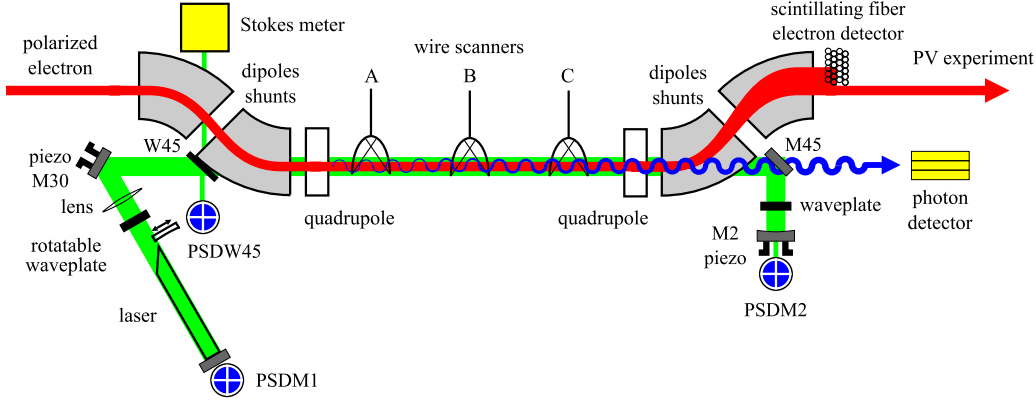


Figure 3.6 A schematic top view of the A4 Compton backscattering polarimeter.

internal cavity is less than the external cavity one. However, using a beam control system that will be discussed in chapter 5, we can make the crossing angle α_c smaller than the fixed crossing angle of the external cavity. It is easy to achieve the crossing angle α_c below 0.5 mrad ($\mathcal{C} \geq 4000$) with the beam control system. If we consider only α_c and P_L to estimate \mathcal{L}_{tot} , the total luminosity for the internal cavity design is 2.4 times higher than the Fabry-Pérot cavity design one.

3.2.3 The A4 Compton Backscattering Polarimeter

The A4 Compton backscattering polarimeter, a destruction-free tool for electron polarization measurement, is shown in figure 3.6 schematically. The polarized electron beam is guided into the interaction region between the two quadrupole magnets by the first two dipole magnets. The second two dipole magnets guide the scattered electron beam into a scintillating fiber electron detector and the main electron beam, independent of the scattering, to the parity violation experiment. Each dipole magnet has a shunt that is connected in parallel to the dipole magnet in order to fine-tune the electron beam trajectory. This topic will be discussed in chapter 5. Two quadrupole magnets are installed so as to compensate horizontal beam dispersions that are caused by the four dipole magnets. This issue will be taken up in more detail in chapter 4. Transverse positions of the electron beam and the laser beam are determined by three wire scanners, installed in the interaction region. Using this position information and control of shunts, the optimum overlap can be achieved. We will discuss them in chapter 5.

The polarized photon beam is generated by an Argon-Ion laser, a Coher-

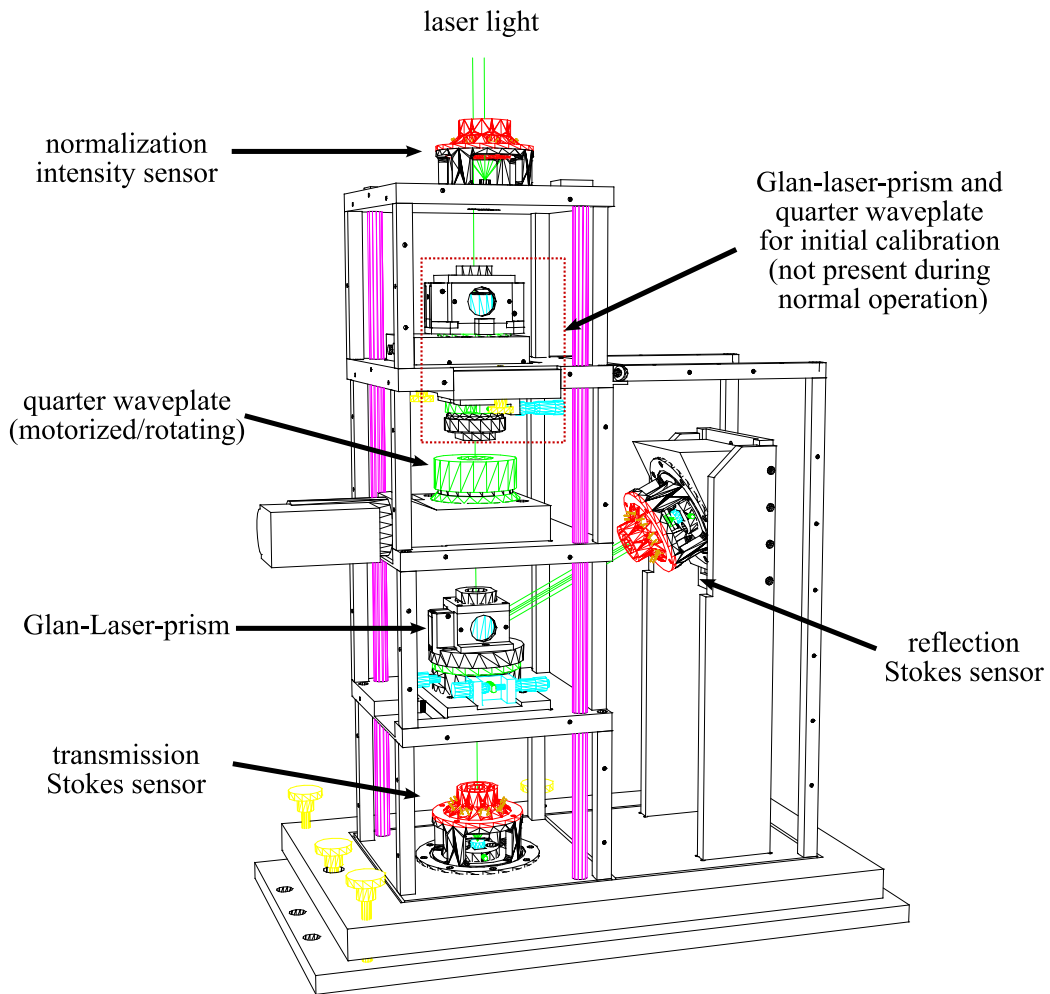


Figure 3.7 New Stokes meter [99] (all covers removed)

ent Innova 425. It is operated on a single line (514.5 nm). The right and left circularly polarization states of the photon beam can be changed by a rotatable quarter-wave plate. Only 0.6% laser light is coupled out by one of the vacuum windows, which is named W45 in figure 3.6, and is used to measure the polarization state of the photon beam by a Stokes meter. The prototype Stokes meter has been successfully operated since 2003 [93, 97, 98]. The new Stokes meter [99] is under development and its drawing is shown in figure 3.7.

The total length of the polarimeter internal cavity is approximately 8 m and the length of the interaction region is 2 m. Since the cavity length is long and all optical components are attached to vacuum chambers directly or indirectly, mechanical vibrations that come from vacuum pumps, cooling

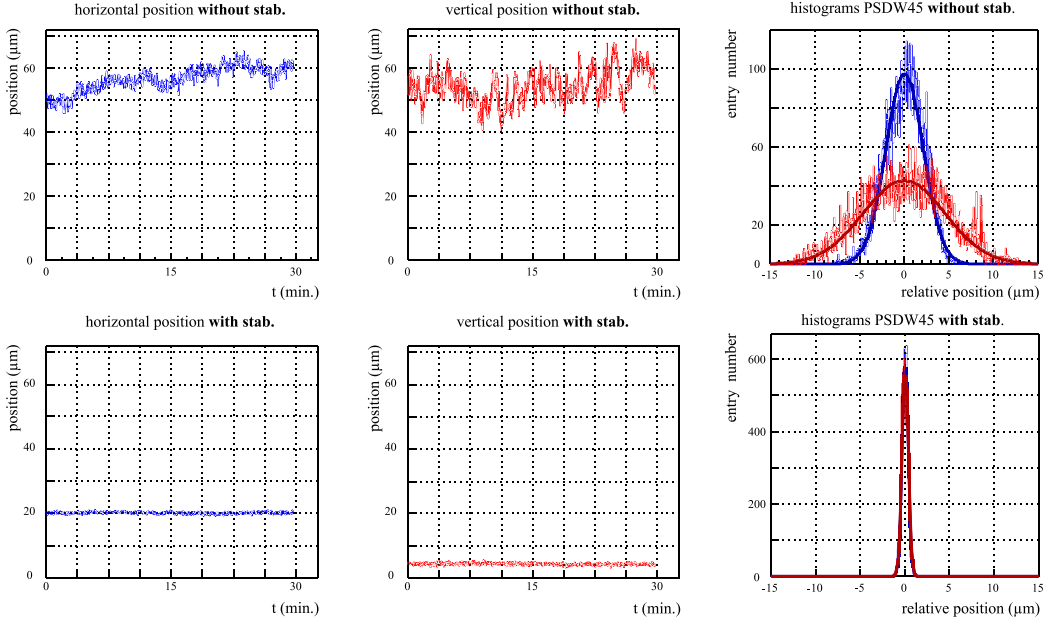


Figure 3.8 Laser beam axis variations with and without the stabilization system. Three top plots are obtained without the stabilization system and bottom plots with the stabilization system. The rightmost plots show the fluctuation about a linear fit to the data. The beam axis stabilization system lessens the laser beam variations significantly [101].

water flow of the dipole and quadrupole magnets, and so on can adversely affect the stability of the laser beam position. A stabilization system of the laser beam position has been installed to keep the instability as small as possible to achieve the better overlap and high laser power [100]. The laser positions on the beam axis are measured by position sensitive detectors (PSDM1, PSDM2, PSDW45) and led to a feedback system that optimizes the alignment of the laser mirrors according to the measured displacements. Therefore, two of mirrors are attached to piezo platforms. Figure 3.8 shows the laser beam positions with and without the stabilization system. During 30 min., the horizontal fluctuations are reduced from 4.2 to less than $0.8 \mu\text{m}$ and the vertical one are reduced from 9.2 to less than $0.8 \mu\text{m}$. And the horizontal long-terms drifts of the laser beam position are changed from 21 to $0.3 \mu\text{m}/\text{h}$ and the vertical long-terms drifts are significantly reduced from 13 to $0.6 \mu\text{m}/\text{h}$ [101].

Two detectors, a photon and an electron detector, play an important role in the A4 Compton backscattering polarimeter. The photon detector

is composed of nine LYSO¹ crystals in the form of the 3×3 matrix. The dimensions of each LYSO crystal are $20 \times 20 \times 200$ mm and each crystal is wrapped by a reflective foil and an additional aluminized-Mylar foil [102]. The radiation length X_0 of the LYSO crystal is 1.22 cm, its decay time is 41 ms, and its peak emission wavelength is 420 nm. The LYSO photon calorimeter is shown in figure 3.11 and the whole detector is in a lead cylinder so as to reduce background rates.

As mentioned before, the scattered electrons have less energy than the main electron beam that is independent of the scattering, and have larger transverse displacement than the main one. Therefore, these scattered electrons can be detected by the electron detector. The fibers that are hit by the scattered electrons are used to select the corresponding energy range of the scattered photons by a coincidence between both detectors. Figure 3.9 shows a diagram of the data acquisition electronics for the A4 Compton backscattering polarimeter.

The prototype electron detector that was composed of 24 scintillating fibers improved the ratio of signal to noise from 1:7.1 to 1:2.1 [92, 97], and gave a limited possibility to analyze the coincidence and background spectra. A new fiber detector, especially a fiber bundle array and mechanical components, was designed to improve each ADC signal quality, detector geometry, and a movement of the detector. This issue will be discussed in detail in chapter 6.

Figure 3.10 shows the results of an asymmetry measurement with the 854.3 MeV electron beam and 92% circularly polarized light, obtained in August 2005 [96]. This measurement was done by a BaF₂ calorimeter as a photon detector and data taking time of one run is 5 minutes. As described before, the polarized electrons are produced by the strained layer GaAs crystal with circularly polarized laser light produced from the MAMI laser system and its helicity is changed within 20 ms. The data around of the green solid line were taken with a $\lambda/2$ plate inserted between the laser system and the GaAs crystal. This reverses the polarization of the electron beam and is used to study systematic effects. Gray bars are runs without the laser beam in order to measure the background. The 5 hours interruption of the asymmetry measurement exists owing to test measurements of the trigger system. Because of the data consistency, this measurement verified the stability of the Compton polarimeter at the early stage.

¹Saint-Gobain PreLude[®] 420 (Lu_{1.8}Y_{0.2}SiO₅ : Ce)

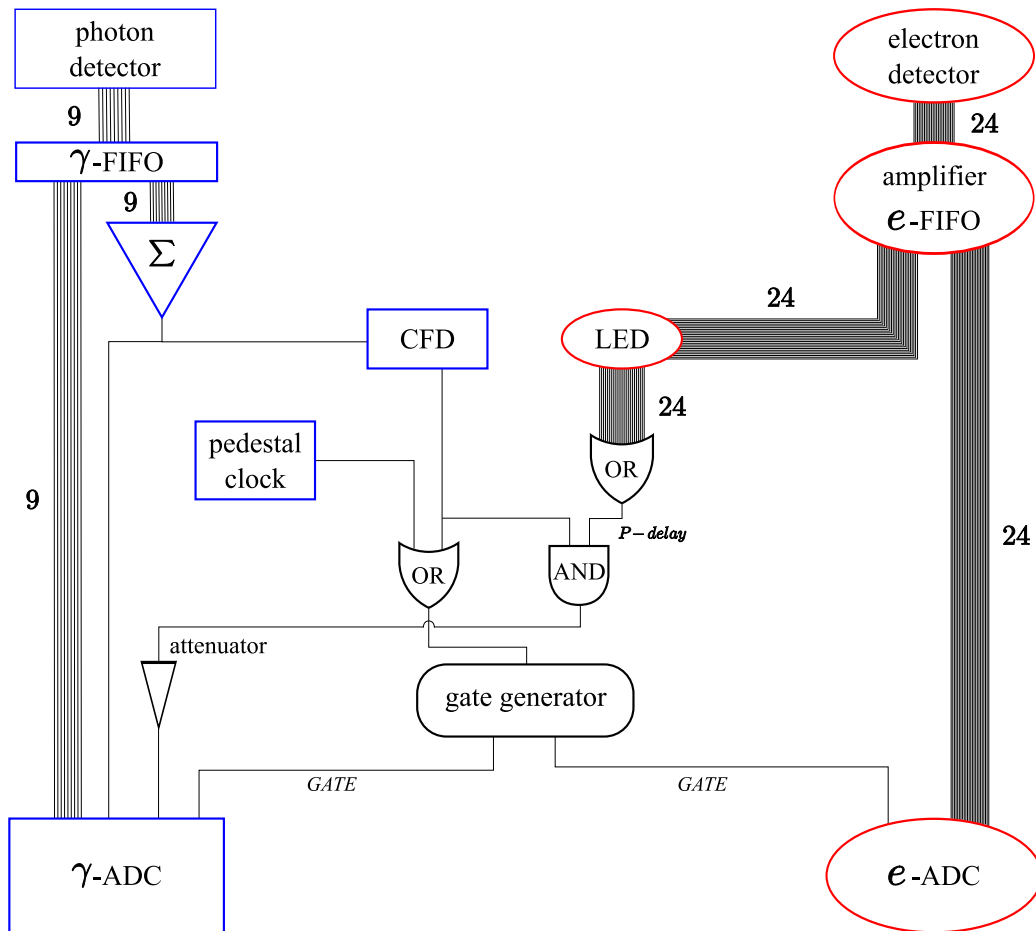


Figure 3.9 A diagram of the data acquisition electronics to take coincidence spectra and electron spectra. There are 9 analog signals of the photon detector and 24 signals of the electron detector. FIFO is a linear fan-in fan-out module, CFD a constant fraction discriminator, LED a leading edge discriminator, $P - delay$ a programmable delay unit, Σ the sum of 9 analog signals of the photon detector, and $GATE$ the gate input of each ADC module.

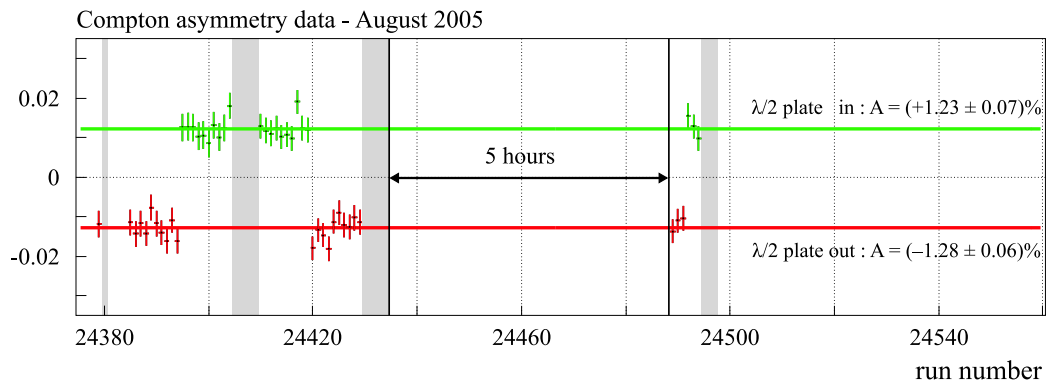


Figure 3.10 The Compton asymmetry as a function of the run number [96]

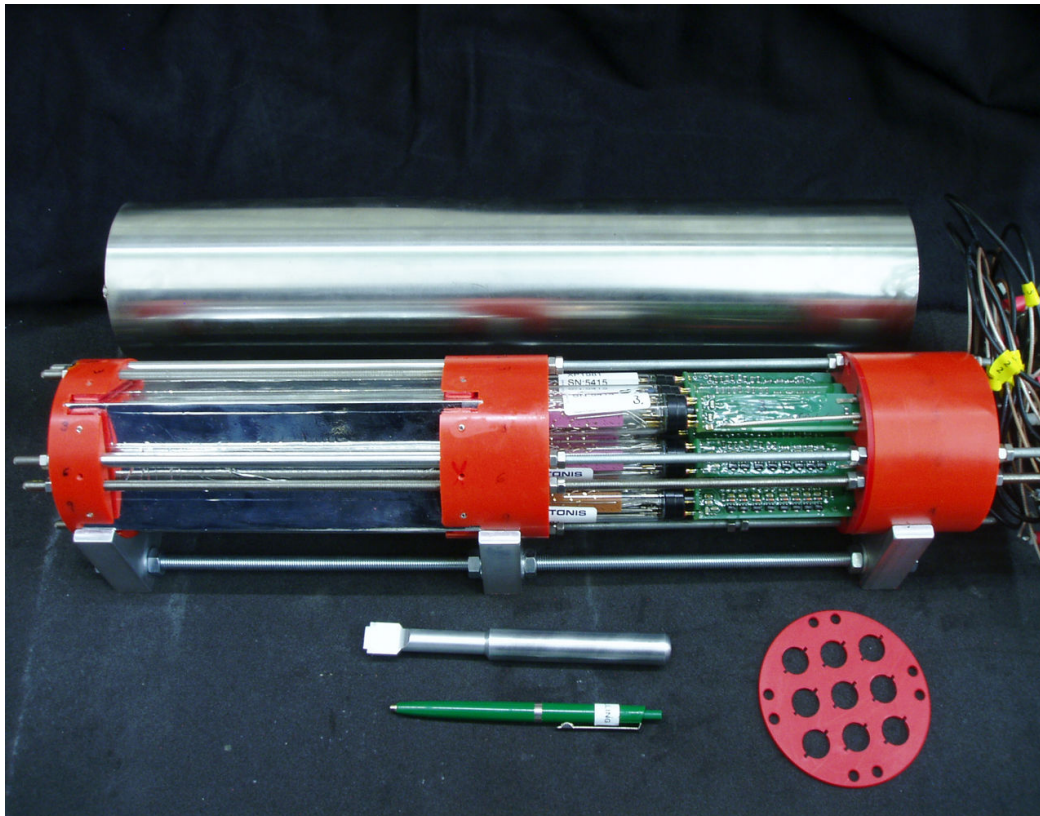


Figure 3.11 The LYSO photon calorimeter without a lead cylinder, which reduces background rates [102]. *Above*, a Mu-metal cylinder for reducing influence of dipole magnetic fields; *below right*, a photomultiplier orientation plate for the same purpose.

Chapter 4

Compton Backscattering Polarimeter Chicane

In the last chapter, we have described what the Compton backscattering polarimeter is and how it works for the electron beam polarization measurement. In addition, we have presented the A4 Compton backscattering polarimeter. In this chapter, we mainly study an electron beam optics of the A4 Compton backscattering polarimeter. These optics consist of four dipole magnets, that guides electrons along a desired path, and two quadrupole magnets, which hold electrons close to the path. They are also elements of an electron beam transport line, which is called a *chicane*.

The Compton backscattering polarimeter chicane will provide the Compton interaction region and is able to deliver the electron beam to a target for the parity violation experiment without any disturbances to the electron beam. Therefore, in this chapter, we will review the electron beam optics, describe the chicane elements, and study the basic and important properties of the chicane for the A4 Compton backscattering polarimeter.

4.1 Beam Optics

In a magnetic field \mathbf{B} , a charged particle experiences the Lorentz force \mathbf{F} , which is

$$\mathbf{F} = q\mathbf{v} \times \mathbf{B}, \quad (4.1)$$

where \mathbf{v} is its velocity and q the charge of the particle. Thus, charged particles can be guided or focused by that force. This application is called beam optics or beam dynamics [103, 104].

4.1.1 Reference Particle and Beam Coordinate

To design and realize a beam transport line in an experimental hall, one should define its start point \mathcal{A} and its end point \mathcal{B} . A *reference trajectory*¹ defines an ideal line that connects \mathcal{A} and \mathcal{B} . A particle on the reference trajectory is called a *reference particle* and its momentum, the *reference momentum*, is denoted as p_0 . In the first-order approximation, the position of the reference particle represents a center position of the beam.

If a uniform and static magnetic field perpendicular to the reference trajectory is activated in a region of the beam transport line, charged particles move along a circular path within that region. The static magnetic field perpendicular to the reference trajectory can be generated by a dipole magnet. The relation between the reference momentum p_0 and the magnetic field B_0 is expressed by

$$p_0 = q \cdot B_0 \cdot \rho, \quad (4.2)$$

where q is the electric charge of the reference particle and ρ the radius of curvature of the reference trajectory. Note that (4.2) can be applied not only to the reference particle but also to any charged particles within the region of B_0 . In more practical units, the relation is rewritten in the following form:

$$33.356 \cdot p_0(\text{GeV}/c) = B_0(\text{kGauss}) \cdot \rho(\text{m}). \quad (4.3)$$

A charged beam is a distribution of charged particles. If a position of the reference particle along the reference trajectory is known, positions of any other particle, of which the beam is composed, can be defined by introducing three quantities as follows: a longitudinal component l_i , a horizontal component x_i , and a vertical component y_i . They are shown in figure 4.1. The longitudinal component l_i is the difference in path length between a given trajectory and the reference trajectory. And three more components are necessary to describe the direction of motion and are defined as follows:

$$x' = \frac{p_x}{p_t}, \quad y' = \frac{p_y}{p_t}, \quad \delta = \frac{\Delta p}{p_0}, \quad (4.4)$$

where p_0 is the reference momentum, x' and y' the ratios of transverse to longitudinal components of momentum p_t , and δ the fractional momentum deviation. The ratios x' and y' at times are called the horizontal angle and the vertical angle respectively with respect to p_0 because p_x and p_y are small compared with p_t [103]. The momentum of a charged particle can be expressed in terms of p_0 and δ as

$$p = p_0 + \Delta p = p_0(1 + \delta),$$

¹It is also called a design trajectory, a design path, or a reference position.

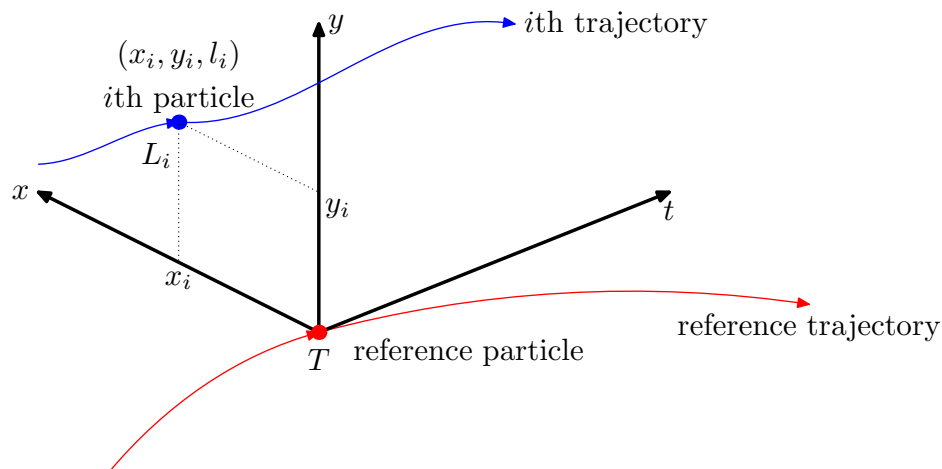


Figure 4.1 Beam coordinate. T represents the travel distance of the reference particle that travels along the reference trajectory and L_i the travel distance of i th particle along i th trajectory. The difference between T and L_i is given as $l_i = T - L_i$. And x_i is the horizontal position with respect to the reference trajectory, y_i the vertical position, and t the longitudinal component of the beam coordinate.

and can be done in terms of its components as

$$p^2 = p_x^2 + p_y^2 + p_t^2.$$

As a result, we can define a vector \mathbf{x} , a single column matrix, that represents an arbitrary charged particle at a position i along the beam line:

$$\mathbf{x}_i = \begin{pmatrix} x_i \\ x'_i \\ y_i \\ y'_i \\ l_i \\ \delta_i \end{pmatrix}. \quad (4.5)$$

4.1.2 Transfer Matrix

In a static magnetic system, the properties of a beam line element can be described by a *transfer matrix* M instead of solving (4.1). If a beam line is composed of a drift space, a dipole magnet, and a quadrupole magnet, the transfer matrix of the beam line could be constructed by multiplying three transfer matrices of elements and is

$$M = M_{\text{quad}} \cdot M_{\text{dipole}} \cdot M_{\text{drift}}, \quad (4.6)$$

where M_{drift} is the transfer matrix of the drift space, M_{dipole} the dipole magnet one, and M_{quad} the quadrupole magnet one. Notice that these transfer matrices M_{drift} , M_{dipole} , and M_{quad} are independent of each other.

If we define a start point \mathcal{A} and an end point \mathcal{B} of a beam line, this beam line is represented by the transfer matrix $M_{\mathcal{B},\mathcal{A}}$. At the point \mathcal{A} , a charged particle is described as the vector $\mathbf{x}_{\mathcal{A}}$, which is defined in (4.5). Using $M_{\mathcal{B},\mathcal{A}}$ and $\mathbf{x}_{\mathcal{A}}$, the vector $\mathbf{x}_{\mathcal{B}}$ that describes the charged particle at \mathcal{B} can be written by

$$\mathbf{x}_{\mathcal{B}} = M_{\mathcal{B},\mathcal{A}} \cdot \mathbf{x}_{\mathcal{A}}, \quad (4.7)$$

where $M_{\mathcal{B},\mathcal{A}}$ can be the transfer matrix of a single element or the resulting matrix of many elements.

If we assume midplane symmetry, i.e.

$$\begin{aligned} B_x(x, y, t) &= -B_x(x, -y, t), \\ B_y(x, y, t) &= B_y(x, -y, t), \end{aligned} \quad (4.8)$$

a transfer matrix M in any static magnetic element takes its most simple form

$$M = \begin{pmatrix} R_{11} & R_{12} & 0 & 0 & 0 & R_{16} \\ R_{21} & R_{22} & 0 & 0 & 0 & R_{26} \\ 0 & 0 & R_{33} & R_{34} & 0 & 0 \\ 0 & 0 & R_{43} & R_{34} & 0 & 0 \\ R_{51} & R_{52} & 0 & 0 & 1 & R_{56} \\ 0 & 0 & 0 & 0 & 0 & 1 \end{pmatrix}. \quad (4.9)$$

As a result, the matrix can be decomposed into two-by-two submatrices, and these submatrices can be treated independently. In the first-order approximation, the determinant of a transfer matrix is unity whether or not we assume the midplane symmetry [103]. This means that the transfer matrix corresponds to an orthogonal transformation. Moreover, since its determinant is +1, the transfer matrix represents a right-handed coordinate system, which is shown in figure 4.1.

4.1.3 Collective Description of a Beam

In principle, the vector \mathbf{x} of a charged particle along a beam line will be calculated by using the transfer matrix of the beam line. This method can describe only one particle at once. Since a beam is composed of many charged particles, it would be useful to consider many particles at a time. For this reason, we consider four-dimensional phase space representation so that we can handle many charged particles at once. For example, the phase space of

the beam at a position i along a beam line is written by

$$\text{phase space}_i \equiv \{x_i, x'_i, y_i, y'_i\}. \quad (4.10)$$

Beam ellipse matrix The contour of the phase space is called a *beam ellipse* and contains all possible states of charged particles. The beam ellipse can be described by a so-called beam ellipse matrix σ . Assuming that the horizontal plane is independent of the vertical one, the symmetric beam ellipse matrix is defined as

$$\sigma = \begin{pmatrix} \sigma_{11} & \sigma_{12} \\ \sigma_{12} & \sigma_{22} \end{pmatrix}, \quad (4.11)$$

in two-dimensional phase space. The beam matrix can also be expressed in accelerator notation²:

$$\sigma = \epsilon \begin{pmatrix} \beta & -\alpha \\ -\alpha & \gamma \end{pmatrix}, \quad (4.12)$$

where ϵ is a *beam emittance*. Thus, the area A inside the beam ellipse is represented by

$$A = \pi \sqrt{|\sigma|} \equiv \pi \epsilon, \quad (4.13)$$

where $|\sigma|$ is the determinant of σ and the relation $\beta\gamma - \alpha^2 = 1$ is used. This relation among Twiss parameters is the result of the properties of the transfer matrix (See section 6.5 in the reference [103]). The beam emittance is constant along the beam transport line owing to Liouville's theorem in the first-order approximation [104, 105].

Using (4.7), we can write the transformation of the beam matrix between the position \mathcal{A} and \mathcal{B} as

$$\sigma(\mathcal{B}) = M_{\mathcal{B}\mathcal{A}} \cdot \sigma(\mathcal{A}) \cdot M_{\mathcal{B}\mathcal{A}}^T, \quad (4.14)$$

where M^T is the transpose of M .

And, in the two-dimensional phase space, the beam matrix elements σ_{ij} can define maximum beam extents x_{\max} and x'_{\max} and a correlation r_{12} between them as

$$x_{\max} = \sqrt{\sigma_{11}}, \quad x'_{\max} = \sqrt{\sigma_{22}}, \quad r_{12} = \frac{\sigma_{12}}{\sqrt{\sigma_{11}\sigma_{22}}}. \quad (4.15)$$

²It is also called Courant-Snyder, beam ellipse, or Twiss parameters

Gaussian distribution A beam composed of N charged particles can be characterized as a bivariate Gaussian distribution in the two-dimensional space if there is no correlation between the transverse phase spaces [106, 107]. The Gaussian distribution is given by

$$f(\mathbf{x}_i) = \frac{1}{2\pi\sqrt{|\sigma(i)|}} \exp\left[-\frac{1}{2}\mathbf{x}_i^T \cdot \sigma^{-1}(i) \cdot \mathbf{x}_i\right], \quad (4.16)$$

where \mathbf{x}_i is the single column matrix at a position i along a beam line, \mathbf{x}_i^T the transpose matrix, $\sigma(i)$ the first-order beam matrix, $\sigma^{-1}(i)$ the inverse matrix, and $|\sigma(i)|$ its determinant. Using (4.5) and (4.11), the distribution is expressed as

$$f(x, x') = \frac{1}{2\pi\sqrt{\sigma_{11}\sigma_{22}(1-r_{12}^2)}} \exp\left[-\frac{1}{2(1-r_{12}^2)}\left(\frac{x^2}{\sigma_{11}} - \frac{2\sigma_{12}xx'}{\sigma_{11}\sigma_{22}} + \frac{x'^2}{\sigma_{22}}\right)\right],$$

and can be rewritten in accelerator notation as

$$f(x, x') = \frac{1}{2\pi\epsilon} \exp\left[-\frac{1}{2\epsilon}(\gamma x^2 + 2\alpha xx' + \beta x'^2)\right],$$

where ϵ is the beam emittance, $\alpha = -\sigma_{12}/\epsilon$, $\beta = \sigma_{11}/\epsilon$, and $\gamma = \sigma_{22}/\epsilon$.

Beam emittance One standard deviation, *one* σ , of the Gaussian distribution in the beam phase space defines the electron beam emittance [108, 109]. The horizontal (h) and vertical (v) emittances of the MAMI electron beam with an energy of 854.3 MeV are [110]

$$\epsilon_h^N = 13\pi \text{ mm} \cdot \text{mrad}, \quad \epsilon_v^N = 0.84\pi \text{ mm} \cdot \text{mrad}, \quad (4.17)$$

respectively. They are normalized emittances ϵ^N that are defined when particles are accelerated. Since the chicane is a beam transport line, it is necessary to convert the normalized emittance ϵ^N to the emittance ϵ . The relation between them is [111]

$$\epsilon_{h,v}^N = \left(\frac{p}{m_e c}\right) \epsilon_{h,v} = \beta\gamma\epsilon_{h,v}, \quad (4.18)$$

where γ the Lorentz factor, m_e the rest mass of the electron, p the momentum, c the speed of light, and β the velocity in terms of the speed of light. Table 4.1 shows the beam emittance inside the chicane for different electron beam energies.

E_e (MeV)	ϵ_h ($\pi 10^{-3}$ mm · mrad)	ϵ_v ($\pi 10^{-3}$ mm · mrad)
854.30	7.78	0.50
570.40	11.65	0.75
315.25	21.07	1.36

Table 4.1 Beam emittance inside the chicane at different beam energies. These emittance are calculated by (4.18). ϵ_h denotes horizontal beam emittance and ϵ_v does vertical one. We assume that the MAMI beam emittance at 570.40 and 315.25 MeV are the same as the emittance at 854.30 MeV.

4.2 Chicane Components

The A4 Compton polarimeter chicane has many components: dipole magnets, quadrupole magnets, vacuum pumps, wire scanners, laser optical devices, cooling system, and so on. If we consider the properties of the electron beam, the chicane consists of four dipole magnets, two quadrupole magnets, and drift spaces. The other components do not contribute to the electron beam properties of the chicane. As a result, in this section, we focus on these components that contribute significantly to the electron beam properties.

4.2.1 Drift Space

A drift space is a region between magnetic components. Thus, it is a field free region. The transfer matrix of a drift space is written by

$$M_d = \begin{pmatrix} 1 & d & 0 & 0 & 0 & 0 \\ 0 & 1 & 0 & 0 & 0 & 0 \\ 0 & 0 & 1 & d & 0 & 0 \\ 0 & 0 & 0 & 1 & 0 & 0 \\ 0 & 0 & 0 & 0 & 1 & 0 \\ 0 & 0 & 0 & 0 & 0 & 1 \end{pmatrix}, \quad (4.19)$$

where d is the length of the drift space. Figure 4.2 shows the definition of all drift spaces of the chicane, and their corresponding lengths are listed in table 4.2.

4.2.2 Dipole Magnet

A vertical static magnetic field B can be generated by two poles of a dipole magnet³. Two poles have different polarities. Therefore, we call B a dipole

³It is also called a bending magnet

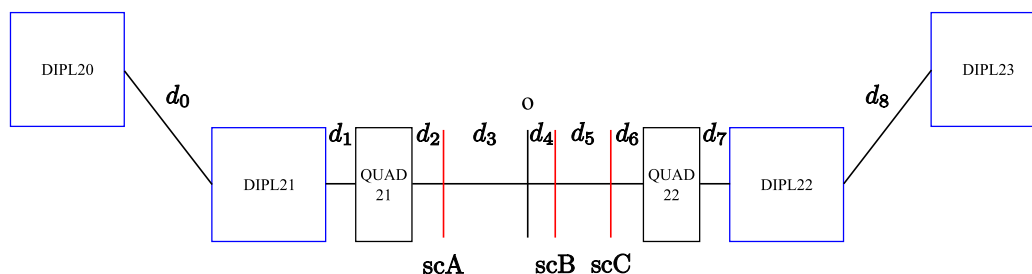


Figure 4.2 Chicane floor layout. d_i denotes the drift space, **scA**, **scB**, and **scC** are three wire scanners that will be described in section 5.1. And **o** connotes the geometric center of the chicane, **DIPL** the dipole magnets, and **QUAD** the quadrupole magnets. The drift spaces from d_2 to d_6 are introduced in order to compare electron beam profiles of a simulation with scanner measurement ones at three wire scanner positions.

drift space	(m)
d_0	1.00
d_1	0.23
d_2	0.22
d_3	0.67
d_4	0.04
d_5	0.63
d_6	0.22
d_7	0.23
d_8	1.00

Table 4.2 The lengths of the drift spaces were obtained from a CAD drawing. This drawing is shown in figure 4.9.

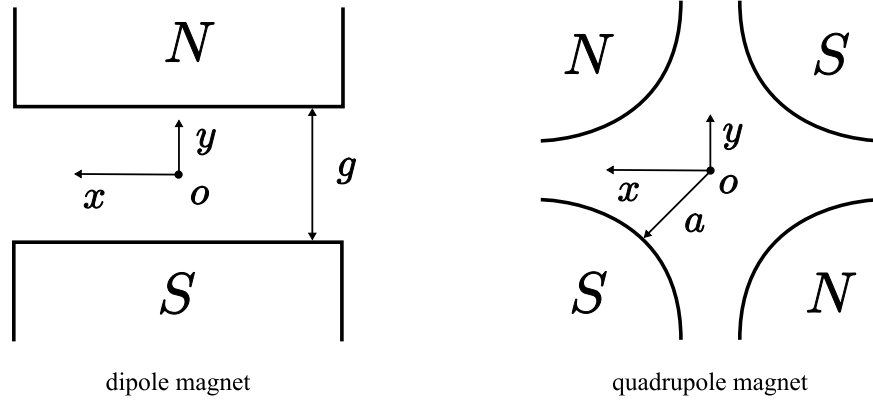


Figure 4.3 Cross section of a dipole and a quadrupole magnet. The beam is going into the paper according to the beam coordinate in figure 4.1. g is the pole gap of the dipole magnet and a the aperture radius of the quadrupole magnet. The magnetic polarities N and S , which are shown here, define the sign of the magnetic field as being positive.

magnet field. The poles are surrounded by a coil that an electric current I flows through. In more practical units, the relation between them is

$$n_w^B I (\text{A} \cdot \text{turns}) = 795.77 \cdot B (\text{kGauss}) \cdot g (\text{cm}), \quad (4.20)$$

where n_w^B is the winding number of the coil around the poles, $n_w^B I$ the total current, and g is the pole gap that is the distance between the poles. Figure 4.3 shows the cross section of a dipole magnet schematically [112, 113].

Sector magnet A sector dipole magnet has an entrance and exit pole face perpendicular to the reference trajectory of the beam. Its first-order transfer matrix is given by

$$\begin{pmatrix} \cos k_x l_d & \frac{1}{k_x} \sin k_x l_d & 0 & 0 & 0 & \frac{h}{k_x^2} (1 - \cos k_x l_d) \\ -k_x \sin k_x l_d & \cos k_x l_d & 0 & 0 & 0 & \frac{h}{k_x} \sin k_x l_d \\ 0 & 0 & \cos k_y l_d & \frac{1}{k_y} \sin k_y l_d & 0 & 0 \\ 0 & 0 & -k_y \sin k_y l_d & \cos k_y l_d & 0 & 0 \\ \frac{h}{k_x} \sin k_x l_d & \frac{h}{k_x^2} (1 - \cos k_x l_d) & 0 & 0 & 1 & -\frac{h^2}{k_x^3} (k_x l_d - \sin k_x l_d) + \frac{l_d}{\gamma^2} \\ 0 & 0 & 0 & 0 & 0 & 1 \end{pmatrix},$$

where l_d is the magnetic length that is the length of the reference trajectory of the beam inside the sector magnet, the curvature h is equal to $1/\rho$, γ is the Lorentz factor, and k_x and k_y are

$$k_x^2 = (1 - n)h^2, \quad k_y^2 = nh^2,$$

where the normalized field index n is

$$n = -\frac{1}{hB_0} \frac{\partial B}{\partial x},$$

where x is the transverse coordinate and B_0 the reference trajectory magnetic field. For more detailed information, see the references [103, 112]. If n is zero, the first-order transfer matrix of the sector magnet has a simple form:

$$M_{\text{sec}} = \begin{pmatrix} \cos \theta_\alpha & \rho \sin \theta_\alpha & 0 & 0 & 0 & \rho(1-\cos \theta_\alpha) \\ -\frac{1}{\rho} \sin \theta_\alpha & \cos \theta_\alpha & 0 & 0 & 0 & \sin \theta_\alpha \\ 0 & 0 & 1 & l_d & 0 & 0 \\ 0 & 0 & 0 & 1 & 0 & 0 \\ \sin \theta_\alpha & \rho(1-\cos \theta_\alpha) & 0 & 0 & 1 & -\rho\left(\theta_\alpha(1-\frac{1}{\gamma^2})-\sin \theta_\alpha\right) \\ 0 & 0 & 0 & 0 & 0 & 1 \end{pmatrix}, \quad (4.21)$$

where ρ is the radius of curvature and θ_α the bending angle, which is equal to l_d/ρ . As we see in the above equation, the magnet acts as a drift space in the vertical plane [103]. We assume that the normalized field derivative n of the dipole magnet is equal to zero.

Pole face rotation matrix If the reference trajectory is not perpendicular to the boundary at the pole face, a so-called fringing field is generated. This field makes an additional focusing or defocusing effect of the dipole magnet depending on the pole face rotation angle. The pole face rotation angle β is defined as the angle between the pole face boundary and the horizontal axis of the reference trajectory. The positive rotation angle means that the defocusing effect is in the horizontal, strictly bending, plane and the defocusing effect exists in the vertical plane. For more detailed information, see the reference [112] page 126 or figure 3.2 in the reference [103]. The transfer matrix of the pole face rotation is

$$M_\beta = \begin{pmatrix} 1 & 0 & 0 & 0 & 0 & 0 \\ \frac{\tan \beta}{\rho_0} & 1 & 0 & 0 & 0 & 0 \\ 0 & 0 & 1 & 0 & 0 & 0 \\ 0 & 0 & -\frac{\tan(\beta-\psi)}{\rho_0} & 1 & 0 & 0 \\ 0 & 0 & 0 & 0 & 1 & 0 \\ 0 & 0 & 0 & 0 & 0 & 1 \end{pmatrix}, \quad (4.22)$$

where ρ_0 in meters is the bending radius of the reference trajectory and

$$\psi = \kappa_1 \left(\frac{g}{\rho_0} \right) \left(\frac{1 + \sin^2 \beta}{\cos \beta} \right) \left[1 - \kappa_1 \kappa_2 \left(\frac{g}{\rho_0} \right) \tan \beta \right], \quad (4.23)$$

radius of curvature ρ	(m)	1
magnetic field B	(kGauss)	12
material		HYPERM 0
weight	(t)	5
pole gap g	(mm)	63.90 ± 0.02
current I	(A)	158
number of turns n_w^B	(turns)	392
ampere turns $n_w I$	(A·turns)	62000
β_1 and β_2	(°)	0 and 26.26

Table 4.3 The original properties of the dipole magnet.

where g is the pole gap in meters, κ_1 an integral related to an extent of the fringing field of the dipole magnet, and κ_2 a second integral related to the extent of the fringing field [114]. We assume that the dipole magnet is a square-edged nonsaturating magnet. With this assumption, $\kappa_1 = 0.45$ and $\kappa_2 = 2.8$ are used to do the chicane simulation [112].

First-order transfer matrix with fringing fields Each dipole magnet has its own entrance pole face angle β_1 and exit angle β_2 because of the geometry of the chicane. Using (4.21) and (4.22), the first-order transfer matrix of the dipole magnet with fringing fields is

$$M_{\text{dipole}} = M_{\beta_2} \cdot M_{\text{sec}} \cdot M_{\beta_1}. \quad (4.24)$$

Dipole magnet properties The dipole magnets, which are components of the A4 Compton backscattering polarimeter, were designed originally for a 360 MeV electron beam. The initial properties of the magnet are listed in table 4.3. Modification of the magnets is necessary for the chicane of the A4 Compton backscattering polarimeter. Using (4.3), the maximum magnetic field $B = 12$ kGauss of the original properties and the reference momentum $P_0 = 1.3$ GeV/ c were used to calculate the radius of the curvature of the reference trajectory and the effective magnetic length of the dipole magnet as follows:

$$\rho_0 = 3.61 \text{ m}, \quad l_d = 0.73 \text{ m}. \quad (4.25)$$

We removed four coil plates per each original dipole magnet because of damaged coil plates. Since n_w^B per each coil plate is 28, the modified n_w^B of the dipole magnet is 280. Since coils in each coil plate were packed and invisible, we cannot count n_w^B directly. Thus, using (4.20) and magnetic field measurement that will be discussed in chapter 5, we can estimate it. Twelve measure-

DIPL	β_1 (mrad)	β_2 (mrad)
20	0	-114.81
21	+114.81	0
22	0	+114.81
23	-114.81	0

Table 4.4 Pole face rotation angles of each dipole magnet.

ments provide the mean of $n_w^B = 278$ and its standard deviation 4. In addition, modified pole face rotation angles of the magnets are listed in table 4.4.

4.2.3 Quadrupole Magnet

The reference trajectory passing through a quadrupole magnet is a straight line and the trajectories of the other particles composing the beam are focused in one plane and are defocused in the other one. Figure 4.3 shows a cross section of the quadrupole magnet that has a horizontal focusing and a vertical defocusing. A magnetic field B_0 at the pole tip is generated by a current I and their relation [115] is

$$n_w^Q I (\text{A} \cdot \text{turns}) = 398 \cdot B_0 (\text{kGauss}) \cdot a (\text{cm}), \quad (4.26)$$

where n_w^Q is the number of turns per pole, a the aperture radius. The so-called effective magnetic length of the quadrupole magnet is given by

$$l_q = l_m + \mathbf{c} \cdot a, \quad (4.27)$$

where l_m is the mechanical length of the pole piece and \mathbf{c} a constant varying between 0.8 and 1.1 depending on dimensions and a position of the quadrupole magnet coil.

The main purpose of the quadrupole magnets is to minimize the spatial and angular dispersion, which will be described in section 4.3.2. To minimize them, we should find the corresponding pole-tip magnetic field B_0 that will be taken up in section 4.3.3.

Quadrupole transfer matrix The first-order transfer matrix of a horizontal focusing quadrupole with a positive magnetic field is given by

$$\begin{pmatrix} \cos k_q l_q & \frac{1}{k_q} \sin k_q l_q & 0 & 0 & 0 & 0 \\ -k_q \sin k_q l_q & \cos k_q l_q & 0 & 0 & 0 & 0 \\ 0 & 0 & \cosh k_q l_q & \frac{1}{k_q} \sinh k_q l_q & 0 & 0 \\ 0 & 0 & k_q \sinh k_q l_q & \cosh k_q l_q & 0 & 0 \\ 0 & 0 & 0 & 0 & 1 & \frac{l_q}{\gamma^2} \\ 0 & 0 & 0 & 0 & 0 & 1 \end{pmatrix},$$

where l_q is the effective magnetic length, γ is the relativistic factor. In addition, k_q^2 is written as

$$k_q^2 = \frac{G}{(B\rho)_R},$$

where $(B\rho)_R$ is the magnetic rigidity of the reference trajectory and the gradient G is

$$G = \frac{B_0}{a}.$$

If the magnetic field is negative, the first two diagonal submatrices are interchanged. As a result, the quadrupole magnet defocuses an electron beam in the horizontal plane and focuses it in the vertical plane.

Quadrupole magnet properties The mechanical length l_m and the radius of the aperture a for the quadrupole magnets used in the chicane are

$$l_m = 200 \text{ mm}, \quad a = 40 \text{ mm}. \quad (4.28)$$

The constant \mathbf{c} , which defines the fringing field effect of the quadrupole magnet, is chosen as an average value between 0.8 and 1.1 by the suggestion of a former MAMI engineer [116]. Thus $\mathbf{c} = 0.95$ and $l_q = 238 \text{ mm}$.

4.3 Study on the Chicane

Since the four dipole magnets, which define the geometry of the chicane for the A4 Compton backscattering polarimeter, are sources of synchrotron radiation when an electron beam is bent inside them. Thus, the synchrotron radiation might be one of disturbances to the parity violating experiment. However, because this subject is outside the scope of the main concern for this thesis, which is a beam control system, we will study an effect of the synchrotron radiation in appendix A. Thus, in this section, we consider only the well-known disturbance, which is known as dispersion. And, we study an periodic system for the chicane and a method of reproducing the idealized beam line with a computer simulation.

4.3.1 Dispersion

If there are dipole magnets in a beam line, dispersion functions are introduced in order to describe a correlation of momentum with transverse position [112]. As mentioned before, since the midplane symmetry is assumed, (4.9) can be

split into the horizontal plane and the vertical one. Using (4.7), the horizontal plane is

$$\begin{pmatrix} x_B \\ x'_B \\ \delta_B \end{pmatrix} = \begin{pmatrix} R_{11} & R_{12} & R_{16} \\ R_{21} & R_{22} & R_{26} \\ 0 & 0 & 1 \end{pmatrix} \begin{pmatrix} x_A \\ x'_A \\ \delta_A \end{pmatrix}. \quad (4.29)$$

Thus,

$$x_B = R_{11}x_A + R_{12}x'_A + R_{16}\delta_A, \quad x'_B = R_{21}x_A + R_{22}x'_A + R_{26}\delta_A, \quad (4.30)$$

where R_{16} represent the position dispersion function D_x and R_{26} the angular dispersion function D'_x respectively. We should minimize the dispersion at the end of the chicane with two quadrupole magnets, which were installed in the center region of the chicane. Finding two optimized magnetic field strengths of the quadrupole magnets is one purpose of the simulation. This issue will be taken up later in section 4.3.3.

4.3.2 Periodic System

To study beam properties and monitor beam profiles along the chicane precisely, it is necessary to measure beam profiles at the entrance of the chicane [117]. But we have no device to do the measurement, and there is not enough room for a new device. To overcome this problem and to understand the properties of the electron beam, we therefore select a periodic system for the chicane even if the chicane is a single pass beam transport line. The periodic system transfers a region in phase space from the entrance to the exit of the chicane without first-order change [103], which can be expressed in terms of the Twiss parameters as follows:

$$\begin{pmatrix} \beta \\ \alpha \\ \gamma \end{pmatrix}_{\text{exit}} \equiv \begin{pmatrix} \beta \\ \alpha \\ \gamma \end{pmatrix}_{\text{entrance}}. \quad (4.31)$$

As a result, we can determine initial Twiss parameters, which are β , α , and γ , of the chicane, which set off a chain of advantages: (1) we calculate the beam size along the chicane; (2) we decide a Rayleigh length of the electron beam in the interaction region, so that we can estimate the luminosity of the A4 Compton backscattering polarimeter; and (3) we use the initial Twiss parameters as input values of the chicane simulation. Note that these advantages are ideal-properties of the chicane.

Initial Twiss parameters

The transfer matrix of the chicane by (4.9) is

$$M_{\text{component}} = \begin{pmatrix} R_{11} & R_{12} \\ R_{21} & R_{22} \end{pmatrix}, \quad (4.32)$$

where R_{ij} is the element of the transfer matrix. And the transfer matrix with the periodic condition can be written in terms of the Twiss parameters [103] as

$$M_{\text{period}} = \begin{pmatrix} \cos \mu + \alpha \sin \mu & \beta \sin \mu \\ -\gamma \sin \mu & \cos \mu - \alpha \sin \mu \end{pmatrix}, \quad (4.33)$$

where μ is the phase advance per period. Thus, since the two transfer matrices are the same

$$M_{\text{component}} \equiv M_{\text{period}}, \quad (4.34)$$

one can calculate that μ is

$$\mu = \cos^{-1} \left(\frac{R_{11} + R_{22}}{2} \right), \quad (4.35)$$

and the Twiss parameters are

$$\alpha = \frac{R_{11} - R_{22}}{2 \sin \mu}, \quad (4.36)$$

$$\beta = \frac{R_{12}}{\sin \mu}, \quad (4.37)$$

$$\gamma = -\frac{R_{21}}{\sin \mu}. \quad (4.38)$$

Using (4.12) and (4.15), α , β , and γ are used to calculate the beam size along the chicane and are the input values of the chicane simulation. Note that (4.34) is only valid for the following condition [103, 105].

$$|\text{Tr}(M)| = |R_{11} + R_{22}| \leq 2, \quad (4.39)$$

where $\text{Tr}(M)$ is the trace of the transfer matrix M . The above condition is strongly related with two quadrupole magnets in the chicane and will be investigated later.

Electron beam Rayleigh length

The periodic system gives a waist condition of the electron beam at the center of the chicane, which is \mathbf{o} in figure 4.2. At the waist position denoted by s_w ,

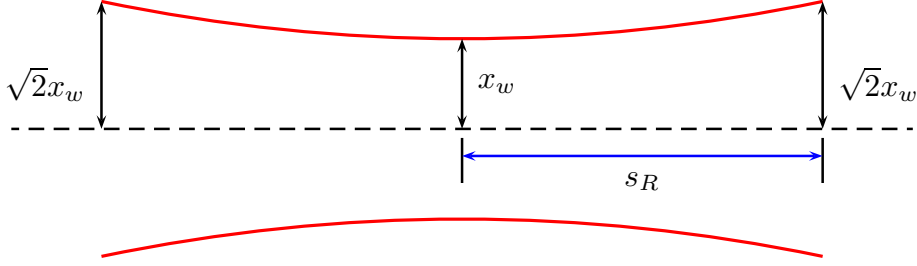


Figure 4.4 The definition of the Rayleigh length s_R . The red solid line is the beam envelope. x_w is the beam transverse size at the waist position.

there are the minimum transverse beam size and an upright phase ellipse, i.e. $\alpha_{h,v} = 0$ and $\gamma_{h,v} = 1/\beta_{h,v}$. For a Gaussian beam, the Rayleigh length s_R is defined as the distance from the waist to a position where the beam size is increased by a factor $\sqrt{2}$ in figure 4.4. As the electron beam can be described by a Gaussian beam, as mentioned in section 4.1.3, we can calculate s_R of the electron beam.

The transverse beam sizes are given by

$$x_h = \sqrt{\epsilon_h \beta_h} \quad x_v = \sqrt{\epsilon_v \beta_v}, \quad (4.40)$$

where ϵ is the emittance and β the Twiss parameter, and the Rayleigh condition is

$$x_R = \sqrt{2}x_w,$$

where x_R is the transverse beam size at s_R and x_w at s_w . Using (4.40) we obtain

$$\beta_R = 2\beta_w. \quad (4.41)$$

As there is only drift space in the interaction region of the chicane, we can use the well-known formula

$$\beta(s) = \beta_0 - 2\alpha_0 s + \gamma_0 s^2,$$

where β_0 , α_0 , and γ_0 are Twiss parameters at an initial position s_0 and $\beta(s)$ at the distance s from s_0 . Therefore, β_R from at the waist position is

$$\beta_R = \beta_w + \frac{s_R^2}{\beta_w}.$$

Thus, using (4.41), we have the remarkably simple result

$$s_R = \pm\beta_w, \quad (4.42)$$

where its unit is meter. If we calculate β_w at the waist position, this corresponds to the Rayleigh length s_R of the electron beam. Note that s_R is independent of the electron beam energy.

4.3.3 The Chicane Simulation with TRANSPORT

The TRANSPORT program uses a matrix formalism to design static magnetic beam transport systems [112]. A beam line is described as a sequence of elements in the simulation of the TRANSPORT program. As mentioned in section 4.2, such elements are the dipole magnets, the quadrupole magnets, and the drift spaces. Furthermore, in the simulation program, we must define additional information that can describe initial electron beam profiles, types of the magnets, and the fringing fields of the dipole magnet. In this section, we assume that a beam centroid, a geometric center of the electron beam in first order, coincides with the reference trajectory at the entrance of the chicane. We call it an *on-axis* beam centroid and will consider an off-axis beam centroid in section 5.1. Main purpose of the chicane simulation in this section is to reproduce the reference trajectory and to understand chicane properties by using the periodic system.

Simulation procedure

The procedure of the chicane simulation has three steps:

- **Step 0** calculates the input values of the TRANSPORT simulation. These are the electron beam energy according to typical results from MAMI energy measurements, the corresponding beam emittance, which is listed in table 4.1, and other values as defined in section 4.2
- **Step 1** makes one TRANSPORT run with the results of Step 0. The run returns the transfer matrix M of the chicane. Using (4.34), initial Twiss parameters can be calculated and are used as additional input values of the next step. In this step, if we replace the two quadrupole magnets with the drift spaces, which means both quadrupole magnets are off, it is impossible to calculate the initial Twiss parameters owing to a violation of the condition (4.39). Thus, it is important to turn on both quadrupole magnets so as that the chicane can be described as a periodic system.
- **Step 2** performs another TRANSPORT run with the results of Step 0 and Step 1. For minimizing the dispersions of the chicane, which are defined in section 4.3.2, this TRANSPORT run has two internal steps. In the first step, it calculates the transfer matrix of the chicane by the beam line elements, then in the second step it tries to find quadrupole magnetic fields in order to satisfy constraints that D_x and D'_x should be zero.

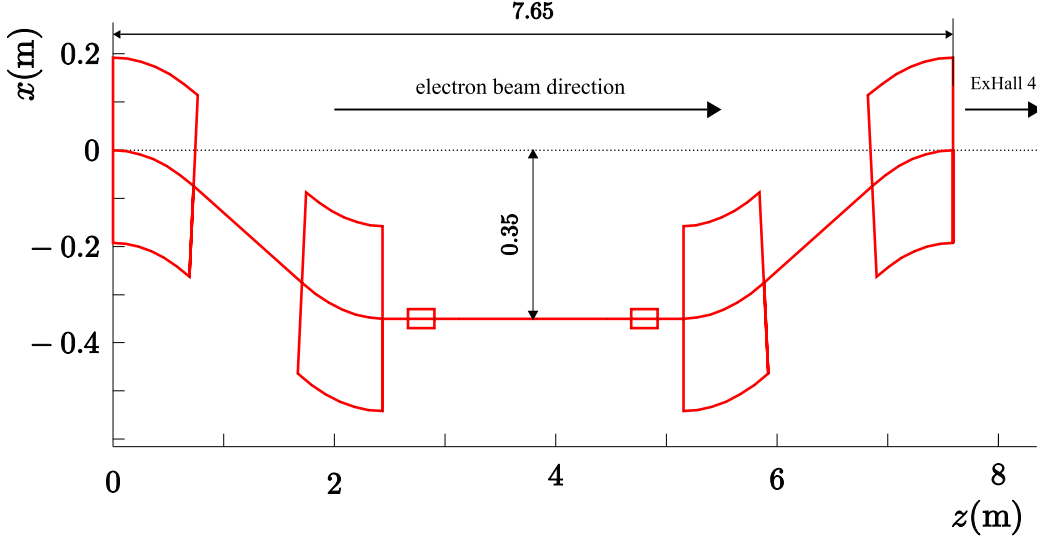


Figure 4.5 The reference trajectory with the four dipole magnets and the two quadrupole magnets in the horizontal plane. The external dimensions of the magnets are selected arbitrary for plotting purposes.

Simulation results

Here, we show the four results of the ideal chicane simulation: (1) the reference trajectory of the chicane; (2) the dispersions along the chicane with and without the quadrupole magnets; (3) the electron beam Rayleigh length; and (4) the Twiss parameters and the electron beam extents along the chicane.

The reference trajectory Figure 4.5 shows the reference trajectory of the electron beam. This trajectory is used for further studies of the chicane, which will be discussed in the next chapter.

The dispersions Figure 4.6 shows the dispersions along the chicane. Without the quadrupole magnets, D_x and D'_x are not zero at the end of the chicane. However, if we use the quadrupole magnets, D_x and D'_x are close to zero at the end. The simulation returns the magnetic field strength for each quadrupole magnets. Using these magnetic fields, in principle, we can minimize the dispersions.

The electron Rayleigh length and luminosity The treatment as a periodic structure leads to a waist condition of the electron beam in the chicane. Therefore, the electron beam Rayleigh length is equal to the Twiss parameter β_w at the waist, which is located in the center of the chicane

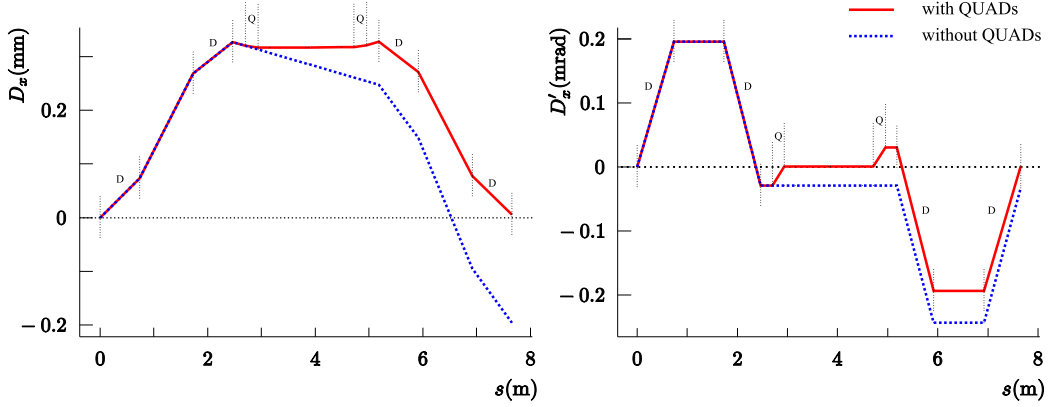


Figure 4.6 Dispersion D_x and D'_x with and without the quadrupole magnets. The left picture is the position dispersion and the right one the angular dispersion in the horizontal plane. The red solid line shows the effects of two quadrupole magnets and the blue dotted line shows the dispersion without the quadrupole magnets. D is the region of a dipole magnet and Q is the region of a quadrupole magnet. s is the distance along the reference trajectory. 854.3 MeV is used as the electron beam energy.

denoted as \mathbf{o} in figure 4.2. The numerical results, which is provided by the simulation, are

$$s_R^{eh} = 4.97 \text{ m}, \quad s_R^{ev} = 12.97 \text{ m}, \quad (4.43)$$

where s_R^{eh} is the horizontal Rayleigh length and s_R^{ev} the vertical one.

Former studies assumed that s_R^{eh} and s_R^{ev} were the same and used $s_R^e = 10$ m as the electron Rayleigh length so as to estimate the luminosity of the polarimeter [93, 118]. With this assumption, the luminosity with the zero crossing angle, i.e. $\alpha_c = 0$, is written as

$$\mathcal{L}^{\text{former}}(l) = \frac{I_e P_L \lambda}{e \pi h c^2} \frac{2}{\epsilon^e + \epsilon^\gamma} \frac{E+1}{\sqrt{(E+1)^2 + \frac{E}{K}(K-1)^2}} \tan^{-1} \left(\frac{l}{2s_R^e} \sqrt{\frac{1+EK}{1+E/K}} \right), \quad (4.44)$$

where l is the length of an overlap between the two beams, I_e the electron current, e the electric charge, P_L the laser power, λ the wavelength of the laser, ϵ^γ the laser emittance, h the Planck constant, c the speed of light, $E = \epsilon^\gamma / \epsilon^e$, $K = s_R^e / s_R^\gamma$, and $\epsilon^e = \sqrt{\epsilon_h^e \cdot \epsilon_v^e}$ the *effective* emittance of the electron beam. For convenience, we call (4.44) the former luminosity $\mathcal{L}^{\text{former}}$.

Since the assumption is not valid in the case of $s_R^{eh} \neq s_R^{ev}$, we calculate the luminosity $\mathcal{L}^{\text{present}}(l)$ as [91]

$$\mathcal{L}^{\text{present}}(l) = \int_{-l/2}^{l/2} \frac{d\mathcal{L}^{\text{present}}(z)}{dz} dz = 2 \int_0^{l/2} \frac{d\mathcal{L}^{\text{present}}(z)}{dz} dz, \quad (4.45)$$

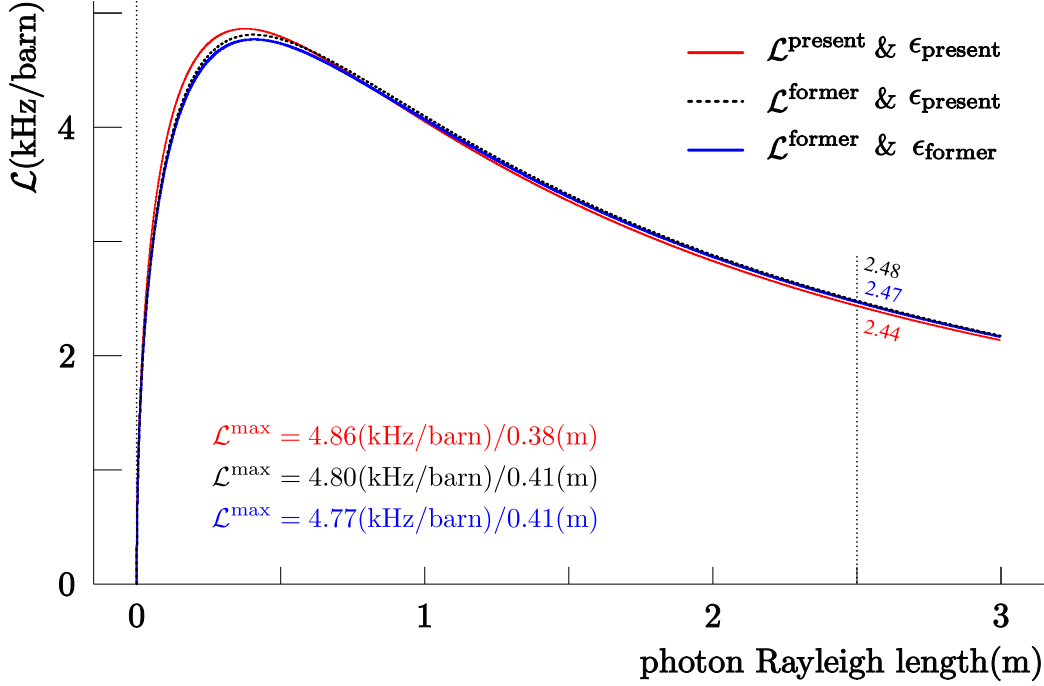


Figure 4.7 Expected luminosities with $l = 2$ m and the 854.3 MeV electron beam. Here, the wavelength of the green laser $\lambda = 514.5$ nm, its power $P_L = 10$ W, and $I_e = 20$ μ A are used. $\mathcal{L}_{\text{former}}$ uses the former luminosity definition (4.44) and $\mathcal{L}_{\text{present}}$ the present luminosity definition (4.45). \mathcal{L}^{max} represents the maximum luminosity with the corresponding photon Rayleigh length s_R^γ . The black dotted line represents the former results [93, 118]. The former studies used the different electron beam emittances. The geometry of the Compton polarimeter determined that s_R^γ is 2.5 m. The expected luminosities are 2.44, 2.47, and 2.48 kHz/barn respectively at $s_R^\gamma = 2.5$ m.

where the differential luminosity $d\mathcal{L}^{\text{present}}(z)/dz$ is

$$\frac{d\mathcal{L}^{\text{present}}(z)}{dz} = \frac{I_e P_L \lambda}{e \pi h c^2} \frac{1}{\sqrt{\epsilon_h^e s_R^{eh} + \epsilon^\gamma s_R^\gamma + z^2 \left(\frac{\epsilon_h^e}{s_R^{eh}} + \frac{\epsilon^\gamma}{s_R^\gamma} \right)} \sqrt{\epsilon_v^e s_R^{ev} + \epsilon^\gamma s_R^\gamma + z^2 \left(\frac{\epsilon_v^e}{s_R^{ev}} + \frac{\epsilon^\gamma}{s_R^\gamma} \right)}}.$$

Here, we call (4.45) the *present* luminosity for convenience.

Figure 4.7 shows three expected luminosities when $l = 2$. The blue solid line is the result of the former studies [93, 118] and is calculated from (4.44) by using $\epsilon_h^e = 8.0\pi \times 10^{-3}$ mm \cdot mrad and $\epsilon_v^e = 0.5\pi \times 10^{-3}$ mm \cdot mrad. For convenience, we call this emittance the *former* emittance ϵ_{former} . In this case, the maximum luminosity is 4.80 kHz/barn, and the corresponding photon

l (m)	$\mathcal{L}^{\text{present}}$ (kHz/barn)		$\mathcal{L}^{\text{former}}$ (kHz/barn)	
	$\epsilon_{\text{present}}$	$\epsilon_{\text{present}}$	$\epsilon_{\text{present}}$	ϵ_{former}
2.00	2.44	2.48	2.48	2.47
1.50	1.86	1.89	1.89	1.89
1.33	1.66	1.69	1.69	1.68
1.00	1.26	1.28	1.28	1.27
0.50	0.63	0.64	0.64	0.64

Table 4.5 Expected luminosities of the former and the present studies. Here, l is the length of an overlap between the electron and the laser beams, $\mathcal{L}^{\text{present}}$ is given in (4.45), and $\mathcal{L}^{\text{former}}$ in (4.44). $\epsilon_{\text{present}}$ represents the emittances listed in table 4.1 and ϵ_{former} does them that were used in the former studies. $l = 1.33$ m is the distance between the wire scanner A and C.

Rayleigh length s_R^γ is 0.41 m. The black dotted line is calculated by using the same former luminosity equation (4.44), but the different beam emittances, which is listed in table 4.1, and the maximum luminosity is 4.77 kHz/barn at $s_R^\gamma = 0.41$ m. We call this the *present* emittance $\epsilon_{\text{present}}$. The red solid line is calculated from (4.45) by using $\epsilon_{\text{present}}$ and the maximum luminosity is 4.86 kHz/barn at $s_R^\gamma = 0.38$ m.

Since the geometry of the Compton backscattering polarimeter determines that the photon Rayleigh length is 2.5 m, these luminosities at $s_R^\gamma = 2.5$ m are calculated and are listed in table 4.5. According to these results, we have no significant difference between the former and the present. Therefore, the assumption, which is that s_R^{eh} and s_R^{ev} were the same and $s_R^e = 10$ m, of the former studies is also valid to estimate the luminosity of the polarimeter with the periodic condition.

Twiss parameters and beam extents Figure 4.8 shows the Twiss parameters (β and α) and the beam sizes or extents along the chicane with the quadrupole magnets. In principle, if the electron beam matches this periodic condition at the entrance of the chicane, the chicane does not disturb the properties of the electron beam at its exit.

4.4 Installation of the Compton Backscattering Polarimeter

Before the installation of the polarimeter, the electron beam went through the whole experimental hall 3 (ExHall3) in a straight vacuum pipe, and entered

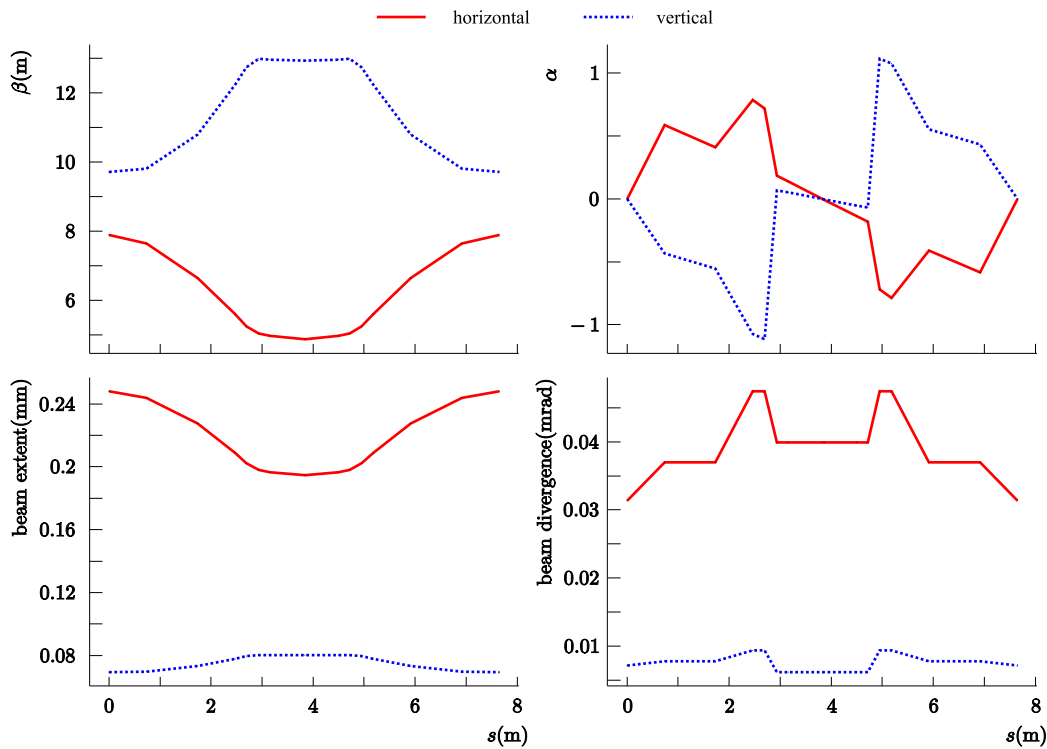


Figure 4.8 Twiss parameters and beam profiles. The initial Twiss parameters are the same as the final ones because of the periodic system. The result is the optimum condition of the chicane. Note that the beam extent and the beam divergence depend on the electron beam energy, which is 854.3 MeV, because different energies have different emittance.

into a liquid hydrogen target in experimental hall 4 (ExHall4), in which the main apparatus for the parity violation experiment is located. The reference trajectory and the poles of four dipole magnets had been designed according to the properties of the dipole magnets and a consideration of the dimensions of the ExHall3. First of all, we measured all basic components that define the geometry of the chicane as follows: (1) stands for the dipole magnets, vacuum chambers, and the quadrupole magnets; (2) return yokes, coil plates, and cooling pipes of the dipole magnets; (3) two quadrupole magnets; and (4) vacuum components. Then, we drew these components in the CAD drawing. They restrict available spaces where we install other components that are the laser optical devices, wire scanners, vacuum pumps, and so on. This CAD drawing, therefore, has been and will be used to be the position reference of the A4 Compton backscattering polarimeter. The top view of the polarimeter is shown in figure 4.9. And, figure 4.10 shows a perspective view.

After removing the straight beam pipe, we defined new beam alignment marks with several theodolites and the Axyz software of Leica Geosystems according to pre-existing beam alignment marks that were on the floor and the wall of the ExHall3. Then, the positions of the four dipole magnets were determined by the beam alignment marks. The A4 Compton backscattering polarimeter was installed in December 2002 and is now fully operational. Figure 4.11 shows the panoramic view of the Compton polarimeter in the ExHall3. More detailed information about the construction process of the polarimeter can be found in the references [93, 100].

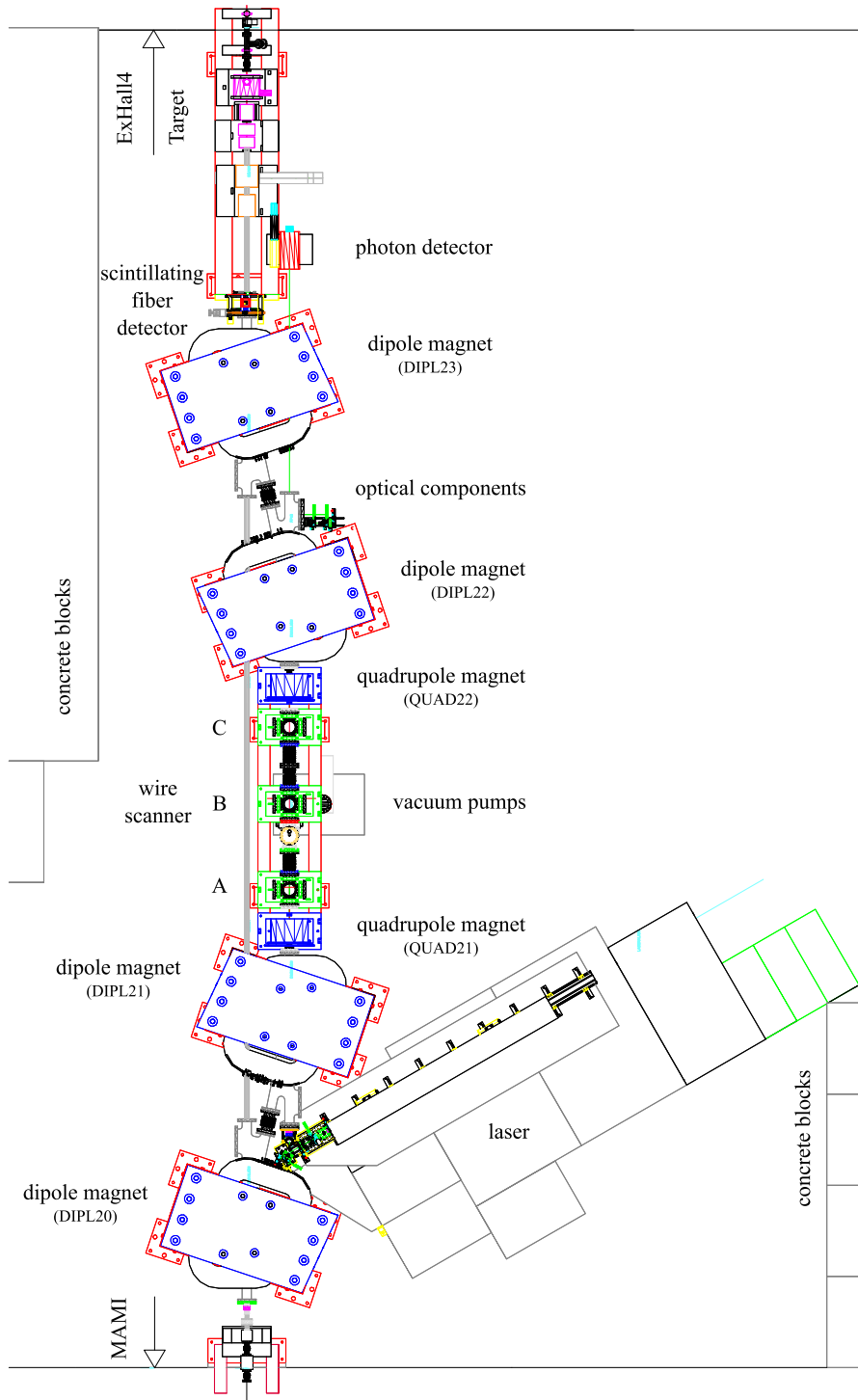


Figure 4.9 The top view of the experimental hall 3 in the CAD drawing.

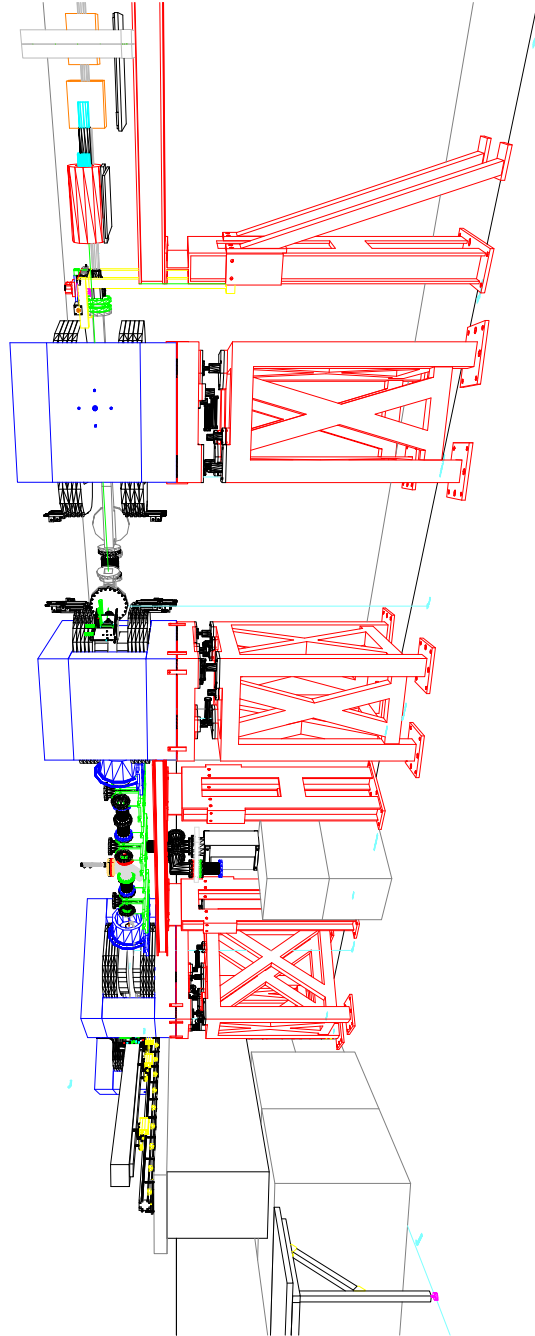


Figure 4.10 The perspective view of the experimental hall 3. The small blue beam alignment marks, which are on the walls and on the floor, are used to define the reference trajectory.

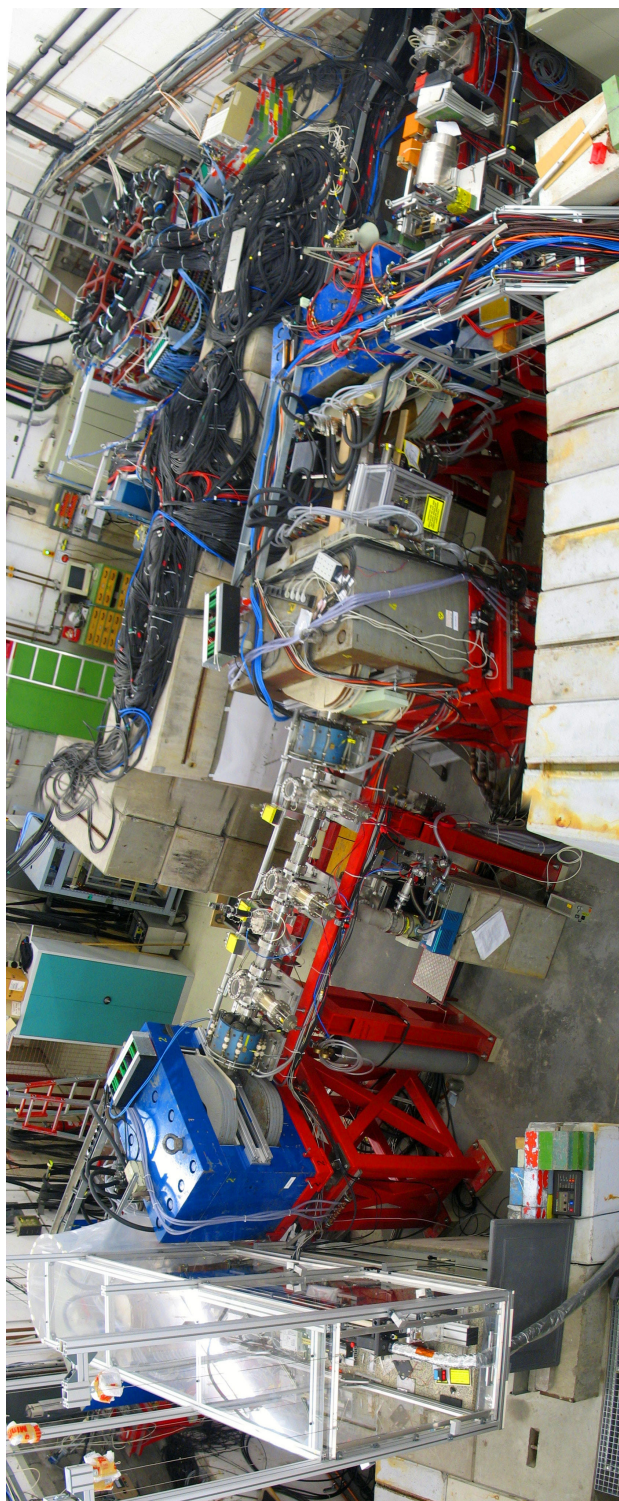


Figure 4.11 The panoramic view of the experimental hall 3.

Chapter 5

Chicane Development

The primary purpose of the chicane development is to design a beam control system that makes an overlap between the electron beam and the laser beam and that satisfies following criteria: (1) a system keeps the crossing angle α_c as small as possible, described in section 3.2.2, (2) a system is easy to use, quick, and reliable, and (3) a system minimizes possible disturbances to the PV experiment. In the last chapter, we studied the chicane with the reference trajectory by using the ideal simulation. However, this idealized chicane is, as we all know, difficult to realized like many ideals. Thus, we must take account of the properties of the real chicane in the beam line simulation, and we make the beam line simulation as close as possible to the real chicane. In the first part of this chapter, we describe an analysis of the wire scanner. And we use this analysis to determine the electron beam position and the laser beam position simultaneously. In the second part of this chapter, we consider the properties of the real chicane and describe how to apply the realistic properties to the chicane simulation. In the last part, we combine the beam position determination and the realistic chicane simulation in order to develop the electron beam control system. And we present the end result of the chicane development and discuss a limited range of the beam control system.

5.1 Wire Scanner Analysis

We use wire scanners to determine the transverse positions of the electron beam and the laser beam. The wire scanners located in the interaction region, which is shown in figure 3.6, of the A4 Compton backscattering polarimeter were developed at MAMI almost twenty years ago and are still used in the MAMI beam line. We call them scA, scB, and scC (sc stands for a scanner

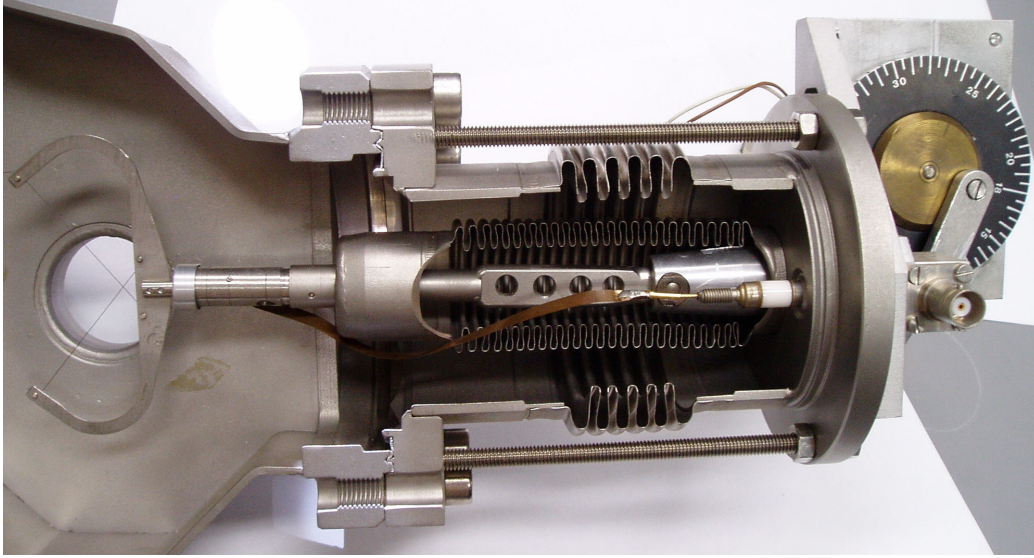


Figure 5.1 A sectional view of the MAMI standard wire scanner

and A, B, C for their positions along the electron beam line). Figure 5.1 shows a photograph of the MAMI standard wire scanner. The wire scanners¹ in the A4 chicane are fixed to six-way cross vacuum chambers. They are modified with regard to the installation geometry and the number of wires. The MAMI method for determining a beam position does not fulfill our purpose of determining two beam positions simultaneously, because the method is valid for only an electron beam. Furthermore, we already have the six-way cross vacuum chamber. Thus, it is not necessary to follow the MAMI installation geometry. The MAMI standard wire scanner has two wires. We add two more wires to the wire scanners in order to improve accuracy of the wire scanner measurement. These four wires also prevent the wire scanner measurement from the risk that wires may be damaged accidentally.

For a scanner measurement during a beam time, we use a small electron beam current (50 nA) and small internal cavity laser power (approximately 0.5 W). When the electron beam hits a wire, Bremsstrahlung and electrons and positron pairs are generated. We record this radiation by a lead glass detector. At the same time, we record the laser power, which decreases when a wire passes through the laser beam. Furthermore, we record a signal that is generated by reference switches of the motor of the wire scanner.

In this section, we study a detailed analysis of the wire scanner mechanics. From this analysis, we derive the equation of motion in relations to three

¹The first two wire scanners (scA and scB) use the 20 μm gold-plated tungsten wire and the last wire scanner (scC) does the 60 μm tungsten wire.

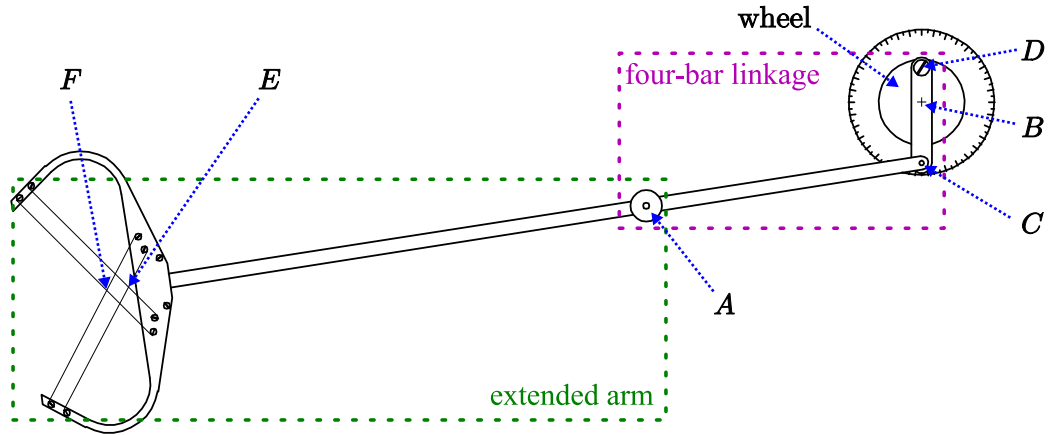


Figure 5.2 The schematic drawing of the wire scanner. The symbols A , B , C , D , E , and F are essential points in order to describe the wire scanner motion; see figure 5.3, 5.4, and 5.5. The motor of the wire scanner is connected to the wheel.

measured signals. Then, we apply this so as to determine electron and laser beam positions.

5.1.1 The Equation of Motion of the Wire Scanner

Figure 5.2 shows the schematic drawing of the wire scanner. In order to find the equation of motion of the wire scanner easily, we separate it into two parts: (1) *plane four-bar linkage*, a concept from mechanical engineering, that is shown on the drawing by a purple dotted box; and (2) an extended arm by a green one. The four-bar linkage of the wire scanner is a vital part of the wire scanner movement and is used to convert the uniform continuous motion of the wheel into the nonuniform oscillation of the scanner arm. The extended arm movement is completely determined by the movement of the plane four-bar linkage.

Plane four-bar linkage

Figure 5.3 shows a plane four-bar linkage schematically. From the vector loop method, we define the plane four-bar linkage as

$$\vec{r}_2 + \vec{r}_3 = \vec{r}_1 + \vec{r}_4. \quad (5.1)$$

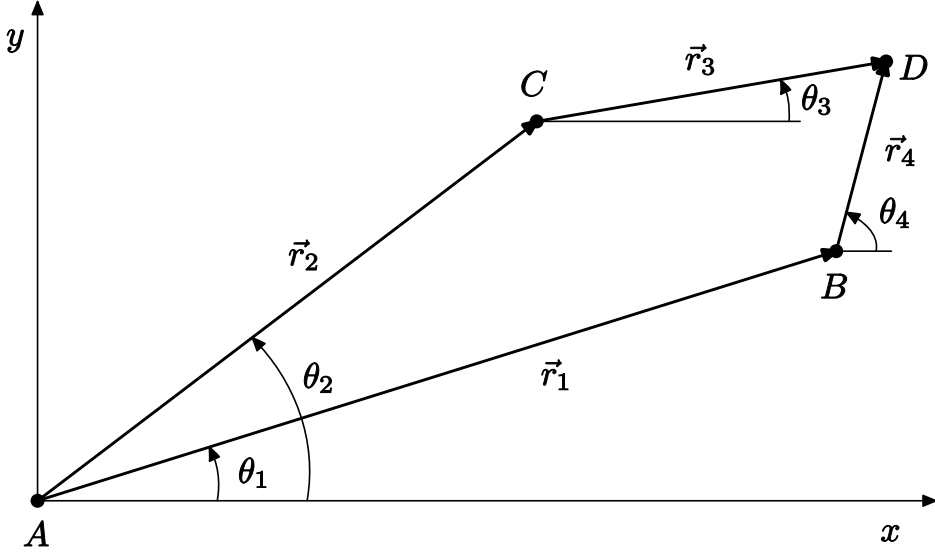


Figure 5.3 The plane four-bar linkage with *nodes* at $A, B, C,$ and D . A and B are fixed, so they are called pivot points. We call each r_k a *link*. Since r_1 has no movement, θ_1 stays constant.

Considering the x - and y -components of the vectors, two algebraic equations are obtained as follows:

$$\begin{aligned} r_3 \cos \theta_3 &= r_1 \cos \theta_1 + r_4 \cos \theta_4 - r_2 \cos \theta_2, \\ r_3 \sin \theta_3 &= r_1 \sin \theta_1 + r_4 \sin \theta_4 - r_2 \sin \theta_2. \end{aligned} \quad (5.2)$$

Since we want to find the relation between θ_2 and θ_4 , we eliminate θ_3 . After some algebra, we have

$$\begin{aligned} -2r_2(r_1 \cos \theta_1 + r_4 \cos \theta_4) \cos \theta_2 - 2r_2(r_1 \sin \theta_1 + r_4 \sin \theta_4) \sin \theta_2 \\ + r_1^2 + r_2^2 - r_3^2 + r_4^2 + 2r_1 r_4 \cos(\theta_1 - \theta_4) = 0. \end{aligned}$$

For simplicity, the above equation is rewritten as follows:

$$K_1(\theta_1, \theta_4) \cos \theta_2 + K_2(\theta_1, \theta_4) \sin \theta_2 + K_3(\theta_1, \theta_4) = 0. \quad (5.3)$$

Now, an intermediate variable $\mu = \tan \frac{\theta_2}{2}$ is introduced to obtain

$$\mu_{\pm} = \tan \frac{\theta_2^{\pm}}{2} = \frac{K_2(\theta_1, \theta_4) \pm \sqrt{K_1(\theta_1, \theta_4)^2 + K_2(\theta_1, \theta_4)^2 - K_3(\theta_1, \theta_4)^2}}{K_1(\theta_1, \theta_4) - K_3(\theta_1, \theta_4)}. \quad (5.4)$$

Finally, we find expressions for θ_2

$$\theta_2^{\pm} = 2 \arctan(\mu_{\pm}). \quad (5.5)$$

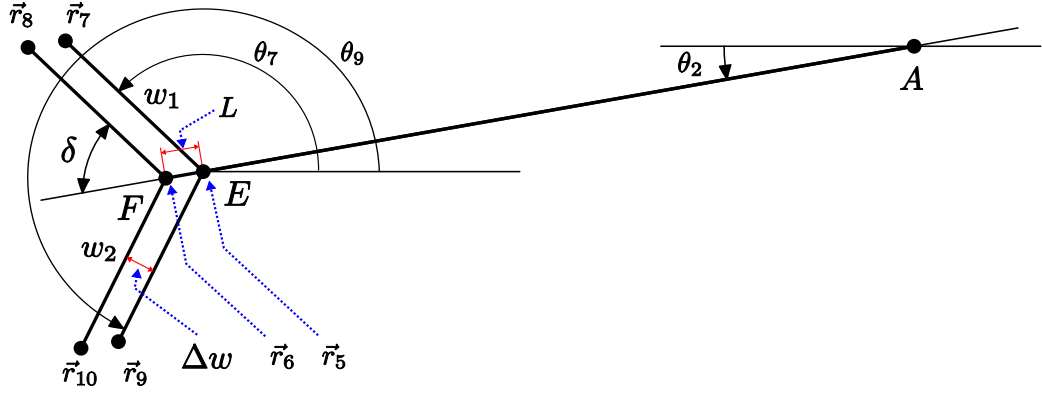


Figure 5.4 The extended arm of the wire scanner. In the drawing, w_i is the length of each wire and Δw the gap between the wires. δ , Δw , and L are related via $L = \Delta w / \sin \delta$.

Furthermore, it is possible to calculate θ_4 as a function of θ_2 by the same procedure. We obtain

$$2r_4(r_1 \cos \theta_1 - r_2 \cos \theta_2) \cos \theta_4 + 2r_4(r_1 \sin \theta_1 - r_2 \sin \theta_2) \sin \theta_4 + r_1^2 + r_2^2 - r_3^2 + r_4^2 - 2r_1 r_2 \cos(\theta_1 - \theta_2) = 0,$$

that is redefined as

$$K'_1(\theta_1, \theta_2) \cos \theta_4 + K'_2(\theta_1, \theta_2) \sin \theta_4 + K'_3(\theta_1, \theta_2) = 0. \quad (5.6)$$

Thus, θ_4 as a function of θ_2 is

$$\nu_{\pm} = \tan \frac{\theta_4^{\pm}}{2} = \frac{K'_2(\theta_1, \theta_2) \pm \sqrt{K'_1(\theta_1, \theta_2)^2 + K'_2(\theta_1, \theta_2)^2 - K'_3(\theta_1, \theta_2)^2}}{K'_1(\theta_1, \theta_2) - K'_3(\theta_1, \theta_2)}. \quad (5.7)$$

And expressions for θ_4 is

$$\theta_4^{\pm} = 2 \arctan(\nu_{\pm}). \quad (5.8)$$

These equations (5.5) and (5.8) are general solutions for a plane four-bar linkage.

Extended arm

Figure 5.4 shows the schematic drawing for the extended arm. From this

drawing, we see that the other parameters are

$$\begin{aligned}
\vec{r}_6 &= \{-r_6 \cos \theta_2, -r_6 \sin \theta_2\}, \\
\vec{r}_7 &= \{w_1 \cos \theta_7 - r_5 \cos \theta_2, w_1 \sin \theta_7 - r_5 \sin \theta_2\}, \\
\vec{r}_8 &= \{w_2 \cos \theta_8 - r_6 \cos \theta_2, w_2 \sin \theta_8 - r_6 \sin \theta_2\}, \\
\vec{r}_9 &= \{w_1 \cos \theta_9 - r_6 \cos \theta_2, w_1 \sin \theta_9 - r_5 \sin \theta_2\}, \\
\vec{r}_{10} &= \{w_2 \cos \theta_{10} - r_5 \cos \theta_2, w_2 \sin \theta_{10} - r_6 \sin \theta_2\},
\end{aligned} \tag{5.9}$$

where $\theta_7 = \pi - \delta + \theta_2 \equiv \theta_8$ and $\theta_9 = \pi + \delta + \theta_2 \equiv \theta_{10}$.

Scanner parameters

In order to demonstrate the motion of the wire scanner explicitly, it is necessary to assign real numbers to its parameters. The parameters w_1 , w_2 , δ , and Δw are determined by taking measurements of the actual wire scanner as follows:

$$\begin{aligned}
\delta &= 53.5^\circ, & \Delta w &= 5 \text{ mm}, \\
w_1 &= 40 \text{ mm}, & w_2 &= 35 \text{ mm}.
\end{aligned} \tag{5.10}$$

Note that the standard MAMI wire scanner has two wires with $\delta = 50^\circ$. For the other parameters, since we cannot measure them directly, we need to find relations between two different notations: one based on the full vertical motion of the wire scanner and the other linked to the definitions of figure 5.3 and 5.4. For convenience, we call the former *the MAMI notation* and the latter *the linkage notation*. The MAMI notation is shown in figure 5.5. Therefore, we know

$$\begin{aligned}
r_3 &= 30 \text{ mm}, \\
h &= 47 \text{ mm}, \\
h' &= 2r_4 = 25 \pm 1 \text{ mm}, \\
l &= r_2 + r_5 = 233 \pm 1 \text{ mm},
\end{aligned} \tag{5.11}$$

where h is the full vertical motion range of the end point E and h' the corresponding range of the other end C .

Using these two notations, we obtain

$$\begin{aligned}
\frac{h'}{h} &= \frac{2r_2 \sin \frac{\varphi}{2}}{2r_5 \sin \frac{\varphi}{2}} = \frac{r_2}{r_5} = \frac{2r_4}{h}, \\
r_5 &= \frac{l}{1 + h'/h}, & r_2 &= \frac{l}{1 + h/h'}, \\
r_3 &= r_1 \sin \theta_1, & r_4 &= r_2 \sin \frac{\varphi}{2}, \\
r_1 &= \sqrt{r_2^2 + r_3^2 - r_4^2}.
\end{aligned} \tag{5.12}$$

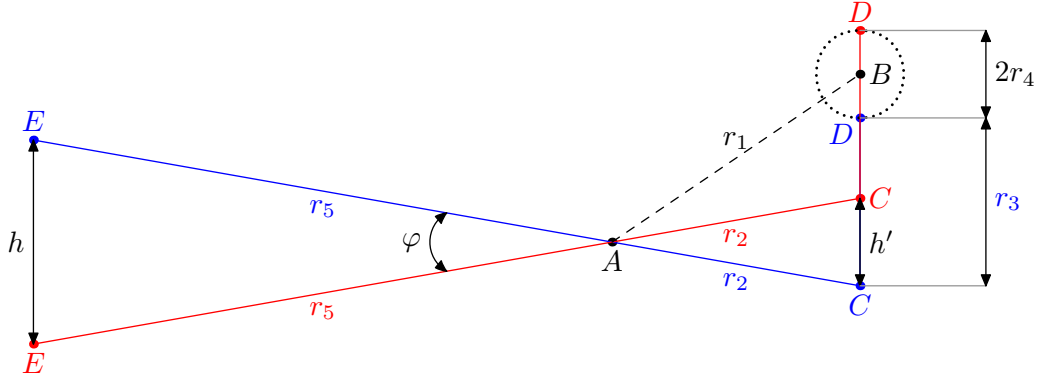


Figure 5.5 The MAMI notation of the parameters of the wire scanner. This drawing shows the full range of the wire scanner motion. In the drawing, $r_2 + r_5$ is called the scanner arm, φ the maximum range of the angle θ_2 , and A and B the pivot points. The solid red line represents the lowermost position of the motion at $\theta_4 = \pi/2$ and the solid blue line the uppermost one at $\theta_4 = 3\pi/2$.

The values of the parameters, which are related to the linkage notation, are determined as follows:

$$\begin{aligned}
 r_1 &= 85 \text{ mm}, & r_2 &= 81 \text{ mm}, \\
 r_3 &= 30 \text{ mm}, & r_4 &= 13 \text{ mm}, \\
 r_5 &= 148 \text{ mm}, & r_6 &= 154 \text{ mm}, \\
 \theta_1 &= 20.6^\circ, & \varphi &= 17.8^\circ.
 \end{aligned} \tag{5.13}$$

The range of θ_2 and the θ_4 range

Since $\tan \frac{\theta}{2}$ must be a real number, the values under the square root of the equation (5.4) and (5.7) need to be greater than or equal to zero. This condition constrains the θ_2 range and the θ_4 range.

From (5.7), the terms under the square root must fulfill the condition as

$$K'_1(\theta_1, \theta_2)^2 + K'_2(\theta_1, \theta_2)^2 - K'_3(\theta_1, \theta_2)^2 \geq 0.$$

Thus, θ_2 has the following range

$$\frac{r_1^2 + r_2^2 - (r_3 + r_4)^2}{2r_1r_2} \leq \cos(\theta_1 - \theta_2) \leq \frac{r_1^2 + r_2^2 - (r_3 - r_4)^2}{2r_1r_2}. \tag{5.14}$$

And, from (5.4), the condition for θ_4 is

$$K_1(\theta_1, \theta_4)^2 + K_2(\theta_1, \theta_4)^2 - K_3(\theta_1, \theta_4)^2 \geq 0.$$

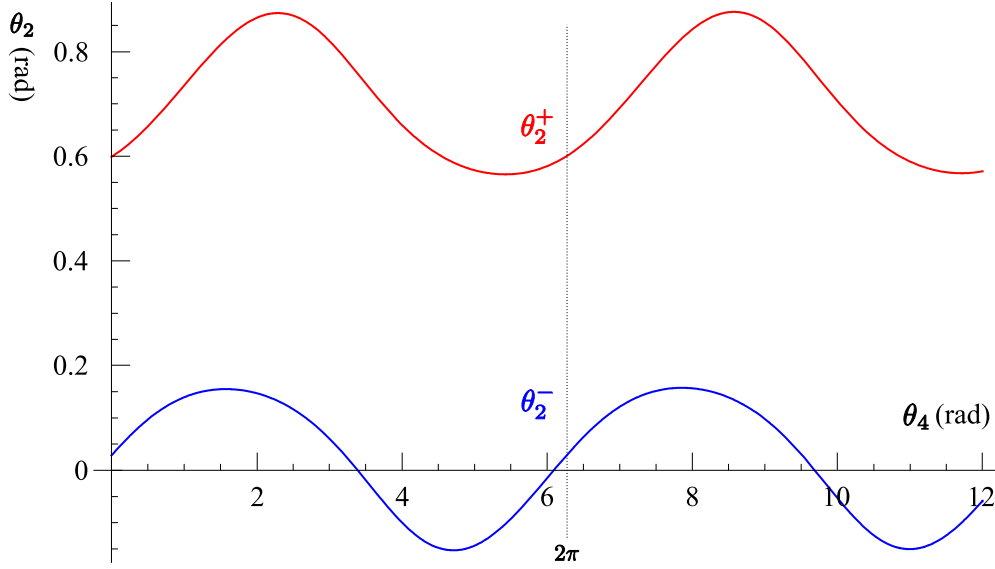


Figure 5.6 Two possible solutions of the angle θ_2 . The blue color (lower) plot shows θ_2^- and the red (upper) one θ_2^+ . Since the angle range is the same as (5.16), θ_2^- corresponds to the real solution to the wire scanner motion. The dotted line represents that $\theta_4 = 2\pi$.

Therefore, the range of θ_4 is

$$\frac{-r_1^2 - r_4^2 + (r_2 - r_3)^2}{2r_1r_4} \leq \cos(\theta_1 - \theta_4) \leq \frac{-r_1^2 - r_4^2 + (r_2 + r_3)^2}{2r_1r_4}. \quad (5.15)$$

Using (5.13), (5.14), and (5.15), θ_2 and θ_4 are in the range of

$$\begin{aligned} -8.9^\circ &\leq \theta_2 \leq 8.9^\circ, \\ -2.8 + 1.5i &\leq \theta_4 \leq 0.4 - 1.5i, \end{aligned} \quad (5.16)$$

respectively. The complex number of θ_4 represents no limit on the angle θ_4 , which can therefore rotate continuously ($-\infty \leq \theta_4 \leq \infty$). And the full range of θ_2 , which is 17.8° , is the same value as the angle φ in (5.13). Therefore, two methods yield the same result of the maximum range of θ_2 .

The equation of motion

Until now, we found the general solutions of the plane four-bar linkage and calculated the possible range of θ_2 and θ_4 . Now, we apply these to the real wire scanner. Since we know that θ_4 rotates continuously according to (5.16), we plot two functions of the angle θ_2 as a function of θ_4 in figure 5.6. Then,

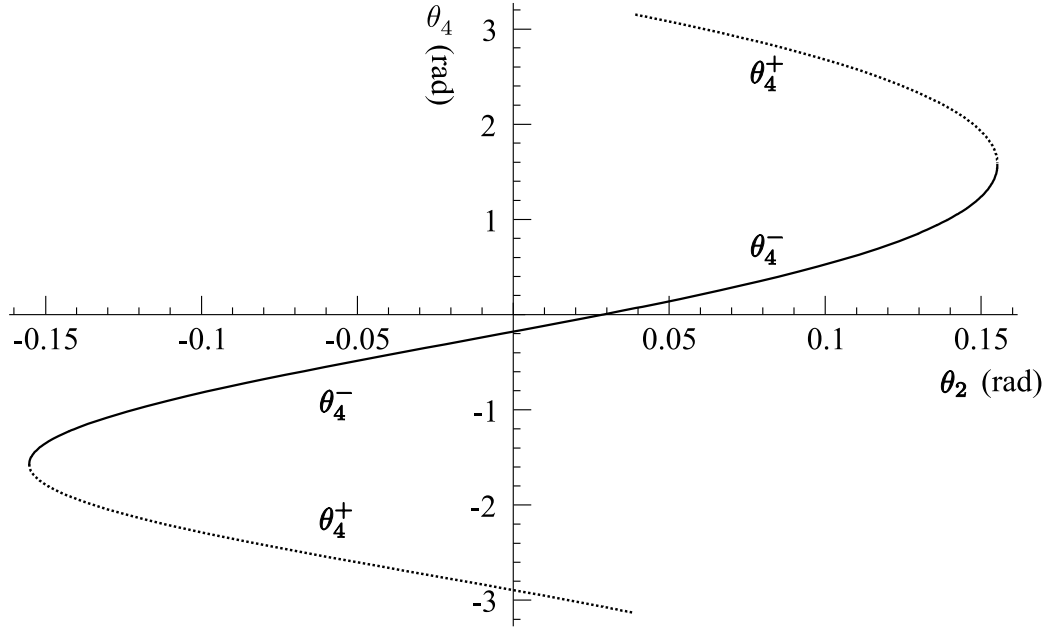


Figure 5.7 Two solutions of the angle θ_4 . The dotted line shows θ_4^+ and the solid line θ_4^- . We see that θ_4 is within the range of $-\pi$ to π when we sum two solutions.

we see that θ_2^- fulfills the angle range shown in (5.16). For this reason, we know that θ_2^- corresponds to the real wire scanner movement. And, using this θ_2 range, we plot two solutions of θ_4 in figure 5.7. Thus, the sum of these solutions describe the movement of the wheel of the wire scanner correctly.

5.1.2 Determination of the Beam Position

Figure 5.8 shows an approach to determine the beam position. For simplicity, in the analysis of the position determination, we use only the outer wires, which are denoted as **wire 1** and **wire 4** in figure 5.8, that correspond to \vec{r}_7 and \vec{r}_9 in figure 5.4 respectively.

When the motor is off, the rest positions of the wires are below the beam position that is shown by the symbol \bullet in figure 5.8. When the motor is on, first, **wire 1** crosses the beam at an arm angle θ_5^r (the superscript r stands for red). The red color symbols represent this instant. After that **wire 4** does the same at another arm angle θ_5^b and this is represented by the blue symbols (b stands for blue). During one cycle of the motor, which is the θ_4 range of 0 to 2π , these moments in figure 5.8 will occur twice.

Since we know the geometric relation between them, we can find the beam

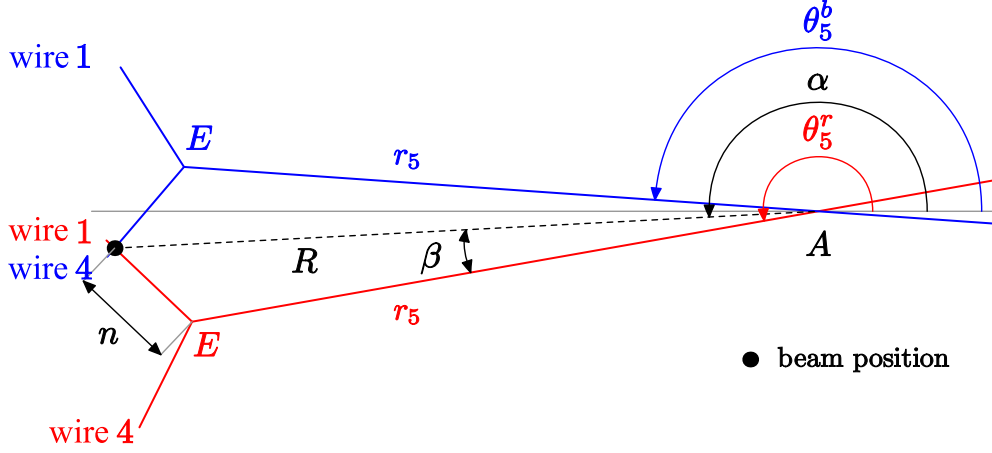


Figure 5.8 Beam position determination. In the drawing, $\theta_5 = \theta_2 + \pi$, $n = \sin \beta / \sin \delta$, and A is the pivot point. E and r_5 are defined in figure 5.4. The outer wires are denoted as **wire 1** and **wire 4**. R is the distance between A and the ideal beam axis (\bullet). A similar drawing applies to the inner wires.

position as

$$x = R \cos \alpha, \quad y = R \sin \alpha, \quad (5.17)$$

where

$$R = \frac{r_5 \sin \delta}{\sin(\delta - \beta)}, \quad (5.18)$$

$$\alpha = \frac{\theta_5^r + \theta_5^b}{2}, \quad \beta = \frac{|\theta_5^r - \theta_5^b|}{2},$$

where δ is defined in figure 5.4. When the inner wire pair is chosen, r_5 is replaced with r_6 . We call the movement from the red one to the blue one *the upward movement* and call the movement from the blue one to the red one *the downward movement* of the wire scanner. In both cases, the angle β is defined as being positive. Thus, we use the absolute value of the difference between θ_5^r and θ_5^b to calculate β .

In that θ_2 is more pertinent to the beam position determination than θ_5 , the beam position (5.17) should be rewritten in terms of θ_2 as

$$x = -R \cos \gamma, \quad y = -R \sin \gamma, \quad (5.19)$$

where

$$\gamma = \frac{\theta_2^r + \theta_2^b}{2}, \quad \beta = \frac{|\theta_2^r - \theta_2^b|}{2}.$$

If we know θ_2^r and θ_2^b , we can calculate the beam position by using the above equation. Since θ_2 is a function of θ_4 in (5.5), we have to know the corresponding θ_4^r and θ_4^b . Eventually, to determine the beam position is the same as to find only two angles of θ_4 that correspond to two moments when two wires, e.g. **wire 1** and **wire 4** shown in figure 5.8, cross the beam.

The angle θ_4

Three signals are necessary to perform the beam position determination. When a wire passes through the electron beam, the radiation is generated and is recorded by a lead glass detector. This detector is located in a beam tunnel between the experimental hall 3 and 4. For convenience, we call this signal recorded by the lead glass detector *the electron signal*. At the same time, we record a significant drop in laser power due to scattering losses and call the recorded power *the laser signal*. In addition, we record *the pulser signal* that is generated by reference switches of the motor of the wire scanner. The pulser signal is used as a position reference signal and to define a revolution of θ_4 . During this revolution, each scanner generates eight peaks in the electron signal as well as in the laser signal. The schematic drawing of these recorded signals is shown in figure 5.9.

If we assume that the angular velocity ω of the motor is constant, we can determine it as

$$\omega = \frac{2\pi}{|s_0 - s_1|}, \quad (5.20)$$

where s_0 and s_1 define one pulser signal period and are shown in figure 5.9. Since we do not know the initial value of the angle θ_4 , θ_4^0 , when the motor is off, we define a raw angle θ_4^{raw} at p_i with $i = 1, 2, \dots, 8$ as

$$\theta_4^{\text{raw}}(p_i) = \theta_4(p_i) + \theta_4^0, \quad (5.21)$$

where $\theta_4^{\text{raw}}(p_i) = \omega p_i$ and $\theta_4(p_i)$ the absolute value of θ_4 according to the angle definition of the plane four-bar linkage.

During one revolution of θ_4 , one wire crosses the beam position twice. One is the upward motion, which is denoted as u , and the other is the downward motion, which is denoted as d . In both case, the same wire has the same angle θ_2 and the different angle θ_4 if we assume that a change of the beam transverse position is slow as compared with the scanner motion. As a result, we know the relation between $\theta_4(p_u)$ and $\theta_4(p_d)$

$$\theta_4(p_d) = \theta_4(p_u) + \theta_4^{\text{raw}}(p_d) - \theta_4^{\text{raw}}(p_u), \quad (5.22)$$

where the corresponding wire number of p_u and p_d is listed in table 5.1.

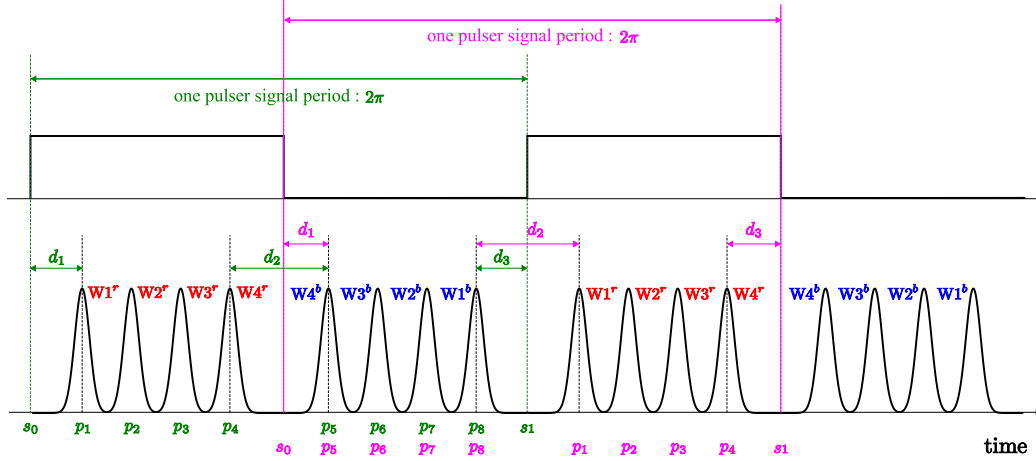


Figure 5.9 A schematic drawing of the record signals. p_i is the peak position. The start of the pulser signal, s_0 , is selected arbitrarily. If $d_1 + d_3 > d_2$, the start position of the wire arm is around the lower turning point. Thus the first peak $W1^r$ corresponds to the wire 1 during its upward movement. The upward movement is shown as the green symbols. And if $d_1 + d_3 < d_2$, the start position is the upper turning point and the first peak $W4^b$ corresponds to the wire 4 during the downward movement. Using these methods, we keep on using $W1^r$ as p_1 and $W4^b$ as p_5 .

wire number	1	2	3	4
p_u	p_1	p_2	p_3	p_4
p_d	p_8	p_7	p_6	p_5

Table 5.1 Relation between the peak number and the wire number. p_u represents the peak number with the upward movement and p_d the peak number does the peak number with the downward movement of the wire scanner. The peak numbers in the same column are generated during upward and downward movement of the same wire. For example, the wire 1 is linked with p_1 and p_8 .

Finally, using the function of θ_2^- (5.5), we have the following relation

$$\theta_2^-(\theta_4(p_u)) = \theta_2^-(\theta_4(p_u) + \delta\theta_4), \quad (5.23)$$

where $\delta\theta_4 = \theta_4^{\text{raw}}(p_d) - \theta_4^{\text{raw}}(p_u)$. Since we calculate $\delta\theta_4$ even if we do not know θ_4^0 , we therefore find θ_4 in (5.23) by using a root-finding algorithm, e.g. the well-known bisection method [119]. And θ_2 follows θ_4 according to θ_2^- defined in (5.5).

Result of beam position determination

Now that we know θ_2 , which corresponds to the peak when a wire crosses a beam, we can calculate three transverse positions of the beam at the positions of scA, scB, and scC from (5.19). Since we record the electron signal and the laser signal during one revolution of a wire scanner and the method applies to both signals, we determine the electron beam position and the laser beam position simultaneously. Figure 5.10 shows one typical result of the wire scanner analysis. For simplicity we use the electron signal to determine the electron beam position that is denoted the small red circle. We can obtain a similar result when we use the laser signal. And we also present eight screen captures of the full motion of the wire scanner for clarity. The direction of the angle θ_4 is a counterclockwise direction according to the angle definition of the plane four-bar linkage. The real motor rotates clockwise. Two rotations make the same peak number pairs, shown in table 5.1. For this reason, we are not concerned with whether the motor rotates clockwise or not.

5.1.3 Determination of the Beam Emittance

In the MAMI accelerator, the wire scanners are installed with 45 degrees inclination. An angle 2δ of the wire scanner is 100° . In that case, when the wire crosses the electron beam, one wire can determine a horizontal beam size and the other one does a vertical beam size because the wire crosses the beam in exactly horizontal or vertical direction. However, we installed the wire scanner to the six-way cross vacuum chamber with 0 degrees inclination and $2\delta = 107^\circ$. In this case, we measure only a correlation between the horizontal and the vertical size of the beam. In the case of round beams with equal horizontal and vertical beam size, one wire scanner should be equipped with three wires oriented at 0° , 90° , and 45° and four wire scanner are necessary to perform beam emittance measurement [111]. Since we have three wire scanners and each wire scanner has only two wires with respect to the orientation angle, we cannot perform the beam emittance measurement correctly by using the wire scanner analysis.

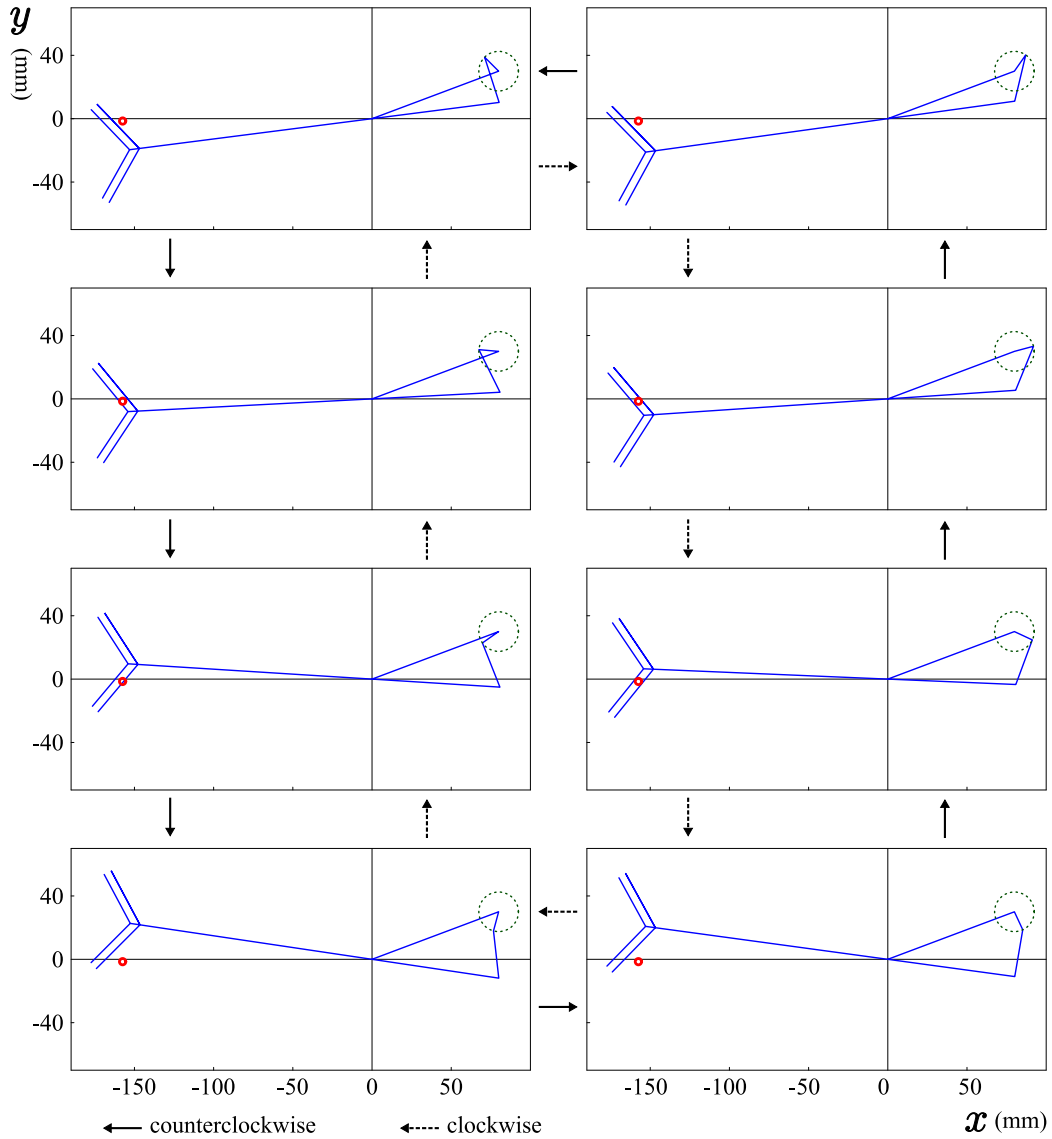


Figure 5.10 Eight screen captures of the full motion of the wire scanner. The small red circle represents the calculated position of the electron beam. We use an arbitrarily chosen number of its size for plotting purposes. The green dotted circle represents the locus of the link \vec{r}_4 and its size is obtained from (5.13). The direction of the electron beam is out of the paper. Conveniently, the pivot point A, which is defined in figure 5.3, is selected as the origin of the plot. The solid arrow represents that the motor rotates counterclockwise and the dashed arrow does the clockwise rotation.

5.2 Realistic Chicane Simulation

In this section, we improve the chicane simulation as close as possible to the real chicane and we call it the realistic chicane simulation. We consider non-ideal properties of the chicane and apply them to the simulation. And we discuss the realistic chicane simulation in more detail.

5.2.1 Non-Ideal Properties of the Chicane

The realistic simulation of the chicane has much the same input parameters as the real chicane has. The real input parameters are currents of the four dipole magnets, percent settings of the shunts, and currents of the two quadrupole magnets. But the chicane simulation needs magnetic fields as its input parameters. Since the four dipole magnets are connected in series, they have the same current. However, the resulting magnetic fields of the dipole magnets may be slightly different from each other due to the intrinsic uncertainty of the magnets. The shunt, which is known as a current controller of the dipole magnet, of the dipole magnet was designed to compensate the intrinsic uncertainty of the magnet and to fine-tune the electron beam trajectory [100]. Thus, it is essential to measure the magnetic field of each dipole magnet as a function of the dipole current and the shunt current as a function of the percent setting of the shunt. And, in effect, the beam centroid is off-axis at the entrance of the chicane. We have to consider the off-axis beam centroid at the entrance of the chicane in the simulation. Furthermore, we study a possible uncertainty that comes from an instability of the current in the dipole magnetic field measurement.

Magnetic field and current measurements

For the dipole magnet, we did not perform magnetic field measurement before we installed the dipole magnet in the beam line. Thus, it is almost impossible to measure magnetic field with high accuracy, because many components of the polarimeter are connected with the magnet directly and indirectly and an available space is limited. We measure the magnetic field strength of each dipole magnet by using F.W.Bell Gaussmeter series 9900 with a probe holder. The holder makes the probe be aligned perpendicular to the magnetic field during the measurement. Although we use the holder in order to get accurate magnetic fields, we do not know how much accuracy the magnetic field measurement has. For the quadrupole magnet, a former MAMI engineer measured the magnetic field of the quadrupole magnet before we installed it in the chicane [116]. And there are only five data points. It is impossible to

measure magnetic field of each quadrupole magnet again except large-scale effort to dissemble and assemble many components of the polarimeter.

For this reason, we have to accept these limited situations, and we use a statistical approach so that we handle these limited data carefully. This statistical approach is used to find the best relation between the real input parameter and the simulation input parameter. Note that we do not consider systematic uncertainties for devices that we use in these measurements.

Field measurement of the dipole magnet From (4.20), we know the magnetic field B_d should be a linear function of the applied current I_d ,

$$B_d = a + b I_d, \quad (5.24)$$

where a and b are regression coefficients. We measure B_d of each dipole magnet by increasing I_d from 0 to 160 A and by decreasing I_d from 160 to 0 A (the subscript d stands for dipole). Figure 5.11 shows B_d as a function of I_d for the first dipole magnet (DIPL20). In the measurement data, we see the hysteresis that the magnetic fields are different for the increasing and decreasing I_d . We multiply the field difference ΔB by 100 so as to distinguish it clearly in the same picture. The average value is 0.03 kGauss roughly. We treat ΔB as uncertainties of the magnetic field that are included in a linear regression.

Since the data points of the magnetic field measurement have no uncertainties, we cannot use the chi-square χ^2 test for goodness of fit. Thus, we must check the linearity of the data points. The linearity describes how well the data follow the linear relation between I_d and B_d . If we have a strong linear relation, then we can say that a and b are reliable to estimate B_d . It can be checked by using the correlation coefficient r_0 and using the probability $Pr(r_0, N)$ with N data points. The correlation coefficient is

$$r_0 = \frac{\sum(I_i - \bar{I})(B_i - \bar{B})}{\sqrt{\sum(I_i - \bar{I})^2 \sum(B_i - \bar{B})^2}} \quad (5.25)$$

where (I_i, B_i) is each data point and \bar{I} and \bar{B} are the mean of I_i and B_i respectively. And $Pr(r_0, N)$ is the probability that N data points can produce a correlation coefficient r with $|r| \geq r_0$ [120, 121] and is expressed by a so-called *incomplete beta function* as

$$Pr(r_0, N) \equiv I_x(l, m) = \frac{\int_0^x u^{l-1}(1-u)^{m-1} du}{\int_0^1 u^{l-1}(1-u)^{m-1} du}, \quad (5.26)$$

where $\nu = N - 2$, $l = \nu/2$, $m = 0.5$, $x = \nu/(\nu - t^2)$, and $t^2 = r_0^2 \nu / (1 - r_0^2)$. The correlation coefficient r_0 and its probability per each magnetic field

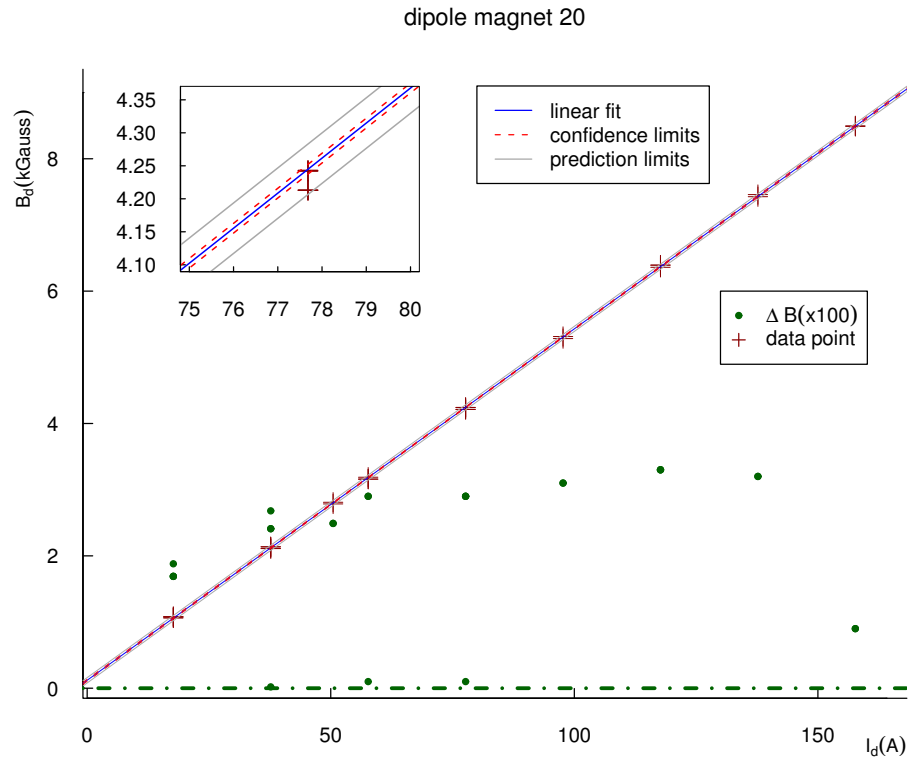


Figure 5.11 Magnetic field measurement for the first dipole magnet (DIPL20). Here, we use the 95% confidence and prediction intervals. ΔB is the field difference due to the hysteresis and is multiplied by 100 for clarity. Since the data points, the linear fit, and the intervals are difficult to distinguish, we draw the zoom plot in the current range of 75 to 80 A. The magnetic field measurements for the other dipole magnets are shown in appendix C.

	DIPL20	DIPL21	DIPL22	DIPL23
data points N	26	17	17	17
degrees of freedom ν	24	15	15	15
correlation				
r_0	0.99997	0.99995	0.99996	0.99997
$Pr(r_0, N)$	< 0.0001	< 0.0001	< 0.0001	< 0.0001
estimator				
\hat{a} (kGauss)	0.1197	0.086	0.135	0.1819
S.E. (\hat{a})	0.0071	0.013	0.011	0.0090
\hat{b} (kGauss/A)	0.053102	0.05343	0.05308	0.05274
S.E. (\hat{b})	0.000082	0.00014	0.00012	0.00010
g.o.f with $\sigma_{B_d} = 1$				
$\tilde{\chi}_0^2$	0.00033	0.00061	0.00046	0.00031
$P(\chi_0^2, \nu)$	1.0	1.0	1.0	1.0
g.o.f				
σ_{B_d} (kGauss)	0.018	0.025	0.022	0.018
$\tilde{\chi}_0^2$	1	1	1	1
$P(\chi_0^2, \nu)$	0.46	0.45	0.45	0.45
t-quantile				
$tQ_{(\frac{\alpha}{2}, \nu)}$	2.06	2.13	2.13	2.13

Table 5.2 Fitting results for the dipole magnet field measurements. **g.o.f** represents goodness of fit and $\tilde{\chi}_0^2$ the reduced chi-square. Since the number of measurements is small, we use Student's t distribution. tQ is the quantile of the Student's t distribution with degrees of freedom ν . Here $\alpha = 0.05$, which means the 95% confidence level, is used to calculate tQ , because the result is considered to be significant only at confidence levels of 95% or better in case of Student's t distribution [124].

measurement are listed in the **correlation** row in table 5.2. From table 5.2, each correlation is highly significant at 0.01% level, because r_0 is close to 1 and Pr is less than 0.0001. Thus, the data points suggest the strong linear relation between I_d and B_d [122, 123, 124].

Therefore, we can find the linear relation (5.24), that is, we can find the best least-squares estimators of a and b , \hat{a} and \hat{b} . We assume that the uncertainties of I_i are negligible and that the magnetic field B_i follows the Gaussian distribution with the standard deviation $\sigma_{B_d^i}$ in the measurement. And, we assume that the standard deviation are all equal, i.e. $\sigma_{B_d^i} = \sigma_{B_d}$. Here, we call the applied current I_i the independent or predictor variable and the measured magnetic field B_i the dependent or response variable. With

these assumptions, the estimators \hat{a} and \hat{b} are

$$\hat{b} = \frac{SS_{xy}}{SS_{xx}}, \quad \hat{a} = \bar{B} - \hat{b}\bar{I}, \quad (5.27)$$

where \bar{I} and \bar{B} are the mean values of I_i and B_i with $i = 1, 2, \dots, N$, and the standard errors in the estimates of \hat{a} and \hat{b} are

$$\text{S.E.}(\hat{a}) = \frac{\sigma_{B_d}}{\sqrt{SS_{xx}}}, \quad \text{S.E.}(\hat{b}) = \sigma_{B_d} \sqrt{\frac{1}{N} + \frac{(\bar{I})^2}{SS_{xx}}}, \quad (5.28)$$

where

$$SS_{xx} \equiv \sum_{i=1}^N (I_i - \bar{I})^2, \quad (5.29)$$

$$SS_{xy} \equiv \sum_{i=1}^N (I_i - \bar{I})(B_i - \bar{B}).$$

In addition, the chi-square probability $P(\chi^2, \nu)$ of obtaining a χ^2 value larger than an input χ_0^2 is given by

$$P(\chi_0^2, \nu) \equiv Q(l, x) = \frac{1}{\Gamma(l)} \int_x^\infty e^{-u} u^{l-1} du, \quad (5.30)$$

where $l = 0.5\nu$ and $x = 0.5\chi_0^2$.

The standard deviation of the magnetic field σ_{B_d} is a prerequisite for calculating the standard errors $\text{S.E.}(\hat{a})$ and $\text{S.E.}(\hat{b})$. However, we do not know σ_{B_d} , because the data points have no uncertainties. As a result, first, we assign σ_{B_d} in each magnetic field measurement to an arbitrary constant so as to calculate $\text{S.E.}(\hat{a})$ and $\text{S.E.}(\hat{b})$. Then, we estimate the best-fit parameter values in \hat{a} and \hat{b} by using (5.28). The estimators and their standard errors are listed in the **estimator** row in table 5.2. In the above calculation, we set $\sigma_{B_d} \equiv 1$. In this case, the chi-square probability, as always, is one, because this procedure is equivalent to the assumption that a fit is good. The corresponding results are listed in the **g.o.f with $\sigma_{B_d} = 1$** row in table 5.2.

Second, the revised standard deviation σ_{B_d} can be calculated by

$$\sigma_{B_d} = \sqrt{\frac{1}{\nu} \sum_{i=1}^N (B_i - \hat{B}_i)^2}, \quad (5.31)$$

where $\nu = N - 2$ and $\hat{B}_i = \hat{a} - \hat{b}I_i$. After calculating σ_{B_d} , one should check the reduced chi-square $\tilde{\chi}^2$ and its probability. We expect that the reduced χ^2

value is equal to one and its probability is approximately 0.5, i.e. so-called *no yes-or-no answer* to test [124]. This is the reason to check the linearity of the data points first. The corresponding σ_{B_d} , $\tilde{\chi}_0^2$, and $P(\chi_0^2, \nu)$ are listed in the **g.o.f** row in table 5.2 and are the same as what we expect. As discussed before, although we cannot test goodness of fit, we calculate them to check whether the results agree with our expectations or not [121, 124, 125].

The $100(1 - \alpha)$ percent confidence interval on a mean response B_0 corresponding to $I_d = I_0$ is [126, 127]

$$\left[\hat{B}_0 - \text{CL}, \hat{B}_0 + \text{CL} \right], \quad (5.32)$$

where

$$\begin{aligned} \hat{B}_0 &= \hat{a} + \hat{b}I_0, \\ \text{CL} &= tQ_{(\frac{\alpha}{2}, \nu)} \cdot \text{S.E.}(\hat{B}_0), \\ \text{S.E.}(\hat{B}_0) &= \sigma_{B_d} \sqrt{\frac{1}{N} + \frac{(I_0 - \bar{I})^2}{SS_{xx}}}. \end{aligned} \quad (5.33)$$

In the above equations, I_0 is any value of the current I_i used in the fitting procedure. And the quantile of the Student's t distribution, tQ , is the upper $\alpha/2$ percentage point of the t_ν distribution ($t_{\alpha/2, \nu}$). The quantile per each measurement is listed in table 5.2. The average width of the confidence intervals for the measurements is 0.03 kGauss approximately. Figure 5.11 shows the upper and lower 95% confidence limits for the dipole magnet 20 field measurement data.

In order to use the regression result of the dipole magnet field measurements in the chicane simulation, it is vital to understand prediction of the new magnetic field \hat{B}_{new} when applying a new current I_{new} . This new applied current is not one of the measured data points but one of future applied currents. The $100(1 - \alpha)$ percent prediction interval on the mean magnetic field strength B_{new} given by the applied current I_{new} is given by [127, 128]

$$\left[\hat{B}_{\text{new}} - \text{PL}, \hat{B}_{\text{new}} + \text{PL} \right], \quad (5.34)$$

where

$$\begin{aligned} \hat{B}_{\text{new}} &= \hat{a} + \hat{b}I_{\text{new}}, \\ \text{PL} &= tQ_{(\frac{\alpha}{2}, \nu)} \cdot \text{S.E.}(\hat{B}_{\text{new}}), \\ \text{S.E.}(\hat{B}_{\text{new}}) &= \sigma_{B_d} \sqrt{1 + \frac{1}{N} + \frac{(I_{\text{new}} - \bar{I})^2}{SS_{xx}}}. \end{aligned} \quad (5.35)$$

	DIPL20	DIPL21	DIPL22	DIPL23
I_{new} (A)	52.8	52.8	52.8	52.8
$\hat{B}_{\text{new}} - \text{PL}$	2.89	2.85	2.89	2.93
\hat{B}_{new} (kGauss)	2.92	2.91	2.94	2.97
$\hat{B}_{\text{new}} + \text{PL}$	2.96	2.96	2.99	3.01

Table 5.3 The estimation of the four dipole magnetic fields with the input current. Here, the 95% prediction intervals (PI) are used. $I_{\text{new}} = 52.8\text{A}$ is the demand current value for a 315 MeV electron beam.

We therefore know the uncertainty range of B_{new} when I_{new} is used to calculate B_{new} . The average width of the 95% prediction intervals is around 0.09 kGauss. Figure 5.11 shows the upper and lower 95% prediction limits for the dipole magnet 20.

Finally, using (5.35), we can calculate the new magnetic field strength per each dipole magnet, which is used to do the chicane simulation. Table 5.3 shows one example for a specific beam energy.

Field measurement of the quadrupole magnet From (4.26), a linear relation between the applied current I_{q} and the quadrupole magnetic field B_{q} is known to be

$$B_{\text{q}} = c + dI_{\text{q}}, \quad (5.36)$$

where c and d are regression coefficients. Figure 5.12 shows the measured B_{q} as a function of I_{q} for the first quadrupole magnet (QUAD21). The fitting procedure of the quadrupole field measurement is the same as in the dipole magnet case. Using (5.32), (5.33), (5.34), and (5.35), we can estimate the confidence and prediction intervals for the quadrupole field measurements. The average width of the 95 percent confidence and prediction intervals are around 0.06 and 0.12 kGauss respectively. The results of the regression are listed in table 5.4. The upper and lower confidence and prediction limits are shown in figure 5.12.

However, this calculation cannot be applied to the chicane simulation, because, in the quadrupole magnet case, the magnetic field is an input parameter and the current an output parameter. The chicane simulation returns the quadrupole magnetic fields that are necessary to minimize the dispersions. And using these magnetic fields we can calculate corresponding currents that are used to apply the real quadrupole magnets. More precisely, we want to estimate a current I_{new} when the field strength B_{new} is given. One possible approach to estimate I_{new} is to do a linear regression in the inverse way as

$$I_{\text{q}} = c' + d' B_{\text{q}}. \quad (5.37)$$

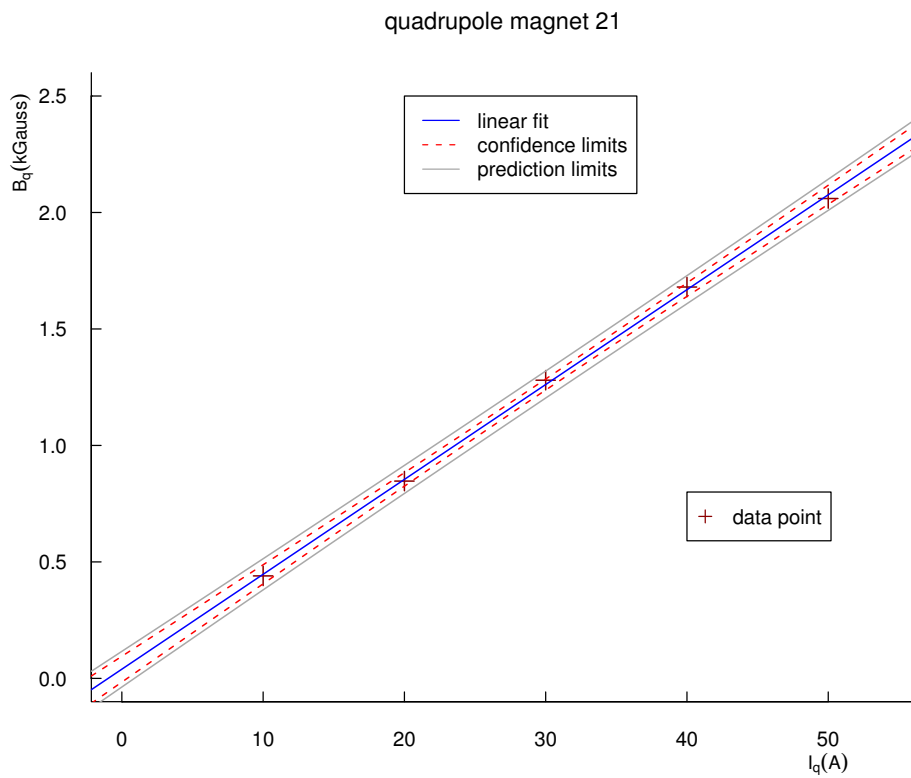


Figure 5.12 Magnetic field measurement for the first quadrupole magnet (QUAD21) [116]. Here, we use the 95% confidence and prediction intervals. The magnetic field measurement for the other quadrupole magnet is shown in appendix C.

	QUAD21	QUAD22
data points N	5	5
degrees of freedom ν	3	3
correlation		
r_0	0.9998	0.9998
$Pr(r_0, N)$	<0.0001	<0.0001
estimator		
\hat{c} (kGauss)	0.040	0.050
S.E. (\hat{c})	0.017	0.015
\hat{d} (kGauss/A)	0.04073	0.04044
S.E. (\hat{d})	0.00053	0.00046
g.o.f with $\sigma_{B_d} = 1$		
$\tilde{\chi}_0^2$	0.00028	0.00021
$P(\chi_0^2, \nu)$	0.99999	1.00000
g.o.f		
σ_{B_q} (kGauss)	0.017	0.015
$\tilde{\chi}_0^2$	1	1
$P(\chi_0^2, \nu)$	0.39	0.39
t-quantile		
$tQ_{(\frac{\alpha}{2}, \nu)}$	3.18	3.18

Table 5.4 Fitting results for the quadrupole magnet field measurements. **g.o.f** represents goodness of fit and $\tilde{\chi}_0^2$ the reduced chi-square. Here $\alpha = 0.05$, which means the 95% confidence level, is used to calculate tQ . Note that $P(\chi_0^2, \nu)$ in the **g.o.f with $\sigma_{B_d} = 1$** row is not one, because ν is too small.

	QUAD21	QUAD22
B_{new} (kGauss)	0.45	0.45
I_{new}^-	8.37	8.38
\hat{I}_{new} (A)	10.05	9.86
I_{new}^+	11.65	11.29

Table 5.5 The estimation of the two quadrupole currents by the magnetic fields. Since we do not know the true current I_{new} , we use \hat{I}_{new} as the demand current. And we use the 95% prediction intervals.

However, this approach is not valid, because I_q is not an observable random variable but is a controlled one in the quadrupole magnet field measurement.

Therefore, we use another approach that is called *calibration* or *inverse regression* [127, 128]. Thus, the $100(1 - \alpha)$ percent prediction interval on I_{new} corresponding to B_{new} is given by

$$[I_{\text{new}}^-, I_{\text{new}}^+], \quad (5.38)$$

where

$$\begin{aligned} I_{\text{new}}^\pm &= \frac{\hat{I}_{\text{new}} - \bar{I}g}{1 - g} \pm F, \\ \hat{I}_{\text{new}} &= \frac{(B_{\text{new}} - \hat{c})}{\hat{d}}, \\ g &= \frac{tQ_{(\alpha/2, \nu)}^2 \sigma_{B_q}^2}{(\hat{d})^2 SS_{xx}}, \\ F &= \frac{tQ_{(\alpha/2, \nu)} \sigma_{B_q}}{\hat{d}(1 - g)} \sqrt{\frac{(\hat{I}_{\text{new}} - \bar{I})^2}{SS_{xx}} + (1 - g) \left(1 + \frac{1}{N}\right)}, \end{aligned} \quad (5.39)$$

with tQ is the quantile of the Student's t distribution and \bar{I} the mean value of I_i . Thus, we calculate the current I_{new} and estimate its uncertainty. Table 5.5 shows one example for a specific electron beam energy.

Current measurement of the shunt The dipole current I_{dipole} per each magnet is

$$I_{\text{dipole}} = I_{\text{MAMI}} - I_{\text{shunt}}, \quad (5.40)$$

where I_{MAMI} is the current provided by the power supply² and I_{shunt} the shunt current. The current range of the shunt is approximately three percent

²DANFYSIK System 8000

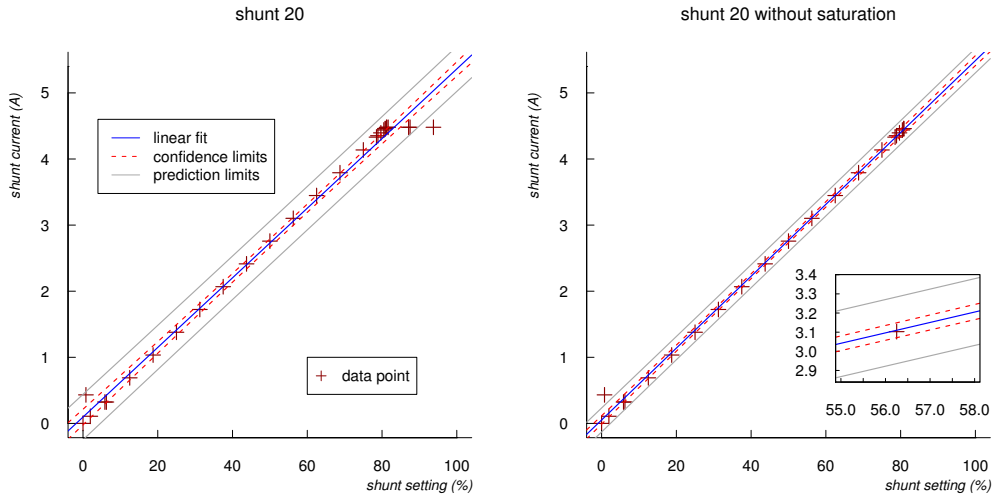


Figure 5.13 Shunt current measurement for the shunt 20 with $I_{\text{MAMI}} = 52.8$ A. We include the saturation points in a linear regression in the left plot and we exclude the saturation points in the right plot. There is one data point appears to disagree with all the others. We suspect that we read the data point by mistake.

of I_{MAMI} . To achieve the maximum possible movement of the electron beam trajectory, 50 percent of the current range of the shunt is recommended as a default setting. Thus, the possible adjusting current range is

$$I_{\text{shunt}} = \pm 0.015 \cdot I_{\text{MAMI}}.$$

The shunt current is set by a digital-to-analog converter (DAC) card. The actual current was measured by a scanning ADC, a common multimeter, and a current sourcemeter³ as a function of the percent setting of the shunt in order to use it in the chicane simulation. The multimeter and sourcemeter measurement are more relevant than the scanning ADC one, because the former are taken on the shunt circuits directly [100]. Figure 5.13 shows the shunt current as a function of the percent setting for the shunt 20. Since the common multimeter and the current sourcemeter yield almost the same values for the current, the sourcemeter measurement is used to plot. The other plots for the shunt measurement are shown in appendix C.

The data show us that the current increases linearly with the shunt setting until reaching its saturation point that is approximately 80 percent of the

³Keithley SourceMeter 2400

DAC range. When we use $I_{\text{MAMI}} = 52.8$ A, the saturation points of the shunt 20, 21, 22, and 23 are 81.2%, 83.1%, 85.9%, and 80.3% respectively. For detailed information about the shunt saturation, consult the reference [100]. When the shunt setting is larger than the saturation point for each dipole magnet, we use the saturation point as the maximum shunt setting. In addition, we apply the same linear regression method as the magnet field measurements to the shunt measurements in order to use them in the chicane simulation. As we ignore the data points that are larger than the saturation point, we have the better regression result. Figure 5.13 shows the result for the shunt 20. For the shunt 21, 22, and 23, the results are shown in figures C.5, C.5, and C.5 in appendix C.

Uncertainties of the measurement We have three measurements that are related with each other directly and indirectly. The magnetic field measurement of the dipole magnet is directly related to the shunt setting measurement in (5.40). And these two measurements are indirectly related to the magnetic field measurement of the quadrupole magnet in the chicane simulation. Furthermore, three measurements are related to the electron beam position in the chicane simulation.

If we consider the uncertainty of the electron beam positions in the interaction region of the polarimeter, these prediction intervals in table 5.3 are not able to guarantee that the uncertainty of the electron beam position remains small.

For example, if true magnetic fields of DIPL20 and DIPL21 are close to 2.89 and 2.85 kGauss respectively, the horizontal position of the electron beam in that region is in the range of +1.4 to -6.2 mm by the ideal chicane simulation. If the magnetic fields are close to 2.89 and 2.96 kGauss, the position is in the range of +4.2 to +17.4 mm. And since the measurement of the quadrupole magnet has only five data points and three degrees of freedom, the predicted value of the quadrupole magnet is more larger uncertainty than the dipole magnet one. In addition, the shunt percent setting is the input parameter in the real chicane and is converted into I_{shunt} as the input parameter in the chicane simulation by using the linear regression (5.34). Moreover, the chicane simulation, TRANSPORT, has its own fitting procedure and returns optimized I_{shunt} in order to move the electron beam close to the laser beam. And we convert I_{shunt} to the shunt percent setting as the input parameter of the real chicane by using the inverse regression (5.38). As a result, in the interaction region of the chicane, when we combine all uncertainties, it is hard to understand a cumulative contribution from these uncertainties to the electron beam trajectory.

We use the statistical approach to overcome the limitations of the magnetic field measurements, to find the best relation between the input parameter of the real chicane and the chicane simulation one, and to estimate the uncertainty of the relation. However, we do not fully understand the cumulative contribution from the uncertainties to the electron beam position. Nevertheless, from the practical point of view, we can ignore the cumulative contribution to the electron beam position, because we measure the electron beam position by the wire scanner at three different positions within the interaction region. It will be discussed in section 5.4.

Off-axis beam centroid

As mentioned before, the beam centroid is the geometric center of the electron beam ellipsoid and has four parameters (x, x', y, y') . Here we consider only the horizontal and vertical phase spaces for simplicity. In the ideal case, the electron beam centroid is considered to be on-axis at the chicane entrance, so that the beam trajectory coincides with the design trajectory and the beam centroid is $(0, 0, 0, 0)$. In reality, however, the beam centroid is off-axis at the chicane entrance, and this initial beam centroid is (x_0, x'_0, y_0, y'_0) . Since, in the center region of the chicane, we obtain three measurements of the electron beam position as explained in section 5.1.2, we can determine the electron beam centroid at the chicane entrance.

Using the matrix formalism, the initial beam centroid is given by

$$\begin{pmatrix} x_0 \\ x'_0 \end{pmatrix} = M_{A0}^{-1} \begin{pmatrix} x_A \\ x'_A \end{pmatrix}, \quad (5.41)$$

where

$$x'_A = \frac{x_B - x_A M_{BA}^{11}}{M_{BA}^{12}}, \quad (5.42)$$

with the electron beam positions x_A and x_B , determined by the wire scanner A and the wire scanner B respectively, M_{A0}^{-1} the inverse matrix of the transfer matrix from the chicane entrance to the scanner A, and M_{BA} the matrix from the scanner A to B. In addition, M_{BA}^{11} and M_{BA}^{12} are the elements of M_{BA} . When we consider the transfer matrix formalism up to third-order so as to increase a simulation accuracy, the transfer matrices are complicated by the fact that the first- and second-transfer matrices are redefined in terms of the first-, second-, and third-order transfer matrices [129]. Since TRANSPORT can calculate the first-, second-, and third-order matrices whether a beam is off-axis or not and has an internal fitting algorithm, we use them so as to calculate the beam centroid at the entrance of the chicane. The displacement

	design value	3 min.	30 min.	8 hr.
$\Delta I/I$ (ppm)	3	< 0.5	< 1	< 2

Table 5.6 Current stability of the power supply unit by the manufacturer. $\Delta I/I$ from the mean output current I of the short term stability, defined as 30 min., is under 1 ppm and $\Delta I/I$ of the long term stability, defined as 8 hr., is less than 2 ppm.

of the beam centroid from the reference trajectory is shown with the first-order transfer matrix in one example output of TRANSPORT in appendix B.

Uncertainty of the dipole magnet field due to a current instability

We study a possible uncertainty that comes from an instability of the current of the dipole magnet, I_{dipole} , in the magnetic field measurement of the dipole magnet. Table 5.6 shows a stability test of the power supply at the maximum current 400 A, which was done by the manufacturer. If we ignore the uncertainty of the shunt current, we can rewrite the dipole current I_{dipole} with the 1σ confidence

$$I_{\text{dipole}} = I \pm \frac{\Delta I}{2\sqrt{2 \ln 2}} = I \pm \delta I. \quad (5.43)$$

We assume that the dipole current I_{dipole} is well-controlled and has more precision than the measured magnetic fields during the field measurements. As a result, we do not consider δI when we find the linear relation (5.24). However, we have to verify this assumption when δI exists.

The total uncertainty σ_{B_d} can be written by

$$(\sigma_{B_d})^2 = (\sigma_B^D)^2 + (\sigma_B^I)^2, \quad (5.44)$$

where σ_B^D is a direct contribution from the purely statistical fluctuations in the magnetic field measurements and σ_B^I an indirect contribution from δI . The first-order indirect contribution is

$$\sigma_B^I = \delta I \cdot \hat{b}, \quad (5.45)$$

where \hat{b} is defined in (5.24). Using (5.45) and (5.44), we calculate the ratio $R_B = \sigma_B^D / \sigma_{B_d}$ that is almost one even if we use $\Delta I/I = 3$ ppm. Furthermore, by using two current $I + \delta I$ and $I - \delta I$, we calculate two magnetic fields per each dipole. We round the magnetic fields to six significant figures and we see no difference between them. Therefore, the assumption, I_{dipole} is well-controlled, is always valid whether δI exists or not [124].

5.2.2 The Realistic Chicane Simulation

We use TRANSPORT in order to do the beam line simulation. The release version of TRANSPORT is Linux binary v1.5a⁴. The realistic chicane simulation has two major steps. Each step needs the input parameters of the real chicane, i.e. the current of the dipole magnet, the percent setting of each shunt, and the current of the quadrupole magnet. Then we convert them to the input parameters of the simulation by using the statistical approach described in section 5.2.1.

- **Step 1** uses the wire scanner analysis, described in section 5.1, to determine the electron beam position and the laser beam position and then reproduces an electron beam trajectory in the simulation. This step has two TRANSPORT runs. The first run calculates a set of ideal Twiss parameters for the given electron beam energy, described in section 4.3.2. And the horizontal and vertical beam emittance are calculated from the MAMI normalized horizontal and vertical emittance, described in section 4.1.3. These Twiss parameters and beam emittances are used in the following run and in the following step. The second run finds out the off-axis beam centroid at the entrance of the chicane, described in 5.2.1. Using the off-axis beam centroid at the entrance of the chicane, finally we can simulate the more realistic electron beam line. We compare the simulated electron beam trajectory to the electron beam position, measured by the wire scanner.
- **Step 2** moves the reproduced electron beam trajectory in **step 1** close to the measured laser beam positions and minimizes the beam centroid at the exit of the chicane. To do this, TRANSPORT calculates the shunt setting by using a fitting procedure in which the laser beam position is defined as a constraint and the shunt setting as fitting parameter. On example input and output of the TRANSPORT is shown in appendix B. In addition, this step find an optimized magnetic field strength of the quadrupole magnet, described in section 4.3.1. We use the inverse regression, described in section 5.2.1, to calculate the corresponding current of the quadrupole magnet. The calculated shunt setting and the calculated current are used as the input parameters of the real chicane.

The realistic chicane simulation plays a vital role in an electron beam control system for the A4 Compton backscattering polarimeter. Results of the realistic chicane simulation, therefore, will be discussed in section 5.4.

⁴FORTRAN 19990614 14:55:00

shunt 20 (%)	shunt 21 (%)	shunt 22 (%)	shunt 23 (%)	top view	description
p_{20}	p_{21}	p_{22}	p_{23}	—	initial settings
$p_{20} + \alpha$	$p_{21} + 2\alpha$	$p_{22} - 2\alpha$	$p_{23} - \alpha$	\odot	clockwise
$p_{20} - \alpha$	$p_{21} - 2\alpha$	$p_{22} + 2\alpha$	$p_{23} + \alpha$	\ominus	counterclockwise
$p_{20} + \alpha$	$p_{21} + \alpha$	$p_{22} + \alpha$	$p_{23} + \alpha$	\uparrow	+ x direction
$p_{20} - \alpha$	$p_{21} - \alpha$	$p_{22} - \alpha$	$p_{23} - \alpha$	\downarrow	- x direction

Table 5.7 Combination of the shunt percent settings for a decoupled transformations of the electron beam so as to achieve good overlap and to eliminate the dispersions. p_{20} is the initial setting of the shunt 20 and α is an additional percent amount of the shunt setting. The axis of the rotation is the geometric center of the chicane and is denoted as \mathbf{o} in figure 4.2.

5.3 Spatial Beam Overlap at the Early Stage

Using the wire scanner analysis, described in section 5.1, we can determine the electron beam position and the laser beam position simultaneously. With this, we calculate the distance between the electron beam position and the laser beam position. And we calculate the crossing point⁵ and the crossing angle α_c . Using the distance, the crossing point, and the crossing angle, we can estimate the quality of the beam overlap.

There are two criteria for the good quality of the beam overlap. One is the smallest crossing angle α_c and the other is the crossing point within the interaction region. In reality, it is a complex and time-consuming process to achieve the crossing point within the interaction region (IR). Thus, the position close to the interaction region is also acceptable. For convenience, we quantify the interaction region with respect to the geometrical center \mathbf{o} , shown in figure 4.2, of the chicane. We define the interaction region as $d_{\text{IR}} = \sum_{i=2}^6 d_i$ by using the drift space, listed in table 4.2. Thus the interaction region is from -0.89 m to 0.89 m. If we have a poor quality of the beam overlap, we move the electron beam close to the laser beam by changing the each percent setting of the shunt. We choose the shunt settings to make a good overlap and to minimize the dispersions. Table 5.7 shows results of a calculation how to perform specific decoupled transformations of the electron beam. The calculation is based on the ideal chicane simulation, described in section 4.3.3. According to table 5.7, a MAMI engineer designed a knob in order to move the electron beam close to the laser beam.

⁵For simplicity, we consider only z coordinate to describe the crossing point.

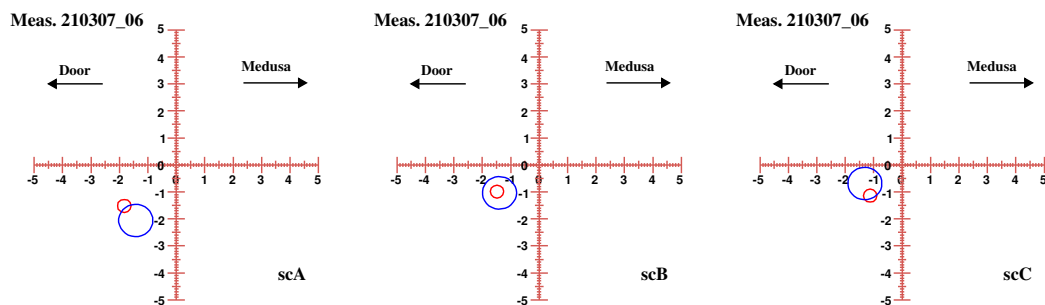


Figure 5.14 Spatial beam overlap. The red circle represents the electron beam and the blue one the laser beam. The origin was set to the ideal beam trajectory as defined by the theodolite measurements, described in section 4.4. On the plot, **Medusa** is the direction of the MEDUSA electronics and **Door** the direction of the door of the ExHall 3. Thus, the direction of the electron beam is out of the paper. **scA**, **scB**, and **scC** represent the scanner A, B, and C respectively. **Meas.210307_06** represents that the measurement was performed in March 21, 2007 and **_6** is the sixth measurement in the same day. Here we use that the diameter of the electron beam is about 0.5 mm. The electron beam diameter is estimated from the ideal chicane simulation in figure 4.8 in section 4.3.3. And we use that the diameter of the laser beam is 1.3 mm. The laser beam diameter is estimated from the configuration of the laser resonator [99]. The unit of the horizontal and vertical axis is millimeter.

At the early stage, we used the combination of the percent settings, shown in table 5.7, in order to move the electron beam close to the laser beam. Figure 5.14 shows a plot of the spatial beam overlap that was performed on March 21, 2007 by using the combination of the shunt settings. And we achieved that the crossing point is 0.1 m, the crossing angle $\alpha_c = 0.87$ mrad, and $\mathcal{C} = (1 + \cos \alpha_c) / \sin \alpha_c = 2290$, described in section 3.2.2. However, as we mentioned earlier, this is a complex and time-consuming process. For this reason, an automation of the beam overlap procedure is indispensable for the A4 Compton backscattering scattering and it will be discussed in the next section.

5.4 End Result of the Chicane Development

In this section, we present the end result of the chicane development for the A4 Compton backscattering polarimeter described in the previous sections. In the first half of this section, we explain the electron beam control system that makes an overlap between the electron beam and the laser beam and

that is easy to use, quick, and reliable. In the second of this section, we present the performance and limitations of the electron beam control system.

5.4.1 Beam Alignment Program

We design a beam alignment program in order to make the electron beam control system and call the program *xChicane*. As TRANSPORT has no graphical user interfaces, we use the ROOT system [120] to make graphical user interfaces between end users and TRANSPORT. And the beam alignment program incorporates an algorithm for the beam position determination from the wire scanner analysis, which is described in section 5.1, the realistic chicane simulation with TRANSPORT, which is described in section 5.2, and a data transfer of the chicane settings between the A4 experiment and the MAMI operator. The chicane settings contain the MAMI current I_{MAMI} , the quadrupole magnet currents, the shunt percent settings, and the *wedler*⁶ currents. Thus, the beam alignment program can partly automate the spatial beam overlap procedure between the electron beam and the laser beam. Figure 5.15 shows a flow chart of the partial automation. The MAMI operator uses the initial chicane settings to optimize the chicane. The initial settings are denoted as **(1)** in figure 5.15. Then we determine the electron beam position and the laser beam position simultaneously and check the quality of the beam overlap. If the overlap quality is not good, we ask the MAMI operator to send the initial chicane settings **(1)** to us. Using the settings **(1)**, we simulate the electron beam trajectory that is close to the electron beam positions by the wire scanner analysis. And we find the suggested chicane settings that are denoted as **(2)** in figure 5.15 so that we move the simulated electron trajectory close to the laser beam positions, measured by the wire scanner analysis, in the realistic chicane simulation. We transfer the suggested settings **(2)** to the MAMI operator such that the operator uses the suggested settings to optimize the chicane again. The modification of the suggested chicane settings for shunt 22 and shunt 23 are necessary. We will discuss it in section 5.4.2. The modified chicane settings are shown as **(3)** in figure 5.15. After that, we determine the electron beam position and the laser beam position again, check the quality of the beam overlap, and compare the measured electron positions to the simulated electron beam trajectory. If the overlap quality is good and is acceptable, we finish the beam overlap procedure. Figure 5.16 shows the screen capture of the beam alignment program.

⁶A steering magnet is called a wedler at MAMI.

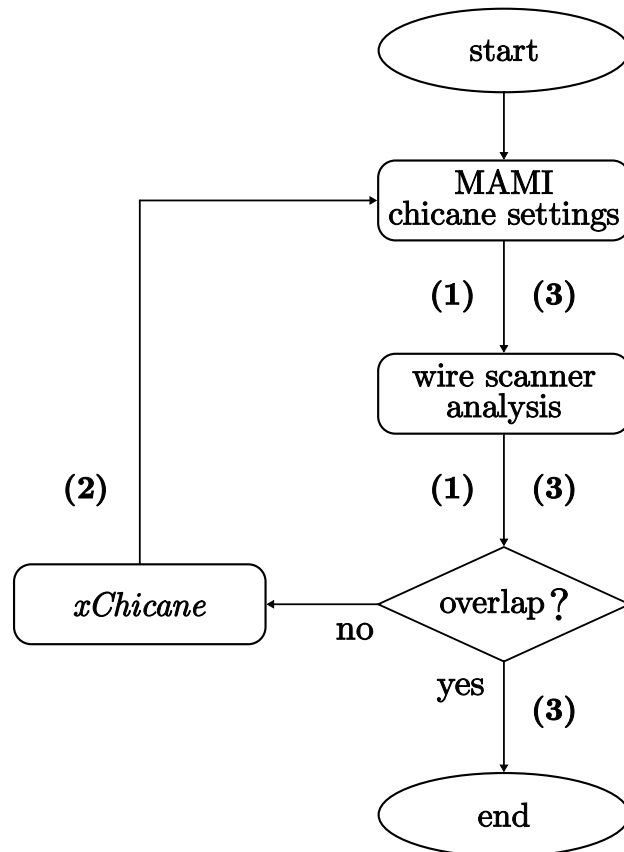


Figure 5.15 Automation of the beam overlap procedure. The chicane settings in the partial sequence are also shown: **(1)**, the initial chicane settings (the input parameters of the real chicane); **(2)**, the suggested chicane settings (the output parameters of the realistic chicane simulation); and **(3)**, the modified chicane settings (the new input parameters of the real chicane).

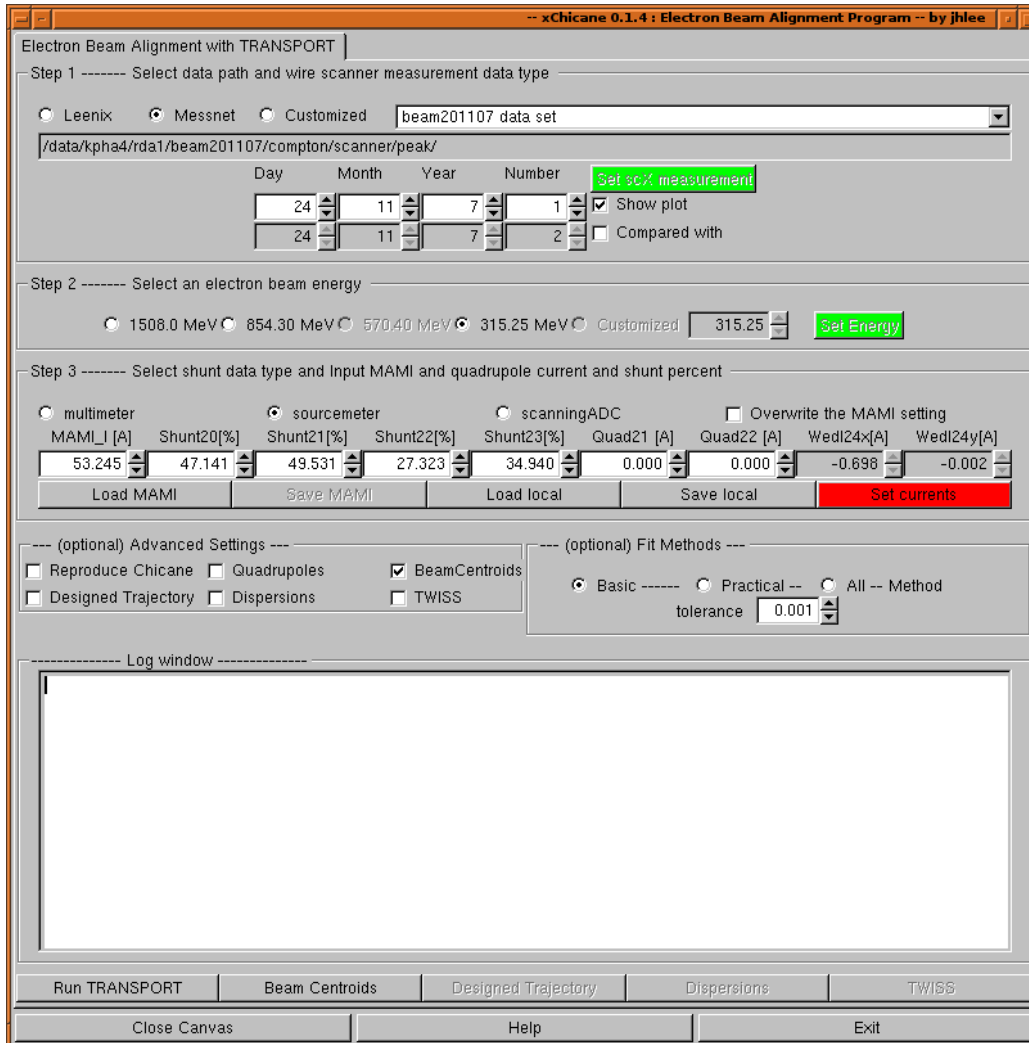


Figure 5.16 Electron beam alignment program - xChicane.

chicane settings		(1)	(2)	(3)
MAMI current I_{MAMI}	(A)	53.245	53.245	53.245
shunt 20	(%)	47.141	40.132	40.132
shunt 21	(%)	49.531	45.126	45.126
shunt 22	(%)	27.323	17.911	17.671
shunt 23	(%)	34.940	26.848	27.478
quadrupole 21 current	(A)	0.000	0.000	0.000
quadrupole 22 current	(A)	0.000	0.000	0.000
wedler 24x	(A)	-0.698	-0.698	-0.817
wedler 24y	(A)	-0.002	-0.002	-0.005

Table 5.8 Chicane settings of figure 5.17. **(1)**, **(2)**, and **(3)** are described in figure 5.15. We see the small modification, which is the boldface number, of the chicane settings for shunt 22 and shunt 23 between **(2)** and **(3)**. In addition, the different values of wedler 24x and wedler 24y between **(2)** and **(3)** are due to the MAMI beam stabilization system.

5.4.2 Performance and Limitations

Performance

The upper plot in figure 5.17 shows the electron beam position and the laser beam position with the initial chicane settings **(1)**, defined in figure 5.15. The initial chicane settings are listed in **(1)** column in table 5.8. And the lower plot in figure 5.17 shows a measurement of the beam positions after the beam overlap procedure. This measurement is performed with the modified chicane settings **(3)**, defined in figure 5.15. The modified chicane settings are listed in **(3)** column in table 5.8.

If we compare the upper plot with the lower plot in figure 5.17, we clearly see that the good quality of the beam overlap is achieved with only one loop of the beam overlap procedure, described in figure 5.15. The crossing point is changed from -4.3 m to -1.1 m and the crossing angle from 0.64 mrad ($\mathcal{C} = 3132$) to 0.30 mrad ($\mathcal{C} = 6564$). Since the crossing point -4.3 m is the outside A4 Compton backscattering polarimeter, the corresponding crossing angle, $\alpha_c = 0.64$, has no physical meaning. Note that the crossing point -1.1 m is acceptable, because the position is approximately the entrance of the quadrupole magnet 21 (QUAD21). In addition, this outstanding overlap was achieved within only two wire scanner measurements. This result guarantees that we can control the electron beam to make a beam overlap as fast and simple as possible.

Figure 5.18 shows simulated electron beam trajectories in the horizontal plane. On the upper plot, there is the simulated electron trajectory with the

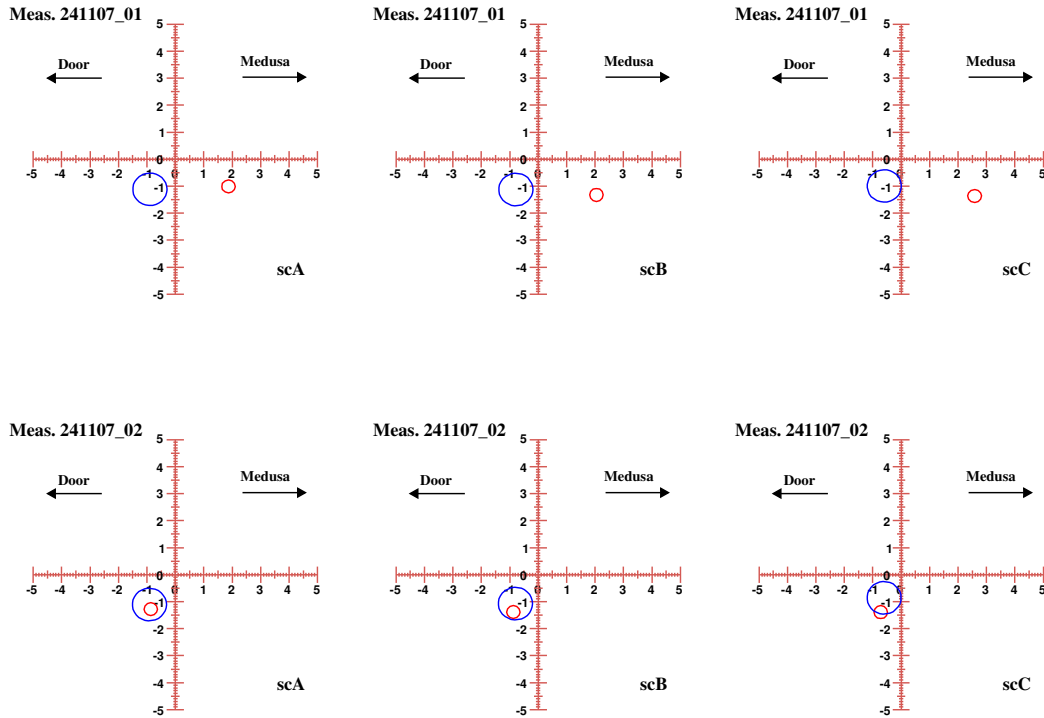


Figure 5.17 The position measurement of the two beams with the initial chicane settings **(1)** and with the modified chicane settings **(3)**. The upper plot represents the beam position measurement with **(1)**. This is a typical situation for the electron beam position and the laser beam position, when the MAMI operator turns on the electron beam. This is the first measurement on November 24. The lower plot represents the position measurement of the two beams with **(3)**. This is the second measurement on November 24. The solid blue circle is the laser beam position and the solid red one the electron beam position. The notation on the plot is the same as figure 5.14.

initial chicane settings **(1)**. The electron trajectory with **(1)** matches three electron beam positions, determined by the wire scanner. Furthermore, on the lower plot, the simulated electron trajectory with the modified chicane settings **(3)** and the measured electron positions match.

Since the simulated electron beam trajectory by the realistic chicane simulation describes the electron trajectory in the real chicane well, we can ignore the cumulative uncertainties, described in section 5.2.1, of the simulated electron trajectory from the magnetic field and shunt current measurements.

Limitations

Now that we develop the electron beam control system, we can determine the relative positions of the electron and the laser beam, we can simulate the electron beam trajectory with the initial chicane settings, we can move the simulated trajectory close to the laser beam position by the realistic chicane simulation in the computer program, and we can move the electron beam trajectory in order to make the beam overlap in the real chicane by using the suggested chicane settings.

However, we have the limitations of the beam control system. First, we find that the quadrupole magnet current, one of the results of the chicane simulation, is inappropriate to the real chicane. When we apply the quadrupole current to set into the MAMI chicane settings, we always met the problem that the electron trajectory at the chicane exit is unmanageable by the MAMI operator and there is a warning for a high radiation level in the experimental hall because the beam scrapes on the beam pipes. This problem reminds us of the assumptions: the dipole magnet has the zero normalized field index ($n = 0$); and the magnet is a square-edged nonsaturating magnet, which are discussed in section 4.2.2. These assumptions might be invalid to describe the real dipole magnets. Thus, one of the simulation purposes, minimizing the dispersions, cannot be achieved by the chicane simulation.

Second, it is necessary to modify the suggested chicane settings **(2)**. Figure 5.19 shows the beam transport line between the chicane exit and the target has two positions monitors, so-called XYMO24 and XYMO27. Since the beam overlap exists between two quadrupole magnets, DIPL22 and DIPL23 have no contribution to the electron beam trajectory within this region. Thus, the MAMI operator uses DIPL20 and DIPL21 to move the electron beam close to the laser beam, can control the electron beam to center it on XYMO24 by using the shunt 22 and shunt 23, and center it on XYMO27 by using WEDL24. As a result, the suggested chicane settings of shunt 22 and shunt 23 are slightly changed and these modifications are listed in table 5.8.

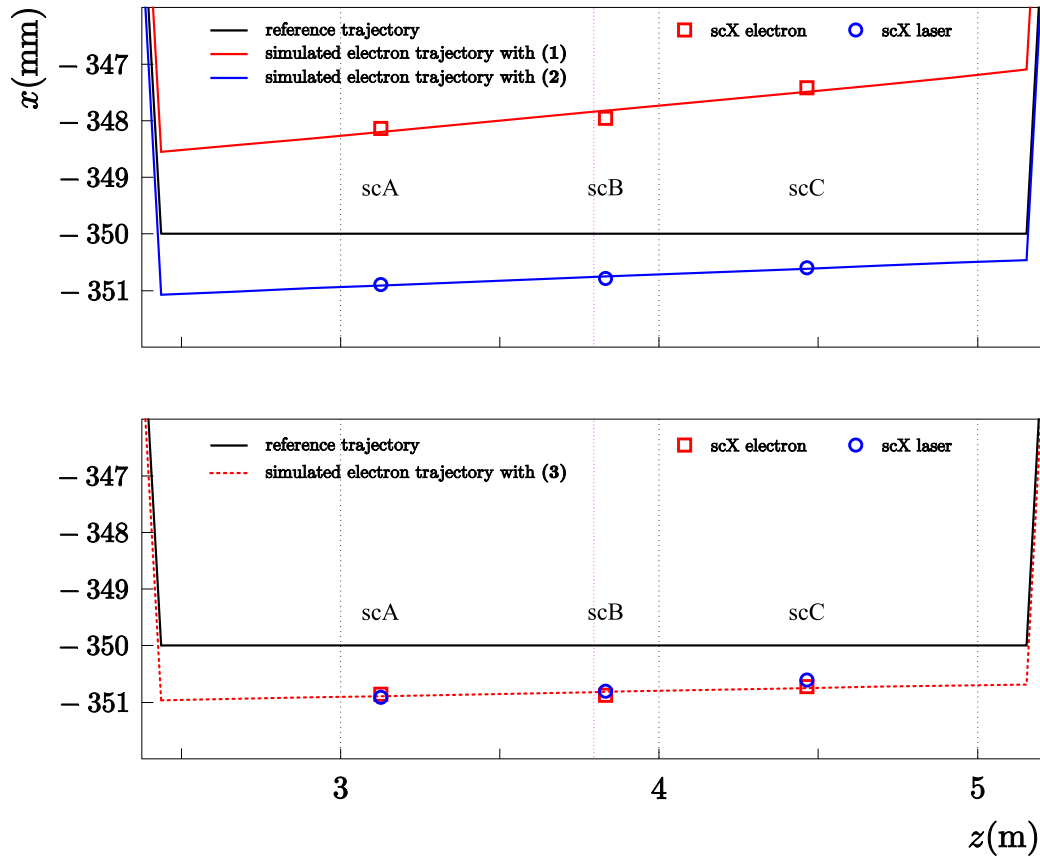


Figure 5.18 Simulated electron beam trajectories calculated by *xChicane* in the horizontal plane. On the plot **scX** represents the position determination by the wire scanner. The purple line is the geometric center of the chicane, denoted as **o** in figure 4.2. The red solid line is the simulated electron beam trajectory with the initial chicane setting **(1)**, shown in figure 5.15 and in table 5.8. The red dotted line represents the simulated electron trajectory with the modified chicane settings **(3)**. The black solid line is the reference trajectory of the chicane. The blue solid line shows the simulated electron trajectory with the suggested chicane settings **(2)**. The simulated electron trajectories match the beam positions, determined by the wire scanner.

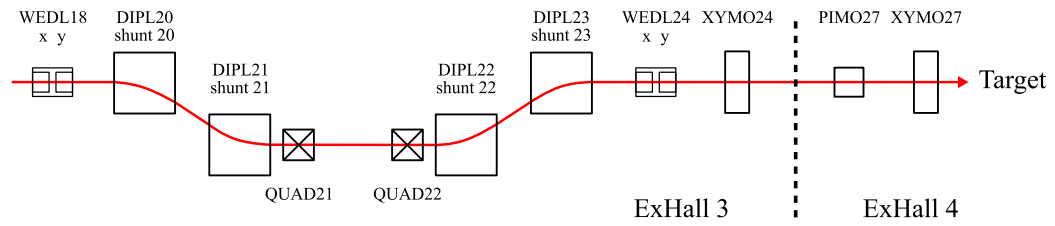


Figure 5.19 The beam transport line with the chicane and the beam monitors. **WEDL** represents a wedler, which is a steering magnet.

Thus, the MAMI operator can practically control and minimize additional effects, which are not controlled by the chicane simulation.

Third, we cannot optimize the vertical position of the electron beam, because the percent setting of the shunt affects only the horizontal position of the electron beam and the current of the quadrupole magnet is unsuitable to move the vertical position.

However, even if the developed beam control system, which is the partial automation, has these limitations, it provides us the most cost-effective way of avoiding a *manual* overlap procedure that is complex and time-consuming and of achieving a reliable beam overlap quickly. And, end users can use the beam control system easily enough during a typical beam time.

Chapter 6

Scintillating Fiber Detector Development

In the Compton backscattering process, the electron loses its energy and the backscattered photon gains the energy. Thus, the scattered electron is more deviated than the reference electron in the magnetic field of the last two dipole magnets. And it passes through a scintillating fiber that is the distance from the reference trajectory. Therefore, the position, where the scattered electron passes through, on the scintillating fiber system provides information on the energy of the scattered electron. And the position is also related with the energy of the backscattered photon because of the energy transfer in the backscattering process.

The purpose of the scintillating fiber detector, as mentioned in chapter 3, is to reduce background in photon spectra by requiring coincidence between the scintillating fiber detector and the photon detector. A prototype fiber detector had been installed and been tested. The signal-to-noise ratio of the photon detector spectra was slightly improved [97]. Our experiences of the prototype detector help us to design an improved detector that is based on the same mechanical concept as the prototype. The scintillating fiber detector has three main components: (1) plastic scintillating fibers that are sensitive to charged particles; (2) a photomultiplier tube that collects optical photons and generates electrical signals for further signal processing; and (3) a movable support frame that allows to adjust the detector position and supports other mechanical parts attached. Minimum design changes of the electron detector are preferable, since we want to take electronics and mechanical parts to be reused.

In this chapter, we present a short introduction about plastic scintillating fibers, discuss the new design concept and several requirements of the detector, and describe the construction of the new detector briefly. Finally, we will

discuss measurements by using the new fiber detector.

6.1 Plastic Scintillating Fiber

Scintillating fibers are widely used for charged particle tracking devices in sundry applications [130, 131]. The scintillating fibers, which we use in the A4 Compton backscattering polarimeter, are a typical organic plastic scintillator. A plastic scintillating fiber is composed of a core and cladding. The core consists of plastic material, such as polystyrene (PS) with dopants that is known as scintillation material. When ionizing particles pass through the core, optical photons are generated inside the material. The core, also called the active area, is coated with thin materials, such as polymethylmethacrylate (PMMA) for single cladding and PMMA and fluorinated polymer (FP) for multi-cladding. The refractive index of the cladding is smaller than the core one. As a result, light can be trapped inside the core in contrast to no cladding due to total internal reflection.

6.1.1 Scintillation Light

To estimate the number of optical photons that can reach the photomultiplier tube, let us define the following two steps: generation and collection of optical photons. At the first stage, generation, charged particles generate optical photons by a scintillating process in the core. These optical photons are distributed in the emission spectrum of a scintillating fiber. If we assume no wavelength dependence, the average number $\langle N_{\text{photon}} \rangle$ can describe the number of optical photons well. In the second stage, collection, optical photons are emitted isotropically in the core, and a fraction of photons can be transferred to the photomultiplier. With the same assumption, the second stage may be parametrized by light collection and transfer efficiency $\langle \text{LCTE} \rangle$ that depends on the construction and optical properties of the fiber. In sum, the number of detected optical photons, N_{optical} , is [130]

$$N_{\text{optical}} = \langle N_{\text{photon}} \rangle \cdot \langle \text{LCTE} \rangle. \quad (6.1)$$

Optical photons

The average photon number is defined as

$$\langle N_{\text{photon}} \rangle = \left\langle \frac{dE}{dx} \right\rangle \cdot \langle \Delta x \rangle \cdot LY, \quad (6.2)$$

where $\langle \Delta x \rangle$ is an average path length, LY the light yield of the scintillating fiber, and $\langle dE/dx \rangle$ an average energy loss per unit path length.

When an electron passes through a fiber at normal incidence, the average path length is

$$\langle \Delta x \rangle = \frac{\pi}{4} \cdot d_{\text{core}}, \quad (6.3)$$

where d_{core} is the diameter of a core, because only this core contributes to the scintillation process.

The average deposited energy is

$$\left\langle \frac{dE}{dx} \right\rangle = \frac{dE}{d(\rho x)} \cdot \rho_{\text{core}}, \quad (6.4)$$

where $dE/d(\rho x)$ is the collision stopping power of scintillation material and ρ_{core} the density of a core.

The light yield LY is defined as the number of optical photons n produced per deposited energy ΔE :

$$LY = \frac{n}{\Delta E}. \quad (6.5)$$

Light collection and transfer efficiency

The light collection and transfer efficiency $\langle \text{LCTE} \rangle$ is written as

$$\langle \text{LCTE} \rangle = \frac{\delta\Omega}{4\pi} [A(x) + R \cdot A_R(x)] \cdot T, \quad (6.6)$$

where the trapping efficiency $\delta\Omega/4\pi$ represents the fraction of scintillation light that is trapped in the fiber, $A(x)$ the attenuation of the scintillation light that is emitted toward the photomultiplier, $A_R(x)$ the attenuation of the scintillation light that is emitted away from the photomultiplier, R the reflection coefficient for the light away from the photomultiplier, T the transmission coefficient between the fiber and the photomultiplier, and x the emitting position of the scintillation light inside the fiber. $A(x)$ and $A_R(x)$ can be expressed as

$$\begin{aligned} A(x) &= \exp(-x/L_a), \\ A_R(x) &= \exp(-2(2L_s - x)/L_a), \end{aligned}$$

where L_a is the fiber attenuation length and L_s the fiber length.

Parameter	Description	
Core	Material	Polystyrene (PS)
	Refractive index n_c	1.59
	Density	1.05 g/cm ³
	Thickness	94% of fiber diameter
Inner Cladding	Material	Polymethylmethacrylate (PMMA)
	Refractive index n_i	1.49
	Density	1.19 g/cm ³
	Thickness	3% of fiber diameter
Outer Cladding	Material	Fluorinated polymer (FP)
	Refractive index n_o	1.42
	Density	1.43 g/cm ³
	Thickness	3% of fiber diameter
Emission	Peak	450 nm
	Color	blue
Decay Time		2.8 ns
Attenuation length	L_a	>4.0 m
Numerical Aperture	NA	0.72
Trapping Efficiency	$\delta\Omega/4\pi$	0.054
Diameter		0.83 mm

Table 6.1 Kuraray SCSF-78M fiber properties [133]

6.1.2 Kuraray SCSF-78M Fiber

We use Kuraray SCSF-78M scintillating fibers with the diameter 0.83 mm so as to construct the new scintillating fiber detector for the scattered electron detection. Table 6.1 shows the detailed characteristics of a Kuraray SCSF-78M fiber. Using these properties of the scintillating fiber, we estimate $N_{optical}$ at the 854.3 MeV electron beam. The average collision stopping power $dE/d(\rho x)$ in the Compton electron energy range is 2.31 MeV cm²/g [132], the light yield LY is 1/120 photon/eV [130], and the average path length is 0.61 mm. Thus $\langle N_{photon} \rangle = 1238$ photon. The fiber length L_s is approximately 147 mm, the emitting position x is 135.5 mm, and the transmission coefficient T among the polystyrene, the air, and the window material of the photomultiplier tube is 0.91. Thus, when $R = 0$ is assumed, the light collection and transfer efficiency $\langle \text{LCTE} \rangle$ is 0.047. On the other hand, using $R = 1$, $\langle \text{LCTE} \rangle = 0.093$. As a result, the number of optical photons that can touch the photocathode of the photomultiplier tube is in the range of 59 to 115.

6.2 Construction of the Fiber Detector

6.2.1 Scintillating Fiber Array

Since the measured position of the scattered electron characterizes the electron momentum, a well-aligned fiber array is a crucial component for the electron fiber detector. Furthermore, large numbers of optical photons are essential for detection efficiency. Thus, following restrictive requirements must be considered to design a new fiber array.

1. The external size of a new fiber array must be compatible with prototype detector components that we want to reuse.
2. The number of fibers that is used to make one *fiber layer* should be the same as the prototype one, since we want to reuse electronics parts of the prototype. We call a group of fibers a *fiber layer* for convenience. Each fiber, which exists in the same layer, has the same z coordinate in the beam coordinate. See figure 6.1.
3. The path length in the detector is larger than the prototype one. Since the fiber diameter is smaller than the prototype one, we have to increase a number of fiber layers, compared with the prototype.
4. The variation of the path length over the detector *width* should be minimized. See figure 6.1.
5. The overlapping between neighboring fibers should be smaller than the prototype so as to achieve better electron momentum resolution.

Figure 6.1 and table 6.2 shows possible layouts for the fiber array because of the requirement **1**. According to table 6.2, we select the layout with the symbol \star is selected to construct the new fiber array. The (1) layout seems to be a good candidate. But, its path length is originated from the overlapping between neighboring fibers. This does not fulfill the requirement **5**.

We used 12 fibers for a layer, and 4 layers to construct the fiber array. Since the two critical parameters (d_x and ϕ) are the same as the fiber detector of the A1/KAOS collaboration [134], we reused their assembly tools that are a position matrix and position jigs with V-shaped grooves. The cross section of the position matrix and fibers are shown in figure 6.3.

The V-shaped grooves of the position matrix and the position jigs prevent fibers from misalignment during painting procedure. The fibers are stuck together by Bicon BC-620 reflector paint. The advantages of this paint are

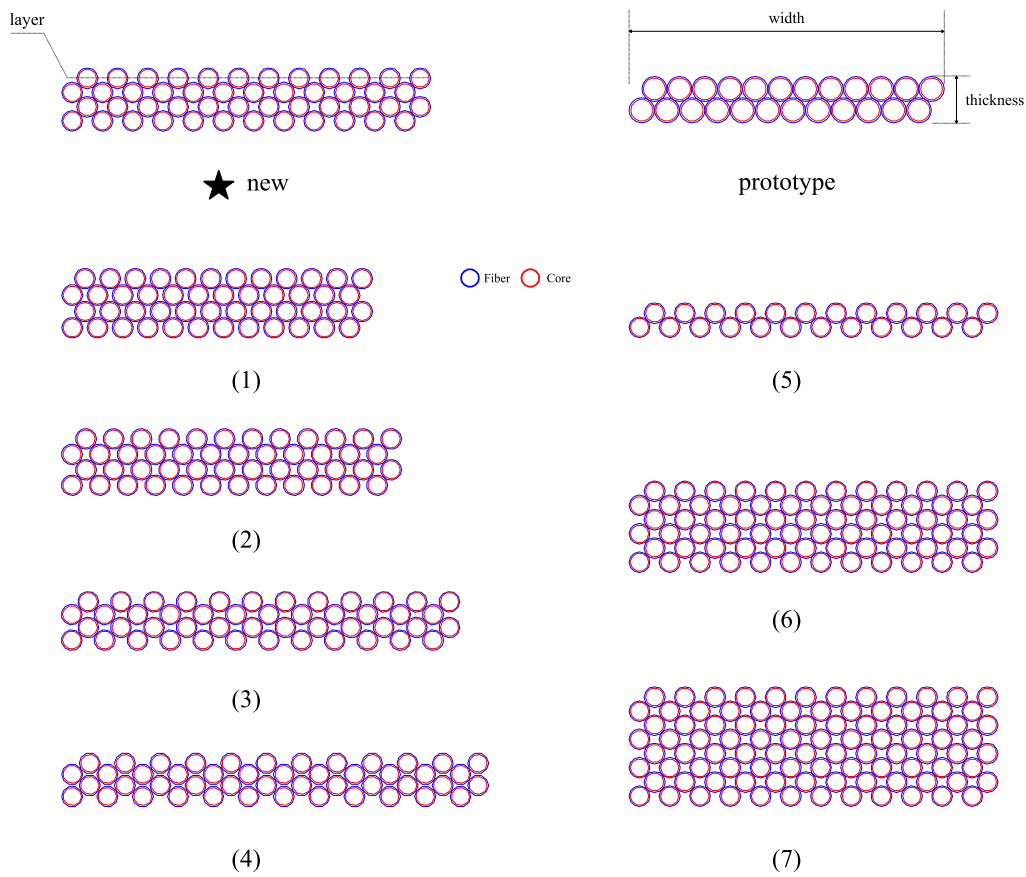


Figure 6.1 Possible layouts for the fiber array

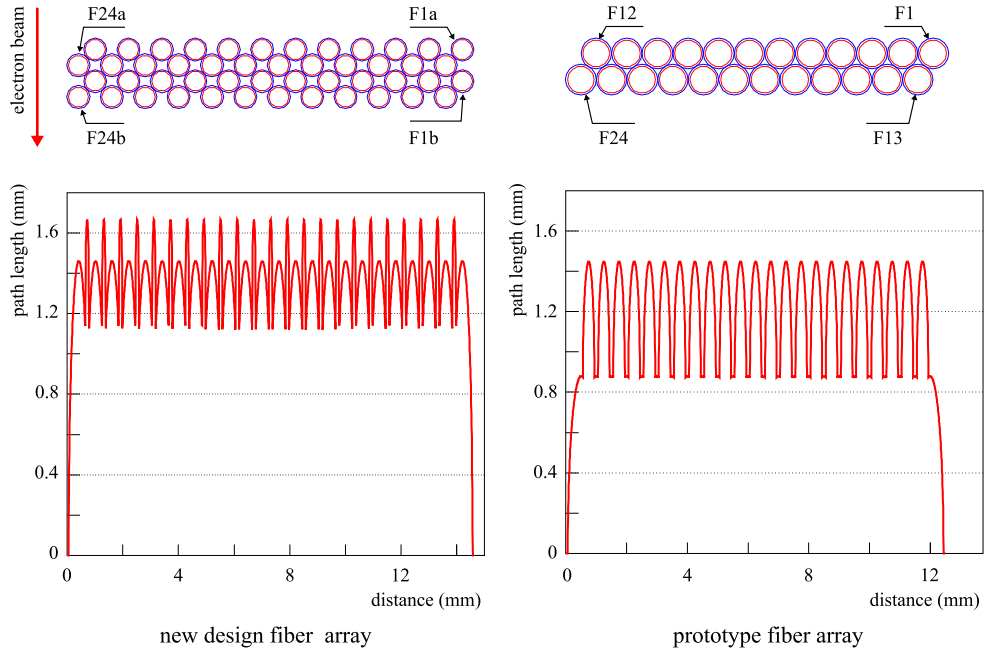


Figure 6.2 Detector path length and schematic layout of the new and prototype fiber array. The solid red arrow represents the direction of the electron beam. In order to stay consistent with the numbering scheme of the prototype detector, we call two fibers, which have the same transverse beam coordinate, which is defined in figure 4.1, $F_{i\mathbf{a}}$ and $F_{i\mathbf{b}}$ with $i = 1, 2, \dots, 24$.

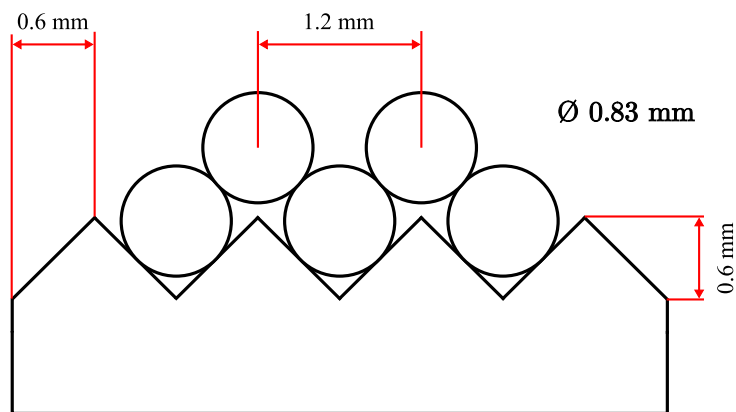


Figure 6.3 Position matrix and fibers cross section

	ϕ	n_{lay}	d_x	$\langle \Delta x \rangle$	$\langle \Delta x \rangle_\sigma$	x	z
prototype	1.00	2	1.0	1.17	0.28	12.50	1.87
★	0.83	4	1.2	1.37	0.20	14.63	2.55
(1)	0.83	4	1.0	1.63	0.35	12.33	2.82
(2)	0.83	4	1.1	1.49	0.26	13.48	2.69
(3)	0.83	4	1.3	1.28	0.19	15.78	2.38
(4)	0.83	4	1.4	1.19	0.27	16.93	2.17
(5)	0.83	2	1.2	0.69	0.10	14.63	1.40
(6)	0.83	6	1.2	2.06	0.29	14.63	3.70
(7)	0.83	8	1.2	2.75	0.39	14.63	4.85

Table 6.2 Eight possible layouts for the scintillating fiber array. Here ϕ is the fiber diameter, n_{lay} the number of layers, d_x the distance between two neighboring fibers in the same layer, $\langle \Delta x \rangle$ the detector path length, $\langle \Delta x \rangle_\sigma$ the standard deviation of the path length, and x and z the external sizes of the fiber array. For convenience, we call x the detector width and z the detector thickness. The unit is millimeter.

good adhesion, excellent resistance to yellowing with age, and ease of application by brushing [135]. And, the paint may minimize the cross-talk between fibers, because its reflectivity is larger than 90 percent in the emission range of the Kuraray SCSF-78M fiber.

Assembly

We sanded the end surfaces of the fibers down lightly before fiber array assembly to prevent accidental damage to the fiber array from polishing. Figure 6.4 shows the 24 fiber pairs \mathbf{F}_i that are main parts of the electron detector and 6 dummy fibers that support the fiber array during the assembly. Twelve fibers and three dummy fibers were carefully put in the particular positions of **layer 1** on the position matrix, and were painted by soft brushes. Before hardening of the paint of the layer 1, we put twelve fibers and two dummy fibers in the position of **layer 2**. Furthermore, we corrected misalignment of fibers by the position jigs, put the jigs on the layer 2, and left them with the two layers for 20 min. roughly. After that, we removed the jigs, and painted fibers thoroughly. In the same manner, we made the other layers. After positioning fibers in **layer 4**, we corrected misalignment by the jigs. Then, we weighted the fiber array down with aluminum rods during 24 hours so as to keep all fibers of the fiber array in place. The fiber array then was separated from the position matrix, and the six dummy fibers were detached from the array carefully. Finally, the fiber array was painted again completely.

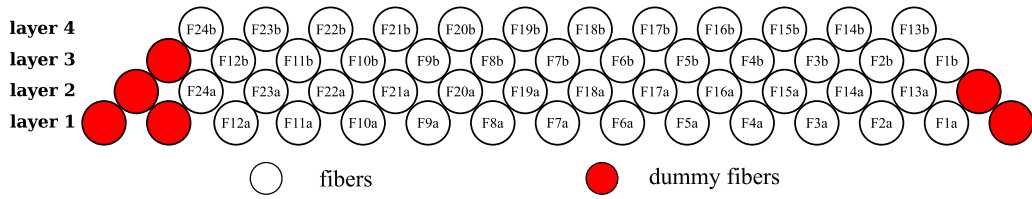


Figure 6.4 Fiber array ordering and dummy fibers. Note that the order of the fibers is different to one of figure 6.2 due to the construction procedure.

We used the *inside fiber bundle holder* shown in figure E.1 and E.2 in appendix E in order to polish the end surface of the fibers. And we used the different grit sizes that are P400, P600, P800, and P1000. After applying sandpapers with distilled water, we polished them again with a special abrasive¹ and a soft cloth. Figure 6.5 shows the fiber array with the holders after the polish.

Wire mount

Ideally, at the end of the chicane, a non-scattered electron with a momentum p_0 , which does not get involved in the Compton scattering, is always on the reference trajectory. In that case, the distance between the fiber array and the trajectory can be determined according to the designed geometry of the electron detector. In section 5.2, we discussed the real situation for the beam trajectory. According to the real situation, we do not know the electron beam position precisely. Since there is no room to install beam position monitors between the chicane end and the fiber detector, we have designed a wire mount that is attached to the fiber array directly. The CAD drawings of the wire mount are shown in figure E.10, in figure E.11, and in figure E.12.

The designed distance between the wire and the closest boundary of the fiber array is 6.1 mm in the drawing. However, one also needs to consider the thickness of the paint. The designed width of the fiber array is 14.63 mm, its true value after paint is 15.10 mm, so the additional thickness is estimated at 0.47 mm. Thus, the distance between the wire and the closest boundary is approximately 5.9 mm.

The fiber array that is connected to a movable cart is able to move in the direction perpendicular to the electron beam. We can determine the relative position of the cart by using a potentiometer².

¹Diamant Universal extra fein Polierpaste

²Megatron MBH K50

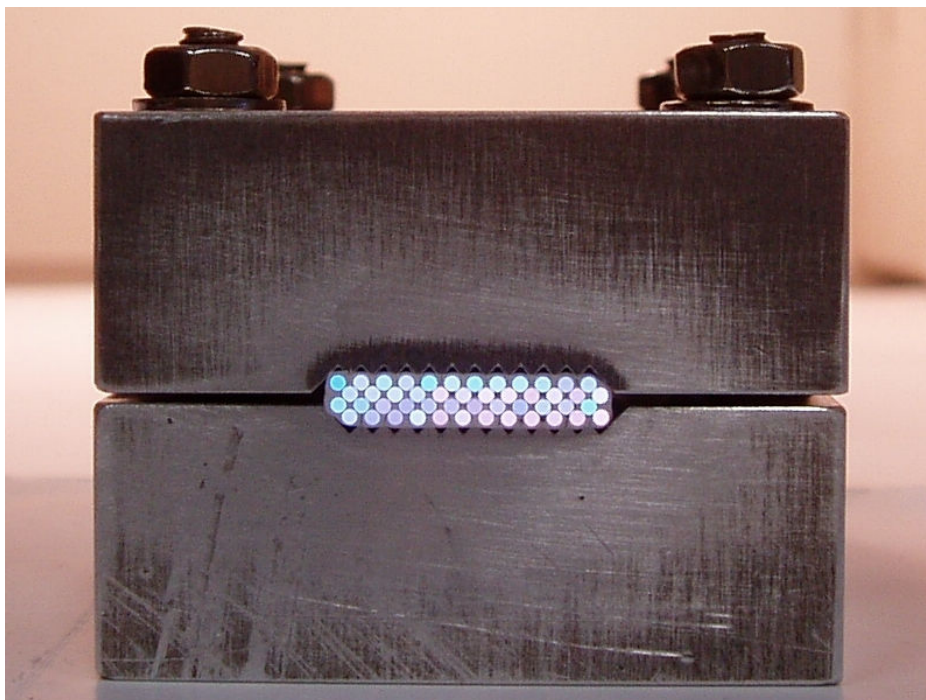


Figure 6.5 The painted fiber array with the V-shaped grooves holders.

6.2.2 Multianode Photomultiplier Tube

Since we have 48 scintillating fibers, in principle, 48 photomultiplier tubes are necessary to collect the scintillation light. However, for this purpose, we use a multianode photomultiplier tube. The HAMAMATSU multianode photomultiplier tube H7546, which is a 8×8 multianode, fast, and low cross-talk photomultiplier tube, is used to collect the scintillation light from the fibers. A housing of H7546 is in the form of a square with the dimensions $\square 30 \pm 0.5$ mm. The window material of H7546 is Borosilicate glass. The spectral and time response of H7546 are suitable for the scintillation light of the SCSF-78M fiber [133]. The left picture in figure 6.6 shows the spectral response of H7546. The detailed characteristics are given in table 6.3. A multianode pattern of H7546 is shown in the right picture of figure 6.6. Each number from P1 to P64 corresponds to one anode pixel. The first electrode plate has four holes of 0.3 mm in diameter used as guide marks for positioning when the fibers are coupled to H7546 [136]. However, the geometrical center of the photomultiplier housing is not the center of the four guide marks. We, therefore, measured the difference between them, and made a correction plate for the particular H7546 used in the detector. Figure E.5 in appendix E shows the correction plate.

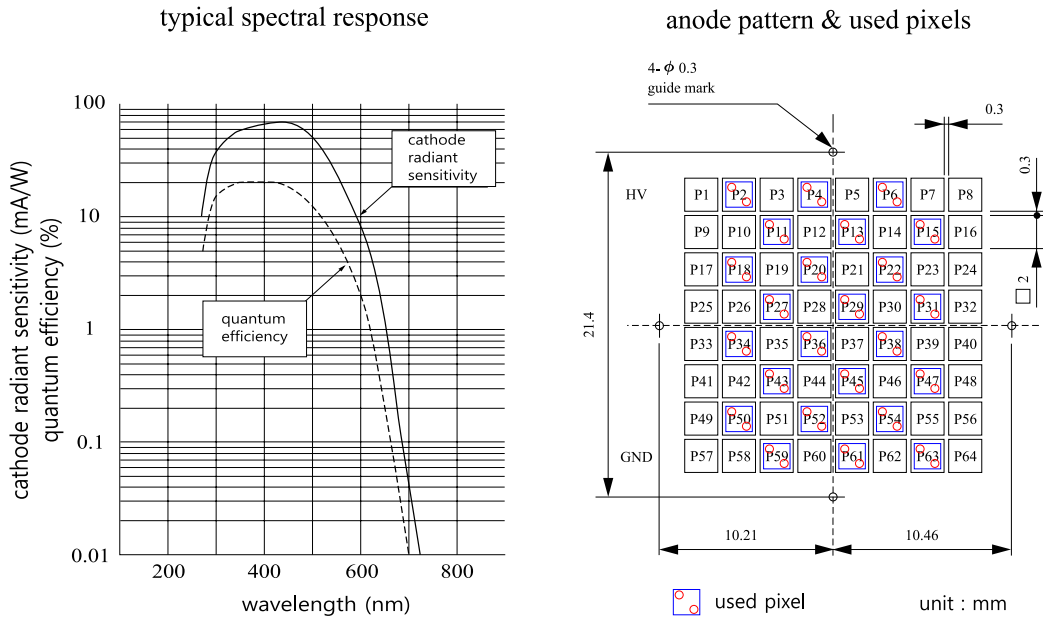


Figure 6.6 Spectral response and anode pattern of the HAMAMATSU multianode photomultiplier tube H7546 [136]. The labels from P1 to P64, correspond to 64 anodes. The 24 used pixels in the right picture are marked by the blue squares. The red circles are the hole pattern of the new fiber array mount.

Parameter	Description
Spectral response	300 ~ 650 nm
Wavelength of maximum response	420 nm
Photocathode material	Bialkali
Window material	Borosilicate Glass
Dynode number of stages	12
Anode size	□ 2 mm
Quantum efficiency at 390 nm	21 %
Maximum supply voltage	-1000 V
Gain	3.0×10^5
Cross-talk with 1mm optical fiber	2 %
Anode pulse rise time	1 ns
Housing size	□ 30 ± 0.5 mm

Table 6.3 Properties of the multianode photomultiplier tube H7546 [136].

6.2.3 Fiber Array Mount

Since we want to reuse the electronic part of the prototype, we use only 24 pixels of the photomultiplier tube. For this reason, two fibers, which are in the same pair $\mathbf{F}i$, are connected to one pixel. The used pixel is denoted by the blue square with two red circles in the left picture of figure 6.6. The red circles represent two holes for the corresponding fibers. The fiber hole pattern was designed to minimize cross-talk between fibers and to reduce difficulties in the production process due to machine tolerance.

The prototype fiber array mount was made of aluminum with a small plastic interface for the photomultiplier tube. The fibers were attached to the prototype mount. The mount was connected to the vacuum chamber through a bellow and directly attached to the motor spindle. In this configuration, maintenance of the fiber array required large-scale disassembling that was very inconvenient due to the limited space. As a result, in the new design, we separate it into two parts: (1) a photomultiplier tube cart that is connected to the vacuum chamber and to the motor directly and has a large hole for the fiber array; and (2) the new fiber array mount that is connected to the cart and has a fiber hole pattern and an interface for the photomultiplier tube. We, therefore, are able to attach the fiber array to the electron detector and detach the array from the detector without difficulties. Figure E.4 in appendix E shows the CAD drawing for the fiber array mount. The more information about the cart will be discussed later.

Fiber-Pixel matching

We have 24 fiber pairs of the fiber array and 24 corresponding hole pairs in the fiber array mount. A fiber pair $\mathbf{F}i$ has two fibers $\mathbf{F}ia$ and $\mathbf{F}ib$. For convenience, $\mathbf{F}ia$ and $\mathbf{F}ib$ are called sub-fibers of $\mathbf{F}i$. In the same manner, a hole pair has two holes. Since a hole pair fits with a pixel of the multianode photomultiplier tube, the pair is called the pixel $\mathbf{P}i$ and the hole is called the sub-pixel from now on. The number of pixels, which are used, is defined in figure 6.6. To address the sub-pixels within one pixel, we call the sub-pixel near the high voltage (HV) connector of the photomultiplier tube $\mathbf{P}i\mathbf{HV}$ and one near the ground (GND) connector $\mathbf{P}i\mathbf{GND}$.

The number of the possible connection between fiber pairs and pixels is simply a permutation of numbers from 1 and 24, which is $P(24, 24) = 24! = 6.2045 \times 10^{23}$. In addition, there are two possible connections between sub-fibers and sub-pixels. For example, if $\mathbf{F}1$ is connected to $\mathbf{P}2$, there are two

Algorithm 1 Gale-Shapley stable marriage algorithm

```

all  $F(i)$ s and all  $P(i)$ s are free
while a free fiber  $F(i)$  and has not proposed to every pixels do
  choose such a  $F(i)$ .
  let a pixel  $P(i)$  be the highest-ranked pixel in the fiber preference list
  to which  $F(i)$  has not yet proposed.
  if  $P(i)$  is free then
     $F(i)$  and  $P(i)$  become engaged.
  else
     $P(i)$  is at this moment engaged to  $F(j)$ 
    if  $P(i)$  prefers  $F(j)$  to  $F(i)$  then
       $F(i)$  remains free
    else
       $F(i)$  and  $P(i)$  become engaged
       $F(j)$  becomes free
    end if
  end if
end while

```

possibilities 1D and 2D as follows:

$$\begin{aligned}
 \mathbf{F1a} - \mathbf{P2GND} \quad & \& \quad \mathbf{F1b} - \mathbf{P2HV} \quad \dots \quad (1D); \\
 \mathbf{F1a} - \mathbf{P2HV} \quad & \& \quad \mathbf{F1b} - \mathbf{P2GND} \quad \dots \quad (2D).
 \end{aligned}$$

The number of the possible connection is even larger than the number $2 \times 24!$ because of three-dimensional space.

For simplicity, we project the pixel or hole pattern of the fiber array mount and the cross section of the fiber array onto two-dimensional plane. Then we calculate *distances* between the fibers and the pixels. We want to use the same length for all fibers, because of the light collection and transfer efficiency (LCTE). As a result, the sole criterion for a choice of the possible connection is to keep the variance of these distances as small as possible. Thus, in the connection between **F1** and **P2**, if the variance of 1D is smaller than that of 2D, we choose 1D, and vice versa. However, in the connection between fiber pairs and pixels, it is difficult to find a method of matching fiber pairs with pixels. For this reason, we use the Gale-Shapley stable marriage algorithm [137, 138, 139] to find the optimum connection between them. This algorithm is summarized in algorithm 1. Here, **F** i is denoted as $F(i)$ and **P** i as $P(i)$.

The stable marriage algorithm is strongly dependent on so-called *preference lists* that contain preferences of a fiber pair and a pixel. We, therefore,

Propose	PL of fiber	PL of pixel	Mean	Variance
Fibers	<i>SPL</i>	<i>SPL</i>	3.79	6.17
Pixels	<i>SPL</i>	<i>SPL</i>	3.79	6.17
Fibers	<i>SPL</i>	<i>DPL</i>	5.35	0.61
Pixels	<i>SPL</i>	<i>DPL</i>	5.54	1.04
Fibers★	<i>DPL</i>	<i>DPL</i>	6.72	0.28
Pixels	<i>DPL</i>	<i>DPL</i>	6.65	5.43
Fibers	<i>DPL</i>	<i>SPL</i>	6.40	0.32
Pixels	<i>DPL</i>	<i>SPL</i>	3.87	1.84

Table 6.4 Possible connections between fibers and pixels. PL is a preference list, *SPL Shortest distance Preference List*, *DPL smallest Deviation Preference List*, Mean the mean value of the distances between fibers and pixels, and Variance the variance of the distances. The optimum connection is **Fibers★**. As expected, when the fiber pairs propose to the pixels, the *DPL* returns the best result due to the criterion, which is the smallest variance. However, using the same *DPLs*, the proposal of the pixels returns larger variance than the fiber pairs one, because two possible connection distances are twice as large as the other ones.

have to define good preference lists for them. First, a fiber pair $\mathbf{F}i$ can be connected with a pixel $\mathbf{P}j$ where $i = 1, 2, \dots, 24$ and $j = 1, 2, \dots, 24$. The distance between $\mathbf{F}i$ and $\mathbf{P}j$ is denoted by d_{ij} . $\mathbf{P}j$ with the shortest d_{ij} is the first rank in the preference list of $\mathbf{F}i$. This preference list is called *Shortest distance Preference List (SPL)* for convenience. Second, using the following equation,

$$\delta d_{ij} = |\bar{d}_i - d_{ij}| \quad \text{and} \quad \bar{d}_i = \sum_j \frac{d_{ij}}{24}, \quad (6.7)$$

we can define *smallest Deviation Preference List (DPL)*, in which the $\mathbf{P}j$ with the smallest δd_{ij} is the first rank of $\mathbf{F}i$.

According to the stable marriage algorithm, the fiber pairs propose to the pixels, and the same applies in reverse. With both proposal methods, two preference lists for a fiber pair, and two preference lists for a pixel, there are eight possible ways to the stable marriage algorithm. Table 6.4 shows the result of the eight possibilities. The optimum result **Fibers★** in table 6.4, in which the fibers propose to the pixels with fiber's *DPL* and pixel's *DPL*, provided the smallest variance of the 24 connections, which means that the distances between the fiber pairs and the pixels are almost the same for all fibers. The detailed matching result is given in table 6.5 and is used to connect the fiber array to the fiber array mount. Note that the connection

Fiber pair	Pixel	sub-fiber $F_i a$	sub-pixel $F_i b$
F1	P47	a-HV	b-GND
F2	P34	a-HV	b-GND
F3	P63	a-HV	b-GND
F4	P20	a-HV	b-GND
F5	P50	a-HV	b-GND
F6	P54	a-HV	b-GND
F7	P52	a-GND	b-HV
F8	P4	a-HV	b-GND
F9	P6	a-GND	b-HV
F10	P43	a-GND	b-HV
F11	P36	a-GND	b-HV
F12	P27	a-GND	b-HV
F13	P38	a-GND	b-HV
F14	P29	a-GND	b-HV
F15	P22	a-GND	b-HV
F16	P59	a-GND	b-HV
F17	P61	a-HV	b-GND
F18	P13	a-GND	b-HV
F19	P11	a-HV	b-GND
F20	P15	a-HV	b-GND
F21	P45	a-HV	b-GND
F22	P2	a-HV	b-GND
F23	P31	a-HV	b-GND
F24	P18	a-HV	b-GND

Table 6.5 Stable fiber pairs and pixels matching. Note that we consider two dimensional space to make the preference lists for fibers and pixels. Thus, there may be better possibilities of fiber pairs and pixels matching.

is considered in two dimensional plane, because it is hard to find proper preference lists of fiber pairs and pixels in three dimensional space.

6.2.4 Hermetic Sealing with Epoxy

The fiber array and its mount are mounted in the interface between the vacuum and the atmosphere. Figure 6.7 shows this interface. As a result, the fiber array mount must have a hermetic sealing. To make it possible, we used the Varian Torr Seal epoxy³ that has low outgassing properties and is

³Loctite Corporation - Hysol 1C

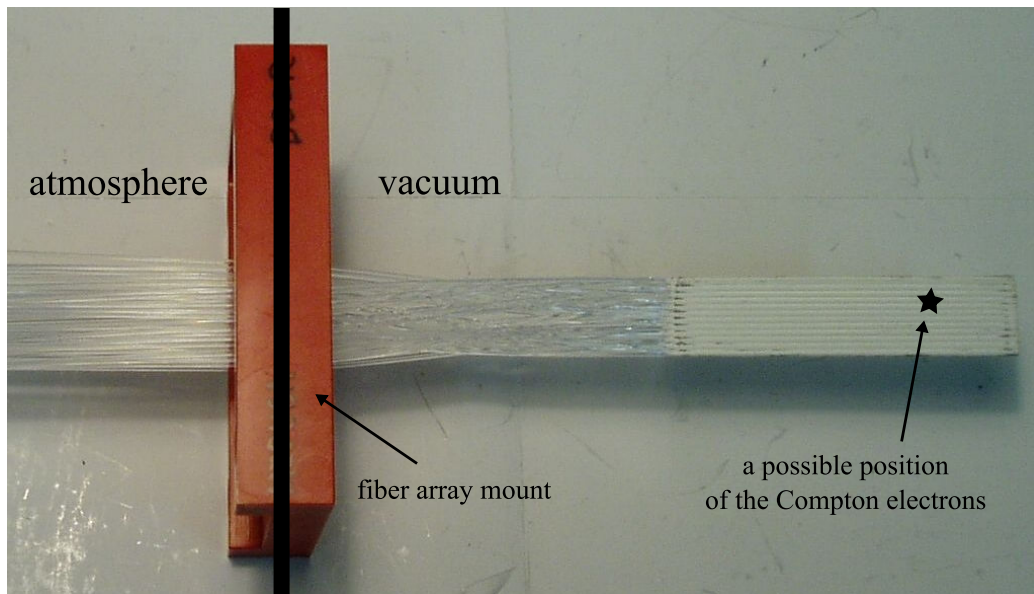


Figure 6.7 Hermetic feedthrough. The right part of the picture, is in a high vacuum (10^{-7} mbar). Scintillating fibers pass from a high vacuum environment to the atmosphere. A hermetic sealing is necessary.

suitable for use in pressures of 10^{-9} mbar and below at temperatures from -45°C to 120°C [140]. The vacuum epoxy also has an off-white color that prevents cross-talk between fibers. Fluorinated polymer, which is the cladding material of the fiber, cannot be ordinarily bonded with conventional epoxy adhesives. There is a method that is described in the reference [141] in order to obtain maximum joint strength. However, we do not need this bonding method, but we need a potting method that make a hermetic feedthrough by combining the fiber array with the fiber mount. Before applying the fiber array mount with the epoxy, we made a small sample test module and it successfully passed a vacuum leakage test.

Potting and polishing

Figure E.3 shows the *outside fiber bundle holder*. The outside fiber bundle holders are combined with the inside fiber bundle holders in section 6.2.1 so as to hold the fiber array and the fiber array mount in place during the potting process. This is shown in the left picture of figure 6.8. For a complete cure, the fiber array mount with the Torr Seal epoxy was left with an incandescent electric lamp during three days.

The other end face of the fiber array mount, in the atmosphere of the

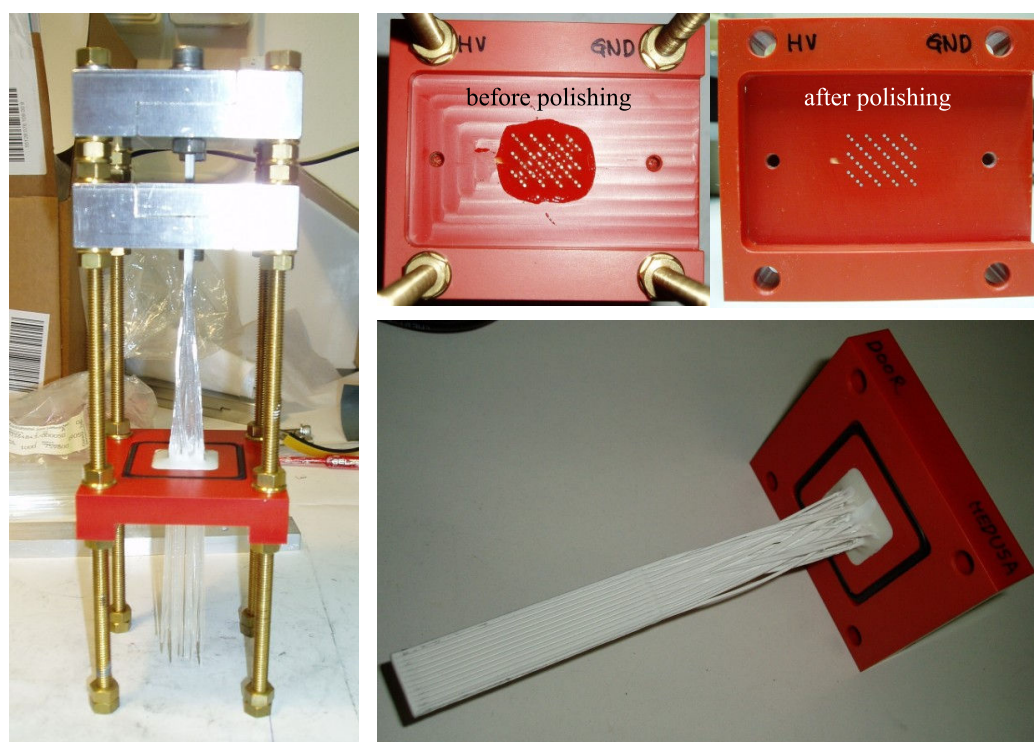


Figure 6.8 Fiber array mount with the fibers

experimental hall 3, is also needed to be polished, because we attach the multianode photomultiplier tube with the correction plate to the fiber array mount. A holder is also necessary so that we can polish them without serious damage to the fibers, just as we used the inside fiber holder during polishing. Since the diameter of the holes of the mount is 0.9 mm and the fiber diameter 0.83 mm, there is very small gap between them. We used a common epoxy⁴ to fill in these small gaps by a vacuum oven. Using the vacuum oven at 60°C for 15 min., we turned on a vacuum pump, and turned it off several times, because the small gaps must be filled with the epoxy. Then the fiber array mount was left in the vacuum oven at 60°C for 45 min. without vacuum for curing. Then, the fiber array mount was left for one day at the room temperature for the full curing. After that, we polished the end face with the same method as before. The upper right pictures in figure 6.8 show one face of the fiber array mount before and after polishing. The fiber array mount with the fibers and the hermetic sealing, which is shown in the lower right picture in figure 6.8, also passed the vacuum leakage test successfully.

6.2.5 Mechanical Parts

Figure 6.9 shows the CAD drawing of all visible components of the new fiber electron detector. The major change of the detector is the fiber array that is invisible in the drawing. The components with the solid symbol (■) were developed for the new electron detector and the other components are reused from the prototype. Figure E.9 in appendix E shows the cart. The cart connects to the spindle of the stepping motor for a linear motion, to linear slides, and to the potentiometer. we can easily separate the fiber array mount with the fibers from the beam line to perform the maintenance of the fibers without dismantling the fiber detector and putting it back together again. For this case, the replacement vacuum cover was designed to seal the vacuum in the beam line. The drawing of the cover is shown in figure E.13. For the linear motion of the detector, we replaced the rail guides of the prototype with LZM miniature slides⁵. Thus, the slide support also was designed and is shown in figure E.8. We also designed a light tight box so as to further suppress ambient light on the photomultiplier tube (figures E.6 and E.7). In the final assembly of the detector, the box has to be wrapped in black tape.

⁴UHU plus endfest 300

⁵SKF Actuation & Motion Control

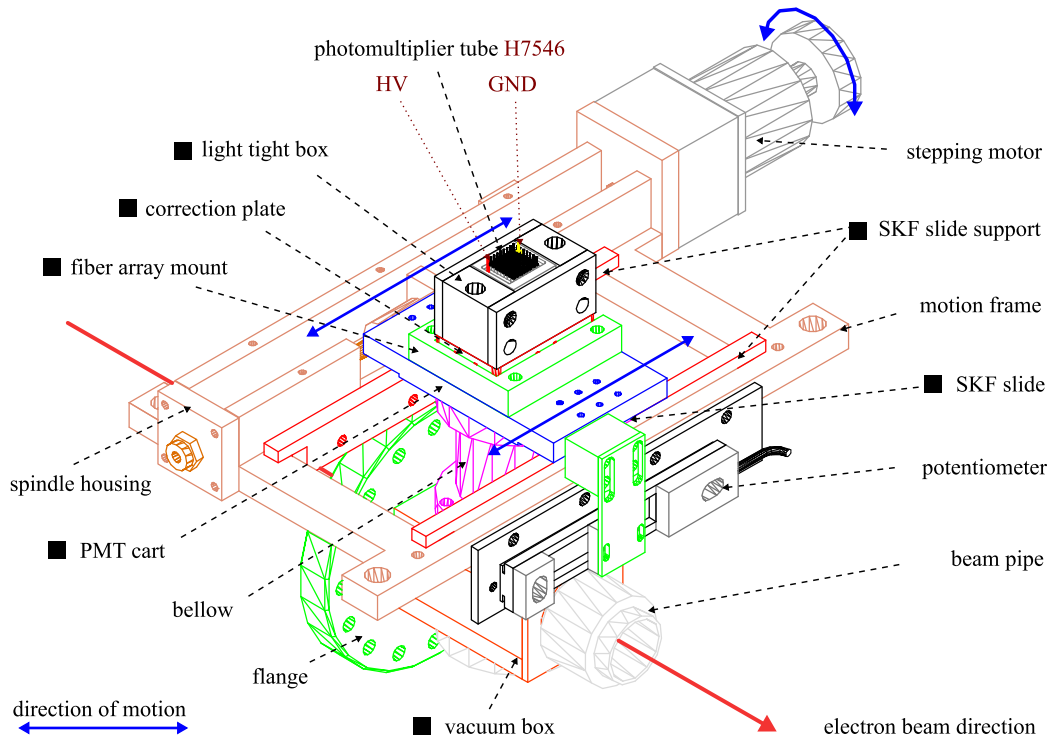


Figure 6.9 The scintillating fiber electron detector. The components with the solid symbol (■) are designed so as to improve the detector. The new fiber array inside the bellow is invisible in the drawing. The high voltage pin is denoted as HV and the ground one as GND. The orientation of the photomultiplier tube is important because of the correction plate and the prototype signal and power connector. All detailed CAD drawings except the vacuum box are shown in appendix E. The new vacuum box was designed by one of the A4 collaborators [142].

6.3 Formulas and Data Handling

In chapter 3, we discuss a general approach to extract the electron beam polarization. However, this approach is not suitable because of experimental consideration. Thus, in this section, we consider the experimental conditions for polarization states of the electron and the photon and redefine the cross sections σ_{\pm} according to their polarization states. And we show how to handle the number of events and how to calculate the Compton asymmetry, the electron polarization, and their errors from the events.

6.3.1 Cross Section Formula

Figure 6.10 shows the cross sections according to polarization states of the electron and the photon. The upper plot that is denoted by **(I)** is the sign convention for the Compton cross sections (3.22). With this convention, we use the electron beam with only one polarization state, which is the electron spin parallel to its direction of motion, and the laser beam with two alternative polarization states, which are left and right circularly polarized states⁶.

However, in actual practice, the polarization state of the electron is randomly changed, described in section 2.4. Thus we have to use the slightly different conventions according to the photon polarization state. If the incident photon is right circularly polarized or has negative helicity, the middle plot **(II)** in figure 6.10 shows the corresponding convention of the cross sections. And when the incident photon is left circularly polarized or has positive helicity, the lower plot **(III)** represents the convention of the cross sections.

During a 2008 polarimeter development beam time, we took several runs with two different $\lambda/2$ plate states. As mentioned in chapter 3, a $\lambda/2$ plate is inserted ($\lambda/2$ *plate in*) or is taken out ($\lambda/2$ *plate out*) between the laser system and the GaAs crystal in the polarized electron source at MAMI. This reverses the polarization pattern of the electron beam, described in chapter 2, and gives us a chance to understand systematic effects of asymmetry measurement. In addition, the polarization pattern is recorded by the A4 data acquisition system. For convenience, we introduce the symbol μ so as to describe the $\lambda/2$ plate states. $\mu = 0$ represents a $\lambda/2$ plate out and $\mu = 1$ does a $\lambda/2$ plate in. And we introduce the symbol k to describe to the polarization pattern of the electron. $k = 0$ is called *pol0* and $k = 1$ is called *pol1*. Note that *pol0* and *pol1* are used to recognize only the relative polarization state of the electron.

⁶A left circularly polarized photon has positive helicity. See the references [143, 89] in detail.

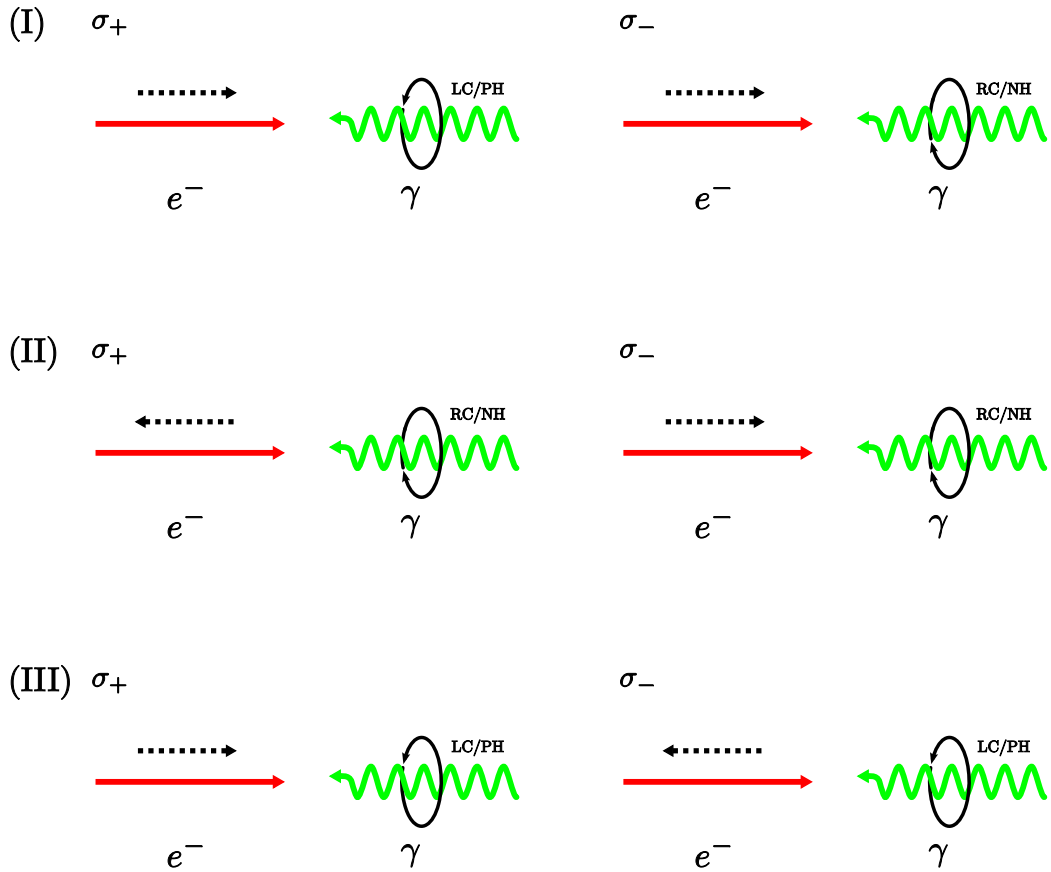


Figure 6.10 Cross sections σ_{\pm} with respect to different polarization states of the electron and the photon. The red arrow is the direction of motion of the electron and the green wavy arrow is the photon one. The dotted arrow is the electron polarization and the elliptical arrow represents the photon polarization. LC/PH is the left circularly polarized photon that has positive helicity and RC/NH is the right circularly polarized photon that has negative helicity.

From the transmission Compton polarimeter measurement, described in section 2.4, we determine two electron polarization state when $\mu = 0$ at electron beam energy of 854.3 MeV. The positive helicity electron corresponds to $k = 1$ (pol1) and the negative helicity electron corresponds to $k = 0$ (pol0). Furthermore, from the photon polarization measurement, done by the prototype Stokes meter, we measure that the photon has positive helicity and its polarization is 0.96317(11). According to these two measurements, our experimental condition of the 2008 polarimeter development beam time is shown in the plot (III) in figure 6.10. In addition, if we consider the electron polarization when a $\lambda/2$ plate is inserted, i.e. $\mu = 1$, the helicity of the electron is changed. Thus, *pol0* represents positive helicity and *pol1* does negative helicity of the electron.

6.3.2 Electron Polarization from A_{exp}^{CT}

As mentioned in section 3.2, using differential polarization measurement, the number of the events per each energy bin $\Delta\rho_i$ is

$$\begin{aligned} n_{\pm}^i &= \mathcal{L}_{\pm} T_{\pm} \int_{\Delta\rho_i} d\rho \epsilon_{\pm}(\rho) \frac{d\sigma_{\pm}}{d\rho} \\ &= \frac{\mathcal{L}T}{2} \int_{\Delta\rho_i} d\rho \epsilon_{\pm}(\rho) \frac{d\sigma_0}{d\rho} [1 \mp P_e P_{\gamma} A_{\text{th}}^{CT}], \end{aligned} \quad (6.8)$$

where \mathcal{L} is the luminosity, T the total measurement time, and $\epsilon(\rho)$ is the detection efficiency of the photon detector. Here we assume $\mathcal{L}_+ T_+ = \mathcal{L}_- T_- = \mathcal{L}T/2$, $\epsilon_+(\rho) = \epsilon_-(\rho) = \epsilon(\rho)$, and $\cos\psi = 1$ for simplicity.

Thus, the experimental Compton asymmetry per $\Delta\rho_i$ is

$$\begin{aligned} (A_{\text{exp}}^{CT})_i &= \frac{n_+^i - n_-^i}{n_+^i + n_-^i} \\ &= -P_e^i P_{\gamma} \frac{\int_{\Delta\rho_i} d\rho \epsilon(\rho) \frac{d\sigma_0}{d\rho} A_{\text{th}}^{CT}}{\int_{\Delta\rho_i} d\rho \epsilon(\rho) \frac{d\sigma_0}{d\rho}} \\ &= -P_e^i P_{\gamma} \langle A_{\text{th}}^{CT} \rangle_i \\ &= -P_e^i P_{\gamma} (\mathbf{A}_{\text{th}}^{CT})_i, \end{aligned} \quad (6.9)$$

where $(\mathbf{A}_{\text{th}}^{CT})_i$ is the center value of the theoretical Compton asymmetry within $\Delta\rho_i$. When a $\lambda/2$ plate is taken out ($\mu = 0$), this experimental asymmetry is expressed in terms of pol0 and pol1 as

$$(A_{\text{exp}}^{CT})_i = \frac{n_{\text{pol1}}^i - n_{\text{pol0}}^i}{n_{\text{pol1}}^i + n_{\text{pol0}}^i}. \quad (6.10)$$

Therefore, the electron polarization P_e^i per each bin $\Delta\rho_i$ is

$$P_e^i = -\frac{1}{P_\gamma} \left(\frac{A_{\text{exp}}^{CT}}{\mathbf{A}_{\text{th}}^{CT}} \right)_i, \quad (6.11)$$

and its error is

$$\delta P_e^i = \left[\frac{\sqrt{(\delta A_{\text{exp}}^{CT})^2 + (\mathbf{A}_{\text{th}}^{CT} \delta P_\gamma / P_\gamma)^2}}{|P_\gamma| |\mathbf{A}_{\text{th}}^{CT}|} \right]_i, \quad (6.12)$$

where $\delta A_{\text{exp}}^{CT}$ is the error of the experimental Compton asymmetry and δP_γ is the error of the photon polarization.

Finally, using a weighted average [122, 124, 144], the electron polarization P_e is

$$P_e = \frac{\sum_i w_i P_e^i}{\sum_i w_i}, \quad (6.13)$$

where

$$w_i = \frac{1}{(\delta P_e^i)^2}.$$

And the uncertainty in P_e is

$$\delta P_e = \frac{1}{\sqrt{\sum_i w_i}}, \quad (6.14)$$

where the sum runs over the bins that we use to calculate the experimental Compton asymmetry.

6.3.3 Photon Spectra and Event Number

Different types of photon spectra

We use two ADC modules for the data acquisition of the Compton backscattering polarimeter. Figure 3.9 shows the diagram of the data acquisition electronics. One module, which is called the photon (γ) ADC, is for the photon detector and the other one, which is called the electron (e) ADC, is for the fiber electron detector. The photon ADC collects 10 signals, which are 9 for the LYSO crystals and one for the sum of 9 signals, of the photon detector with the gate signal. In this data analysis we use only the sum signal. We call the recorded photon spectrum *the photon spectrum with trigger γ* . And, the photon ADC records an attenuated signal from the coincidence between the

symbol	μ	ν	k	l
0	$\lambda/2$ plate out	trigger γ	pol0	background
1	$\lambda/2$ plate in	trigger $\gamma + e$	pol1	signal + background

Table 6.6 The meaning of the symbols μ , ν , k , and l .

photon discriminator (CFD) and the electron discriminator (LED). If the attenuated signal has an adequate charge in order to distinguish an event exists on the electron detector, we save the corresponding event from the photon detector in an additional spectrum by a software. And we call this additional spectrum *the photon spectrum with trigger γ and e* . For convenience, we introduce the symbol ν to represent these two trigger conditions, i.e. $\nu = 0$ corresponds to trigger γ and $\nu = 1$ corresponds to trigger γ and e .

In addition, when the attenuated signal exits, i.e. scattered electrons hit any of the fibers, the software checks the status of each channel of the electron ADC. If one channel has an event, the backscattered photon event is redistributed into an additional photon spectrum with respect to the channel of the electron ADC. For convenience, we call this photon spectrum a *photon spectrum of a fiber pair*, because each ADC channel corresponds to each fiber pair. We can activate channels of the electron ADC at the same time by a so-called *multiplicity* that is in the range of 1 to 99. If the multiplicity is one, the software saves a photon spectrum when only one channel of the electron ADC has an event. Since we used *ninety-nine* multiplicity during this development beam time, there are multiple counts in the photon spectra of the fiber pairs.

And the photon spectrum has two different polarization states, which are denoted as *pol0* and *pol1*, of the electron. We use the symbol k to represent the electron helicity, which are discussed in section 6.3.1.

Furthermore, there are two spectrum measurements : (1) signal and background spectrum measurement and (2) background measurement. We introduce the symbol l to describe two measurements. $l = 1$ represents the signal and background measurement and $l = 0$ does the background measurement. During the signal and background spectrum measurement ($l = 1$), we use the electron beam and the laser beam and see the Compton events in the photon spectrum. And during the background measurement ($l = 0$), the laser beam is blocked using a shutter. Therefore, no Compton event is detected by the photon detector in this measurement.

In summary, table 6.6 shows the meaning of the four symbols, μ , ν , k , and l .

Number of the events

We define the number of the events that we record by the photon detector according to table 6.6. Thus, the number of the events for a bin i and a run j is

$$n^{ij}(\mu\nu kl), \quad (6.15)$$

and its error is

$$\delta n^{ij}(\mu\nu kl) = \sqrt{n^{ij}(\mu\nu kl)}, \quad (6.16)$$

because n^{ij} follows the Poisson distribution.

The number of the Compton events is expressed by

$$n_c^{ij}(\mu\nu k) = n^{ij}(\mu\nu k1) - n^{ij}(\mu\nu k0), \quad (6.17)$$

where the subscript c stands for Compton. Here we use the direct and simple bin-wise subtraction. And its error is

$$\begin{aligned} \delta n_c^{ij}(\mu\nu k) &= \sqrt{[\delta n^{ij}(\mu\nu k1)]^2 + [\delta n^{ij}(\mu\nu k0)]^2} \\ &= \sqrt{n^{ij}(\mu\nu k1) + n^{ij}(\mu\nu k0)}. \end{aligned} \quad (6.18)$$

The experimental Compton asymmetry of a bin i and a run j is

$$A^{ij}(\mu\nu) = \frac{n_c^{ij}(\mu\nu 1) - n_c^{ij}(\mu\nu 0)}{n_c^{ij}(\mu\nu 1) + n_c^{ij}(\mu\nu 0)}, \quad (6.19)$$

and its error is

$$\delta A^{ij}(\mu\nu) = 2 \frac{\sqrt{[\delta n_c^{ij}(\mu\nu 1) n_c^{ij}(\mu\nu 0)]^2 + [n_c^{ij}(\mu\nu 1) \delta n_c^{ij}(\mu\nu 0)]^2}}{[n_c^{ij}(\mu\nu 1) + n_c^{ij}(\mu\nu 0)]^2}. \quad (6.20)$$

Note that (6.19) is valid for only the 2008 polarimeter development beam time, because the convention of the cross section formula is changed according to initial polarization states of the electron and the photon.

Independent measurements

We carried out independent measurements of the Compton spectra and combine several runs that have the same $\lambda/2$ plate state. When a $\lambda/2$ plate is taken out ($\mu = 0$), sixty-four signal and background runs ($l = 1$) and twenty-three background runs ($l = 0$) have good quality to calculate Compton asymmetry. When a $\lambda/2$ plate is inserted ($\mu = 1$), seventy-nine signal and background runs ($l = 1$) and thirty-three background runs ($l = 0$) are suitable for the same purpose. We summarize these run numbers in table 6.7.

$\lambda/2$ plate status	μ	0		1	
laser status	l	0	1	0	1
run number	$J_{\mu l}$	23	64	33	79

Table 6.7 Available run number $J_{\mu l}$ with respect to μ and l during the 2008 polarimeter development beam time.

Since we have different run numbers between $l = 0$ and $l = 1$, we average the number of the events per each bin i such that we calculate the number of the mean Compton events. We assume that $n^{ij}(\mu\nu kl)$ per each bin i is extracted from the same parent population and the same uncertainties. Thus the mean event number per each bin i is

$$N^i(\mu\nu kl) = \frac{1}{J_{\mu l}} \sum_{j=1}^{J_{\mu l}} n^{ij}(\mu\nu kl), \quad (6.21)$$

and its error per each bin i [124] is

$$\delta N^i(\mu\nu kl) = \sqrt{\frac{N^i(\mu\nu kl)}{J_{\mu l}}}. \quad (6.22)$$

And the number of the mean Compton events is

$$N_c^i(\mu\nu k) = N^i(\mu\nu k1) - N^i(\mu\nu k0), \quad (6.23)$$

and its error is

$$\delta N_c^i(\mu\nu k) = \sqrt{[\delta N^i(\mu\nu k1)]^2 + [\delta N^i(\mu\nu k0)]^2}. \quad (6.24)$$

Thus, the mean Compton asymmetry of a bin i is

$$A^i(\mu\nu) = \frac{N_c^i(\mu\nu 1) - N_c^i(\mu\nu 0)}{N_c^i(\mu\nu 1) + N_c^i(\mu\nu 0)}, \quad (6.25)$$

and its error is

$$\delta A^i(\mu\nu) = 2 \frac{\sqrt{[\delta N_c^i(\mu\nu 1) N_c^i(\mu\nu 0)]^2 + [N_c^i(\mu\nu 1) \delta N_c^i(\mu\nu 0)]^2}}{[N_c^i(\mu\nu 1) + N_c^i(\mu\nu 0)]^2}. \quad (6.26)$$

6.4 Preliminary Result of the Fiber Detector Development

In this section, we present preliminary result that lives up to our expectations in the electron beam polarization measurement by using the redesigned scintillating fiber electron detector. First, we use only two runs such that we take a look at the status of the scintillating fiber detector and examines background reduction by the coincidence between the electron fiber detector and the photon detector. After that, we consider all available runs, taken during the 2008 beam time for the polarimeter development, so as to minimize the statistical fluctuations. Finally, we estimate the experimental Compton asymmetry, the electron polarization, and their errors. This preliminary result provides a starting point for more studies that are needed to measure the electron polarization precisely and that are in progress [142].

6.4.1 Detector Status and Background Reduction

One run, Run 56483, is a photon spectrum measurement with the 854.3 MeV electron beam and the 2.41 eV laser beam. This measurement has $\mu = 0$ and $l = 1$. And the other run, Run 56482, is one with the electron beam and has $\mu = 0$ and $l = 0$.

Figure 6.11 shows three contour plots of the photon spectra of the fiber pairs with the sum of two electron polarization states, i.e.

$$n^{ij}(l) = \sum_{k=0}^1 n^{ij}(0, 1, k, l).$$

The left upper plot, which is denoted as (1), and the right upper plot (2) show the photon spectra in the coincidence with each fiber pair noted in the x -axis with $l = 1$ and $l = 0$ respectively. Thus, the left upper plot (1) contains the Compton events and background and the right upper plot does only background. Using the direct and simple bin-wise subtraction of the data of Run 56482 from the data of Run 56483, we obtain the lower plot (3). No further corrections are applied.

We clearly see a linear correlation between the fiber pair number and the photon energy (ADC channel) in the plots. After we find the peak positions of each photon spectrum of the fiber pair by the Gaussian fit, we confidently argue that the correlation between the fiber pair number and the ADC channel is shown. More precisely, the correlation is highly significant, because the correlation coefficient r_0 , described in section 5.2.1, is 0.99994 and the probability Pr of getting a correlation coefficient $|r| \geq 0.99994$ from the fiber

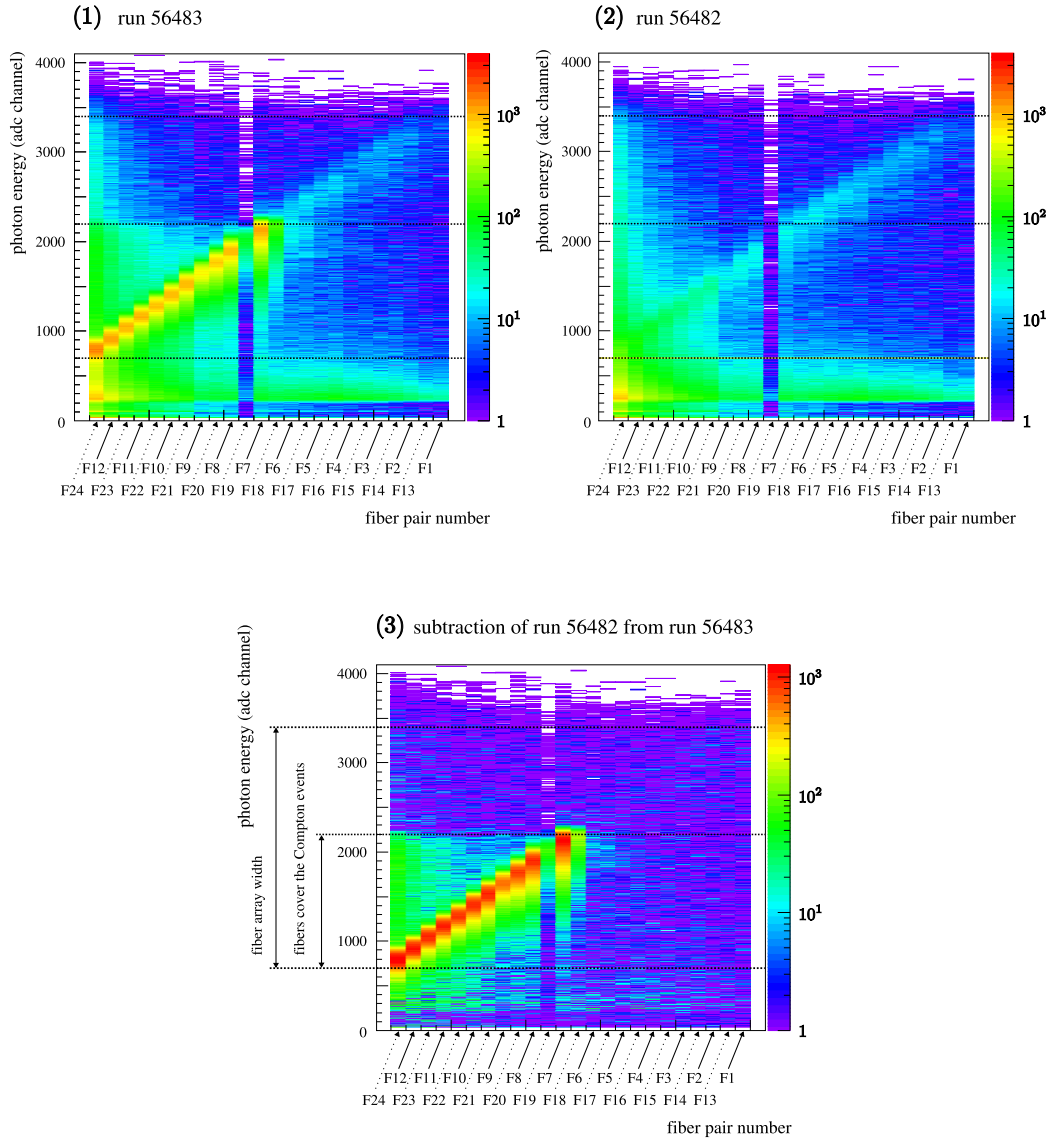


Figure 6.11 Contour plots of the photon detector spectra of the fiber pairs. Two above plots (1) and (2) show the coincidence spectra of each fiber pair with and without the laser beam. The below plot (3) shows the naive subtraction and represents only the Compton events. Here we perform no possible corrections that may be overlaps of the detector path length and records of the multiple hit of the electron to the fibers. The F19 bin shows a malfunction of the corresponding amplifier and shows fewer entries than other bins. For the sake of graphical simplicity, we merge four bins of the ADC channel in one bin.

pair number and the ADC channel is much less than 0.001%. In addition, we simulate the horizontal deviation of the scattered electron at the exit of the chicane as a function of the backscattered photon energy by using the ideal chicane simulation, described in chapter 4. The simulation result shows that $r_0 = 0.99997$ and $Pr = 2.2 < 10^{-16}$. Thus the correlation between the backscattered photon energy and the horizontal deviation of the scattered electron is highly significant because the probability is far less than 0.001%. These two correlations suggest that the fiber array, of which we do the complete redesign, is well-aligned.

In the background plot (2) shown in figure 6.11, we see interesting areas that are a horizontal green area at about 300 ADC channel, a vertical area at F24 and F12, and a green and light blue linear correlation area. We suspect that they come from electron halos of the main electron beam trajectory, random coincidences of the Bremsstrahlung, multiple hits of the scattered electron on the fibers, and the multiplicity of the data acquisition software. More studies on the background are needed for precise measurement of the electron polarization and are in progress [142].

Using the same runs, figure 6.12 shows photon detector spectra with two different states of the electron polarization ($k = 0, 1$), two different trigger conditions ($\nu = 0, 1$), and two different spectrum measurements ($l = 0, 1$). We see a suppression of the background when imposing the coincidence ($\nu = 1$) in the above plot of figure 6.12. And, when we calculate the number of the Compton events, $n_c^{ij}(\mu\nu k)$, by subtracting the background ($l = 0$) from the signal and background ($l = 1$), in the below plot of figure 6.12, $n_c^{ij}(\mu\nu k)$ is almost unchanged within the ADC channel range that the scintillating fiber array covers. Note that we are interested in only the range, is covered by the fiber array, because the outside range has smaller the theoretical asymmetry than the range does, shown in figure 3.5.

In order to quantify them, we introduce the Compton event ratio R_c , the Compton event error ratio $R_{\delta c}$, the background ratio R_b , and the asymmetry error ratio $R_{\delta A}^{ij}$ as follows:

$$\begin{aligned} R_c^{ij}(\mu k) &= \frac{n_c^{ij}(\mu 1 k)}{n_c^{ij}(\mu 0 k)}, & R_{\delta c}^{ij}(\mu k) &= \frac{\delta n_c^{ij}(\mu 1 k)}{\delta n_c^{ij}(\mu 0 k)}, \\ R_b^{ij}(\mu k) &= \frac{n_c^{ij}(\mu 1 k 0)}{n_c^{ij}(\mu 0 k 0)}, & R_{\delta A}^{ij}(\mu) &= \frac{\delta A^{ij}(\mu 1)}{\delta A^{ij}(\mu 0)}. \end{aligned} \quad (6.27)$$

For convenience, these ratios are named for *trigger efficiencies* and are listed in table 6.8. In the ADC channel range of 1000 to 2000, we see that $R_c = 0.98$, $R_{\delta c} = 0.67$, $R_b = 0.14$, and $R_{\delta A} = 0.68$. Therefore, when the coincidence between the scintillating fiber detector and the photon detector is used, the

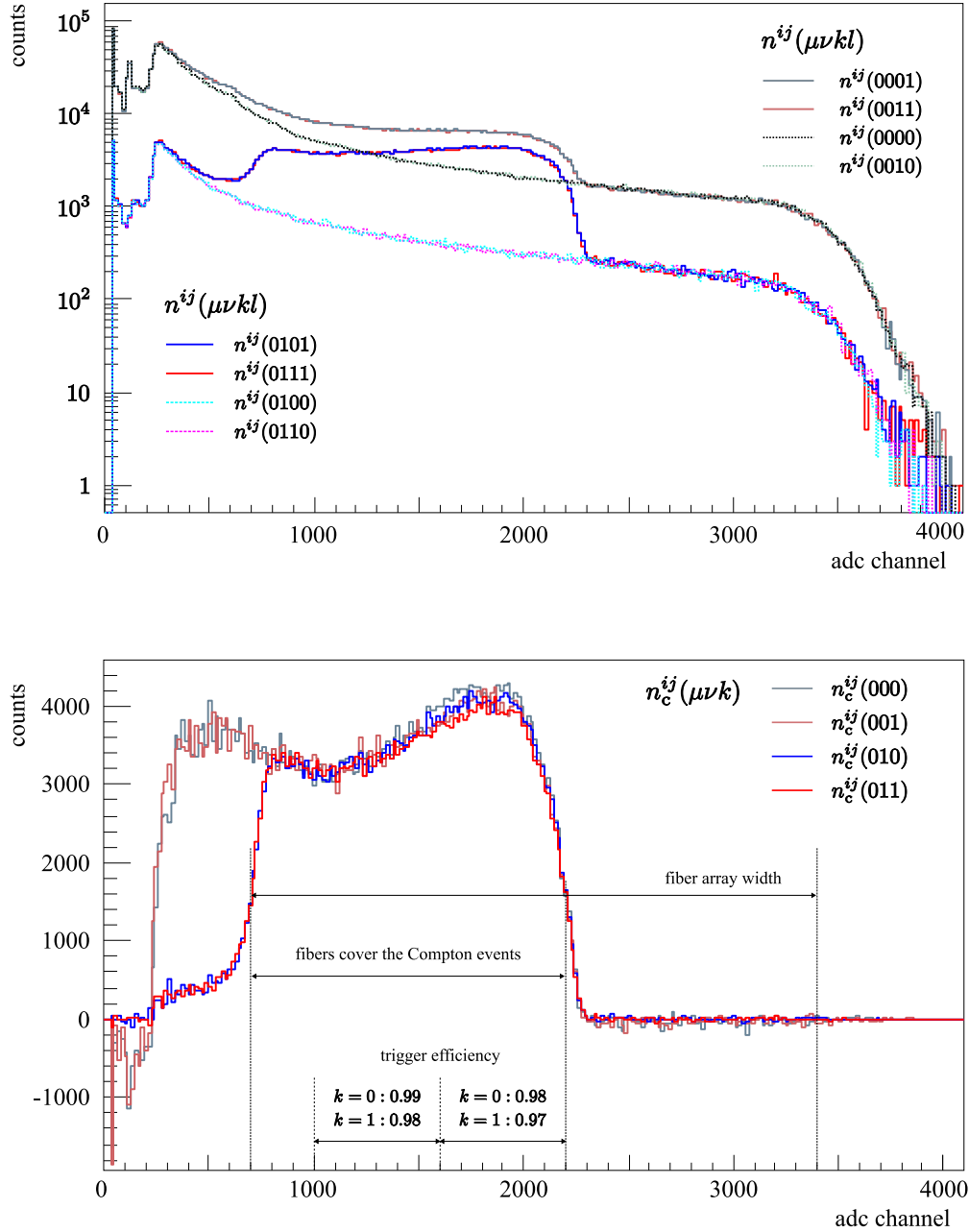


Figure 6.12 Photon detector spectra with different trigger conditions ($\nu = 0, 1$) and different spectrum measurements ($l = 0, 1$). The simple and direct subtraction is used to get the below plot. In the plots, $n^{ij}(\mu\nu kl)$ and $n_c^{ij}(\mu\nu k)$ are defined in (6.15) and (6.17) respectively. We merge 16 bins of the ADC channel in one bin for sake of graphical simplicity.

ADC channel		$R_c(\mu k)$		$R_{\delta c}(\mu k)$		$R_b(\mu k)$		$R_{\delta A}(\mu)$
from	to	(00)	(01)	(00)	(01)	(00)	(01)	(0)
1000	2000	0.98	0.98	0.67	0.67	0.14	0.14	0.68
735	2208	0.98	0.98	0.63	0.64	0.13	0.13	0.64
735	868	0.95	0.93	0.50	0.50	0.12	0.13	0.53
869	1002	0.99	0.99	0.56	0.56	0.12	0.13	0.56
1003	1136	0.99	1.00	0.59	0.59	0.13	0.14	0.59
1137	1270	1.00	0.99	0.62	0.62	0.14	0.13	0.61
1271	1404	0.98	0.98	0.65	0.64	0.14	0.14	0.65
1405	1538	0.98	0.98	0.67	0.68	0.14	0.14	0.68
1539	1672	0.98	0.96	0.70	0.70	0.14	0.15	0.71
1673	1806	0.96	0.96	0.72	0.72	0.15	0.14	0.74
1807	1940	0.98	0.98	0.73	0.74	0.14	0.15	0.75
1941	2074	0.98	0.97	0.74	0.74	0.15	0.15	0.75
2075	2208	0.95	0.99	0.69	0.70	0.15	0.15	0.70

Table 6.8 Trigger efficiencies. The ADC channel ranges are selected according to the fiber pairs with a rough approximation. $R_c(\mu k)$ is called Compton event ratio, $R_{\delta c}$ the Compton event error ratio, R_b the background ratio, and the asymmetry error ratio $R_{\delta A}$. The Compton events with the coincidence has only 2% less than the events without the coincidence in the range of 735 to 2208 ADC channel.

background is reduced by more than 80%. Thus the uncertainty of the Compton asymmetry decreases by about 30% and the number of the Compton photons is almost unchanged.

In figure 6.12, there is no significant difference between the measured Compton spectra of the two polarization states of the electron ($k = 0, 1$), because of statistical fluctuations. But, if several runs that have the same $\lambda/2$ plate state are combined by using the method described in section 6.3.3, it is significant that the one polarization state ($k = 0$) has larger Compton photon number than the other state ($k = 1$) does. We clearly see the difference in figure 6.13. And, table 6.9 shows that $R_c = 0.97$, $R_{\delta c} = 0.58$, $R_b = 0.15$, and $R_{\delta A} = 0.60$ in the range of 1000 to 2000. Therefore, when we use the number of the mean Compton events, the uncertainty of the mean Compton asymmetry decreases by about 40% and the number of the Compton photons remains intact.

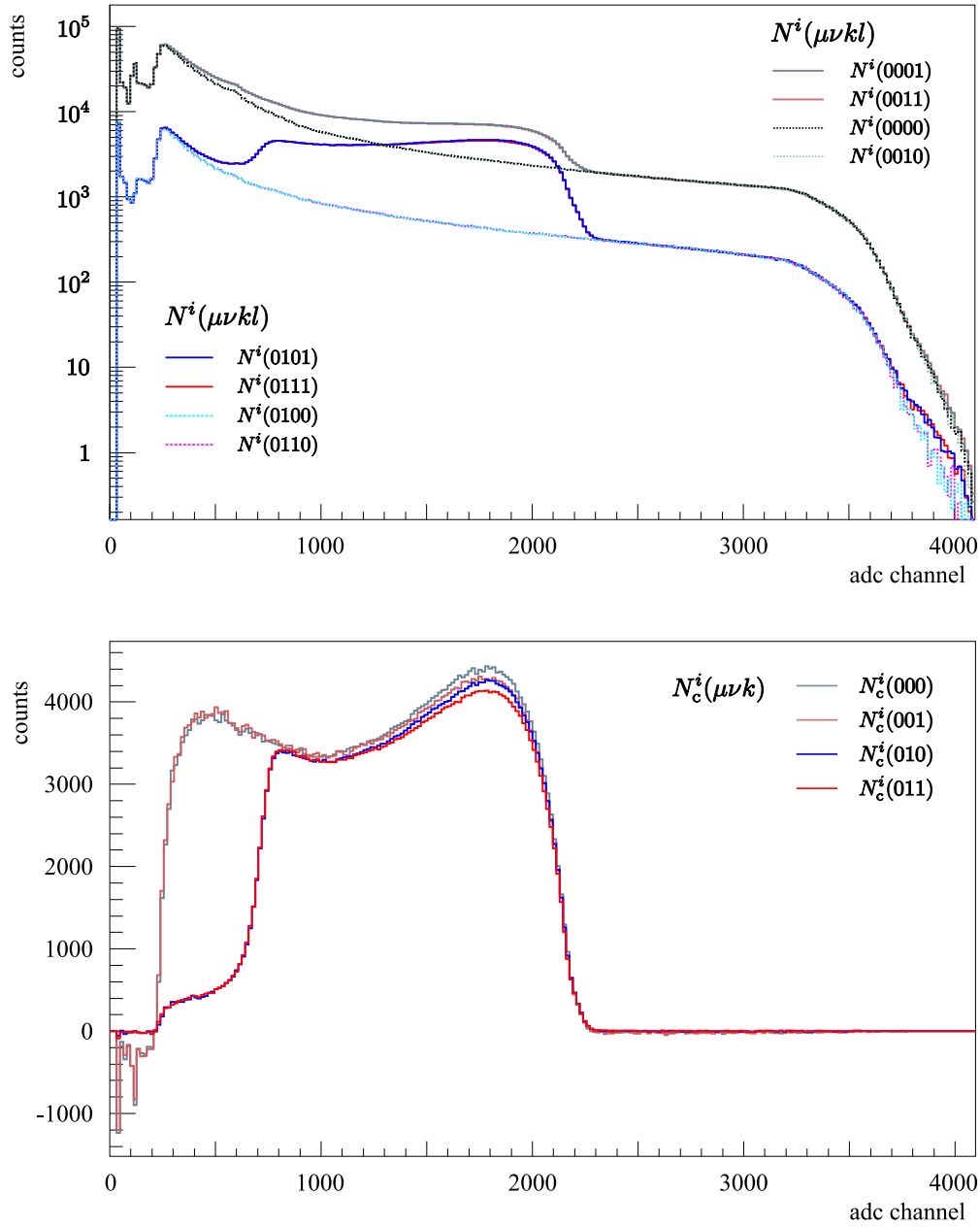


Figure 6.13 Average photon detector spectra with different trigger conditions ($\nu = 0, 1$) and different spectrum measurements ($l = 0, 1$). The simple and direct subtraction is used to get the below plot. In the plots, $N^i(\mu\nu kl)$ and $N_c^i(\mu\nu k)$ are defined in (6.21) and (6.23) respectively. We merge 16 bins of the ADC channel in one bin for sake of graphical simplicity.

ADC channel		$R_c(\mu k)$		$R_{\delta c}(\mu k)$		$R_b(\mu k)$		$R_{\delta A}(\mu)$
from	to	(00)	(01)	(00)	(01)	(00)	(01)	(0)
1000	2000	0.97	0.97	0.58	0.58	0.15	0.15	0.60
735	2208	0.97	0.97	0.55	0.55	0.15	0.15	0.57

Table 6.9 Average trigger efficiencies with $\lambda/2$ plate out. For simplicity, we presents only the first two ADC channel ranges, which are in table 6.8.

6.4.2 Experimental Compton Asymmetry

Figure 6.14 shows the experimental Compton asymmetries with two different $\lambda/2$ plate states ($\mu = 0, 1$) and with two trigger conditions ($\nu = 0, 1$) in the ADC channel range of 600 to 2200. For convenience, we call this ADC channel range the Compton range. As mentioned before, the theoretical Compton asymmetry changes its sign at ρ_γ and reaches the largest value at $\rho = 1$. In these plots, we easily notice that the experimental Compton asymmetry follows the theoretical asymmetry pattern, shown in figure 3.5, whether a $\lambda/2$ plate is inserted or not. It changes sign at about 1000 ADC channel and reaches the maximum value of the asymmetry at about 2000 ADC channel. And, we see that the error of the experimental Compton asymmetry with $\nu = 1$ is smaller than the error with $\nu = 0$ in the plots.

6.4.3 Electron Polarization Estimation

Before we study the detector response function, i.e. the photon detection efficiency and the energy calibration of the photon detector, we cannot determine the electron polarization and its error with accuracy. However, if we assume a perfect detection efficiency and use a naive energy calibration, we can estimate the electron polarization and the error of the electron polarization.

If we assume that the channel 2200 corresponds to $\rho = 1$ and the channel 114 does $\rho = 0$, the normalized energy ρ_i is expressed in terms of the ADC channel i as

$$\rho_i = \frac{k_f^i}{k_f^{\max}} = \frac{i - 114}{2200 - 114}, \quad (6.28)$$

where k_f^{\max} is the maximum energy of the backscattered photon and k_f^i is the backscattered photon energy of the ADC channel i . Thus, using (3.24), (6.11), and (6.12), we can calculate P_e^i and δP_e^i . Then, we can estimate the electron polarization $P_e(\mu\nu)$ and its error $\delta P_e(\mu\nu)$ using (6.13) and (6.14).

Table 6.10 shows the electron polarization and the error of the polarization with two different trigger conditions ($\nu = 0, 1$) and with two different $\lambda/2$ states ($\mu = 0, 1$). In the table, we use four different ADC channel ranges

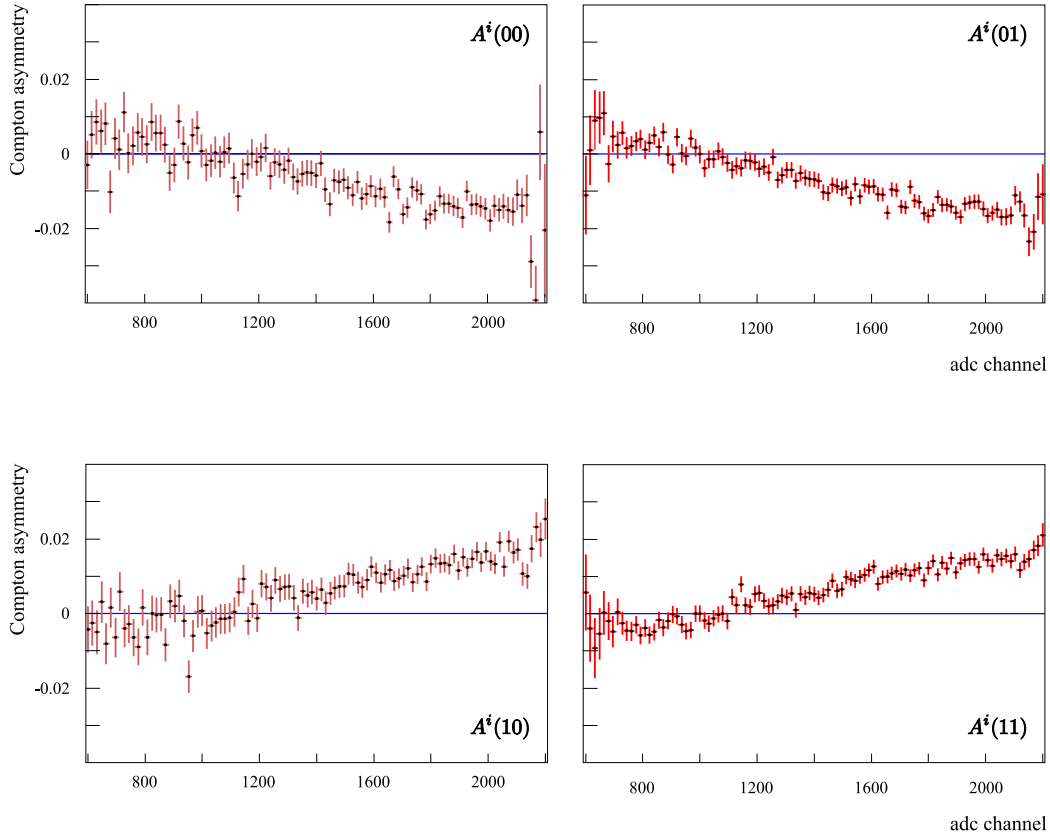


Figure 6.14 Compton asymmetries and their errors with two different $\lambda/2$ plate states within the Compton range. Here the asymmetries are calculated by using all available runs that were taken during the 2008 beam time. *Above left*, the Compton asymmetries without the coincidence and with a $\lambda/2$ plate out; *above right*, the asymmetries with the coincidence and the same plate state; *below left*, the asymmetries without the coincidence and with the $\lambda/2$ plate in; *below right*, the asymmetries with the coincidence and the plate in state. Data points represent asymmetries and the solid lines do the errors associated with the points. $A^i(\mu\nu)$ is defined in (6.25). Here, we merge 8 bins of the ADC channel in one bin.

$\lambda/2$ plate status	trigger condition		ADC channel range (<i>from</i> \rightarrow <i>to</i>)				
			<i>1400</i>	<i>1400</i>	<i>1400</i>	<i>1400</i>	<i>1400</i>
(μ)	(ν)		\downarrow	\downarrow	\downarrow	\downarrow	\downarrow
			<i>2000</i>	<i>1900</i>	<i>1800</i>	<i>1700</i>	<i>1600</i>
out	(1)	$P_e(01)$	0.632	0.665	0.695	0.710	0.732
	(1)	$\delta P_e(01)$	0.014	0.017	0.022	0.029	0.042
(0)	(0)	$P_e(00)$	0.613	0.636	0.660	0.671	0.723
	(0)	$\delta P_e(00)$	0.022	0.027	0.034	0.048	0.067
		$R_{\delta P_e}(0)$	0.64	0.64	0.63	0.60	0.62
in	(1)	$P_e(11)$	-0.584	-0.595	-0.617	-0.664	-0.735
	(1)	$\delta P_e(11)$	0.013	0.016	0.020	0.027	0.038
(1)	(0)	$P_e(10)$	-0.588	-0.592	-0.590	-0.631	-0.698
	(0)	$\delta P_e(10)$	0.020	0.025	0.032	0.043	0.062
		$R_{\delta P_e}(1)$	0.65	0.65	0.64	0.63	0.61

Table 6.10 The error ratio of the electron polarization with two different trigger conditions ($\nu = 0, 1$) and with two different $\lambda/2$ plate states ($\mu = 0, 1$). Because of statistical fluctuations, the estimated $P_e(\mu\nu)$ is larger than 100% in several bins of the ADC channel. Since more than 100% polarization has no physical meaning, we merge 16 bins of the ADC channel in one bin and exclude an electron polarization $P_e^i(\mu\nu)$ to calculate $P_e(\mu\nu)$ when $P_e^i(\mu\nu)$ has no physical meaning. Therefore, the channel range from *1400* to *2000* represents the range from *1393* to *2000* more precisely. In the calculations, the error ratio is rounded to two significant figures and the rounding is done at the end of the calculations to reduce the inaccuracies.

to estimate $P_e(\mu\nu)$ and $\delta P_e(\mu\nu)$. The electron polarization $P_e(01)$ changes from 63.2% to 73.2% with respect to the ADC channel range. However, if we use the ADC channel 2000 as $\rho = 1$, $P_e(01)$ changes from 52.5% to 54.4% with respect to the same ADC channel range. Thus, we cannot calculate the electron beam polarization correctly without a further study on the energy calibration and the detector response function of the photon detector.

Nevertheless, we introduce an error ratio $R_{\delta P_e}(\mu) = \delta P_e(\mu 1)/\delta P_e(\mu 0)$ so that we see how much the error of the electron polarization is reduced when we use the coincidence between the fiber detector and the photon detector in this preliminary result. They are shown as a bold type in table 6.10. Thus, when we use the coincidence ($\nu = 1$), the error of the electron beam polarization decreases by about 40 percent.

Further, we can estimate how much the parity violating (PV) asymmetry A_{phys}^{PV} will be changed using these electron polarizations, if we assume that the electron polarization is independent of an electron beam energy. Using the Møller polarimeter measurement and considering the systematic effect of applying the Møller measurement to A_{phys}^{PV} , the electron polarization P_e is 0.683 ± 0.040 . With this electron polarization, A_{phys}^{PV} at the backward angles is (-17.41 ± 1.18) ppm. Note that this recent PV asymmetry is different with the preliminary PV asymmetry at the backward angles, shown in (2.43).

From table 6.10, we choose the electron polarizations with $\mu = 0$ and $\nu = 0, 1$ in the column of the ADC range of 1400 to 1800. When we use $P_e = 0.660 \pm 0.034$ ($\mu = 0, \nu = 0$), the PV asymmetry is (-18.01 ± 1.16) ppm. And if we use $P_e = 0.695 \pm 0.022$ ($\mu = 0, \nu = 1$), the PV asymmetry is (-17.11 ± 1.00) ppm. Therefore, in this preliminary result, the error of the PV asymmetry decreases two percent if we use only the photon detector, i.e. $\nu = 0$, during the electron polarization measurement. And when we use the coincidence, $\nu = 1$, between the scintillating fiber detector and the photon detector, the error of the PV asymmetry is reduced by around 15 percent.

Since the photon spectra that were measured during only two days are used to calculate the electron polarization, there may be room for error reduction in the electron beam polarization and in the PV asymmetry.

Chapter 7

Summary and Outlook

In this thesis, we have succeeded in developing the A4 Compton backscattering polarimeter chicane that provides the Compton interaction region. The chicane is also the beam transport line that is able to deliver successfully the electron beam to a target for the parity violation experimental program. After studying the properties of the chicane components, we have developed the electron beam control system, which is quick, easy to use, and reliable, that makes an overlap between the electron beam and the laser beam. Using the system, we can achieve that the beam crossing point is as close to the Compton interaction region as possible and that the crossing angle is less than 0.5 mrad. They guarantees to achieve the high luminosity of the A4 Compton backscattering polarimeter in the cost-effective method.

Further, we have developed the scintillating fiber electron detector in order to minimize the statistical error in the polarization measurement. We have clearly seen that the background is reduced by about 80 percent and the Compton spectrum remains intact when we use the coincidence between the complete redesigned scintillating fiber detector and the photon detector. The statistical error of the Compton asymmetry with the coincidence is reduced by about 40 percent if it is compared with the asymmetry error without the coincidence. As a result, the error of the electron beam polarization decreases by about 40 percent. They are the significant progress in measuring a degree of polarization of the electron beam.

Moreover, for future improvements of the Compton backscattering polarimeter, we suggest that a beam monitoring system, which can determine the beam positions, directions, and emittances, to install at the beginning, the center, and the end of the chicane. The more precise beam monitoring system will help understand a luminosity of the Compton polarimeter in detail. And, we suggest a precise study of the beam control system that contains especially the dipole magnets, their shunts, and the quadrupole magnets ac-

ording to a beam transport line of a whole accelerator beam line. Finally, which background sources, that are visible in the photon spectra, contribute to signals of the fiber electron detector remain hitherto unknown. This may have to be taken into account using a Monte Carlo simulation.

The development of the chicane and the electron detector are parts of the A4 Compton backscattering polarimeter and they are strongly connected with the other parts, which are the laser optics system, the photon detector, the Stokes meter, and the data analysis of the Compton asymmetry measurement. The vibrant development of the other parts or, more precisely, the new Stokes meter and the data analysis of the photon detector with a Monte Carlo detector simulation are in progress. We will soon achieve the electron beam polarization measurement with accuracy. At the same time, the A4 Compton backscattering polarimeter will be a non-destructive online monitoring tool for the beam polarization. This promising result may reduce the error in the parity violating asymmetry and provide an opportunity for studying the strangeness contributions to the structure of the nucleon with a high degree of accuracy.

Bibliography

- [1] **A4** Collaboration, F. E. Maas *et al.*, “Measurement of strange quark contributions to the nucleon’s form factors at $Q^2 = 0.230 \text{ (GeV/c)}^2$,” *Phys. Rev. Lett.* **93** (2004) 022002, `nucl-ex/0401019`.
- [2] **A4** Collaboration, F. E. Maas *et al.*, “Evidence for strange quark contributions to the nucleon’s form factors at $Q^2 = 0.108 \text{ (GeV/c)}^2$,” *Phys. Rev. Lett.* **94** (2005) 152001, `nucl-ex/0412030`.
- [3] **A4** Collaboration, F. E. Maas *et al.*, “Measurement of the transverse beam spin asymmetry in elastic electron proton scattering and the inelastic contribution to the imaginary part of the two-photon exchange amplitude,” *Phys. Rev. Lett.* **94** (2005) 082001, `nucl-ex/0410013`.
- [4] **Gargamelle Neutrino** Collaboration, F. J. Hasert *et al.*, “Observation of neutrino-like interactions without muon or electron in the Gargamelle neutrino experiment,” *Phys. Lett.* **B46** (1973) 138–140.
- [5] P. Q. Hung and J. J. Sakurai, “Tests of the Single Z Boson Hypothesis in Neutral Current Processes,” *Phys. Lett.* **B69** (1977) 323.
- [6] P. Q. Hung and J. J. Sakurai, “The structure of neutral currents,” *Ann. Rev. Nucl. Part. Sci.* **31** (1981) 375–438.
- [7] C. Y. Prescott, “Parity violation in electron scattering,”. Published in the International School on Electron and Pion Interactions with Nuclei at Intermediate Energies Electron and Pion Interactions with Nuclei at Intermediate Energies, Rome, Italy, 18-29 Jun 1979, SLAC-PUB-3506.
- [8] J. D. Bjorken, “Model-independent remarks on electron-quark parity-violating neutral-current couplings,” *Phys. Rev. D* **18** (Nov, 1978) 3239–3243.

- [9] C. Y. Prescott *et al.*, “Parity non-conservation in inelastic electron scattering,” *Phys. Lett.* **B77** (1978) 347–352.
- [10] C. Y. Prescott *et al.*, “Further Measurements of Parity Nonconservation in Inelastic electron Scattering,” *Phys. Lett.* **B84** (1979) 524.
- [11] W. Heil *et al.*, “Improved limits on the weak, neutral, hadronic axial vector coupling constants from quasielastic scattering of polarized electrons,” *Nucl. Phys.* **B327** (1989) 1–31.
- [12] P. A. Souder *et al.*, “Measurement of parity violation in the elastic scattering of polarized electrons from ^{12}C ,” *Phys. Rev. Lett.* **65** (Aug, 1990) 694–697.
- [13] D. H. Perkins, *Introduction to high energy physics*. Cambridge University Press, 2000.
- [14] D. H. Beck and B. R. Holstein, “Nucleon structure and parity-violating electron scattering,” *Int. J. Mod. Phys.* **E10** (2001) 1–41, [hep-ph/0102053](#).
- [15] W. S. C. Williams, *Nuclear and Particle Physics*. Clarendon Press, Oxford, 1994.
- [16] **CCFR** Collaboration, A. O. Bazarko *et al.*, “Determination of the strange quark content of the nucleon from a next-to-leading order QCD analysis of neutrino charm production,” *Z. Phys.* **C65** (1995) 189–198, [hep-ex/9406007](#).
- [17] D. H. Beck and R. D. McKeown, “Parity-violating electron scattering and nucleon structure,” *Ann. Rev. Nucl. Part. Sci.* **51** (2001) 189–217, [hep-ph/0102334](#).
- [18] **NuTeV** Collaboration, T. Adams *et al.*, “Strange content of the nucleon (NuTeV),” [hep-ex/9906038](#).
- [19] **NuTeV** Collaboration, D. Mason *et al.*, “Measurement of the Nucleon Strange-Antistrange Asymmetry at Next-to-Leading Order in QCD from NuTeV Dimuon Data,” *Physical Review Letters* **99** (2007), no. 19, 192001.
- [20] T. P. Cheng, “The Zweig Rule and the pi n Sigma Term,” *Phys. Rev.* **D13** (1976) 2161.

- [21] T. P. Cheng, “Chiral Symmetry and the Higgs Nucleon Coupling,” *Phys. Rev.* **D38** (1988) 2869.
- [22] T. P. Cheng and R. Dashen, “Is $SU(2) \otimes SU(2)$ a Better Symmetry than $SU(3)$?,” *Phys. Rev. Lett.* **26** (Mar, 1971) 594–597.
- [23] R. Koch, “A New Determination of the πN Sigma Term Using Hyperbolic Dispersion Relations in the (ν^2, t) Plane,” *Z. Phys.* **C15** (1982) 161–168.
- [24] A. W. Thomas and W. Weise, *The Structure of the Nucleon*. Wiley-Vch verlag, 2001.
- [25] J. F. Donoghue and C. R. Nappi, “The Quark Content of the Proton,” *Phys. Lett.* **B168** (1986) 105.
- [26] J. Gasser, H. Leutwyler, and M. E. Sainio, “Form-factor of the sigma term,” *Phys. Lett.* **B253** (1991) 260–264.
- [27] J. Gasser, H. Leutwyler, and M. E. Sainio, “Sigma term update,” *Phys. Lett.* **B253** (1991) 252–259.
- [28] X.-D. Ji, “A QCD analysis of the mass structure of the nucleon,” *Phys. Rev. Lett.* **74** (1995) 1071–1074, hep-ph/9410274.
- [29] M. M. Pavan, , *et al.*, “The pion nucleon Sigma term is definitely large: Results from a GWU analysis of πN scattering data,” *PiN Newslett.* **16** (2002) 110–115, hep-ph/0111066.
- [30] J. Ellis and R. Jaffe, “Sum rule for deep-inelastic electroproduction from polarized protons,” *Phys. Rev. D* **9** (Mar, 1974) 1444–1446.
- [31] **European Muon** Collaboration, J. Ashman *et al.*, “A measurement of the spin asymmetry and determination of the structure function g_1 in deep inelastic muon proton scattering,” *Phys. Lett.* **B206** (1988) 364.
- [32] **European Muon** Collaboration, J. Ashman *et al.*, “An investigation of the spin structure of the proton in deep inelastic scattering of polarized muons on polarized protons,” *Nucl. Phys.* **B328** (1989) 1.
- [33] **E143** Collaboration, K. Abe *et al.*, “Precision measurement of the proton spin structure function $g_1(p)$,” *Phys. Rev. Lett.* **74** (1995) 346–350.

- [34] **Spin Muon (SMC) Collaboration**, D. Adams *et al.*, “Spin structure of the proton from polarized inclusive deep-inelastic muon proton scattering,” *Phys. Rev.* **D56** (1997) 5330–5358, [hep-ex/9702005](#).
- [35] **COMPASS Collaboration**, V. Y. Alexakhin *et al.*, “The Deuteron Spin-dependent Structure Function g_1^d and its First Moment,” *Phys. Lett.* **B647** (2007) 8–17, [hep-ex/0609038](#).
- [36] D. B. Kaplan and A. Manohar, “Strange Matrix Elements in the Proton from Neutral Current Experiments,” *Nucl. Phys.* **B310** (1988) 527.
- [37] R. D. Mckeown, “Sensitivity of Polarized Elastic electron Proton Scattering to the Anomalous Baryon Number Magnetic Moment,” *Phys. Lett.* **B219** (1989) 140–142.
- [38] D. H. Beck, “Strange-quark vector currents and parity-violating electron scattering from the nucleon and from nuclei,” *Phys. Rev. D* **39** (Jun, 1989) 3248–3256.
- [39] J. Arvieux *et al.*, “Electromagnetic radiative corrections in parity-violating electron proton scattering,” *Eur. Phys. J.* **A26** (2005) 429–439, [hep-ph/0511229](#).
- [40] M. J. Musolf, “Electroweak radiative corrections, renormalization and neutral current parity violation,”. Invited talk given at Caltech Workshop on Parity Violation in Electron Scattering, Pasadena, CA, Feb 1990.
- [41] M. J. Musolf *et al.*, “Intermediate-energy semileptonic probes of the hadronic neutral current,” *Phys. Rept.* **239** (1994) 1–178.
- [42] W. M. Alberico, S. M. Bilenky, and C. Maieron, “Strangeness in the nucleon: Neutrino nucleon and polarized electron nucleon scattering,” *Phys. Rept.* **358** (2002) 227–308, [hep-ph/0102269](#).
- [43] K. S. Kumar and P. A. Souder, “Strange quarks and parity violation,” *Prog. Part. Nucl. Phys.* **45** (2000) S333–S395.
- [44] **SAMPLE Collaboration**, B. Mueller *et al.*, “Measurement of the proton’s neutral weak magnetic form factor,” *Phys. Rev. Lett.* **78** (1997) 3824–3827, [nucl-ex/9702004](#).

- [45] **SAMPLE** Collaboration, D. T. Spayde *et al.*, “Parity violation in elastic electron proton scattering and the proton’s strange magnetic form-factor,” *Phys. Rev. Lett.* **84** (2000) 1106–1109, nucl-ex/9909010.
- [46] **SAMPLE** Collaboration, R. Hasty *et al.*, “Strange magnetism and the anapole structure of the proton,” *Science* **290** (2000) 2117, nucl-ex/0102001.
- [47] S.-L. Zhu, S. J. Puglia, B. R. Holstein, and M. J. Ramsey-Musolf, “The nucleon anapole moment and parity-violating e p scattering,” *Phys. Rev.* **D62** (2000) 033008, hep-ph/0002252.
- [48] M. J. Ramsey-Musolf, “Parity-Violating Electron Scattering: How Strange a Future,” nucl-th/0302049.
- [49] R. D. McKeown and M. J. Ramsey-Musolf, “The nucleon’s mirror image: Revealing the strange and unexpected,” *Mod. Phys. Lett.* **A18** (2003) 75–84, hep-ph/0203011.
- [50] **SAMPLE** Collaboration, T. M. Ito *et al.*, “Parity-violating electron deuteron scattering and the proton’s neutral weak axial vector form factor,” *Phys. Rev. Lett.* **92** (2004) 102003, nucl-ex/0310001.
- [51] **SAMPLE** Collaboration, D. T. Spayde *et al.*, “The strange quark contribution to the proton’s magnetic moment,” *Phys. Lett.* **B583** (2004) 79–86, nucl-ex/0312016.
- [52] E. J. Beise, M. L. Pitt, and D. T. Spayde, “The SAMPLE experiment and weak nucleon structure,” *Prog. Part. Nucl. Phys.* **54** (2005) 289–350, nucl-ex/0412054.
- [53] **HAPPEX** Collaboration, K. A. Aniol *et al.*, “Measurement of the neutral weak form factors of the proton,” *Phys. Rev. Lett.* **82** (1999) 1096–1100, nucl-ex/9810012.
- [54] **HAPPEX** Collaboration, K. A. Aniol *et al.*, “New measurement of parity violation in elastic electron proton scattering and implications for strange form factors,” *Phys. Lett.* **B509** (2001) 211–216, nucl-ex/0006002.
- [55] **HAPPEX** Collaboration, K. A. Aniol *et al.*, “Parity-violating electroweak asymmetry in $\vec{e}p$ scattering,” *Phys. Rev.* **C69** (2004) 065501, nucl-ex/0402004.

- [56] **HAPPEX** Collaboration, K. A. Aniol *et al.*, “Parity-violating electron scattering from ^4He and the strange electric form factor of the nucleon,” *Phys. Rev. Lett.* **96** (2006) 022003, nucl-ex/0506010.
- [57] **HAPPEX** Collaboration, K. A. Aniol *et al.*, “Constraints on the nucleon strange form factors at $Q^2 \sim 0.1\text{GeV}^2$,” *Phys. Lett.* **B635** (2006) 275–279, nucl-ex/0506011.
- [58] **HAPPEX** Collaboration, A. Acha *et al.*, “Precision Measurements of the Nucleon Strange Form Factors at $Q^2 \sim 0.1\text{GeV}^2$,” *Phys. Rev. Lett.* **98** (2007) 032301, nucl-ex/0609002.
- [59] D. S. Armstrong, “New results from the HAPPEX experiments at $Q^2 = 0.1\text{GeV}/c^2$,” *Eur. Phys. J.* **A32** (2007) 451–455.
- [60] J. Arvieux, “Parity violation experiments at Jefferson Laboratory: HAPPEX and G0,” *Prog. Part. Nucl. Phys.* **55** (2005) 297–307.
- [61] S. Kox, “The G0 backangle measurements,” *Eur. Phys. J.* **A32** (2007) 469–472.
- [62] J. S. Real, “Results from the forward G0 experiment: Strange quark contribution to the nucleon structure,” *Eur. Phys. J.* **A32** (2007) 463–468.
- [63] **G0** Collaboration, D. S. Armstrong *et al.*, “Strange quark contributions to parity-violating asymmetries in the forward G0 electron proton scattering experiment,” *Phys. Rev. Lett.* **95** (2005) 092001, nucl-ex/0506021.
- [64] T. Hammel, *Luminositätsmessung und Korrektur helizitätskorrelierter Effekte für ein Experiment zur Messung der Paritätsverletzung in der elastischen Elektronenstreuung*. PhD thesis, Johannes Gutenberg-Universität Mainz, Institut für Kernphysik, October, 2003.
- [65] S. Baunack, *Einzelspin-Asymmetrien in der elastischen Elektron-Proton-Streuung und die Beiträge der Strange-Quarks zu den Formfaktoren des Nukleons*. PhD thesis, Johannes Gutenberg-Universität Mainz, Institut für Kernphysik, August, 2005.
- [66] I. Altarev *et al.*, “A high power liquid hydrogen target for the Mainz A4 parity violation experiment,” *Nucl. Instrum. Meth.* **A564** (2006) 13–25, nucl-ex/0504024.

- [67] T. Hammel *et al.*, “A luminosity monitor for the A4 parity violation experiment at MAMI,” *Nucl. Instrum. Meth.* **A564** (2006) 1–12, nucl-ex/0504017.
- [68] P. Achenbach, *Aufbau eines Bleifluorid-Kalorimeters zur Messung der Paritätsverletzung in der elastischen Elektronenstreuung*. PhD thesis, Johannes Gutenberg-Universität Mainz, Institut für Kernphysik, January, 2001.
- [69] K. Grimm, *Aufbau eines Lichtauslesesystems für ein Bleifluorid-Kalorimeter zur Messung der Paritätsverletzung in der elastischen Elektronenstreuung*. PhD thesis, Johannes Gutenberg-Universität Mainz, Institut für Kernphysik, February, 2002.
- [70] P. Achenbach *et al.*, “Radiation resistance and optical properties of lead fluoride Cherenkov crystals,” *Nucl. Instrum. Meth.* **A416** (1998) 357–363.
- [71] R. Kothe, *Aufbau und Betrieb einer schnellen Kalorimerelektronik für ein Experiment zur Messung der Paritätsverletzung in der elastischen Elektronenstreuung*. PhD thesis, Johannes Gutenberg-Universität Mainz, Institut für Kernphysik, January, 2008.
- [72] L. Capozza, *Investigations on the response of the A4 calorimeter in the region $\Delta(1232)$ resonance using Monte Carlo simulations*. Diplomarbeit, Johannes Gutenberg-Universität Mainz, Institut für Kernphysik, October, 2004.
- [73] **A4** Collaboration, C. Weinrich, “The transmission Compton polarimeter of the A4 experiment,” *Eur. Phys. J.* **A24S2** (2005) 129–130.
- [74] C. Weinrich, *Entwicklung eines Transmissions-Compton-Polarimeters für das A4-Experiment*. Diplomarbeit, Johannes Gutenberg-Universität Mainz, Institut für Kernphysik, July, 2000.
- [75] V. Tioukine and K. Aulenbacher, “Operation of the MAMI accelerator with a Wien filter based spin rotation system,” *Nucl. Instrum. Meth.* **A568** (2006) 537–542.
- [76] C. Weinrich, “The A4 Transmission Compton Polarimeter,”. Poster given at Workshop, PESP 2004, Mainz, Germany, October 7-9, 2004.

- [77] H. Weigel *et al.*, “On the strange vector form-factors of the nucleon in the NJL soliton model,” *Phys. Lett.* **B353** (1995) 20–26, hep-ph/9503241.
- [78] B. Gläser, *Entwicklung und Realisierung eines experimentellen Aufbaus für die Messung der paritätsverletzenden Asymmetrie in Elektron-Proton-Streuung unter Rückwärtswinkeln*. Diplomarbeit, Johannes Gutenberg-Universität Mainz, Institut für Kernphysik, August, 2005.
- [79] **A4** Collaboration, B. Glaser, “Redesign of the A4 calorimeter for the measurement at backward angles,” *Eur. Phys. J.* **A24S2** (2005) 141.
- [80] B. Glaser. PhD thesis, Johannes Gutenberg-Universität Mainz, Institut für Kernphysik, (in preparation).
- [81] L. Capozza. PhD thesis, Johannes Gutenberg-Universität Mainz, Institut für Kernphysik, (in preparation).
- [82] S. Baunack, “The parity violation A4 experiment at forward and backward angles,” *Eur. Phys. J.* **A32** (2007) 457–461.
- [83] L. Capozza, “Transverse single spin asymmetry at the A4 experiment: Preliminary backward-scattering results,” *Eur. Phys. J.* **A32** (2007) 497–499.
- [84] D. Balaguer Ríos, *Measurement of the asymmetry in the cross section of the quasielastic scattering of transversely polarized electrons off deuterium*. Diplomarbeit, Johannes Gutenberg-Universität Mainz, Institut für Kernphysik, April, 2008.
- [85] **A4** Collaboration, F. E. Maas, “The Mainz A4 parity violation experiment (single spin asymmetries in elastic scattering),” *Prog. Part. Nucl. Phys.* **55** (2005) 320–331.
- [86] **A4** Collaboration, S. Baunack, “Single spin asymmetries from the Mainz A4 experiment,” *Nucl. Phys.* **A755** (2005) 249–252.
- [87] **A4** Collaboration, S. Baunack, “Transverse spin asymmetry at the A4 experiment,” *Eur. Phys. J.* **A24S2** (2005) 35–38.
- [88] A. H. Compton, “A Quantum Theory of the Scattering of X-rays by Light Elements,” *Phys. Rev.* **21** (May, 1923) 483–502.

- [89] C. Y. Prescott, “Spin Dependent Compton Scattering for Use in Analyzing Electron Beam Polarizations,”. SLAC-TN-73-001.
- [90] H. Frauenfelder and E. M. Henley, *Subatomic Physics*. Prentice Hall, second ed., 1991.
- [91] G. Bardin *et al.*, “Conceptual Design Report of a Compton Polarimeter for CEBAF Hall A,”. Internal report DAPNIA-SPhN-96-14.
- [92] Y. Imai, “Progress report on the A4 Compton backscattering polarimeter,” *Eur. Phys. J.* **A24S2** (2005) 127–128.
- [93] Y. Imai, *Entwicklung eines optischen Systems für ein Compton-Rückstreupolarimeter*. Diplomarbeit, Johannes Gutenberg-Universität Mainz, Institut für Kernphysik, February, 2003. Chapter 3.
- [94] J. P. Jorda *et al.*, “A Fabry-Perot cavity for Compton polarimetry,” *Nucl. Instrum. Meth.* **A412** (1998) 1–18.
- [95] **HAPPEX** Collaboration, N. Falletto *et al.*, “Compton scattering off polarized electrons with a high finesse Fabry-Perot cavity at JLab,” *Nucl. Instrum. Meth.* **A459** (2001) 412–425.
- [96] J. Diefenbach, Y. Imai, J. Han Lee, F. Maas, and S. Taylor, “Laser Compton polarimetry at JLab and MAMI,” *Eur. Phys. J.* **A32** (2007) 555–559.
- [97] Y. Imai, “The Compton backscattering polarimeter of the A4 experiment,” *Prog. Part. Nucl. Phys.* **55** (2005) 332–335.
- [98] Y. Imai, “The optical system of the A4 laser Compton polarimeter,”. Proceedings of From Parity Violation to Hadronic Structure and more ... (PAVI2006), Milos, Greece 2006, 269-72.
- [99] Y. Imai. PhD thesis, Johannes Gutenberg-Universität Mainz, Institut für Kernphysik, (in preparation).
- [100] J. Diefenbach, *Aufbau einer elektronischen Stabilisierung für das A4-Compton-Polarimeter*. Diplomarbeit, Johannes Gutenberg-Universität Mainz, Institut für Kernphysik, February, 2003.

- [101] J. Diefenbach, "Stabilization system of the laser system of the A4 Compton backscattering polarimeter," *Eur. Phys. J.* **A24S2** (2005) 131.
- [102] M. C. Mora Espí, *Development of a new photon detector for the A4-Compton backscattering polarimeter at MAMI*. Diplomarbeit, Johannes Gutenberg-Universität Mainz, Institut für Kernphysik, August, 2007.
- [103] D. C. Carey, *The Optics of Charged Particle Beams*. Harwood Academic Publishers, 1992.
- [104] H. Wiedemann, *Particle Accelerator Physics I: Basic Principles and Linear Beam Dynamics*. Springer-Verlag, 1999.
- [105] J. B. Rosenzweig, *Fundamentals of Beam Physics*. Oxford University Press, 2003.
- [106] M. Della Negra, "Multiple Coulomb Scattering of Beam Particles in the Phase Space Ellipse Formalism,". SLAC-TN-71-001.
- [107] M. Sands, "The Physics of Electron Storage Rings: An Introduction,". SLAC-R-121.
- [108] K. Potter, "Beam Profiles,". In *Gif-sur-yvette 1984, Proceedings, General Accelerator Physics, Vol. 1*, 301-317.
- [109] J. Rossbach and P. Schmueser, "Basic course on accelerator optics,". In *Jyvaeskylae 1992, Proceedings, General accelerator physics, vol. 1* 17-88. CERN Geneva - CERN-94-01 (94/01,rec.Mar.) 17-88.
- [110] **MAMI B1** Collaboration, "MAMI main parameters." <http://www.kph.uni-mainz.de/B1/>.
- [111] M. Minty and F. Zimmermann, *Measurement and Control of Charged Particle Beams*. Springer-Verlag, 2003.
- [112] D. C. Carey *et al.*, "Third order TRANSPORT with MAD input: A Computer Program for Designing Charged Particle Beam Transport Systems,". SLAC-R-0530, FERMILAB-PUB-98-310.
- [113] H. Wiedemann, *Synchrotron Radiation*. Springer-Verlag, 2003.
- [114] A. Septier, *Focusing of Charged Particles*, vol. II. Academic Press New York, 1967. 203-264.

- [115] H. Enge, "Quadrupole Engineering Data." Industiral Coils, Inc, Birch Street, Middleton, Massachusetts 01949, USA.
- [116] J. Müller and K.-H. Kaiser. private communication.
- [117] P. J. Bryant, "Beam transfer lines," In *Jyvaeskylae 1992, Proceedings, General accelerator physics, vol. 1* 219-238. CERN Geneva - CERN-94-01 (94/01,rec.Mar.) 219-238.
- [118] W. Ketter, *Entwurf zum Bau eines optischen Resonators für ein Comptonrückstreupolarimeter*. Diplomarbeit, Johannes Gutenberg-Universität Mainz, Institut für Kernphysik, December, 1998.
- [119] A. Kelley and I. Pohl, *A Book on C: Programming in C*. Addison-Wesley Professional, fourth ed., 1997.
- [120] R. Brun *et al.*, "ROOT-An Object Oriented Data Analysis Framework," *Proceedings AIHENP* **96** (1997) 81–86.
- [121] W. H. Press *et al.*, *Numerical Recipes in C: the art of scientific computing*. Cambridge University Press, New York, NY, USA, 1988.
- [122] J. R. Taylor, *An Introduction to Error Analysis*. University Science Books, 1997.
- [123] E. M. Puch and G. H. Wilslow, *The Analysis of Physical Measurements*. Addison-Wesley, 1966.
- [124] P. R. Bevington and D. K. Robinson, *Data Reduction and Error Analysis for the Physical Sciences*. McGraw-Hill Higher Education, 2003.
- [125] L. Lyons, *Statistics for Nuclear and Particle Physicists*. Cambridge University Press, 1986.
- [126] G. E. P. Box *et al.*, *Statistics for Experimenters*. John Wiley & Sons, Inc, 1978.
- [127] D. C. Montgomery, *Introduction to Linear Regression Analysis*. John Wiley & Sons, Inc, 2001.
- [128] N. R. Draper, *Applied Regression Analysis*. John Wiley & Sons, Inc, 1981.

- [129] D. C. Carey, “Functional dependence, broad-band fitting, and ancillary conditions,”. To be published in the proceedings of International Computational Accelerator Physics Conference (ICAP 98), Monterey, CA, 14-18 Sep 1998.
- [130] R. C. Ruchti, “The use of scintillating fibers for charged-particle tracking,” *Ann. Rev. Nucl. Part. Sci.* **46** (1996) 281–319.
- [131] **K2K** Collaboration, A. Suzuki *et al.*, “Design, construction, and operation of SciFi tracking detector for K2K experiment,” *Nucl. Instrum. Meth.* **A453** (2000) 165–176, hep-ex/0004024.
- [132] M. Berger *et al.*, *ESTAR, PSTAR, and ASTAR: Computer Programs for Calculating Stopping-Power and Range Tables for Electrons, Protons, and Helium Ions (version 1.2.3)*. National Institute of Standards and Technology, Gaithersburg, MD, 2005.
<http://physics.nist.gov/Star>.
- [133] *Kuraray Technical Information, Scintillation Materials, Kuraray Co., Ltd.* Nihonbashi, Chou-ku, Tokyo 103-8254, Japan.
- [134] C. A. Ayerbe Gayoso, *Development of a fibre detector for a kaon spectrometer at MAMI*. Diplomarbeit, Johannes Gutenberg-Universität Mainz, Institut für Kernphysik, April, 2004.
- [135] *BC-620 Reflector Paint for Plastic Scintillators Product Data Sheet, Saint-Gobain Crystals*. P.O. Box 3093, 3670 DB Soest, The Netherlands.
- [136] *HAMAMATSU Photomultiplier Tube Assembly H7546A, H7546B data sheet*. 315-5, Shimokanzo, Toyooka-village, Iwata-gun, Shizuoka-ken, 438-0193, Japan, 2002.
- [137] D. Gale and L. S. Shapley, “College Admissions and the Stability of Marriage,” *Am. Math. Monthly* **69** (1962) 9–15.
- [138] R. Sedgewick, *Algorithms in C*. Addison-Wesley, 1990.
- [139] É. Tardos and J. Kleinberg, *Algorithm Design*. Pearson/Addison-Wesley, 2006.
- [140] *Torr Seal Specifications, Varian Vacuum Technologies*. 121 Hartwell Avenue, Lexington, MA 02173-3133, USA.
- [141] C. A. May and Y. Tanaka, *Epoxy Resins*. Marcel Dekker, Inc., 1973.

- [142] J. Diefenbach. PhD thesis, Johannes Gutenberg-Universität Mainz, Institut für Kernphysik, (in preparation).
- [143] J. D. Jackson, *Classical Electrodynamics*. John Wiley & Sons, Inc, third ed., 1998.
- [144] G. F. Knoll, *Radiation Detection and Measurement*. John Wiley & Sons, Inc, second ed., 1989.
- [145] A. Hofmann, “Characteristics of Synchrotron Radiation,”. Lecture given at CERN Accelerator School on Synchrotron Radiation, Chester, England, Apr 6-13, 1989.
- [146] A. Thompson *et al.*, *X-Ray Data Booklet*. Lawrence Berkeley National Laboratory, 2001. <http://xdb.lbl.gov>.
- [147] M. Galassi *et al.*, *GNU Scientific Library: Reference Manual*. Network Theory Ltd., Bristol, UK, revised second ed., 2006.
- [148] J. Hubbel and S. Seltzer, *Tables of X-Ray Mass Attenuation Coefficients and Mass Energy-Absorption Coefficients (version 1.4)*. National Institute of Standards and Technology, Gaithersburg, MD, 2006. <http://physics.nist.gov/xaamdi>.
- [149] C. Chantler *et al.*, *X-Ray Form Factor, Attenuation and Scattering Tables (version 2.1)*. National Institute of Standards and Technology, Gaithersburg, MD, 2006. <http://physics.nist.gov/ffast>.
- [150] M. Berger *et al.*, *XCOM: Photon Cross Sections Database (version 1.3)*. National Institute of Standards and Technology, Gaithersburg, MD, 2005. <http://physics.nist.gov/xcom>.
- [151] *Dichtomatik O-Ring Handbook, Dichtomatik North America*. 47620 East Anchor Court, Plymouth, MI 48170, USA.

Appendix A

Synchrotron Radiation

As we have mentioned in section 4.3, the four dipole magnets, which define the geometry of the A4 Compton polarimeter chicane, are sources of synchrotron radiation when an electron beam is bent inside them. We therefore should study the amount of energy loss of the electron and see if this has an effect upon the A4 experiment. Furthermore, we should verify if the synchrotron radiation could contribute to background of the photon detector. In this section, we assume perfect vacuum conditions in the vacuum chamber, the midplane symmetry in the dipole magnets, and no effect of the quadrupole magnets. With these assumptions, we discuss general properties of the synchrotron radiation, then we study its practical effects on the parity violation experiment and the photon detector.

A.1 Overview of Synchrotron Radiation

A.1.1 Instantaneous synchrotron radiation power

The instantaneous synchrotron radiation power of a relativistic electron, which propagates in a direction perpendicular to the magnetic field, and is given by [107, 145, 113]

$$P_0 = \frac{2}{3} \frac{e^2}{4\pi\epsilon_0 c} \frac{\gamma^4 \beta^4 c^2}{\rho^2} = \frac{2}{3} r_e m c^3 \frac{\gamma^4 \beta^4}{\rho^2}, \quad (\text{A.1})$$

where r_e is the classical electron radius, m the rest mass of the electron, c the speed of light, γ the Lorentz factor, β the velocity in terms of the speed of light, and ρ the bending radius of the dipole magnet. The above equation can be written in more practical units as

$$P_0 (\text{GeV/s}) = \frac{c (\text{m/s})}{2\pi} C_0 (\text{m/GeV}^3) \frac{E^4 (\text{GeV}^4)}{\rho^2 (\text{m}^2)}, \quad (\text{A.2})$$

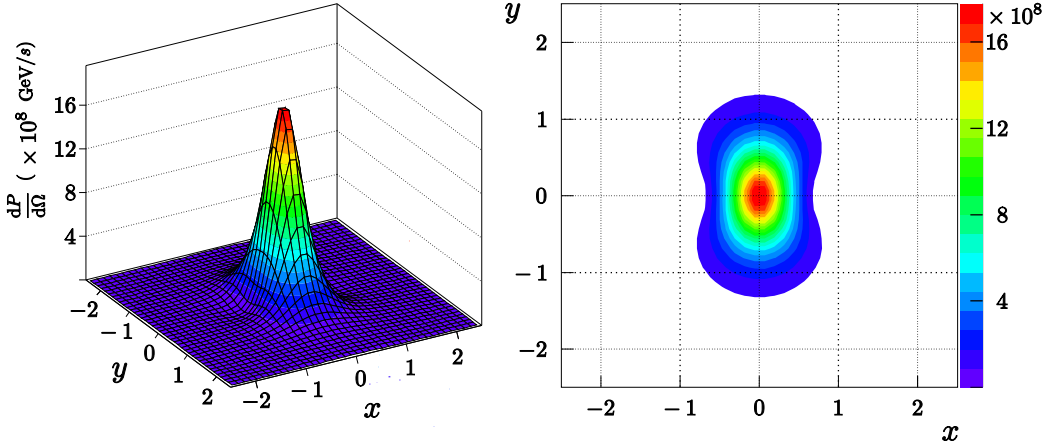


Figure A.1 The angular distribution of the synchrotron radiation of a 854.30 MeV electron. The normalized angle $\eta = \gamma \sin \theta$ is used to plot the distribution, thus $x = \eta \cos \phi$ and $y = \eta \sin \phi$. In the contour plot that is the $x - y$ plane from an observer's point of view, the synchrotron radiation is known to be a highly collimated beam.

where C_0 is Sand's radiation constant $C_0 = 8.84628 \times 10^{-5} \text{ (m/GeV}^3\text{)}$ and E the electron energy [107]. The synchrotron radiation power is strongly dependent on the energy of the electron.

A.1.2 Angular distribution

The angular distribution of the synchrotron radiation power is [145, 113]

$$\frac{dP}{d\Omega} = P_0 \frac{3}{2\pi} \frac{1}{\gamma^4} \left[\frac{(1 - \beta \cos \theta)^2 - (1 - \beta^2) \sin^2 \theta \cos^2 \phi}{(1 - \beta \cos \theta)^5} \right], \quad (\text{A.3})$$

where P_0 is the instantaneous synchrotron radiation power (A.1), θ the angle between the direction of electron momentum and the direction of the emitted photon, and ϕ the azimuth angle. Figure A.1 shows the angular distribution of the synchrotron radiation on a detector position. The emitted radiation is strongly concentrated around the forward direction within an angle of $\theta_\gamma = \pm 1/\gamma$ with respect to the direction of the electron momentum.

A.1.3 Spectral distribution

As we are interested in the number and energy of the emitted photon that hits the photon detector, we need to discuss the spectral distribution of synchrotron radiation.

Critical photon energy Synchrotron radiation is continuously emitted along the path of an accelerated particle. Since a fixed observer can see the synchrotron light for a only short duration, the spectrum will reach up to a critical photon energy during the duration. The critical photon energy is given by [145, 113]

$$\varepsilon_c = \hbar\omega_c = \frac{3}{2}\hbar c \frac{\gamma^3}{\rho}, \quad (\text{A.4})$$

where ω_c is the critical frequency, γ the Lorentz factor, and ρ the bending radius of the dipole magnet. In more practical units, the critical photon energy is

$$\varepsilon_c(\text{eV}) = \frac{3\hbar c}{2(mc^2)^3} \frac{E_e^3(\text{GeV}^3)}{\rho(\text{m})}. \quad (\text{A.5})$$

This critical photon energy ε_c defines an upper limit of the spectrum of synchrotron radiation.

Power spectrum The power spectrum is given by [107]

$$\mathcal{P}(\omega) = \frac{P_0}{\omega_c} S(\omega/\omega_c), \quad (\text{A.6})$$

where

$$S(\xi) = \frac{9\sqrt{3}}{8\pi} \xi \int_{\xi}^{\infty} K_{5/3}(s) ds, \quad (\text{A.7})$$

with ω_c is a critical frequency and $K_{5/3}(\xi)$ is a modified Bessel function of the second kind. Here $S(\xi)$ is called *the spectral function* or *normalized power spectrum* of synchrotron radiation. Figure A.2 shows the form of $S(\xi)$.

Photon flux The spectral photon flux per a deflection angle in a bending magnet is generated by an electron beam and is defined as [113, 146]

$$\frac{d\dot{n}_0}{d\varphi} = C_\varphi E (\text{GeV}) I(\text{A}) \frac{\Delta\omega}{\omega} S(\omega/\omega_c), \quad (\text{A.8})$$

where $\Delta\omega/\omega$ is called a *bandwidth* (usually 0.1%), I the electron current, and

$$C_\varphi = 3.967 \times 10^{19} \frac{\text{photons}}{\text{s rad A GeV}}.$$

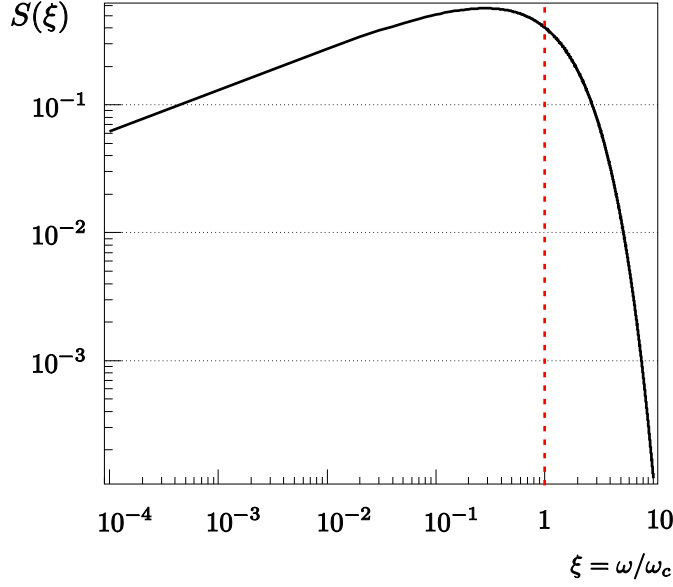


Figure A.2 Normalized power spectrum $S(\xi)$ of synchrotron radiation. $\mathcal{P}(\omega)$ has the same shape as $S(\xi)$ does with a different scale. The red dotted line represents the critical energy of the emitted synchrotron light.

A.2 Energy Loss in the Chicane

By integrating (A.2) along the effective length l_d of one dipole magnet, defined in (4.25), the energy loss per dipole magnet can be written as

$$U_0 = \int P_0 dt \approx \frac{C_0 E^4}{2\pi \rho^2} l_d, \quad (\text{A.9})$$

where C_0 is Sand's radiation constant and ρ the bending radius of the dipole magnet. Notice that the energy loss per dipole magnet depends on only the fourth power of the electron energy E . As the electron beam energy range 854.30 – 315.25 MeV, the energy loss for one electron per dipole magnet is between 0.42 and 0.01 keV, and the total energy loss $U_c = 4U_0$ in the chicane between 1.69 and 0.03 keV. Figure A.3 shows the energy loss U_c as a function of the electron energy. Moreover, U_0 and U_c for the different electron energies are listed in table A.1. The energy loss of the electron in the chicane, which is below 2 keV, is smaller than the error of the MAMI energy measurement.

In addition, we should evaluate the electron energy difference between before and after the chicane. As we see in table A.2, we could say that the energy loss is negligible, since the uncertainties of the electron beam $\Delta E = 160$ keV and the energy loss $U_c < 2$ keV.

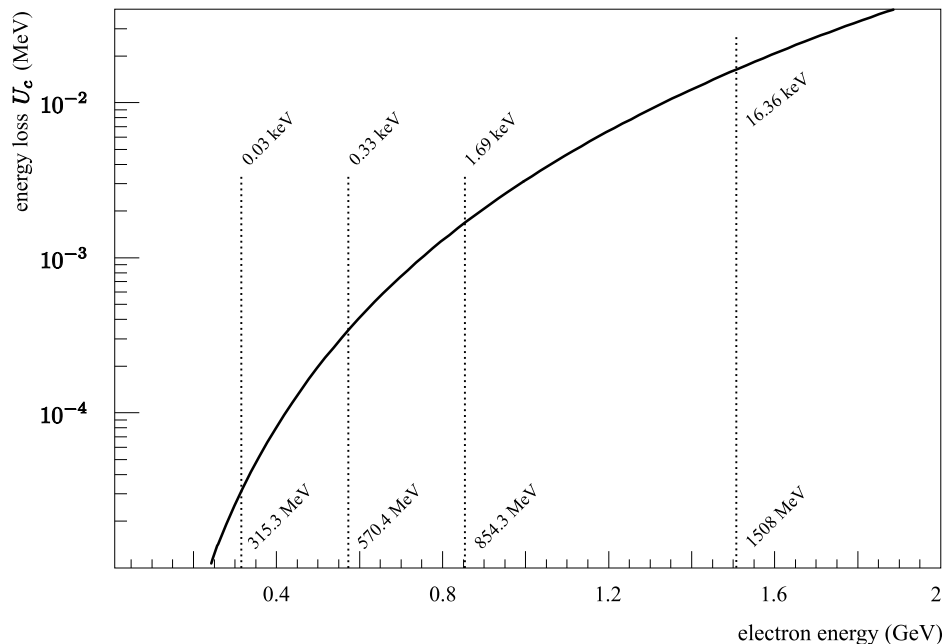


Figure A.3 The energy loss of an electron in the chicane as a function of the electron energy. Three energies are selected to calculate U_c , because these energies are the A4 experimental beam conditions. In addition, we also calculate U_c at 1508 GeV.

E (MeV)	U_0 (keV)	U_c (keV)
854.30(16)	0.42129(32)	1.6852(13)
570.40(16)	0.083726(94)	0.33490(38)
315.25(16)	0.007812(16)	0.031248(63)
1508.00(16*)	4.0902(17*)	16.3609(69*)

Table A.1 The energy loss due to the synchrotron radiation. E is the electron energy, U_0 the energy loss of one electron, and U_c the energy loss of the electron inside the chicane. As the chicane has the same four dipole magnets, $U_c = 4 \times U_0$. The uncertainties are stated with two significant figures in a concise form. Note that the uncertainty value of 1508 MeV does not come from the MAMI energy measurement. We assume that the uncertainty is the same as the other energy measurements. We denote these uncertainties as the * symbol.

U_c (keV)	E_{before} (MeV)	E_{after} (MeV)
1.6852(13)	854.30(16)	854.30(16)
0.33490(38)	570.40(16)	570.40(16)
0.031248(63)	315.25(16)	315.25(16)
16.3609(69)	1508.00(16*)	1508.00(16*)

Table A.2 The energy difference between before and after the chicane. E_{before} is the electron energy before the chicane and E_{after} the electron energy after the chicane. Notice that there are no differences between E_{before} and E_{after} within two significant figures. In the 1508 MeV case, $E_{\text{after}} = 1507.99591(16000^*)$ MeV with five significant figures.

Moreover, to confirm no effect of the energy loss on the parity violating asymmetry measurement, we should check that a squared four momentum transfer Q^2 is unchanged. The momentum transfer is

$$Q^2 = 4EE' \sin^2 \frac{\theta}{2}, \quad (\text{A.10})$$

with

$$E' = \frac{E}{1 + \frac{2E}{M} \sin^2 \frac{\theta}{2}},$$

and its uncertainty is

$$\delta Q^2 = 2M \left(1 - \frac{E'^2}{E^2} \right) \delta E, \quad (\text{A.11})$$

where E is the energy of the incident electron, E' the energy of the scattered electron, and we assume, for convenience, that the scattering angle θ has no uncertainty and can ignore the uncertainty of the proton mass M .

In case of the forward scattering, the scattering angle θ varies in the range of 30° to 40° that covers seven rings of the calorimeter [65]. We use mean scattering angles of the rings to calculate them. We calculate all Q^2 over the rings of the calorimeter and their average \bar{Q}^2 without and with U_c . In the calculations, the uncertainties were rounded to two significant figures and the rounding was done at the end of the calculations to reduce the inaccuracies. These results are listed in table A.3. We see that there are some differences in Q^2 and E' , especially at 1.508 GeV, if we compare the **without** U_c columns with the **with** U_c columns. However, when we directly calculate the differences, listed in the **difference** columns, between with and without the energy loss U_c in the chicane due to the synchrotron radiation, the Q^2 differences within their uncertainties are consistent with zero. It causes

E	1.50800(16)			0.85430(16)		
	without U_c	with U_c	difference	without U_c	with U_c	difference
R1 E'	1.107142(86)	1.107139(36)	0.00000(12)	0.70890(11)	0.70889(11)	0.00000(16)
Q^2	0.75223(14)	0.75222(14)	0.00000(20)	0.272859(94)	0.272858(94)	0.00000(13)
R2 E'	1.129270(90)	1.129268(90)	0.00000(13)	0.71790(11)	0.71790(11)	0.00000(16)
Q^2	0.71070(13)	0.71070(13)	0.00000(19)	0.255956(88)	0.255956(88)	0.00000(12)
R3 E'	1.150921(93)	1.150918(93)	0.00000(13)	0.72659(12)	0.72659(12)	0.00000(16)
Q^2	0.67007(13)	0.67007(13)	0.00000(18)	0.239650(83)	0.239650(83)	0.00000(12)
R4 E'	1.171744(97)	1.171741(97)	0.00000(14)	0.73484(12)	0.73484(12)	0.00000(17)
Q^2	0.63100(12)	0.63100(12)	0.00000(17)	0.224179(78)	0.224179(78)	0.00000(11)
R5 E'	1.19183(10)	1.19183(10)	0.00000(14)	0.74269(12)	0.74269(12)	0.00000(17)
Q^2	0.59330(11)	0.59330(11)	0.00000(16)	0.209448(73)	0.209448(73)	0.00000(10)
R6 E'	1.21114(10)	1.21113(10)	0.00000(15)	0.75014(12)	0.75014(12)	0.00000(17)
Q^2	0.55708(11)	0.55707(11)	0.00000(15)	0.195466(69)	0.195466(69)	0.00000(97)
R7 E'	1.22977(11)	1.22976(11)	0.00000(15)	0.75724(13)	0.75724(13)	0.00000(18)
Q^2	0.52212(10)	0.52212(10)	0.00000(14)	0.182134(64)	0.182134(64)	0.00000(91)
\bar{Q}^2	0.633787(45)	0.633784(45)	0.00003(64)	0.225670(30)	0.225670(30)	0.00000(42)

Table A.3 The effect of the synchrotron radiation on E' (GeV) and Q^2 (GeV/c)². Here, we state uncertainties with two significant figures. If the incident electron energy is 570.4 MeV or 315.25 MeV, there are no differences between **without** and **with** U_c . So, we omitted them from this table. In the table, \bar{Q}^2 is the average of all Q^2 s and **R** i rings of the calorimeter with $i = 1, 2, \dots, 7$. Since the rounding is done at the end of each calculation, we see some different values in **without** and **with** U_c .

this discrepancy that a number is rounded off at the end of each calculation. Therefore, the Q^2 and E' differences in the **difference** columns are correct. If the incident electron energy is 854.30 MeV, 570.40 MeV, or 315.25 MeV, we can ignore the energy loss due to the synchrotron radiation inside the chicane. However, the result suggests that by the time we use 1508 MeV electron beam in prospect, we should consider the synchrotron radiation effect in order to analyze 1508 MeV experimental data, although it is considerably small.

A.3 Radiation on the Photon Detector

As the synchrotron radiation from the third dipole magnet (DIPL 22) has an effect on the photon detector, in this section, we study a so-called *exposure angle* and a *transmitted photon number*. The exposure angle is the fairly narrow angle within which the detector is exposed to the synchrotron radiation. The transmitted photon number is the number of the emitted photon that hits the photon detector.

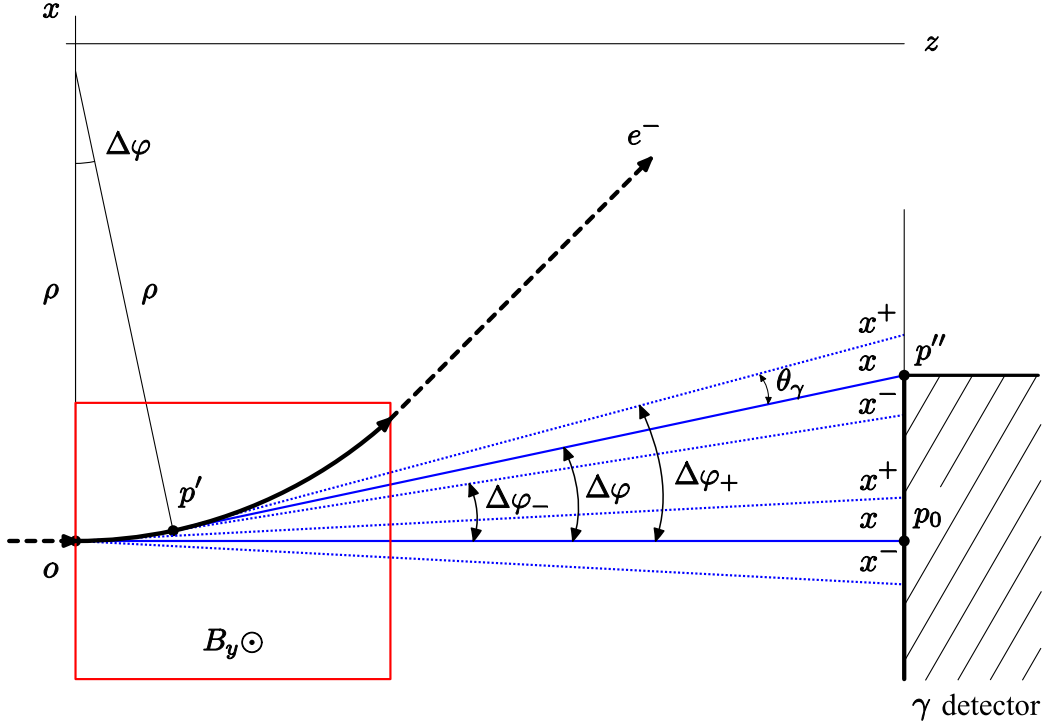


Figure A.4 Synchrotron radiation on the photon detector. The red box represents the area of the magnetic field B_y oriented in the $+y$ direction. The blue solid lines ($\overline{op_0}$ and $\overline{p'p''}$) represent the center of the synchrotron light along the electron momentum, the blue dotted ones define the boundary of the light at $\pm\theta_\gamma$. Here, $\Delta\varphi_\pm = \Delta\varphi \pm \theta_\gamma$, γ detector the photon detector, and x and x^\pm are defined as the horizontal distances between p_0 and positions where the synchrotron light are incident on the photon detector.

A.3.1 Exposure angle

An important feature of the synchrotron radiation is that the photon beam is highly collimated within $2\theta_\gamma$, which is in figure A.1. Only a small amount of the collimated light is detected by the photon detector, because the photon detector does not cover the full bending angle α , which is defined in (4.21), of the dipole magnet. Figure A.4 shows a schematic picture of the synchrotron radiation on the photon detector. We call $\Delta\varphi$ the exposure angle. Within this narrow angle, the photon detector is exposed to the synchrotron radiation. For convenience, in figure A.4, o , p_0 , p' , and p'' are chosen in terms

Energy (MeV)	$\Delta\varphi_+^{max}$ (mrad)	$\Delta\varphi^{max}$ (mrad)	$\Delta\varphi_-^{max}$ (mrad)
854.30	9.19	9.79	10.38
570.40	8.89	9.79	10.68
315.25	8.16	9.79	11.41
1508.00	9.45	9.79	10.12

Table A.4 The maximum exposure angles $\Delta\varphi^{max}$ and $\Delta\varphi_{\pm}^{max}$

of coordinates as

$$\begin{aligned}
o &= (0, 0), \\
p_0 &= (z_0, 0), \\
p' &= (\rho \sin \Delta\varphi, \rho (1 - \cos \Delta\varphi)), \\
p'' &= (0, x_0),
\end{aligned} \tag{A.12}$$

where ρ is the bending radius of the dipole magnet, z_0 the distance between the entrance of DIPL 22 and the photon detector, and x_0 the horizontal detector size with respect to the beam coordinate defined in figure 4.1. Thus, x and x^{\pm} can be represented by the following equations:

$$\begin{aligned}
x &= z_0 \tan \Delta\varphi + \rho (1 - \sec \Delta\varphi), \\
x^{\pm} &= z_0 \tan \Delta\varphi_{\pm} + \rho (1 - \cos \theta_{\gamma} \sec \Delta\varphi_{\pm}).
\end{aligned} \tag{A.13}$$

We therefore calculate the maximum exposure angles $\Delta\varphi^{max}$ and $\Delta\varphi_{\pm}^{max}$, which are reached if x and x^{\pm} are equal to x_0 respectively by either using the bisection algorithm, the false position algorithm, or the Brent-Dekker method [147]. These algorithms return the same results, which are listed in table A.4.

We introduce a new parameter R so as to find the exposure angle

$$R = \frac{\mathcal{E}}{|x_+ - x_-|}, \tag{A.14}$$

where \mathcal{E} is the horizontal spot size of the synchrotron radiation on the photon detector

$$\mathcal{E} = \begin{cases} |x_+ - x_-| & 0 \leq \Delta\varphi < \Delta\varphi_+^{max} \\ |x_0 - x_-| & \Delta\varphi_+^{max} \leq \Delta\varphi < \Delta\varphi_-^{max} \\ 0 & \Delta\varphi_-^{max} \leq \Delta\varphi \end{cases}.$$

Figure A.5 shows the plot of R as a function of $\Delta\varphi$ at 854.3 MeV. The parameter R starts to decrease linearly at $\Delta\varphi_+^{max}$, is approximately 0.5 at $\Delta\varphi^{max}$, and is zero at $\Delta\varphi_-^{max}$.

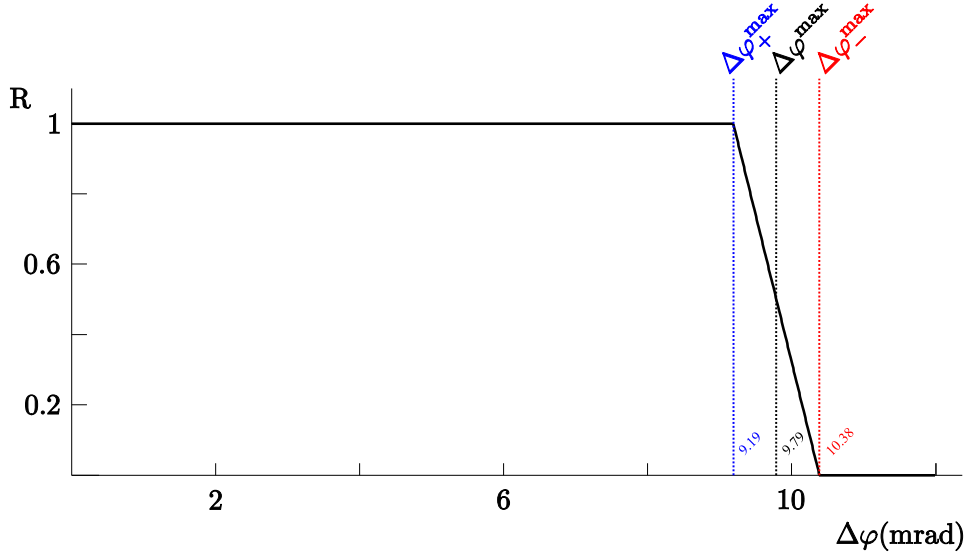


Figure A.5 R is a function of $\Delta\varphi$ at 854.3 MeV.

Moreover, since the horizontal spot size of the synchrotron radiation is around ± 1.6 mm about the light center on the photon detector and 68% intensity of the synchrotron radiation is within ± 0.45 mm, we ignore the spot size of the synchrotron radiation when $\Delta\varphi > \Delta\varphi^{\max}$. We therefore use $\Delta\varphi^{\max}$ as a good approximation as the exposure angle.

Transmitted photon number The synchrotron radiation is generated in the vacuum of the beam pipe and the photon detector is in the air of the experimental hall. Thus, the synchrotron radiation is absorbed by some material, e.g. an aluminum flange of the beam pipe and the air of the experimental hall. Figure A.6 shows possible absorption of the synchrotron radiation. Since we are interested to know the synchrotron radiation effect on the photon detector, it is necessary to calculate the number of transmitted photons that is equivalent to the synchrotron light hits the photon detector.

Using (A.8) and the exposure angle $\Delta\varphi^{\max}$, the number of transmitted photons $\dot{n}(\epsilon)$ [144] is written by

$$\dot{n}(\epsilon) \left(\frac{\text{photons}}{\text{sec}} \right) = \dot{n}_0^\varphi(\epsilon) \exp \left[- \sum_i \left\{ \frac{\mu}{\rho}(\epsilon) \right\}_i x_i \right], \quad (\text{A.15})$$

where

$$\dot{n}_0^\varphi(\epsilon) = C_\varphi EI \frac{\Delta\epsilon}{\epsilon} S(\epsilon/\epsilon_c) \Delta\varphi^{\max},$$

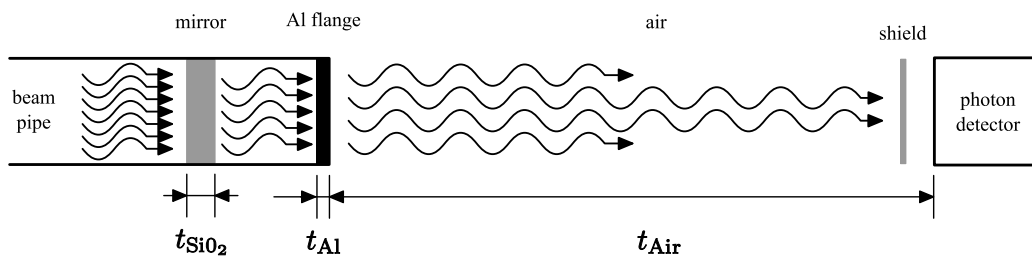


Figure A.6 Possible absorption of the synchrotron radiation. The solid wave line and the black box represent the synchrotron radiation and the aluminum flange, respectively. The **shield** will be some materials in order to reduce the synchrotron radiation on the photon detector and to protect the detector from the synchrotron radiation. In addition, the shield must be translucent for the Compton photons. The distance between the beam pipe and the photon detector is $t_{\text{Air}} = 1.5$ m, the thickness of the flange $t_{\text{Al}} = 0.52$ mm, and the thickness of the mirror $t_{\text{SiO}_2} = 9$ mm.

and x_i the mass thicknesses of the absorber materials, and $\{\mu/\rho(\epsilon)\}_i$ mass attenuation coefficients, which are dependent on the photon energy. The absorber materials are the aluminum, the air, and the fused silica (synthetic quartz glass). The energy band width $\Delta\epsilon/\epsilon = 0.001$ is used. Detailed information about the mass attenuation coefficients is shown in appendix D.

The total transmitted photon rate \dot{n} at 854.30, 570.40, and 315.25 MeV are 2.4×10^{-10} , 1.6×10^{-43} , and 1.1×10^{-196} Hz, respectively. As the photon numbers seen by the photon detector are small, we could say that the synchrotron radiation at the three beam energies has no effect on the photon detector. However, the total transmitted photon rate at 1508 MeV is 4.9×10^6 Hz. Thus we need a *shield* in order to reduce the synchrotron radiation rate. Figure A.7 shows the photon flux $\dot{n}_0^\varphi(\epsilon)$ and the transmitted photon number $\dot{n}(\epsilon)$ at 1508 MeV.

The measured rate of the Compton photon is on the order of 3 kHz at 854.3 MeV. Since the Compton cross section at 1508 MeV is a slightly different from the 854.3 MeV one, we can use the 3 kHz rate to estimate a *pile-up* rate of the 1508 MeV electron beam on the photon detector. Without any shield, the pile-up rate is approximately 2.9 kHz and is 98% of the Compton rate. Since we want to reduce the pile-up rate below 1% of the Compton photon rate by using a shield, the total transmitted photon rate has to be less than 50 kHz. Figure A.8 shows the total transmitted photon rate ratios $\dot{n}(x_{\text{shield}})/\dot{n}$ where x_{shield} is the thickness of the shield. In this calculation, we use aluminum or lead as the shield. To reduce the pile-up rate below 1% of the Compton photon rate, we need a 10 mm aluminum or a 0.1 mm lead.

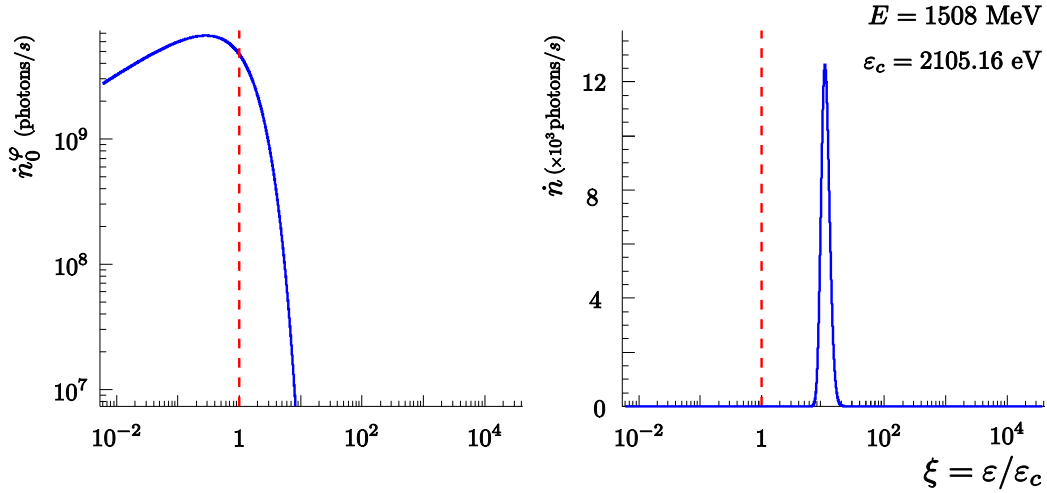


Figure A.7 The photon flux and the transmitted photon number at the front of the photon detector. ϵ_c is the critical photon energy defined in (A.5). The dashed red lines represent $\epsilon = \epsilon_c$. Here we do not present the results for the incident electron beam energy E is 854.30, 570.40, or 315.25 MeV, because their transmitted photon numbers are smaller than the number of the 1508 MeV electron beam. Thus, we ignore them.

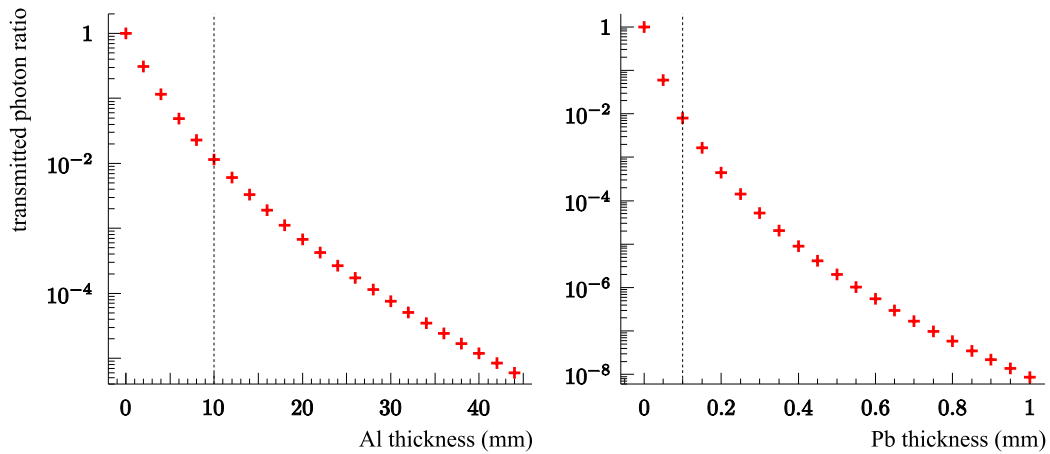


Figure A.8 The total transmitted photon rate ratio as a function of the Al and the Pb thickness at the 1.508 GeV electron beam.

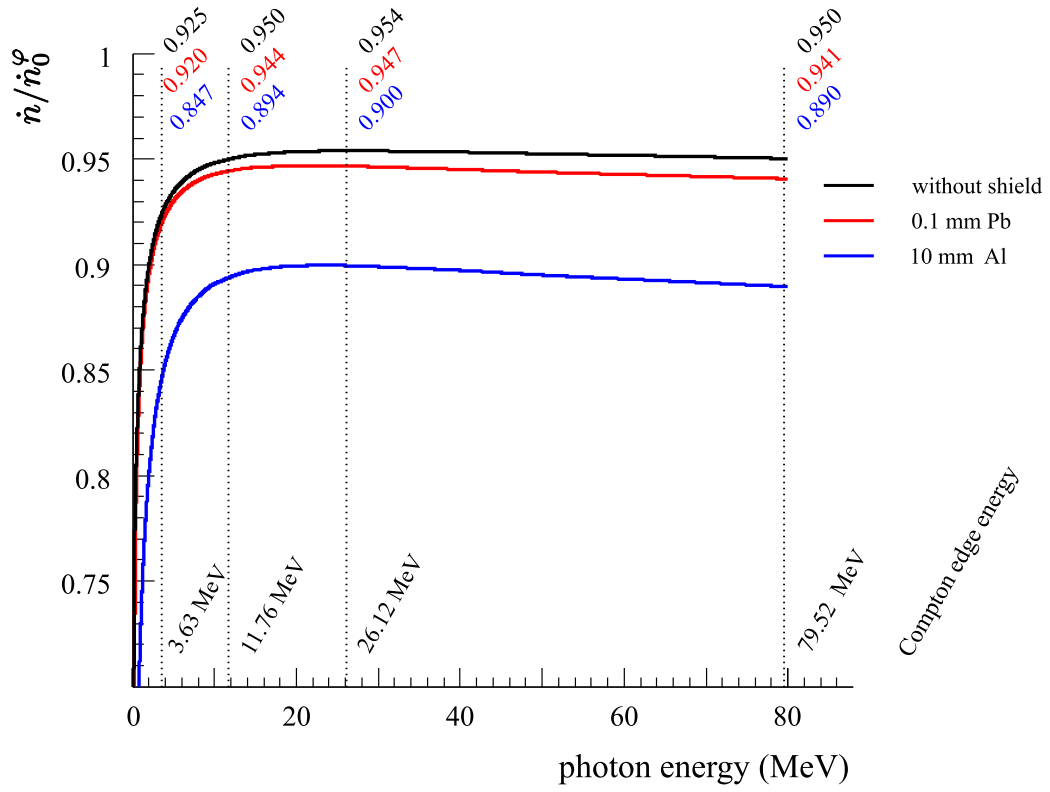


Figure A.9 The estimation of the translucence of the shields. The Compton edge energy represents the maximum photon energy of the Compton scattering.

In addition, the shield must be translucent for the Compton photons that have higher energies than the synchrotron radiation. If we use only the exponential function in (A.15), we can estimate the translucence of the shield. The corresponding exponential functions are shown in figure A.9. Without any shield, almost 95% Compton photons can be detected by the photon detector. When we use the 0.1 mm lead foil as the shield, 1% Compton photons will be absorbed in this shield. However, with 10 mm aluminum plate, we will lose more than 5% Compton photons over all the Compton photon energy region. Thus, the 0.1 mm lead will be the suitable shield in order that the photon detector is free from the synchrotron radiation background.

Appendix B

Input and Output of TRANSPORT

Here we present the input and the output of the TRANSPORT program about the A4 Compton backscattering polarimeter chicane. The input and the output are related to the movement of the reproduced electron beam close to the laser beam in **Step 2** as described in section 5.2.2.

B.1 Input

```
!=====
'A4 Compton Backscattering Polarimeter Chicane at Mainz
!=====
0
UMM

DRI0:=0.9999568; DRI1:=0.2309980; DRI2:=0.2209994; DRI3:=0.6684666;
DRI4:=0.0370209; DRI5:=0.6316000; DRI6:=0.2210004; DRI7:=0.2309996;
DRI8:=0.9999556; DRI9:=0.0500000;
EENERGY:=0.31525;
DMFS1:=+2.9100000; DMFS2:=-2.9100000;
DMFS3:=-2.9100000; DMFS4:=+2.9100000;

PARAM, F20= -0.0340715; PARAM, F21 = -0.0432654;
PARAM, F22= -0.0095116; PARAM, F23 = -0.0061925;
PARAM, QF1= -0.0395000; PARAM, QF2 = -0.0498000;
PARAM, XC1=-15.0534570; PARAM, XPC1= +1.1975832;
PARAM, YC1= -0.2052141; PARAM, YPC1= -0.2480189;

PLOT, L, ZFLOOR, XFLOOR, XC, XPC, YC, YPC, DLC;
MAGNET, WIDTH=0.385, HEIGHT=0.0639, TYPE=DM;
MAGNET, WIDTH=0.040, HEIGHT=0.0400, TYPE=QD;
PRINT, PRECISE;
NORDER: ORDER, N=3;

EBEAM : BEAM, BETAX=+7.9000086, ALPHAX=+0.1265824, EPSX=+0.0210721, &
        BETAY=+9.7221079, ALPHAY=+0.1028578, EPSY=+0.0013616, PO=EENERGY;
PRINT, FLOOR;
```

```

PRINT, TRANS, ON;
PRINT, BEAM, ON;

G2A  : SPEC, HGAP =31.95000;
K1A  : SPEC, FINT = 0.45000;
K2A  : SPEC, FINT2= 2.80000;
EMASS : SPEC, PMASS= 0.00511;

CENTROID, X=XC1, Y=YC1, XP=XPC1, YP=YPC1, DEL=0.0000;

DM20 : SBEND, L=0.73355807, B=DMFS1, N=0, E1=0.0, E2=-114.8077582,&
      RMPS=F20, TILT=0.0, TYPE=DM;
DRIFT0: DRIFT, L=DRI0;
DM21 : SBEND, L=0.73355807, B=DMFS2, N=0, E1=+114.8077582, E2=0.0,&
      RMPS=F21, TILT=0.0, TYPE=DM;
DRIFT1: DRIFT, L=DRI1;
QUAD21: QUAD, L=0.238, B=QF1, APER=40, TILT=0.0, TYPE=QD;
DRIFT2: DRIFT, L=DRI2;
FITAL1: FIT, NAME=XC, VALUE=-0.8937939, TOLER=0.001;
FITAL2: FIT, NAME=YC, VALUE=-1.1160175, TOLER=0.001;
DRIFT3: DRIFT, L=DRI3;
DRIFT4: DRIFT, L=DRI4;
FITBL1: FIT, NAME=XC, VALUE=-0.7866950, TOLER=0.001;
FITBL2: FIT, NAME=YC, VALUE=-1.1223086, TOLER=0.001;
DRIFT5: DRIFT, L=DRI5;
FITCL1: FIT, NAME=XC, VALUE=-0.5942881, TOLER=0.001;
FITCL2: FIT, NAME=YC, VALUE=-0.9916791, TOLER=0.001;
DRIFT6: DRIFT, L=DRI6;
QUAD22: QUAD, L=0.238, B=QF2, APER=40, TILT=0.0, TYPE=QD;
DRIFT7: DRIFT, L=DRI7;
DM22 : SBEND, L=0.73355807, B=DMFS3, N=0, E1=0.0, E2=+114.8077582,&
      RMPS=F22, TILT=0.0, TYPE=DM;
DRIFT8: DRIFT, L=DRI8;
DM23 : SBEND, L=0.73355807, B=DMFS4, N=0, E1=-114.8077582, E2=0.0,&
      RMPS=F23, TILT=0.0, TYPE=DM;

FITE1 : FIT, NAME=XC, VALUE=+0.0000000, TOLER=0.001;
FITE2 : FIT, NAME=XPC, VALUE=+0.0000000, TOLER=0.001;
FITE3 : FIT, NAME=YC, VALUE=-1.1485550, TOLER=0.001;
FITE4 : FIT, NAME=YPC, VALUE=-0.1820150, TOLER=0.001;
VARY, F20; VARY, F21;
VARY, F22; VARY, F23;
SENTINEL

```

B.2 Output

```

CHANGEDATE(TRMAIN FORTRAN 19990614 14:55:00)
1
0 "A4 COMPTON BACKSCATTERING POLARIMETER CHICANE AT MAINZ "
0
5 UMM
+
+ ( 1 ELEMENTS)
+
+ DRI0:=0.9999568; DRI1:=0.2309980; DRI2:=0.2209994; DRI3:=0.6684666; ( 1 )
+ DRI4:=0.0370209; DRI5:=0.6316000; DRI6:=0.2210004; DRI7:=0.2309996; ( 5 )
+ DRI8:=0.9999566; DRI9:=0.0500000; ( 9 )
+ EENERGY:=0.31525; ( 11 )
10
+ DMFS1:=+2.9100000; DMFS2:=-2.9100000; ( 12 ELEMENTS)
+ DMFS3:=-2.9100000; DMFS4:=+2.9100000; ( 14 )
+
+ ( 16 )
+
+ PARAM, F20= -0.0340715; PARAM, F21 = -0.0432654; ( 16 )

```

```

+      15  PARAM, F22= -0.0095116; PARAM, F23 = -0.0061925;          ( 18 )
+
+      PARAM, QF1= -0.0395000; PARAM, QF2 = -0.0498000;          ( 20 ELEMENTS)
+
+      PARAM, XC1=-15.0534570; PARAM, XPC1= +1.1975832;          ( 22 )
+
+      PARAM, YC1= -0.2052141; PARAM, YPC1= -0.2480189;          ( 24 )
+
+
+
+
+      20  PLOT, L, ZFLOOR, XFLOOR, XC, XPC, YC, YPC, DLC;        ( 26 )
+
+      MAGNET, WIDTH=0.385, HEIGHT=0.0639, TYPE=DM;             ( 27 ELEMENTS)
+
+      MAGNET, WIDTH=0.040, HEIGHT=0.0400, TYPE=QD;             ( 28 )
+
+      PRINT, PRECISE;                                           ( 29 )
+
+      NORDER: ORDER, N=3;                                       ( 30 )
+
+
+      25
+
+      EBAM : BEAM, BETAX=+7.9000086, ALPHAX=+0.1265824, EPSX=+0.0210721, & ( 31 ELEMENTS)
+
+      BETAY=+9.7221079, ALPHAY=+0.1028578, EPSY=+0.0013616, P0=EENERGY; ( 31 )
+
+      PRINT, FLOOR;                                             ( 32 )
+
+      PRINT, TRANS, ON;                                         ( 33 )
+
+
+      30  PRINT, BEAM, ON;                                       ( 34 )
+
+
+
+
+      G2A : SPEC, HGAP =31.95000;                                ( 35 )
+
+      K1A : SPEC, FINT = 0.45000;                                ( 36 )
+
+      K2A : SPEC, FINT2= 2.80000;                                ( 37 )
+
+
+      35  EMASS : SPEC, PMASS= 0.00511;                           ( 38 )
+
+
+
+
+      CENTROID, X=XC1, Y=YC1, XP=XPC1, YP=YPC1, DEL=0.0000;   ( 39 )
+
+
+
+      DM20 : SBEND, L=0.73355807, B=DMFS1, N=0, E1=0.0, E2=-114.8077582,& ( 40 )
+
+      RMPS=F20, TILT=0.0, TYPE=DM;                               ( 40 )
+
+      DRIFT0: DRIFT, L=DRI0;                                     ( 41 ELEMENTS)
+
+
+      DM21 : SBEND, L=0.73355807, B=DMFS2, N=0, E1=+114.8077582, E2=0.0,& ( 42 )
+
+      RMPS=F21, TILT=0.0, TYPE=DM;                               ( 42 )
+
+      DRIFT1: DRIFT, L=DRI1;                                     ( 43 )
+
+
+      45  QUAD21: QUAD, L=0.238, B=QF1, APER=40, TILT=0.0, TYPE=QD; ( 44 )
+
+      DRIFT2: DRIFT, L=DRI2;                                     ( 45 ELEMENTS)
+
+
+      FITAL1: FIT, NAME=XC, VALUE=-0.8937939, TOLER=0.001;     ( 46 )
+
+      FITAL2: FIT, NAME=YC, VALUE=-1.1160175, TOLER=0.001;     ( 47 )
+
+      DRIFT3: DRIFT, L=DRI3;                                     ( 48 )
+
+
+      50  DRIFT4: DRIFT, L=DRI4;                                   ( 49 )
+
+
+      FITBL1: FIT, NAME=XC, VALUE=-0.7866950, TOLER=0.001;     ( 50 ELEMENTS)
+
+      FITBL2: FIT, NAME=YC, VALUE=-1.1223086, TOLER=0.001;     ( 51 )
+
+      DRIFT5: DRIFT, L=DRI5;                                     ( 52 )
+
+
+      FITCL1: FIT, NAME=XC, VALUE=-0.5942881, TOLER=0.001;     ( 53 )
+
+      FITCL2: FIT, NAME=YC, VALUE=-0.9916791, TOLER=0.001;     ( 54 )
+
+      55  DRIFT6: DRIFT, L=DRI6;                                   ( 55 ELEMENTS)
+
+
+      QUAD22: QUAD, L=0.238, B=QF2, APER=40, TILT=0.0, TYPE=QD; ( 56 )
+
+      DRIFT7: DRIFT, L=DRI7;                                     ( 57 )
+
+
+      DM22 : SBEND, L=0.73355807, B=DMFS3, N=0, E1=0.0, E2=+114.8077582,& ( 58 )
+
+      RMPS=F22, TILT=0.0, TYPE=DM;                               ( 58 )
+
+      DRIFT8: DRIFT, L=DRI8;                                     ( 59 ELEMENTS)
+
+
+      DM23 : SBEND, L=0.73355807, B=DMFS4, N=0, E1=-114.8077582, E2=0.0,& ( 60 )
+
+      RMPS=F23, TILT=0.0, TYPE=DM;                               ( 60 )
+
+
+
+
+
+      FITE1 : FIT, NAME=XC, VALUE=+0.0000000, TOLER=0.001;     ( 61 )
+
+      FITE2 : FIT, NAME=XPC, VALUE=+0.0000000, TOLER=0.001;     ( 61 )
+
+      FITE3 : FIT, NAME=YC, VALUE=-1.1485550, TOLER=0.001;     ( 62 ELEMENTS)
+
+      FITE4 : FIT, NAME=YPC, VALUE=-0.1820150, TOLER=0.001;     ( 63 )
+
+
+      VARY, F20; VARY, F21;                                     ( 64 )
+
+
+      70  VARY, F22; VARY, F23;                                   ( 65 )
+
+
+
+
+      SENTINEL
+      0 65 ELEMENTS USED OUT OF A MAXIMUM ALLOWABLE 4001
+      251 NUMBERS USED OUT OF A MAXIMUM ALLOWABLE 12001

```

1A4 COMPTON BACKSCATTERING POLARIMETER CHICANE AT MAINZ

```

( 31) *3RD ORDER*  NORDER      GAUSSIAN DISTRIBUTION  3.  3.
( 32) *BEAM*      EBEAM      0.31525 GEV/C
      0.000 M      0.0000 0.0000 7.9000 9.7221 0.1266 0.1029 0.0000 0.0000 0.0000 0.0000
( 36) *HGAP *      G2A      0.31950E+02
( 37) *FINT *      K1A      0.45000E+00
( 38) *FINT2 *     K2A      0.28000E+01
( 39) *PMASS *     EMASS     0.51100E-02
( 40) *CENT SHIFT*
      -15.05346 MM  1.19758 MR  -0.20521 MM  -0.24802 MR  0.00000 MM  0.00000 PM
      0.000 M      0.0000 0.0000 0.0000 M  0.000 0.000 0.000 MR
      -15.053 0.408 MM
      1.198 0.052 MR  -0.126
      -0.205 0.115 MM  0.000 0.000
      -0.248 0.012 MR  0.000 0.000 -0.102
      0.000 0.000 MM  0.000 0.000 0.000 0.000
      0.000 0.000 PM  0.000 0.000 0.000 0.000 0.000
( 41) * *          DM20      0.00000 MR
( 41) *SBEND*      DM20      0.73356 M      2.81085 KG  0.00000 ( 3.614 M , 202.99860 MR )
( 41) * *          DM20      -114.80775 MR
      0.734 M      -0.0742 0.0000 0.7285 M  -202.999 0.000 0.000 MR
      -11.368 0.397 MM
      9.219 0.064 MR  -0.564
      -0.387 0.115 MM  0.000 0.000
      -0.263 0.013 MR  0.000 0.000 0.327
      2.947 0.082 MM  -0.999 0.602 0.000 0.000
      0.000 0.000 PM  0.000 0.000 0.000 0.000 0.000
*TRANSFORM 1*
  0.98121 0.72612 0.00005 0.00010 0.00000 0.07119 -11.36794
 -0.08523 0.95609 0.00000 0.00004 0.00000 0.19155 9.21948
 -0.00005 0.00002 1.00142 0.73082 0.00000 0.00000 -0.38676
  0.00001 -0.00005 0.03871 1.02684 0.00000 -0.00001 -0.26262
 -0.20170 -0.07509 0.00001 0.00018 1.00000 -0.00477 2.94688
  0.00000 0.00000 0.00000 0.00000 0.00000 1.00000 0.00000
( 42) *DRIFT*      DRIFT0      0.99996 M
      1.734 M      -0.2758 0.0000 1.7080 M  -202.999 0.000 0.000 MR
      -2.149 0.365 MM
      9.219 0.064 MR  -0.438
      -0.649 0.119 MM  0.000 0.000
      -0.263 0.013 MR  0.000 0.000 0.420
      2.904 0.082 MM  -0.983 0.597 0.000 0.000
      0.000 0.000 PM  0.000 0.000 0.000 0.000 0.000
*TRANSFORM 1*
  0.89598 1.68218 0.00006 0.00014 0.00000 0.26273 -2.14886
 -0.08523 0.95609 0.00000 0.00004 0.00000 0.19155 9.21948
 -0.00004 -0.00002 1.04012 1.75761 0.00000 -0.00001 -0.64937
  0.00001 -0.00005 0.03871 1.02684 0.00000 -0.00001 -0.26262
 -0.20092 -0.08391 0.00002 0.00045 1.00000 -0.00627 2.90435
  0.00000 0.00000 0.00000 0.00000 0.00000 1.00000 0.00000
( 43) * *          DM21      114.80775 MR
( 43) *SBEND*      DM21      0.73356 M      -2.78410 KG  0.00000 ( -3.614 M , -202.99860 MR )
( 43) * *          DM21      0.00000 MR
      2.467 M      -0.3500 0.0000 2.4365 M  0.000 0.000 0.000 MR
      1.454 0.331 MM
      0.493 0.081 MR  -0.624
      -0.860 0.127 MM  0.000 0.000
      -0.288 0.015 MR  0.000 0.000 0.704
      3.129 0.021 MM  -0.315 0.938 0.000 0.001
      0.000 0.000 PM  0.000 0.000 0.000 0.000 0.000
*TRANSFORM 1*
  0.79450 2.30518 -0.00002 -0.00016 0.00000 0.31985 1.45368
 -0.15955 0.79565 -0.00002 -0.00006 0.00000 -0.02684 0.49264
  0.00002 -0.00007 1.09659 2.55826 0.00000 0.00000 -0.85953
 -0.00002 -0.00004 0.07924 1.09677 0.00000 -0.00002 -0.28828
 -0.02785 0.31629 0.00009 0.00077 1.00000 0.05529 3.12873
  0.00000 0.00000 0.00000 0.00000 0.00000 1.00000 0.00000
( 44) *DRIFT*      DRIFT1      0.23100 M
      2.698 M      -0.3500 0.0000 2.6675 M  0.000 0.000 0.000 MR
      1.567 0.320 MM
      0.493 0.081 MR  -0.588
      -0.926 0.129 MM  0.000 0.000
      -0.288 0.015 MR  0.000 0.000 0.718
      3.129 0.021 MM  -0.271 0.938 0.000 0.001
      0.000 0.000 PM  0.000 0.000 0.000 0.000 0.000
*TRANSFORM 1*
  0.75764 2.48897 -0.00003 -0.00017 0.00000 0.31365 1.56748
 -0.15955 0.79565 -0.00002 -0.00006 0.00000 -0.02684 0.49264
  0.00002 -0.00008 1.11490 2.81161 0.00000 0.00000 -0.92613
 -0.00002 -0.00004 0.07924 1.09677 0.00000 -0.00002 -0.28828
 -0.02783 0.31620 0.00009 0.00085 1.00000 0.05535 3.12869
  0.00000 0.00000 0.00000 0.00000 0.00000 1.00000 0.00000
( 45) *SROT*      0.00000 DEG
      2.698 M      -0.3500 0.0000 2.6675 M  0.000 0.000 0.000 MR
( 45) *QUAD*      QUAD21      0.23800 M      -0.03950 KG  40.00000 MM ( -44.70284 M )
      2.936 M      -0.3500 0.0000 2.9055 M  0.000 0.000 0.000 MR
( 45) *SROT*      0.00000 DEG
      2.936 M      -0.3500 0.0000 2.9055 M  0.000 0.000 0.000 MR
      1.689 0.310 MM
      0.529 0.078 MR  -0.482
      -0.992 0.131 MM  0.000 0.000
      -0.267 0.013 MR  -0.001 0.000 0.618
      3.129 0.021 MM  -0.222 0.961 0.001 0.001
      0.000 0.000 PM  0.000 0.000 0.000 0.000 0.000
*TRANSFORM 1*
  0.72165 2.68513 -0.00003 -0.00019 0.00000 0.30809 1.68900
 -0.14303 0.85344 -0.00002 -0.00006 0.00000 -0.01993 0.52901
  0.00002 -0.00009 1.13077 3.06494 0.00000 -0.00001 -0.99221
 -0.00002 -0.00003 0.05413 1.03107 0.00000 -0.00004 -0.26683
 -0.02782 0.31610 0.00010 0.00092 1.00000 0.05541 3.12865
  0.00000 0.00000 0.00000 0.00000 0.00000 1.00000 0.00000
( 46) *DRIFT*      DRIFT2      0.22100 M
      3.157 M      -0.3500 0.0000 3.1265 M  0.000 0.000 0.000 MR
      1.806 0.302 MM
      0.529 0.078 MR  -0.438
      -1.051 0.133 MM  0.000 0.000
      -0.267 0.013 MR  -0.001 0.000 0.632
      3.129 0.021 MM  -0.173 0.961 0.001 0.001
      0.000 0.000 PM  0.000 0.000 0.000 0.000 0.000
*TRANSFORM 1*
  0.69004 2.87374 -0.00004 -0.00020 0.00000 0.30369 1.80591
 -0.14303 0.85344 -0.00002 -0.00006 0.00000 -0.01993 0.52901
  0.00001 -0.00009 1.14274 3.29280 0.00000 -0.00002 -1.05118
 -0.00002 -0.00003 0.05413 1.03107 0.00000 -0.00004 -0.26683
 -0.02780 0.31600 0.00010 0.00098 1.00000 0.05547 3.12861
  0.00000 0.00000 0.00000 0.00000 0.00000 1.00000 0.00000

```

```

( 47) *FIT*      FITAL1  XC      -0.89379 /0.00100 ( 1.80591 )
( 48) *FIT*      FITAL2  YC      -1.11602 /0.00100 ( -1.05118 )
( 49) *DRIFT*    DRIFT3   0.66847 M 0.0000 3.7949 M 0.000 0.000 0.000 MR
      3.826 M -0.3500
      2.160 0.283 MM
      0.529 0.078 MR -0.283
      -1.230 0.139 MM 0.000 0.000
      -0.267 0.013 MR -0.001 0.000 0.669
      3.128 0.021 MM -0.007 0.961 0.001 0.001
      0.000 0.000 PM 0.000 0.000 0.000 0.000 0.000
*TRANSFORM 1*
  0.59443 3.44423 -0.00006 -0.00024 0.00000 0.29036 2.15953
 -0.14303 0.85344 -0.00002 -0.00006 0.00000 -0.01993 0.52901
  0.00000 -0.00012 1.17892 3.98204 0.00000 -0.00004 -1.22955
 -0.00002 -0.00003 0.05413 1.03107 0.00000 -0.00004 -0.26683
 -0.02775 0.31570 0.00011 0.00116 1.00000 0.05566 3.12850
  0.00000 0.00000 0.00000 0.00000 0.00000 1.00000 0.00000
( 50) *DRIFT*    DRIFT4   0.03702 M 0.0000 3.8320 M 0.000 0.000 0.000 MR
      3.863 M -0.3500
      2.179 0.282 MM
      0.529 0.078 MR -0.274
      -1.239 0.139 MM 0.000 0.000
      -0.267 0.013 MR -0.001 0.000 0.671
      3.128 0.021 MM 0.002 0.961 0.001 0.001
      0.000 0.000 PM 0.000 0.000 0.000 0.000 0.000
*TRANSFORM 1*
  0.58914 3.47583 -0.00006 -0.00025 0.00000 0.28963 2.17912
 -0.14303 0.85344 -0.00002 -0.00006 0.00000 -0.01993 0.52901
  0.00000 -0.00012 1.18092 4.02021 0.00000 -0.00005 -1.23943
 -0.00002 -0.00003 0.05413 1.03107 0.00000 -0.00004 -0.26683
 -0.02775 0.31568 0.00011 0.00117 1.00000 0.05567 3.12849
  0.00000 0.00000 0.00000 0.00000 0.00000 1.00000 0.00000
( 51) *FIT*      FITBL1  XC      -0.78670 /0.00100 ( 2.17912 )
( 52) *FIT*      FITBL2  YC      -1.12231 /0.00100 ( -1.23943 )
( 53) *DRIFT*    DRIFT5   0.63160 M 0.0000 4.4636 M 0.000 0.000 0.000 MR
      4.494 M -0.3500
      2.513 0.273 MM
      0.529 0.078 MR -0.104
      -1.408 0.145 MM 0.000 0.000
      -0.267 0.013 MR 0.000 0.000 0.702
      3.128 0.021 MM 0.176 0.961 0.001 0.001
      0.000 0.000 PM 0.000 0.000 0.000 0.000 0.000
*TRANSFORM 1*
  0.49880 4.01486 -0.00007 -0.00029 0.00000 0.27704 2.51324
 -0.14303 0.85344 -0.00002 -0.00006 0.00000 -0.01993 0.52901
 -0.00001 -0.00014 1.21511 4.67144 0.00000 -0.00007 -1.40796
 -0.00002 -0.00003 0.05413 1.03107 0.00000 -0.00004 -0.26683
 -0.02770 0.31540 0.00012 0.00135 1.00000 0.05584 3.12838
  0.00000 0.00000 0.00000 0.00000 0.00000 1.00000 0.00000
( 54) *FIT*      FITCL1  XC      -0.59429 /0.00100 ( 2.51324 )
( 55) *FIT*      FITCL2  YC      -0.99168 /0.00100 ( -1.40796 )
( 56) *DRIFT*    DRIFT6   0.22100 M 0.0000 4.6846 M 0.000 0.000 0.000 MR
      4.715 M -0.3500
      2.630 0.272 MM
      0.529 0.078 MR -0.041
      -1.467 0.147 MM 0.000 0.000
      -0.267 0.013 MR 0.000 0.000 0.712
      3.128 0.021 MM 0.237 0.961 0.001 0.001
      0.000 0.000 PM 0.000 0.000 0.000 0.000 0.000
*TRANSFORM 1*
  0.46719 4.20348 -0.00008 -0.00030 0.00000 0.27263 2.63015
 -0.14303 0.85344 -0.00002 -0.00006 0.00000 -0.01993 0.52901
 -0.00002 -0.00015 1.22708 4.89931 0.00000 -0.00008 -1.46694
 -0.00002 -0.00003 0.05413 1.03107 0.00000 -0.00004 -0.26683
 -0.02768 0.31530 0.00012 0.00141 1.00000 0.05590 3.12834
  0.00000 0.00000 0.00000 0.00000 0.00000 1.00000 0.00000
( 57) *SRGT*    DM22     0.00000 DEG 0.0000 4.6846 M 0.000 0.000 0.000 MR
      4.715 M -0.3500
( 57) *QUAD*    QUAD22   0.23800 M 0.0000 -0.04980 KG 40.00000 MM ( -35.44889 M )
      4.953 M -0.3500 0.0000 4.9226 M 0.000 0.000 0.000 MR
( 57) *SRGT*    DM22     0.00000 DEG 0.0000 4.9226 M 0.000 0.000 0.000 MR
      4.953 M -0.3500
      2.765 0.272 MM
      0.605 0.078 MR 0.125
      -1.525 0.149 MM 0.000 0.000
      -0.225 0.011 MR -0.001 0.000 0.504
      3.128 0.021 MM 0.303 0.983 0.001 0.001
      0.000 0.000 PM 0.000 0.000 0.000 0.000 0.000
*TRANSFORM 1*
  0.43468 4.42093 -0.00008 -0.00032 0.00000 0.26579 2.76502
 -0.13033 0.97488 -0.00003 -0.00007 0.00000 -0.01238 0.60498
 -0.00002 -0.00015 1.23583 5.12801 0.00000 -0.00009 -1.52545
 -0.00002 -0.00003 0.01941 0.88972 0.00000 -0.00008 -0.22465
 -0.02766 0.31517 0.00013 0.00146 1.00000 0.05597 3.12829
  0.00000 0.00000 0.00000 0.00000 0.00000 1.00000 0.00000
( 58) *DRIFT*    DRIFT7   0.23100 M 0.0000 5.1536 M 0.000 0.000 0.000 MR
      5.184 M -0.3500
      2.905 0.275 MM
      0.605 0.078 MR 0.189
      -1.577 0.150 MM 0.000 0.000
      -0.225 0.011 MR 0.000 0.000 0.516
      3.128 0.021 MM 0.364 0.983 0.001 0.001
      0.000 0.000 PM 0.000 0.000 0.000 0.000 0.000
*TRANSFORM 1*
  0.40457 4.64612 -0.00009 -0.00034 0.00000 0.26593 2.90477
 -0.13033 0.97488 -0.00003 -0.00007 0.00000 -0.01238 0.60498
 -0.00003 -0.00016 1.24032 5.33353 0.00000 -0.00011 -1.57735
 -0.00002 -0.00003 0.01941 0.88972 0.00000 -0.00008 -0.22465
 -0.02764 0.31504 0.00013 0.00151 1.00000 0.05603 3.12825
  0.00000 0.00000 0.00000 0.00000 0.00000 1.00000 0.00000
( 59) * * * * * DM22     0.00000 MR 0.00000 ( -3.614 M , -202.99860 MR )
( 59) *SBEND*   DM22     0.73356 M -2.88232 KG 0.00000
( 59) * * * * * DM22     114.80775 MR 0.0000 5.8821 M 202.999 0.000 0.000 MR
      5.918 M -0.2758
      2.581 0.286 MM
      -1.568 0.074 MR 0.065
      -1.745 0.155 MM 0.000 0.000
      -0.289 0.015 MR -0.001 0.001 0.795
      3.759 0.069 MM 0.984 0.240 0.000 0.000
      0.000 0.000 PM 0.000 0.000 0.000 0.000 0.000
*TRANSFORM 1*
  0.30149 5.26183 -0.00019 -0.00106 0.00000 0.17817 2.58104
 -0.15965 0.53030 -0.00006 -0.00027 0.00000 -0.23184 -1.56813
  0.00002 -0.00030 1.25671 5.99499 0.00000 -0.00015 -1.74477
 -0.00004 -0.00020 0.06586 1.10991 0.00000 -0.00012 -0.28880
  0.04432 1.32376 0.00022 0.00206 1.00000 0.10399 3.75862

```

```

( 60) 0.00000 0.00000 0.00000 0.00000 0.00000 1.00000 0.00000
      *DRIFT* DRIFTS 0.99996 M
      6.918 M -0.0742 0.0000 6.8615 M 202.999 0.000 0.000 MR
      1.013 0.300 MM
      -1.568 0.074 MR 0.308
      -2.034 0.166 MM 0.000 0.000
      -0.289 0.015 MR -0.001 0.001 0.826
      3.757 0.069 MM 0.998 0.242 0.000 0.000
      0.000 0.000 PM 0.000 0.000 0.000 0.000 0.000
      *TRANSFORM 1* REF
      0.14185 5.79211 -0.00026 -0.00133 0.00000 -0.05366 1.01299
      -0.15965 0.53030 -0.00006 -0.00027 0.00000 -0.23184 -1.56813
      -0.00002 -0.00050 1.32257 7.10486 0.00000 -0.00027 -2.03356
      -0.00004 -0.00020 0.06586 1.10991 0.00000 -0.00012 -0.28880
      0.04407 1.32460 0.00024 0.00238 1.00000 0.10389 3.75735
      0.00000 0.00000 0.00000 0.00000 0.00000 1.00000 0.00000
( 61) * DM23 -114.80775 MR
( 61) *SBEND* DM23 0.73356 M 2.89198 KG 0.00000 ( 3.614 M , 202.99860 MR )
( 61) * DM23 0.00000 MR
      7.651 M 0.0000 0.0000 7.5901 M 0.000 0.000 0.000 MR
      0.285 0.308 MM
      -0.376 0.069 MR 0.113
      -2.297 0.179 MM 0.000 0.000
      -0.364 0.020 MR 0.000 0.001 0.925
      3.671 0.012 MM 0.462 -0.829 0.005 0.005
      0.000 0.000 PM 0.000 0.000 0.000 0.000 0.000
      *TRANSFORM 1* REF
      0.01929 5.92444 -0.00012 -0.00017 0.00000 -0.14645 0.28540
      -0.16873 0.01731 0.00004 0.00032 0.00000 -0.02201 -0.37552
      -0.00012 -0.00081 1.40449 8.09968 0.00000 -0.00040 -2.29712
      -0.00002 0.00008 0.11459 1.37287 0.00000 -0.00017 -0.36403
      0.02746 0.13154 0.00047 0.00383 1.00000 0.12683 3.67077
      0.00000 0.00000 0.00000 0.00000 0.00000 1.00000 0.00000
( 62) *FIT* FITE1 XC 0.0 /0.00100 ( 0.28540 )
( 63) *FIT* FITE2 XPC 0.0 /0.00100 ( -0.37552 )
( 64) *FIT* FITE3 YC -1.14856 /0.00100 ( -2.29712 )
( 65) *FIT* FITE4 YPC -0.18202 /0.00100 ( -0.36403 )
0 *LENGTH* 7.65123 M
0 *CORRECTIONS*
  *NUMBER OF VARIED PARAMETERS = 4 *
  *NUMBER OF CONSTRAINTS = 10 *
0.10000E+01 ( 0.27507E+08) 0.0074 0.0051 0.0095 0.0074
0.10000E+01 ( 0.15686E+07) -0.29E-03 -0.24E-03 -0.11E-03 -0.44E-04
0.10000E+01 ( 0.15322E+07) 0.92E-05 0.95E-05 -0.24E-07 -0.53E-07
0.10000E+01 ( 0.15322E+07) -0.29E-06 -0.38E-06 0.32E-09 -0.28E-10
0.10000E+01 ( 0.15322E+07) 0.11E-07 0.18E-07 -0.12E-10 -0.12E-09
0 *COVARIANCE (FIT 0.15322E+07 )
  0.000
  0.988 0.000
  -0.856 -0.911 0.000
  -0.559 -0.591 0.775 0.000
( 17) *PARAM* "F20 " -0.26944488E-01
      VARIED
( 18) *PARAM* "F21 " -0.38426332E-01
      VARIED
( 19) *PARAM* "F22 " -0.78748330E-04
      VARIED
( 20) *PARAM* "F23 " 0.11277135E-02
      VARIED
1A4 COMPTON BACKSCATTERING POLARIMETER CHICAGO AT MAINZ
( 31) *3RD ORDER* NORDER GAUSSIAN DISTRIBUTION 3. 3.
( 32) *BEAM* EBEBAM 0.31525 GEV/C
      0.0000 0.0000 7.9000 9.7221 0.1266 0.1029 0.0000 0.0000 0.0000 0.0000
( 36) *HGAP * G2A 0.31950E+02
( 37) *FINT * K1A 0.45000E+00
( 38) *FINT2 * K2A 0.28000E+01
( 39) *PMASS * EMASS 0.51100E-02
( 40) *CENT SHIFT*
      -15.05346 MM 1.19758 MR -0.20521 MM -0.24802 MR 0.00000 MM 0.00000 PM
      0.000 M 0.0000 0.0000 0.0000 M 0.0000 0.000 MR
      -15.053 0.408 MM
      1.198 0.052 MR -0.126
      -0.205 0.115 MM 0.000 0.000
      -0.248 0.012 MR 0.000 0.000 -0.102
      0.000 0.000 MM 0.000 0.000 0.000 0.000
      0.000 0.000 PM 0.000 0.000 0.000 0.000 0.000
( 41) * DM20 0.00000 MR
( 41) *SBEND* DM20 0.73356 M 2.83159 KG 0.00000 ( 3.614 M , 202.99860 MR )
( 41) * DM20 -114.80775 MR
      0.734 M -0.0742 0.0000 0.7285 M -202.999 0.000 0.000 MR
      -11.893 0.397 MM
      7.804 0.064 MR -0.565
      -0.387 0.115 MM 0.000 0.000
      -0.262 0.013 MR 0.000 0.000 0.324
      2.947 0.082 MM -0.999 0.603 0.000 0.000
      0.000 0.000 PM 0.000 0.000 0.000 0.000 0.000
      *TRANSFORM 1* REF
      0.98092 0.72602 0.00005 0.00010 0.00000 0.07170 -11.89274
      -0.08562 0.95610 0.00000 0.00005 0.00000 0.19290 7.80411
      -0.00005 0.00002 1.00142 0.73078 0.00000 0.00000 -0.38675
      0.00001 -0.00005 0.03831 1.02654 0.00000 -0.00001 -0.26246
      -0.20168 -0.07509 0.00001 0.00018 1.00000 -0.00450 2.94659
      0.00000 0.00000 0.00000 0.00000 0.00000 1.00000 0.00000
( 42) *DRIFT* DRIFTO 0.99996 M
      1.734 M -0.2758 0.0000 1.7080 M -202.999 0.000 0.000 MR
      -4.089 0.365 MM
      7.804 0.064 MR -0.439
      -0.649 0.119 MM 0.000 0.000
      -0.262 0.013 MR 0.000 0.000 0.416
      2.916 0.082 MM -0.982 0.599 0.000 0.000
      0.000 0.000 PM 0.000 0.000 0.000 0.000 0.000
      *TRANSFORM 1* REF
      0.89531 1.68208 0.00006 0.00014 0.00000 0.26459 -4.08897
      -0.08562 0.95610 0.00000 0.00005 0.00000 0.19290 7.80411
      -0.00004 -0.00002 1.03972 1.75728 0.00000 -0.00001 -0.64921
      0.00001 -0.00005 0.03831 1.02654 0.00000 -0.00001 -0.26246
      -0.20101 -0.08255 0.00002 0.00045 1.00000 -0.00604 2.91610
      0.00000 0.00000 0.00000 0.00000 0.00000 1.00000 0.00000
( 43) * DM21 114.80775 MR
( 43) *SBEND* DM21 0.73356 M -2.79818 KG 0.00000 ( -3.614 M , -202.99860 MR )
( 43) * DM21 0.00000 MR
      2.467 M -0.3500 0.0000 2.4365 M 0.000 0.000 0.000 MR
      -1.074 0.331 MM
      0.246 0.082 MR -0.625

```



```

-0.266 0.013 MR 0.000 0.000 0.708
2.657 0.021 MM 0.236 0.961 0.001 0.001
0.000 0.000 PM 0.000 0.000 0.000 0.000 0.000
REF
*TRANSFORM 1*
0.46502 4.20239 -0.00008 -0.00030 0.00000 0.27485 -0.56253
-0.14358 0.85280 -0.00002 -0.00006 0.00000 -0.01997 0.22406
-0.00002 -0.00015 1.22446 4.89689 0.00000 -0.00008 -1.46580
-0.00002 -0.00003 0.05340 1.03025 0.00000 -0.00004 -0.26648
-0.02816 0.31806 0.00012 0.00140 1.00000 0.05659 2.65707
0.00000 0.00000 0.00000 0.00000 0.00000 1.00000 0.00000
( 57) *SRGT* 0.00000 DEG
4.715 M -0.3500 0.0000 4.6846 M 0.000 0.000 0.000 MR
( 57) *QUAD* QUAD22 0.23800 M -0.04980 KG 40.00000 MM ( -35.44889 M )
4.953 M -0.3500 0.0000 4.9226 M 0.000 0.000 0.000 MR
( 57) *SRGT* 0.00000 DEG
4.953 M -0.3500 0.0000 4.9226 M 0.000 0.000 0.000 MR
-0.511 0.272 MM
0.209 0.078 MR 0.125
-1.524 0.149 MM 0.000 0.000
-0.224 0.011 MR -0.001 0.000 0.499
2.657 0.021 MM 0.302 0.984 0.001 0.001
0.000 0.000 PM 0.000 0.000 0.000 0.000 0.000
REF
*TRANSFORM 1*
0.43237 4.41968 -0.00008 -0.00032 0.00000 0.27101 -0.51104
-0.13095 0.97420 -0.00003 -0.00007 0.00000 -0.01227 0.20894
-0.00002 -0.00015 1.23305 5.12540 0.00000 -0.00010 -1.52424
-0.00002 -0.00003 0.01876 0.88896 0.00000 -0.00008 -0.22433
-0.02815 0.31802 0.00012 0.00146 1.00000 0.05665 2.65706
0.00000 0.00000 0.00000 0.00000 0.00000 1.00000 0.00000
( 58) *DRIFT* DRIFT7 0.23100 M
5.184 M -0.3500 0.0000 5.1536 M 0.000 0.000 0.000 MR
-0.463 0.275 MM
0.209 0.078 MR 0.190
-1.576 0.150 MM 0.000 0.000
-0.224 0.011 MR 0.000 0.000 0.511
2.657 0.021 MM 0.363 0.984 0.001 0.001
0.000 0.000 PM 0.000 0.000 0.000 0.000 0.000
REF
*TRANSFORM 1*
0.40212 4.64472 -0.00009 -0.00033 0.00000 0.26818 -0.46277
-0.13095 0.97420 -0.00003 -0.00007 0.00000 -0.01227 0.20894
-0.00002 -0.00016 1.23738 5.33076 0.00000 -0.00011 -1.57606
-0.00002 -0.00003 0.01876 0.88896 0.00000 -0.00008 -0.22433
-0.02815 0.31797 0.00013 0.00151 1.00000 0.05671 2.65704
0.00000 0.00000 0.00000 0.00000 0.00000 1.00000 0.00000
( 59) * * DM22 0.00000 MR
( 59) *SBEND* DM22 0.73356 M -2.90977 KG 0.00000 ( -3.614 M , -202.99860 MR )
( 59) * * DM22 114.80775 MR
5.918 M -0.2758 0.0000 5.8821 M 202.999 0.000 0.000 MR
-0.307 0.285 MM
0.224 0.074 MR 0.066
-1.743 0.154 MM 0.000 0.000
-0.287 0.014 MR -0.001 0.001 0.790
2.579 0.069 MM 0.984 0.244 0.000 0.000
0.000 0.000 PM 0.000 0.000 0.000 0.000 0.000
REF
*TRANSFORM 1*
0.29844 5.25897 -0.00019 -0.00106 0.00000 0.17952 -0.30678
-0.16022 0.52731 -0.00006 -0.00027 0.00000 -0.23433 0.22442
0.00002 -0.00030 1.26319 5.99175 0.00000 -0.00015 -1.74324
-0.00004 -0.00020 0.06431 1.10544 0.00000 -0.00012 -0.28737
0.04323 1.32652 0.00022 0.00205 1.00000 0.10505 2.57915
0.00000 0.00000 0.00000 0.00000 0.00000 1.00000 0.00000
( 60) *DRIFT* DRIFT8 0.99996 M
6.918 M -0.0742 0.0000 6.8615 M 202.999 0.000 0.000 MR
-0.082 0.289 MM
0.224 0.074 MR 0.310
-2.031 0.166 MM 0.000 0.000
-0.287 0.014 MR -0.001 0.001 0.822
2.579 0.069 MM 0.998 0.244 0.000 0.000
0.000 0.000 PM 0.000 0.000 0.000 0.000 0.000
REF
*TRANSFORM 1*
0.13822 5.78626 -0.00026 -0.00133 0.00000 -0.05481 -0.08237
-0.16022 0.52731 -0.00006 -0.00027 0.00000 -0.23433 0.22442
-0.00002 -0.00050 1.31750 7.09715 0.00000 -0.00028 -2.03061
-0.00004 -0.00020 0.06431 1.10544 0.00000 -0.00012 -0.28737
0.04326 1.32640 0.00024 0.00237 1.00000 0.10537 2.57908
0.00000 0.00000 0.00000 0.00000 0.00000 1.00000 0.00000
( 61) * * DM23 -114.80775 MR
( 61) *SBEND* DM23 0.73356 M 2.91328 KG 0.00000 ( 3.614 M , 202.99860 MR )
( 61) * * DM23 0.00000 MR
7.651 M 0.0000 0.0000 7.5901 M 0.000 0.000 0.000 MR
0.001 0.307 MM
0.000 0.069 MR 0.115
-2.292 0.179 MM 0.000 0.000
-0.362 0.020 MR 0.000 0.001 0.922
2.579 0.013 MM 0.464 -0.827 0.005 0.005
0.000 0.000 PM 0.000 0.000 0.000 0.000 0.000
REF
*TRANSFORM 1*
0.01545 5.91708 -0.00012 -0.00018 0.00000 -0.14884 0.00087
-0.16896 0.01243 0.00004 0.00032 0.00000 -0.02291 -0.00044
-0.00012 -0.00091 1.39765 8.08568 0.00000 -0.00041 -2.29224
-0.00002 0.00008 0.11233 1.36536 0.00000 -0.00017 -0.36171
0.02764 0.13438 0.00047 0.00381 1.00000 0.12886 2.57866
0.00000 0.00000 0.00000 0.00000 0.00000 1.00000 0.00000
( 62) *FIT* FITE1 XC 0.0 /0.00100 ( 0.00087 )
( 63) *FIT* FITE2 XPC 0.0 /0.00100 ( -0.00044 )
( 64) *FIT* FITE3 YC -1.14856 /0.00100 ( -2.29224 )
( 65) *FIT* FITE4 YPC -0.18202 /0.00100 ( -0.36171 )
0 *LENGTH* 7.65123 M

```


Appendix C

Magnetic Field and Shunt Current Measurements

The 95% confidence and prediction intervals are used in the following measurements.

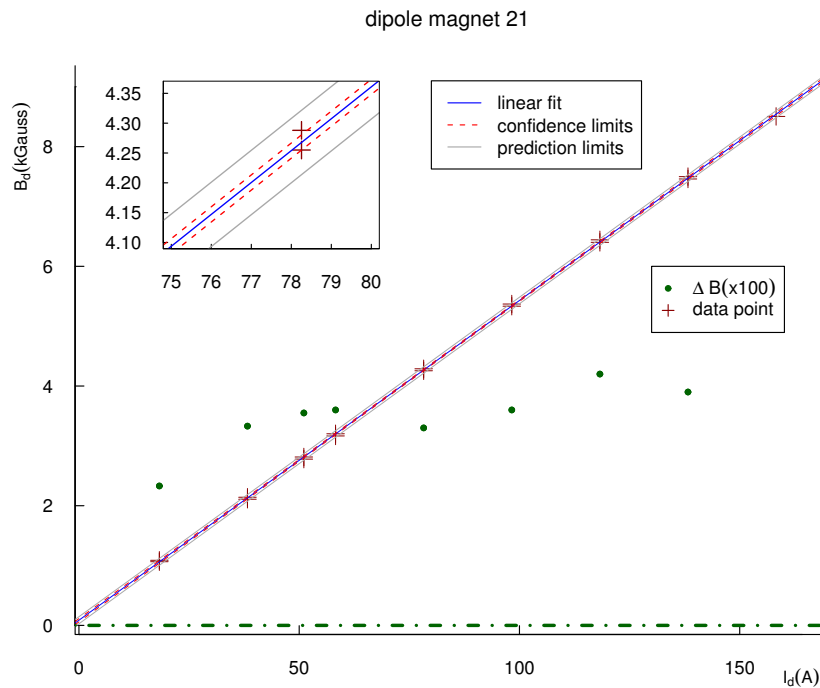


Figure C.1 Magnetic field measurement for the dipole magnet 21. For detailed information, see the section 5.2.1.

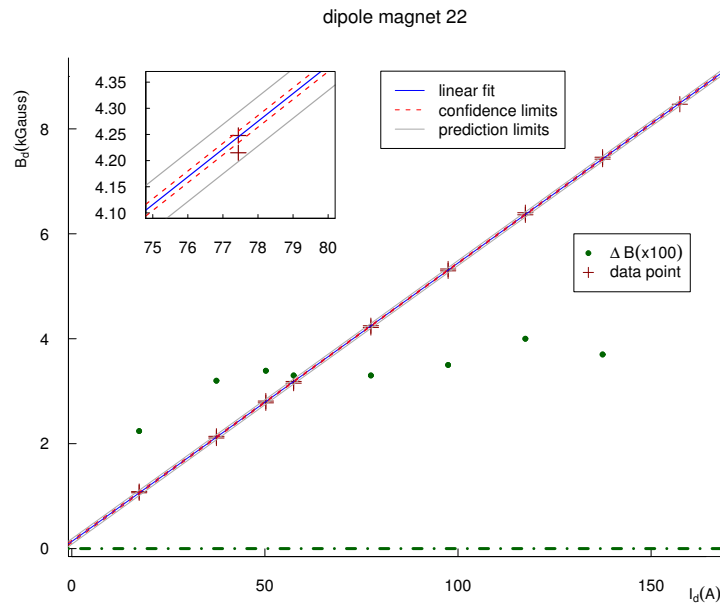


Figure C.2 Magnetic field measurement for the dipole magnet 22. For detailed information, see the section 5.2.1.

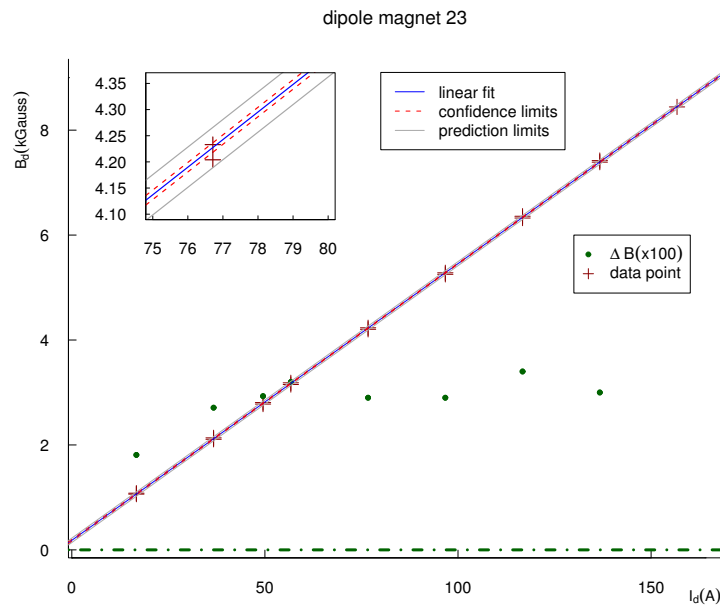


Figure C.3 Magnetic field measurement for the dipole magnet 23. For detailed information, see the section 5.2.1.

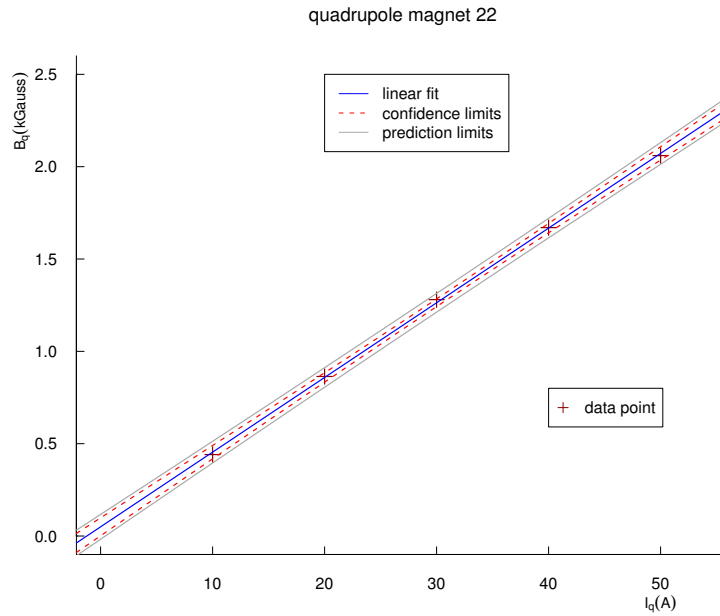


Figure C.4 Magnetic field measurement for the quadrupole magnet 22 [116]. For detailed information, see the section 5.2.1.

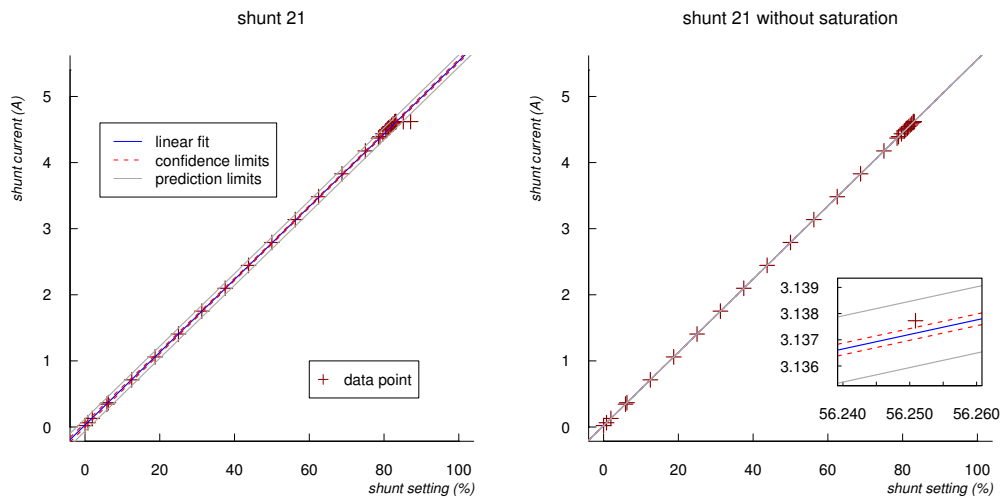


Figure C.5 Shunt current measurement for the shunt 21 with $I_{\text{MAMI}} = 52.8$ A. For detailed information, see the section 5.2.1.

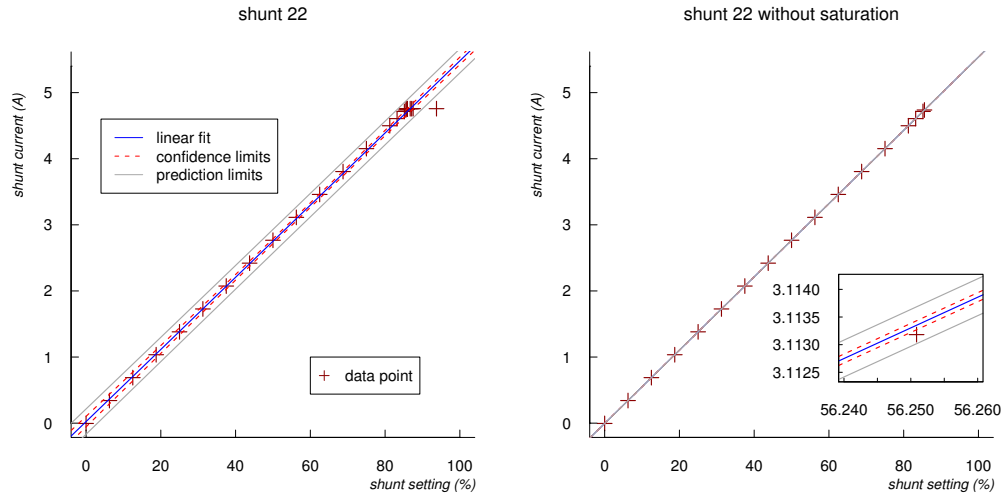


Figure C.6 Shunt current measurement for the shunt 22 with $I_{\text{MAMI}} = 52.8$ A. For detailed information, see the section 5.2.1.

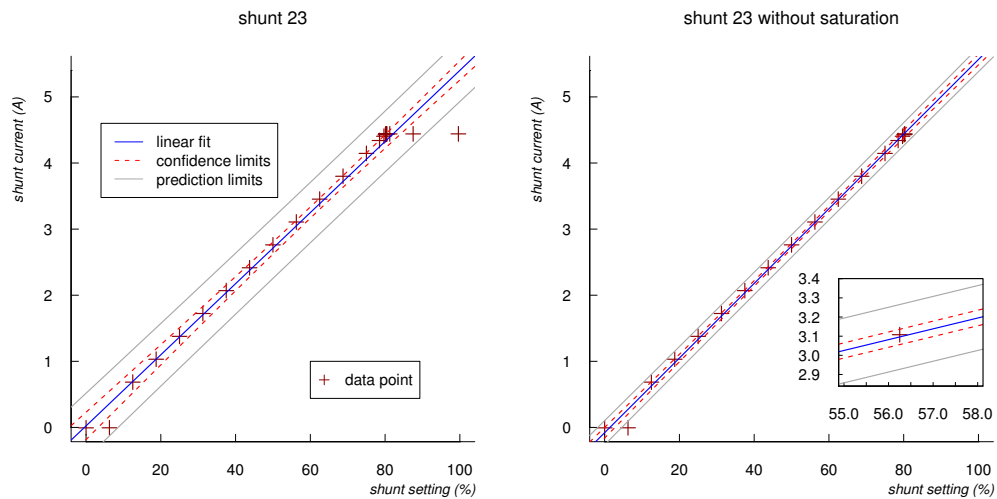


Figure C.7 Shunt current measurement for the shunt 23 with $I_{\text{MAMI}} = 52.8$ A. For detailed information, see the section 5.2.1.

Appendix D

Mass Attenuation Coefficients

It is necessary to know the mass attenuation coefficients μ/ρ of aluminum, air, lead, and fused silica so as to calculate the transmitted photon number, described in section A.3.1. We use three databases of National Institute of Standards and Technology (NIST): the XAAMDI database [148], the FFAST database [149], and the XCOM database [150]. The XAAMDI database covers energies from 1 keV to 20 MeV, the FFAST database does energies from threshold to 433 keV, and the XCOM database does energies from 1 keV to 100 GeV. As a result, using the Akima spline interpolation [147], we combine three databases to extend the energy range, thus this range can cover the range of the synchrotron radiation and the Compton photon.

However, FFAST has no mass attenuation coefficient of the air. XAAMD does not has the fused silica one, but XCOM has. Therefore, we have to use the following equation with the assumption that these two absorbers are homogeneous to calculate μ/ρ of the air and the fused silica from their element mass attenuation coefficients.

$$\left(\frac{\mu}{\rho}\right)_{\text{compounds}} = \sum_i w_i \left(\frac{\mu}{\rho}\right)_i, \quad (\text{D.1})$$

where i is the element and w_i the fraction by weight of the i th atomic constituent. Table D.1 shows detailed information about the absorbers and figure D.1 shows the mass attenuation coefficients. The red points represent the combined values from the three databases and the solid lines are the results that show smooth interpolations of the original data points. We use these interpolation results in order to calculate the transmitted photon rate and to estimate the translucence of shields in section A.3.1.

material	Z/A	ρ (g/cm^3)	Composition:Z	w
Aluminum	0.48181	2.699	—:13	—
Lead	0.39575	11.35	—:82	—
Air	0.49919	1.205×10^{-3}	C:6 N:7 O:8 Ar:18	0.000124 0.755268 0.231781 0.012827
Fused Silica (SiO_2)	0.49930	2.200	Si:14 O:8	0.467435 0.532565

Table D.1 Material constants and composition of Al, Pb, air, and SiO_2 [149, 148]. Z/A represents the atomic number-to-mass for Al and Pb and does the mean ratio of atomic number-to-mass, ρ the density, and w the fraction by weight.

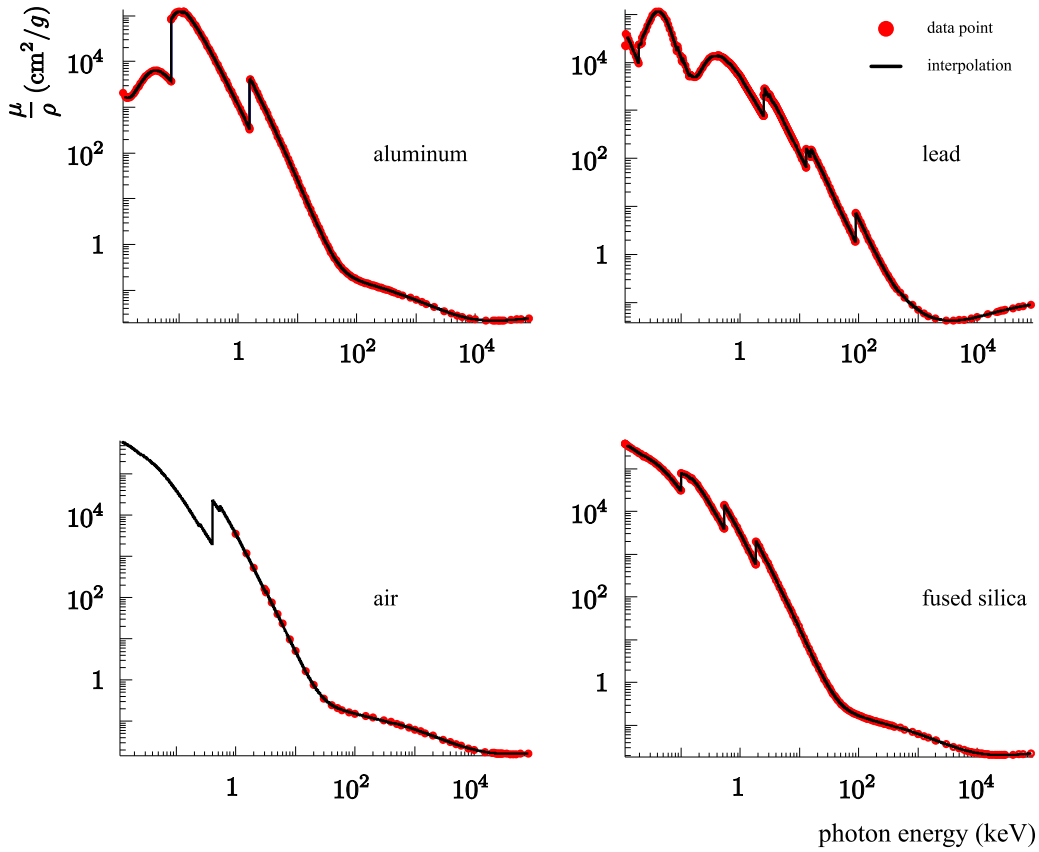


Figure D.1 The mass attenuation coefficients of the absorbers. The red circle data points [149, 148, 150] are well match to the result of the Akima spline interpolation [147].

Appendix E

Drawings of the Scintillating Fiber Electron Detector

Note that the drawings with a \blacklozenge symbol have some modifications during the production process due to some technical reasons.

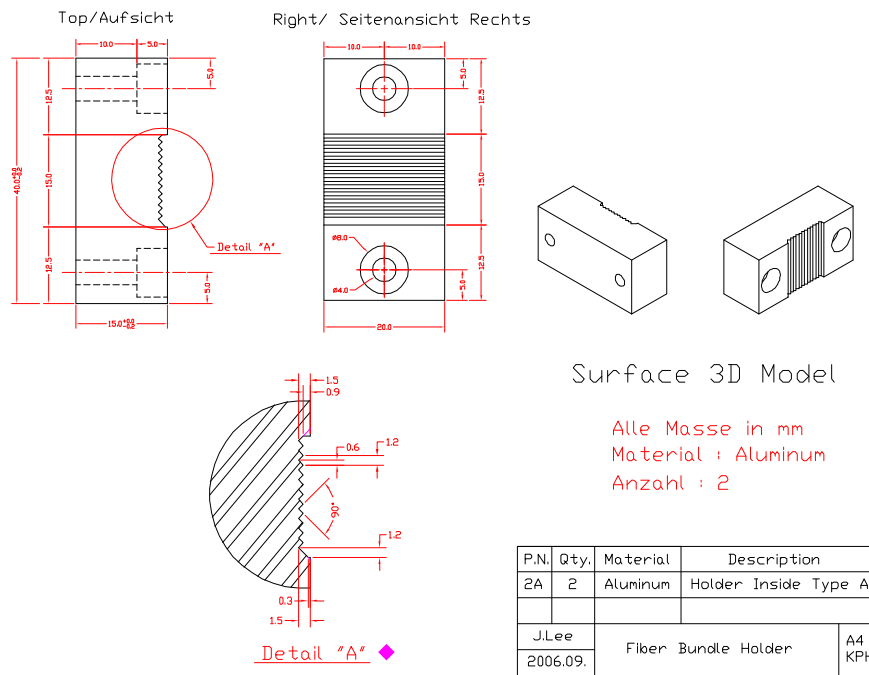


Figure E.1 Fiber Bundle Holder Inside Type A \blacklozenge

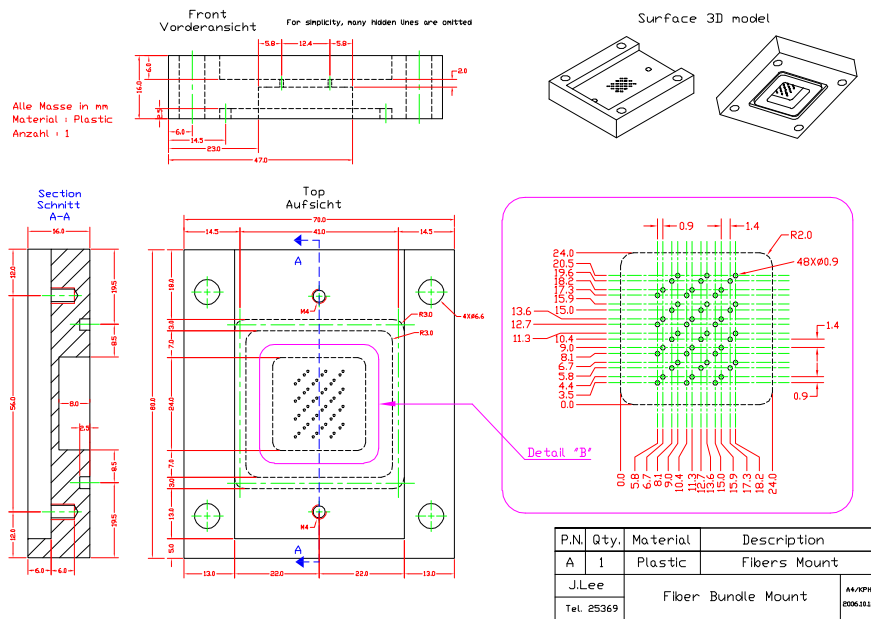


Figure E.4 Fiber Array Mount Type I ♦

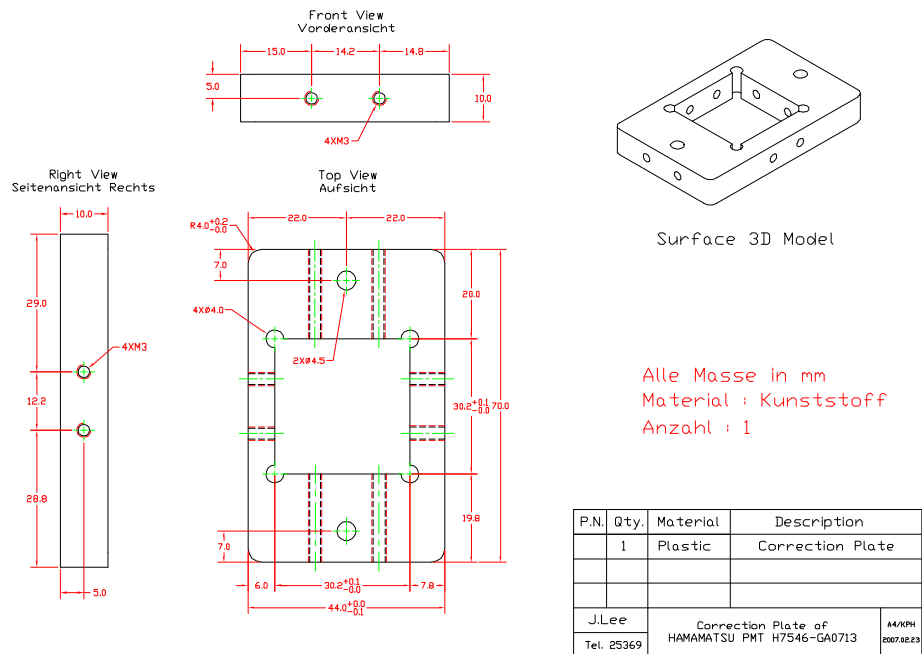


Figure E.5 H7546-GA07123 Correction Plate

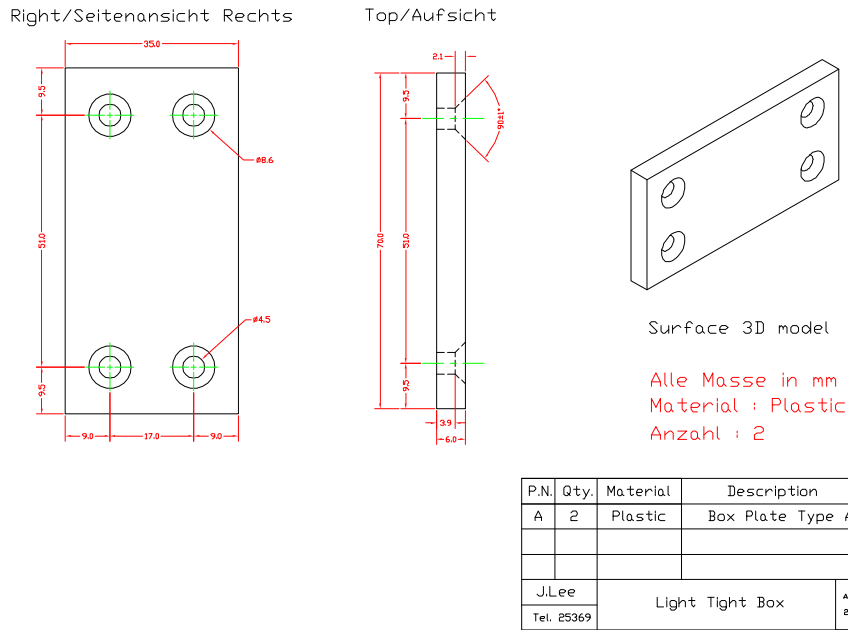


Figure E.6 Light Tight Box Type A for H7546

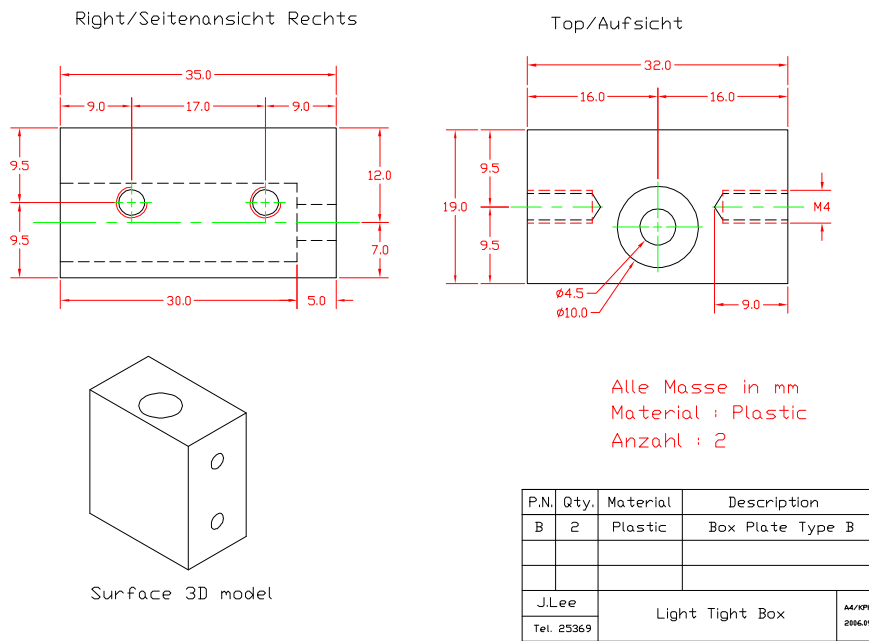


Figure E.7 Light Tight Box Type B for H7546

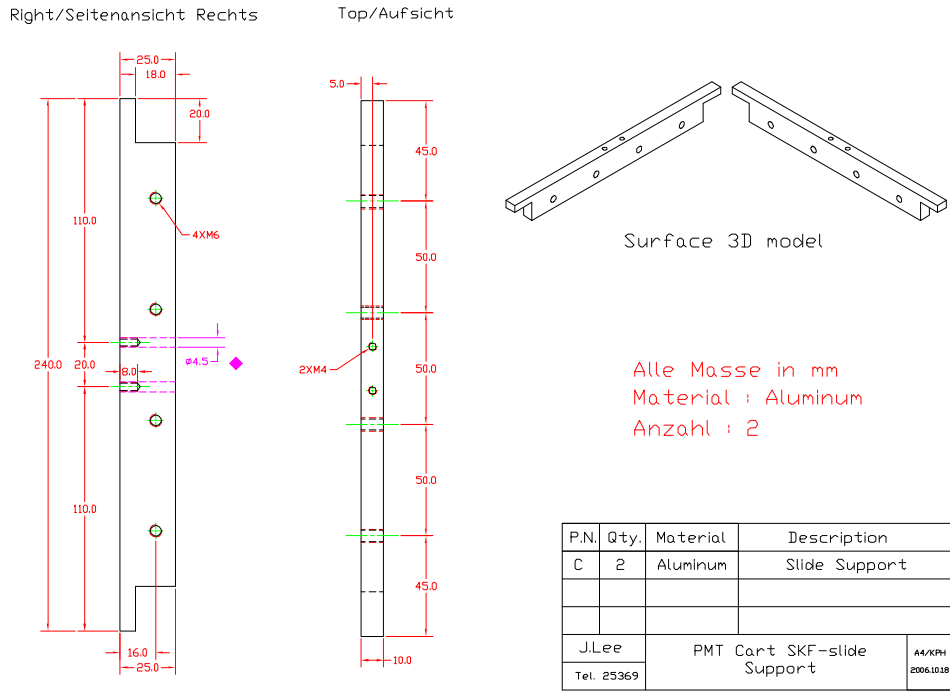


Figure E.8 SKF Slide Support ♦

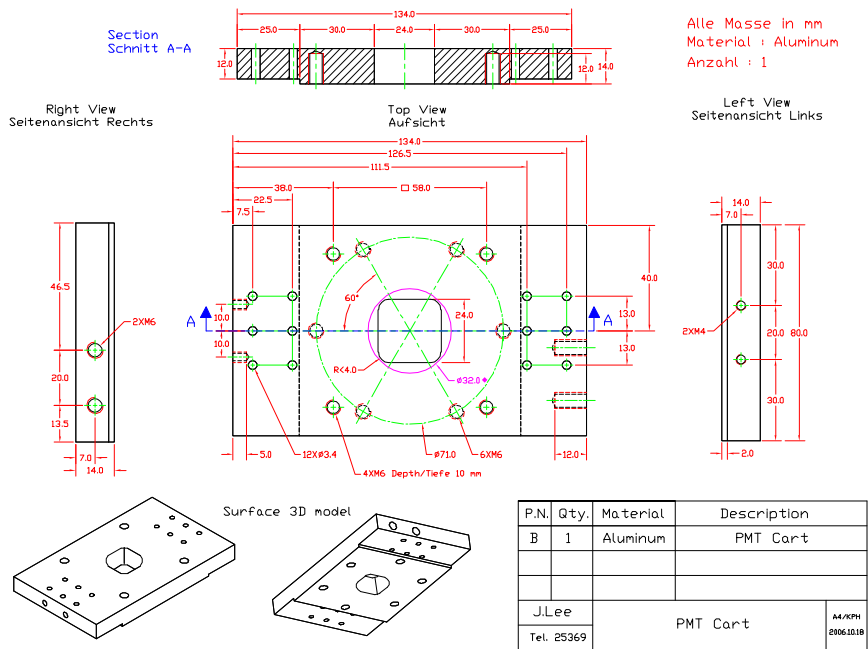
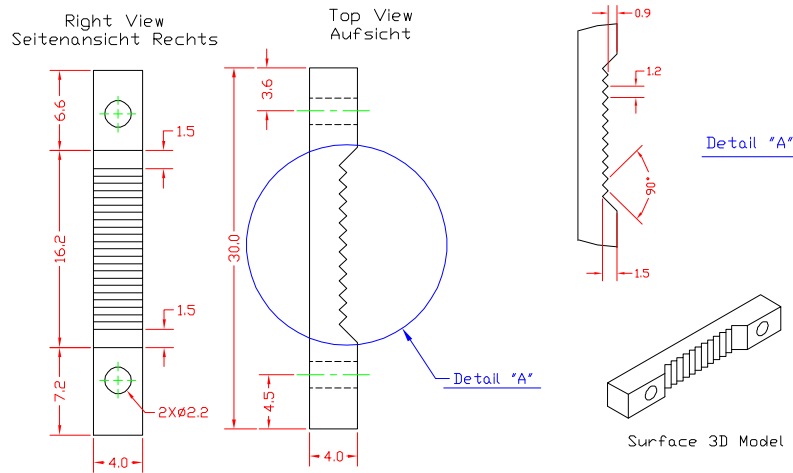


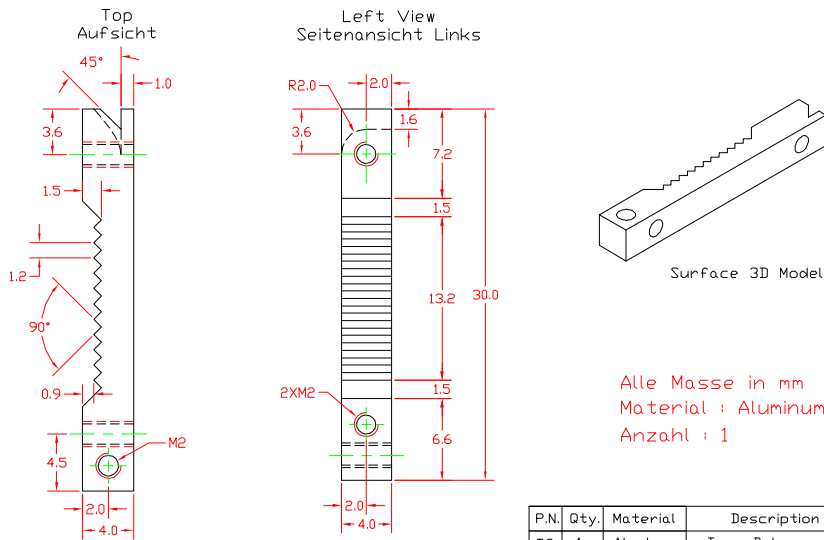
Figure E.9 Photomultiplier Tube Cart ♦



Alle Masse in mm
Material : Aluminum
Anzahl : 2

P.N.	Qty.	Material	Description
A	2	Aluminum	Wire Mount Type A
J.Lee Tel. 25369	Wire Mount of the Fiber Detector		M/KPH 2007/06/17

Figure E.10 Wire Mount Type A



Alle Masse in mm
Material : Aluminum
Anzahl : 1

P.N.	Qty.	Material	Description
B2	1	Aluminum	Type B lower part
J.Lee Tel. 25369	Wire Mount of the Fiber Detector		M/KPH 2007/06/17

Figure E.11 Wire Mount Type B-Down ♦

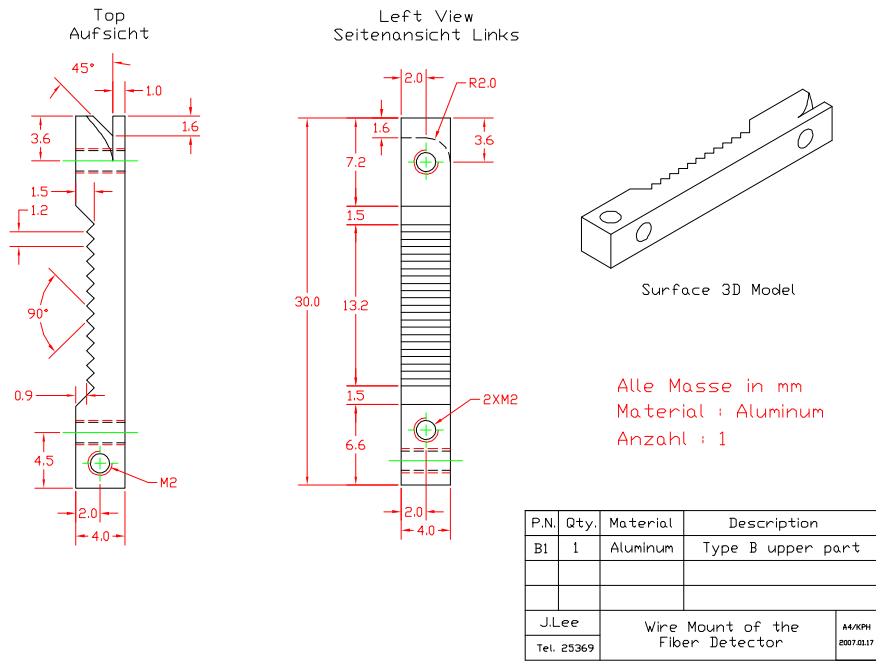


Figure E.12 Wire Mount Type B-Up ♦

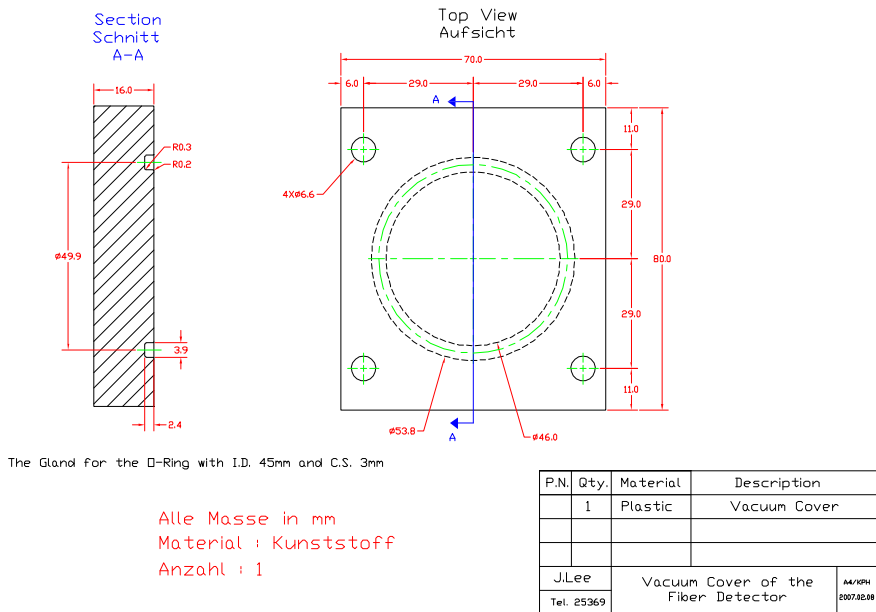


Figure E.13 Vacuum Cover

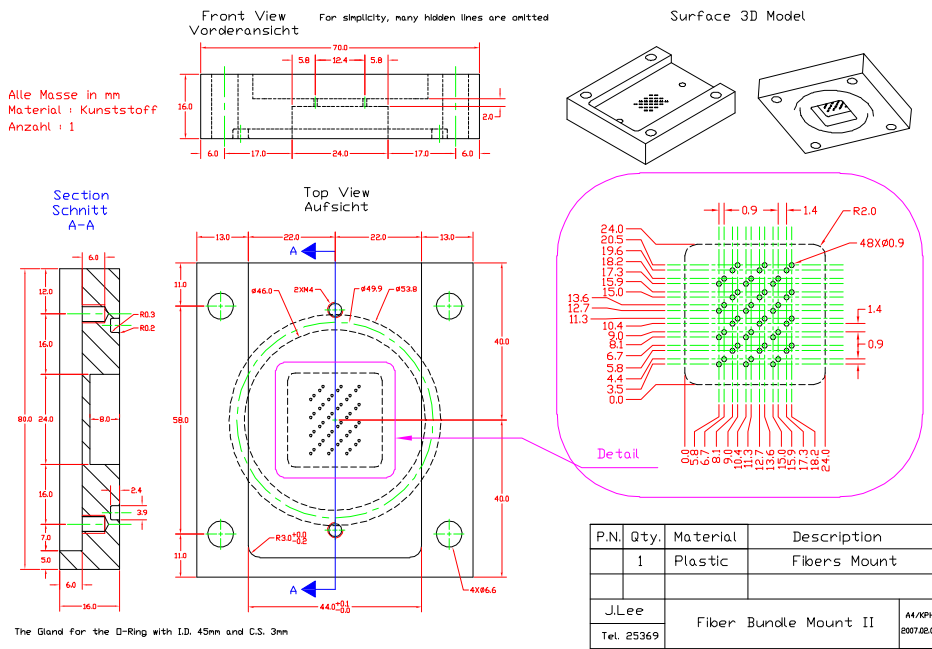


Figure E.14 Fiber Array Mount Type II

Appendix F

O-ring Gland for the Vacuum Sealing

O-ring gland of the fiber array mount was designed according to the suggestion of one vacuum engineer at MAMI. Even though the fiber mount array passed the vacuum leakage test, the exact dimensions of the O-ring gland are needed to select the proper O-ring.

Five dimensions, which are O-ring inner diameter (O_{id}), O-ring cross section (O_{cs}), gland inner diameter (G_{id}), gland depth (G_d), and gland width (G_w), are defined in order to select a suitable O-ring and a correct gland. These dimensions are determined by considering four parameters: (1) interference or stretch; (2) gland fill; (3) compression squeeze; and (4) compression ratio. The interference is defined as

$$\text{Interference} = \frac{G_{id}}{O_{id}} - 1,$$

the gland fill

$$\text{Gland Fill} = \frac{\text{O-ring Cross Section Area}}{\text{Gland Cross Section Area}} = \frac{\pi(O_{cs}/2)^2}{G_w \cdot G_d},$$

the compression squeeze

$$\text{Compression Squeeze} = O_{cs} - G_d,$$

and the compression ratio

$$\text{Compression Ratio} = 1 - \frac{G_d}{O_{cs}}.$$

The fiber array mount is the external pressure face seal. In this case, there are recommended values for four parameters suitable for pressures up

	Design Value	Recommended Value		
		Target	Minimum	Maximum
O-ring Inner Diameter (mm)	45.0	-	-	-
Cross Section (mm)	3.0	-	-	-
Gland Inner Diameter (mm)	46.0	-	-	-
Outer Diameter (mm)	53.8	-	-	-
Depth (mm)	2.4	-	-	-
Width (mm)	3.9	-	-	-
Interference (%)	2.2	2	0	5
Gland Fill (%)	75.5	75	65	85
Compression Squeeze (mm)	0.6	> 0.1	0.1	-
Compression Ratio (%)	20	25	10	35

Table F.1 Design values of dimensions and parameters for O-ring and the gland for the vacuum seal

to 103 bar [151]. The designed values of dimensions and the corresponding parameters are shown in table F.1. The resulting parts are shown in figure E.13 and E.14.